

Andrés Cathey Cevallos

## **Non-linear magnetohydrodynamic simulations of edge localised modes (ELMs)**

**IPP 2021-14**  
**Oktober 2021**



Technische Universität München

Max-Planck-Institut für Plasmaphysik

**Non-linear magnetohydrodynamic simulations of edge  
localised modes (ELMs)**

**Andrés Cathey Cevallos**

Vollständiger Abdruck der von der Fakultät für Physik der Technischen Universität München zur Erlangung der akademischen Grades eines

Doktors der Naturwissenschaften  
genehmigten Dissertation.

Vorsitzende: Prof. Dr. Christine Papadakis

Prüfer der Dissertation:  
1. Hon. Prof. Dr. Sibylle Günter  
2. Prof. Dr. Katharina Krischer

Die Dissertation wurde am 03.05.2021 bei der Technischen Universität München eingereicht und durch die Fakultät für Physik am 24.08.2021 angenommen.





DEPARTMENT OF PHYSICS  
TECHNISCHE UNIVERSITÄT MÜNCHEN

# Non-linear magnetohydrodynamic simulations of edge localised modes (ELMs)

Author: Andrés Cathey Cevallos  
Supervisor: Hon. Prof. Dr. Sibylle Günter  
Advisors: Dr. Matthias Hoelzl  
Submission Date: -----



**HELMHOLTZ**  
RESEARCH FOR GRAND CHALLENGES



 **EUROfusion**



---

## Abstract

The main goal of magnetic confinement fusion is the controlled production of energy through thermonuclear reactions which occur in ionised plasmas at extremely large temperatures ( $\gtrsim 10^8$  K). The tokamak is an axisymmetric toroidal device that is thought to be the closest to achieving such a goal. One of the remaining challenges in tokamaks is the adequate control of plasma instabilities called edge localised modes (ELMs). These instabilities appear in the so-called high confinement mode (H-mode), which is characterised by an edge pressure pedestal together with large edge current density. The magnetic confinement that prevents the hot plasma from touching the material walls becomes repetitively disturbed by ELMs. As a result, plasma is quasi-periodically expelled from the magnetic ‘cage’ and is directed towards the plasma facing components (PFC). Unmitigated type-I ELMs are predicted to cause an unacceptable reduction of the PFC lifetime in the ITER tokamak. Operational regimes without ELMs or with small ELMs and methods to mitigate/suppress large type-I ELMs have been developed and applied in various existing experiments. The risk posed by unmitigated ELMs and the uncertainties in the applicability of ELM control methods have been translated to significant efforts in understanding ELMs and their dynamics through experiments, theory, and simulations. This thesis focuses on the latter.

The non-linear extended MHD code JOREK is used to simulate ELMs in ASDEX Upgrade. In contrast to past simulation efforts, the modelling presented here does not consider initial conditions which are unstable to ELMs. Using initially unstable pedestal profiles makes it impossible to study ELMs in a predictive way because the ELM size will depend on how unstable the initial profiles are. Stable initial conditions are considered, and the pedestal is built-up with *ad-hoc* stationary diffusion coefficients and sources. The simulated build-up represents a simplified approach with the main goal of understanding the behaviour of the instabilities as a stability threshold is crossed. A more sophisticated model for the pedestal build-up will be required for predictive simulations of ELMs, but goes beyond the scope of the present work.

Simulations with sufficiently slow temperature pedestal evolution result in small, quasi-continuous, relaxations of the plasma edge which prevent the excitation of type-I ELMs. These small relaxations show several qualitative similarities to the quasi-continuous exhaust (QCE) regime, which is a small/no-ELM scenario that might be an attractive alternative for ITER. This is an encouraging finding that will be further studied in the

---

future to verify whether quantitative agreement can be obtained. By increasing input heating power the temperature pedestal evolution is accelerated.

At sufficiently large heating power, the small relaxations disappear and the pedestal builds up and a type-I ELM is excited. The type-I ELM rapidly reduces the pressure pedestal and expels roughly 11% of the stored energy. The pressure pedestal begins to build-up again until a second ELM is excited; two further ELMs are then simulated. The initial conditions of the seed perturbations are observed to influence the ELM behaviour. The first simulated ELM is borne out of arbitrary seed perturbations, but the three subsequent ELMs are borne out of seed perturbations that are consistent with the prior occurrence of an ELM crash (as is the case in experimental conditions). The difference in the seed perturbations cause the ELM size and duration to change (between the first ELM and the other simulated ELMs), therefore highlighting the importance of multi-ELM simulations for predictive purposes. These spontaneous type-I ELMs are then compared in detail to pellet-triggered ELMs. The triggered ELM simulations are obtained from [S. Futatani *et al* *Nuclear Fusion* **61**, 046043 (2021)] and were produced by using the pedestal build-up established in this thesis. ELMs are triggered prematurely in the build-up resulting in lower ELM sizes. However, it is observed that pellet-triggered ELMs deposit their energy on a roughly 30% smaller area than spontaneous ELMs.

---

## Zusammenfassung

Das Hauptziel der magnetischen Einschlussfusion ist die kontrollierte Energieerzeugung durch thermonukleare Reaktionen, die in ionisierten Plasmen bei extrem hohen Temperaturen auftreten ( $\gtrsim 10^8$  K). Der Tokamak ist eine achsensymmetrische toroidale Konfiguration, von der angenommen wird, dass sie dem Erreichen eines solchen Ziels am nächsten kommt. Eine der verbleibenden Herausforderungen bei Tokamaks ist die zuverlässige Kontrolle von Plasmainstabilitäten, die als Edge Localized Moden (ELMs) bezeichnet werden. Diese Instabilitäten treten in der sogenannten High-Confinement-Mode (H-Mode) auf, die durch einen Druckpedestal zusammen mit einer großen Randstromdichte gekennzeichnet ist. Der magnetische Einschluss, der verhindert, dass das heiße Plasma die Materialwände berührt, wird wiederholt durch ELMs gestört. Infolgedessen wird Plasma quasi periodisch aus dem magnetischen „Käfig“ zu den Wand-Komponenten ausgestoßen. Es wird vorausgesagt, dass uneingeschränkte Typ-I-ELMs eine inakzeptable Verringerung der Wandlebensdauer im ITER-Tokamak verursachen. Betriebsregime ohne ELMs oder mit kleinen ELMs und Methoden zur Abschwächung bzw. Unterdrückung großer Typ-I-ELMs wurden entwickelt und in verschiedenen bestehenden Experimenten angewendet. Das Risiko unmitigierter ELMs und die Unsicherheiten in der Anwendbarkeit von ELM-Kontrollmethoden wurden durch Experimente, Theorie und Simulationen in erhebliche Anstrengungen zum Verständnis von ELMs und ihrer Dynamik untersucht. Diese Arbeit konzentriert sich auf die Dynamik von ELMs.

Der nichtlineare erweiterte MHD-Code JOREK wird verwendet, um ELMs in ASDEX Upgrade zu simulieren. Im Gegensatz zu früheren Simulationen beruht die hier vorgestellte Modellierung nicht auf Anfangsbedingungen, die für ELMs instabil sind. Die Verwendung von anfänglich instabilen Sockelprofilen macht es unmöglich, ELMs auf prädiktive Weise zu untersuchen, da die ELM-Größe davon abhängt, wie instabil die anfänglichen Profile sind. Es werden stabile Anfangsbedingungen verwendet, und der Sockel wird mit stationären Diffusionskoeffizienten und -quellen *ad-hoc* aufgebaut. Der simulierte Aufbau stellt einen vereinfachten Ansatz dar, mit dem Hauptziel, das Verhalten der Instabilitäten beim Überschreiten einer Stabilitätsschwelle zu verstehen. Für prädiktive Simulationen von ELMs wird ein komplexeres Modell für den Sockelaufbau benötigt, das jedoch über den Rahmen der vorliegenden Arbeit hinausgeht.

---

Simulationen mit ausreichend langsamer Temperaturpedestalwicklung führen zu kleinen, quasi kontinuierlichen Relaxationen des Pedestals, die die Anregung von Typ-I-ELMs verhindern. Diese kleinen Relaxationen weisen mehrere qualitative Ähnlichkeiten mit dem QCE-Regime (Quasi-Continuous Exhaust) auf, bei dem es sich um ein Szenario mit kleinen ELMs handelt, das für ITER eine attraktive Alternative darstellen könnte. Dies ist eine ermutigende Erkenntnis, die in Zukunft weiter untersucht wird, um zu überprüfen, ob eine quantitative Übereinstimmung mit dem Experiment erzielt werden kann. Durch Erhöhen der Eingangsheizleistung wird die Entwicklung des Temperatursockels beschleunigt.

Bei ausreichend großer Heizleistung verschwinden die kleinen Relaxationen und der Sockel baut sich auf bis ein Typ-I-ELM angeregt wird. Der Typ-I-ELM reduziert schnell den Drucksockel und stößt ungefähr 11% der gespeicherten Energie aus. Der Drucksockel beginnt sich wieder aufzubauen, bis ein zweiter ELM angeregt wird. Anschließend werden zwei weitere ELMs simuliert. Es wird beobachtet, dass die Anfangsbedingungen der Keimstörungen das ELM-Verhalten beeinflussen. Der erste simulierte ELM wird aus willkürlichen Keimstörungen getragen, aber die drei nachfolgenden ELMs entwickeln sich aus Keimstörungen, die von dem vorherigen Auftreten eines ELMs stammen (wie dies unter experimentellen Bedingungen der Fall ist). Der Unterschied in den Keimstörungen führt dazu, dass sich die ELM-Größe und -Dauer ändern (zwischen dem ersten ELM und den anderen simulierten ELMs), was die Bedeutung von Multi-ELM-Simulationen für Vorhersagezwecke hervorhebt. Diese spontanen Typ-I-ELMs werden dann im Detail mit Pellet-ausgelösten ELMs verglichen. Die Pellet-induzierten ELM-Simulationen kommen dabei aus [S. Futatani *et al* *Nuclear Fusion* **61**, 046043 (2021)] und wurden unter Verwendung des in dieser Arbeit erstellten simulationssetups berechnet. ELMs werden im Aufbau vorzeitig ausgelöst, was zu geringeren ELM-Größen führt. Es wird jedoch beobachtet, dass durch Pellets ausgelöste ELMs ihre Energie auf einer ungefähr 30% kleineren Fläche ablagern als spontane ELMs.

---

## List of publications

Publications in peer-reviewed journals

- **A. Cathey**, M. Hoelzl, S. Futatani, P.T. Lang, K. Lackner, G.T.A. Huijsmans, S.J.P. Pamela, S. Günter, the JOREK team, the ASDEX Upgrade Team, and the EUROfusion MST1 Team. ‘Comparing spontaneous and pellet-triggered ELMs via non-linear extended MHD simulations’. Accepted for publication in *Plasma Physics and Controlled Fusion*, 2021. doi:[10.1088/1361-6587/abf80b](https://doi.org/10.1088/1361-6587/abf80b).
- **A. Cathey**, M. Hoelzl, K. Lackner, G.T.A. Huijsmans, M.G. Dunne, E. Wolfrum, S.J.P. Pamela, F. Orain, and S. Günter. ‘Non-linear extended MHD simulations of type-I edge localised mode cycles in ASDEX Upgrade and their underlying triggering mechanism’. *Nuclear Fusion*, **60** 124007, 2020. doi:[10.1088/1741-4326/abbc87](https://doi.org/10.1088/1741-4326/abbc87)
- S. Futatani, **A. Cathey**, M. Hoelzl, P.T. Lang, G.T.A. Huijsmans, M.G. Dunne, and the EUROfusion MST1 team. ‘Transition from no-ELM response to pellet ELM triggering during pedestal build-up—insights from extended MHD simulations’. *Nuclear Fusion*, **61** 046043, 2021. doi:[10.1088/1741-4326/abdfb4](https://doi.org/10.1088/1741-4326/abdfb4)
- W. Zhang, **A. Cathey**, M. Hoelzl, W. Tierens, V. Bobkov, the ASDEX Upgrade team, and the EUROfusion MST1 team. ‘Scattering of ion cyclotron range of frequency waves by filaments and ELMs’. *Nuclear Fusion*, **60** 096001, 2020.  
doi:[10.1088/1741-4326/ab9a0b](https://doi.org/10.1088/1741-4326/ab9a0b)
- M Hoelzl, GTA Huijsmans, SJP Pamela, M Becoulet, E Nardon, FJ Artola, B Nkonga, CV Atanasiu, V Bandaru, A Bhole, D Bonfiglio, A Cathey, O Czarny, et al. ‘The JOREK non-linear extended MHD code and applications to large-scale instabilities and their control in magnetically confined fusion plasmas’. Accepted for publication in *Nuclear Fusion*, 2021. doi:[10.1088/1741-4326/abf99f](https://doi.org/10.1088/1741-4326/abf99f).
- A. Jansen van Vuuren, B. Geiger, P.A. Schneider, K. Bogar, P.Zs. Poloskei, **A. Cathey**, M. Hoelzl, A.S. Jacobsen, M. Cavedon, R. Dux, and the ASDEX Upgrade Team. ‘Experimental study of ELM induced fast-ion transport using passive FIDA spectroscopy at the ASDEX Upgrade tokamak’. *Nuclear Fusion* **61** 046001, 2021. doi:[10.1088/1741-4326/abd4b7](https://doi.org/10.1088/1741-4326/abd4b7)
- W. Zhang, W. Tierens, V. Bobkov, **A. Cathey**, I. Cziegler, M. Griener, M. Hoelzl, O. Kardaun, the ASDEX Upgrade team, and the EUROfusion team. ‘Interaction between filaments and ICRF in the plasma edge’. *Nuclear Materials and Energy* **26** 100941, 2021. doi:[10.1016/j.nme.2021.100941](https://doi.org/10.1016/j.nme.2021.100941)

---

## Contributions at conferences, seminars, and workshops

- **Invited talk:** A. Cathey, M. Hoelzl, K. Lackner, G.T.A. Huijsmans, M.G. Dunne, E. Wolfrum, S.J.P. Pamela, F. Orain, S. Günter, the JOREK Team, the ASDEX Upgrade Team, and the EUROfusion MST1 Team. ‘MHD simulations of multiple type-I ELM cycles and bifurcation to different ELM types in ASDEX Upgrade’. 47<sup>th</sup> EPS Conference on Plasma Physics, Remote Talk, 2021  
<http://ocs.ciemat.es/EPS2021ABS/pdf/I4.102.pdf>
- **Oral presentation:** A. Cathey, M. Hoelzl, M.G. Dunne, G.T.A. Huijsmans, K. Lackner, F. Orain, S.J.P. Pamela, E. Wolfrum, and S. Günter. ‘JOREK simulations of multiple type-I ELMs and small ELMs in ASDEX Upgrade’. Max Planck Princeton Centre seminar, Remote Talk, 2020 <https://plasmacenter.princeton.edu/events/mppc-seminar>
- **Invited talk:** A. Cathey, M. Hoelzl, K. Lackner, G.T.A. Huijsmans, M.G. Dunne, E. Wolfrum, S.J.P. Pamela, F. Orain, S. Günter, the JOREK Team, the ASDEX Upgrade Team, and the EUROfusion MST1 Team. ‘JOREK simulations of multiple type-I ELMs and small ELMs in ASDEX Upgrade’. 4<sup>th</sup> Asia-Pacific Conference on Plasma Physics, Remote Talk, 2020 <http://aappsdp.org/DPP2020/pdf/MF2-I7.pdf>
- **Oral presentation:** A. Cathey, M. Hoelzl, M.G. Dunne, G.T.A. Huijsmans, K. Lackner, F. Orain, E. Wolfrum, S.J.P. Pamela, and S. Günter. ‘JOREK simulations of multiple type-I ELMs and small ELMs in ASDEX Upgrade’. 37<sup>th</sup> ITPA PEP meeting, Remote Talk, 2020
- **Oral presentation:** A. Cathey, M. Hoelzl, K. Lackner, G.T.A. Huijsmans, M.G. Dunne, E. Wolfrum, S.J.P. Pamela, F. Orain, and S. Günter. ‘MHD simulations of ELM cycles in ASDEX Upgrade’. HEPP Autumn Colloquium, Remote Talk, 2020
- **Oral presentation:** A. Cathey, M. Hoelzl, K. Lackner, G.T.A. Huijsmans, F. Orain, S.J.P. Pamela, M.G. Dunne, S. Günter. ‘JOREK simulations of the ELM cycle’. E2M Programme Seminar, Remote Talk, 2020
- **Oral presentation:** A. Cathey, M. Hoelzl, K. Lackner, G.T.A. Huijsmans, F. Orain, S.J.P. Pamela, M.G. Dunne, S. Günter. ‘Non-linear MHD simulations of type-I ELMs’. ASDEX Upgrade Seminar, Garching, 2020 <https://www.ipp.mpg.de/events/23680/3866883>
- **Oral presentation:** A. Cathey, M. Hoelzl, K. Lackner, G.T.A. Huijsmans, F. Orain, S.J.P. Pamela, M.G. Dunne, S. Günter. ‘Non-linear MHD simulations of type-I ELMs’. IPP Theory Meeting, Berlin, 2019

- 
- **Poster presentation:** A. Cathey, M. Hoelzl, E. Wolfrum, M.G. Dunne, F. Orain, G.F. Harrer, S.J.P. Pamela, G.T.A. Huijsmans, K. Lackner, S. Günter, the JOREK Team, the ASDEX Upgrade Team, and the EUROfusion MST1 Team. ‘Non-linear simulations of ELMs and edge localised instabilities during the inter-ELM pedestal recovery at ASDEX Upgrade’. 17<sup>th</sup> International Workshop on H-mode Physics and Transport Barriers, Shanghai, 2019
  - **Oral presentation:** A. Cathey, M. Hoelzl, M.G. Dunne, G.T.A. Huijsmans, and S. Günter.  
‘Towards ELM cycle simulations for ASDEX Upgrade’. JOREK Annual Meeting, Garching, 2019
  - **Oral presentation:** A. Cathey, M. Hoelzl, M.G. Dunne, G.T.A. Huijsmans, and S. Günter.  
‘Towards inter-ELM and ELM cycle simulations for ASDEX Upgrade’. HEPP Seminar, Garching, 2019
  - **Poster presentation:** A. Cathey, M. Hoelzl, M.G. Dunne, G.T.A. Huijsmans, and S. Günter.  
‘Non-linear simulations of inter-ELM activity in ASDEX Upgrade’. DPG-Frühjahrstagung der Sektion Materie und Kosmos (SMuK), Munich, 2019 <https://www.dpg-verhandlungen.de/year/2019/conference/muenchen/part/p/session/18/contribution/97>
  - **Poster presentation:** A. Cathey, M. Hoelzl, M.G. Dunne, G.T.A. Huijsmans, and S. Günter.  
‘Towards non-linear simulations of inter-ELM activity and ELM cycles’. FuseNet PhD event, ITER, 2018
  - **Oral presentation:** A. Cathey, M. Hoelzl, M.G. Dunne, G.T.A. Huijsmans, and S. Günter.  
‘Towards ELM cycle simulations for ASDEX Upgrade’. IPP Theory Meeting, Ringberg, 2018
  - **Oral presentation:** A. Cathey, M. Hoelzl, M.G. Dunne, G.T.A. Huijsmans, and S. Günter.  
‘Towards ELM cycle simulations for ASDEX Upgrade’. AUG Ringberg Meeting, Ringberg, 2018
  - **Poster presentation:** A. Cathey, M. Hoelzl, M.G. Dunne, A.F. Mink, E. Wolfrum, G.T.A. Huijsmans, and S. Günter. ‘Towards non-linear simulations of inter-ELM activity and ELM cycles’. Joint Varenna-Lausanne International Workshop on Theory of Fusion Plasmas, Varenna, 2018
  - **Oral presentation:** A. Cathey, M. Hoelzl, M.G. Dunne, A.F. Mink, E. Wolfrum, G.T.A. Huijsmans, and S. Günter. ‘Towards ELM cycle simulations for ASDEX Upgrade’. HEPP Seminar, Garching, 2018

- 
- **Oral presentation:** A. Cathey, M. Hoelzl, M.G. Dunne, A.F. Mink, E. Wolfrum, G.T.A. Huijsmans, and S. Günter. ‘Towards ELM cycle simulations for ASDEX Upgrade’. JOREK Annual Meeting, Culham, 2018
  - **Poster presentation:** A. Cathey, M. Hoelzl. and F. Orain. ‘Towards nonlinear simulations of full ELM cycles’. DPG-Frühjahrstagung der Sektion Atome, Moleküle, Quantenoptik und Plasmen (SAMOP), Erlangen, 2018 <https://www.dpg-verhandlungen.de/year/2018/conference/erlangen/part/p/session/11/contribution/2>

# Contents

<b>1</b>	<b>Introduction</b>	<b>1</b>
1.1	General introduction . . . . .	1
1.2	The tokamak . . . . .	2
1.2.1	Transport and confinement . . . . .	3
1.2.2	H-mode . . . . .	5
1.3	Macroscopic edge instabilities . . . . .	6
1.3.1	Type-I edge localised modes (ELMs) . . . . .	6
1.3.2	ELM control and small/no ELM regimes . . . . .	7
1.4	Thesis structure . . . . .	9
<b>2</b>	<b>Physical model and the JOREK code</b>	<b>11</b>
2.1	Derivation of magnetohydrodynamics (MHD) equations . . . . .	11
2.2	MHD for magnetic confinement . . . . .	15
2.2.1	Coordinate system . . . . .	15
2.2.2	Ideal MHD – infinitely conducting plasma . . . . .	18
2.2.3	Plasma equilibrium – Grad-Shafranov equation . . . . .	19
2.2.4	Reduced MHD . . . . .	21
2.2.5	Extended MHD . . . . .	22
2.2.6	What else is missing in MHD? . . . . .	24
2.3	MHD edge instabilities . . . . .	25
2.3.1	Classification of ideal MHD instabilities . . . . .	27
2.3.2	Pressure gradient-driven modes . . . . .	29
2.3.3	Current-driven modes . . . . .	29
2.3.4	Stability of non-stationary plasmas . . . . .	31
2.4	JOREK . . . . .	32
2.4.1	Temporal discretisation . . . . .	32
2.4.2	Spatial discretisation . . . . .	33
2.4.3	Governing equations . . . . .	35
<b>3</b>	<b>Overview of experiments and MHD simulations</b>	<b>39</b>
3.1	High confinement mode (H-mode) . . . . .	39
3.1.1	Role of the radial electric field . . . . .	40
3.1.2	Type-I ELMs and other ELM types . . . . .	41
3.1.3	Naturally ELM-free regimes . . . . .	42
3.1.4	ELM mitigated or suppressed regimes . . . . .	43
3.2	The type-I ELM cycle . . . . .	45
3.2.1	Phase I: $\nabla n_e$ and $\nabla T_i$ saturation . . . . .	45

3.2.2	Phase II: $\nabla T_e$ saturation . . . . .	47
3.2.3	Pre-ELM phase: constant gradients and pedestal widening . . . . .	47
3.2.4	ELM crash . . . . .	48
3.3	Simulations of ELMs . . . . .	51
3.4	Small ELMs and QCE at ASDEX Upgrade (AUG) . . . . .	54
3.4.1	QCE regime . . . . .	54
3.4.2	Small ELMs with bad confinement . . . . .	55
<b>4</b>	<b>Small ELMs at low triangularity</b>	<b>57</b>
4.1	Simulation set-up . . . . .	57
4.1.1	Axisymmetric pedestal build-up . . . . .	59
4.1.2	Bootstrap current density source . . . . .	59
4.1.3	Limitations of the present approach . . . . .	60
4.2	Non-axisymmetric simulations . . . . .	62
4.2.1	Linear growth phase – mode velocity . . . . .	62
4.2.2	Importance of extended MHD . . . . .	65
4.2.3	Non-linear phase . . . . .	67
4.2.4	Filamentary transport . . . . .	68
4.2.5	Divertor heat deposition . . . . .	70
4.3	Two simple paths to type-I ELMs . . . . .	71
4.3.1	Increasing heating power – stronger radial electric field . . . . .	72
4.3.2	Decreasing separatrix density . . . . .	75
4.4	Conclusions . . . . .	78
<b>5</b>	<b>Type-I ELMs</b>	<b>81</b>
5.1	Simulation set-up . . . . .	81
5.2	Non-axisymmetric linear and early non-linear evolution . . . . .	83
5.2.1	Early non-linear growth phase – mode coupling . . . . .	84
5.3	Type-I ELM cycles . . . . .	86
5.3.1	ELM crash and inter-ELM activity . . . . .	87
5.3.2	Seed perturbations . . . . .	88
5.3.3	Heating power dependency . . . . .	90
5.3.4	Varying the scrape-off layer density . . . . .	92
5.4	ELM triggering mechanism . . . . .	93
5.4.1	The role of resistivity – magnetic reconnection . . . . .	94
5.4.2	Heat and particle transport in stochastic magnetic fields . . . . .	94
5.5	Conclusions . . . . .	97
<b>6</b>	<b>Pellet-triggered ELMs</b>	<b>99</b>
6.1	Introduction . . . . .	99
6.2	Pellet module in JOREK . . . . .	101
6.2.1	Previous pellet-triggered ELM JOREK simulations . . . . .	102
6.3	Simulation set-up and parameters . . . . .	102
6.3.1	Pellet injection – sizes and trajectory . . . . .	103

6.4	Spontaneous and pellet-triggered ELMs . . . . .	105
6.4.1	Spontaneous ELMs . . . . .	105
6.4.2	Pellet-triggered ELMs . . . . .	109
6.4.3	Comparison of Sp-318 and Tr-08-14ms . . . . .	114
6.4.4	Mode structures . . . . .	116
6.5	Comparison between spontaneous and pellet-triggered ELM . . . . .	118
6.5.1	ELM-induced thermal energy losses . . . . .	119
6.5.2	Toroidal mode spectrum . . . . .	120
6.5.3	Heat flux and energy fluence comparison . . . . .	121
6.6	Conclusions . . . . .	126
<b>7</b>	<b>Conclusions and Outlook</b>	<b>129</b>
7.1	Resistive peeling-ballooning modes during the QCE regime . . . . .	130
7.2	The importance of seed perturbations . . . . .	130
7.3	Pellet-triggered ELMs and spontaneous ELMs . . . . .	131
7.4	Outlook . . . . .	132
<b>Bibliography</b>		<b>135</b>

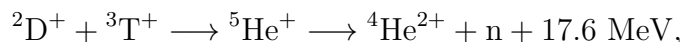


# 1 Introduction

## 1.1 General introduction

Nuclear fusion is the physical process that governs the merging of atomic nuclei and the associated energy release. The energy and the atomic nuclei produced by stars is a result of nuclear fusion reactions taking place in the stellar core. The idea behind said process, now known as stellar nucleosynthesis, was first posed roughly 100 years ago by Eddington [1]. The stellar core is constituted of hot ( $\sim 10^7$  K  $\equiv 859$  eV) and dense ( $\sim 10^5$  kg/m<sup>3</sup>) plasma, i.e., ionised gas displaying collective behaviour with positively charged ions and negatively charged electrons that move independently of each other. Achieving energy production through controlled nuclear fusion has been pursued for the past  $\sim 80$  years. One of the leading approaches for such endeavour takes advantage of the fact that charged particles remain helically bound to a magnetic field line by the Lorentz force and is called magnetic confinement fusion (MCF) [2].

Several devices have been conceptualised and developed for MCF, but fusing deuterium and tritium in the tokamak (conceived in the 1950s by Russian physicists Andrei Sakharov and Igor Tamm) is the closest to ‘breakeven’ at present; namely, generating as much energy as is consumed. Deuterium, D, and tritium, T, are isotopes of hydrogen with one and two neutrons, respectively. Their fusion reaction,



ultimately results in an  $\alpha$ -particle ( $^4\text{He}^{2+}$ ) and a neutron, with a combined kinetic energy of 17.6 MeV<sup>1</sup>. The ratio of the energy produced through controlled D-T nuclear fusion and the total power feeding energy to the device is called the fusion power amplification factor (fusion  $Q$ -factor)  $Q = P_{\text{fusion}}/P_{\text{total}}$  [3]. At the moment, not a single concept that attempts to generate energy through controlled nuclear fusion has reached the breakeven point,  $Q = 1$ , in steady-state operation. Most present-day devices operate with a pure D plasma because the 14.1 MeV neutron produced by D – T fusion activates wall materials and complicates operation, and also because T is an extremely scarce radioactive element which does not exist in nature.

Achieving  $Q \geq 1$  is the main goal of the ITER tokamak, presently under construction in France;  $Q = 10$  is estimated for ITER high-performance operation [4]. The heat produced by the ITER tokamak will not be turned into electricity. If

---

<sup>1</sup>The  $\alpha$ -particle has an energy of 3.5 MeV which, as a charged particle, can remain confined and heat the plasma. The neutron holds the remaining energy.

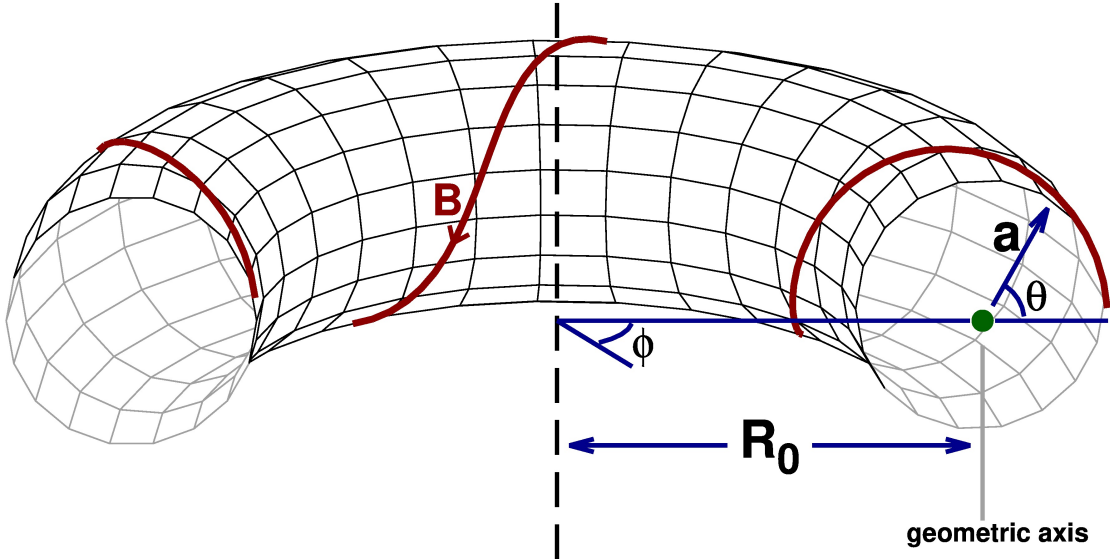


Figure 1.1: Toroidal geometry with minor radius ( $a$ ), major radius ( $R_0$ ), and geometric axis. The toroidal and poloidal angles,  $\phi$  and  $\theta$  respectively, are depicted. Finally, a magnetic field line with  $q = 0.2$ , i.e., in 1 toroidal turn it makes 5 poloidal turns, is shown in dark red colour. The safety factor below unity is not realistic; it is chosen for illustrative purposes only.

all the power requirements would be considered, and the energy lost in converting heat into electricity, ITER would roughly reach net breakeven [5]. The tokamak concept, and large-scale instabilities that could be deleterious for ITER, will be introduced in this chapter. Finally, a few sentences describe the thesis structure.

## 1.2 The tokamak

Tokamaks are toroidal devices that confine plasma through adequately configured near-axisymmetric magnetic fields. Figure 1.1 shows a torus and the definitions of major radius ( $R_0$ ), minor radius ( $a$ ), and geometric axis. The toroidal and poloidal angles are also shown, and are denoted by  $\phi$  and  $\theta$ , respectively. The strongest magnetic field in a tokamak is the toroidal magnetic field,  $B_{\text{tor}}$ , but this alone cannot produce a stable configuration. The magnetic fields necessary to hold the plasma in equilibrium are generated by toroidal field coils, poloidal field coils, vertical stability coils, and by the plasma current ( $I_p$ ). It is also possible to confine plasma in an MCF device with  $I_p = 0$ ; however, this requires non-axisymmetric, i.e., 3D, coils to produce the magnetic fields required for stability. Such devices with 3D coils are called stellarators [6]. For tokamaks, the magnetic fields that confine the plasma are wound around the torus; think of the protrusions of a screw as the winding magnetic field lines. The dark red line in fig. 1.1 exemplifies a winding magnetic field ( $\mathbf{B}$ ).

The number of toroidal turns made by a magnetic field line per single poloidal turn is called the safety factor,  $q$ . Small values of the safety factor relate to magnetic configurations which are unstable to current-driven macroscopic instabilities. The meaning behind its name comes from the fact that this value must be above 2 at the edge of the confined plasma in order to maintain stability (to external kink modes) [7]. At constant toroidal magnetic field strength, the safety factor decreases with increasing  $I_p$ . Therefore, it is not possible to operate a tokamak with arbitrarily large plasma current due to the potential excitation of current-driven instabilities, but it is also not possible to operate with  $I_p = 0$ . Another problem related to the plasma current is that most of it is typically induced by a transformer coil in the centre of the torus and, therefore, it is intrinsically pulsed, which represents an important problem for tokamak steady-state operation. Advanced scenarios that use non-inductive current need to be developed for future fusion power plants; in AUG an advanced scenario with  $\gtrsim 90\%$  non-inductive current fraction has been transiently achieved [8].

For optimal energy production, the confined ion temperature has to be more than ten times hotter than the stellar core ( $\sim 10 - 20$  keV). However, due to operational limits<sup>2</sup>, the plasma density and pressure have to be significantly smaller ( $\sim 10^{-7}$  kg/m<sup>3</sup> and a few bar, respectively). Thanks to the confining magnetic fields, the hot plasma mostly avoids contact with the material walls. Otherwise, the plasma facing components (PFCs), which experience melting and/or erosion at ‘small’ temperatures (electron temperatures above  $\sim 10$  eV) [10], would become damaged. Such high temperatures at the plasma core are indeed routinely obtained in several tokamak experiments worldwide. Albeit at more extreme circumstances, the heat insulation provided by the magnetic fields is roughly 10 times better than Styrofoam used for insulating buildings [3].

### 1.2.1 Transport and confinement

The good thermal insulation provided by the near-axisymmetric magnetic fields is not perfect. Unfavourable outward heat and particle diffusion is present in tokamaks. The responsible mechanisms of such outward transport are classical, neoclassical, and turbulent transport. The latter makes up most of the heat and particle radial transport in tokamaks and it is driven by gradients in the temperature and density. Classical transport represents only a minor percentage (< 0.01%) of the total heat and particle transport. It is calculated by considering Coulomb collisions only in cylindrical geometry. Neoclassical transport results from Coulomb collisions in the presence of a toroidal geometry, and it is greatly enhanced with respect to classical transport. The relevant modifications due to the toroidal geometry are related to charged particles trapped to so-called banana trajectories shown in fig. 1.2: ② and ③ [11].

---

<sup>2</sup>The *Greenwald density limit* restricts the plasma density below  $n_{GW,[10^{20} \text{ m}^{-3}]} = I_{p,[\text{MA}]} / (\pi a^2)$ , where  $a$  is the tokamak minor radius in m [9].

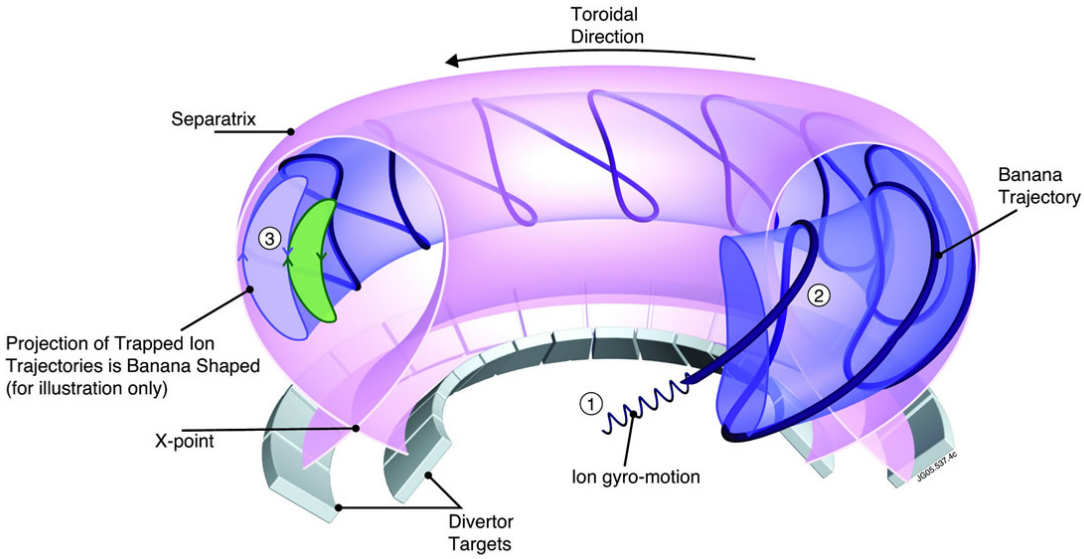


Figure 1.2: Schematic representation of the plasma confined in a diverted tokamak geometry with a single magnetic X-point. The magnetic field amplitude decreases with increasing distance from the centre of the device. The device traps the charged electrons and ions with magnetic fields. The particles describe helical trajectories along the magnetic field lines ①. Due to the inhomogeneous magnetic field, the charged particles can experience a magnetic mirror effect and describe so-called banana trajectories ②. Projected to a poloidal plane, the banana trajectories describe a banana ③. Figure reproduced from Ref. [12].

In addition to causing outward transport, neoclassical physics also causes modifications to the plasma resistivity, and, in the presence of pressure gradients, the formation of a self-generated current, dubbed bootstrap current [13, 14]. A simplified, linear, relationship between the pressure gradient and the bootstrap current density is  $j_{bs} \propto \sqrt{r/R_0} \nabla p / B_{pol}$ , where  $r$  is the minor radius and  $B_{pol}$  is the poloidal magnetic field [15]. The confined plasma has hotter temperatures and larger densities in the core, i.e., near the magnetic axis, than in the edge.

The characteristic time required for the plasma energy to become diffused away (in the absence of external heating sources) by the above described mechanisms is the energy confinement time,  $\tau_E$ . In addition to adequate ionic core temperature and density, a sufficiently long energy confinement time (in the order of a few seconds) is required for a feasible reactor [7]. It may be determined by the ratio between the confined energy,  $W$ , and the rate of energy loss,  $P_L$ ; in steady-state operation and without  $\alpha$ -particle heating (most present-day devices operate with pure deuterium),  $P_L$  balances with the input heating power  $P_{heat}$ . In the early developments of tokamak physics (approximately up to the 1980s), the favourable relation  $\tau_E \propto n a^2$  (where  $a$  is the machine minor radius) was observed, but  $\tau_E$  showed an

unfavourable relation with increasing plasma temperature. Namely, as the heating power was increased,  $\tau_E$  decreased because of the excitation of temperature gradient-driven micro-instabilities [11, 16].

### 1.2.2 H-mode

Fortunately, a sudden increase in  $\tau_E$  and in the core plasma density and temperature was observed in 1982 in the ASDEX tokamak as the input heating power was sufficiently increased. This increase in confinement was dubbed high confinement mode, H-mode, in contrast to the previous state of ‘normal’ operation which later became called low confinement mode, L-mode [17]. The improved confinement was observed for the first time with a divertor (as shown in fig. 1.2), which was originally installed to achieve appropriate exhaust of impurities, and with significant beam heating, which provides both heating and torque input to the plasma. However, the divertor geometry, which allowed for plasmas with lower impurity contents, is not imperative to obtain H-mode conditions [18, 19], and nor is the torque input from beam heating, which causes a toroidal acceleration of the plasma [20, 21].

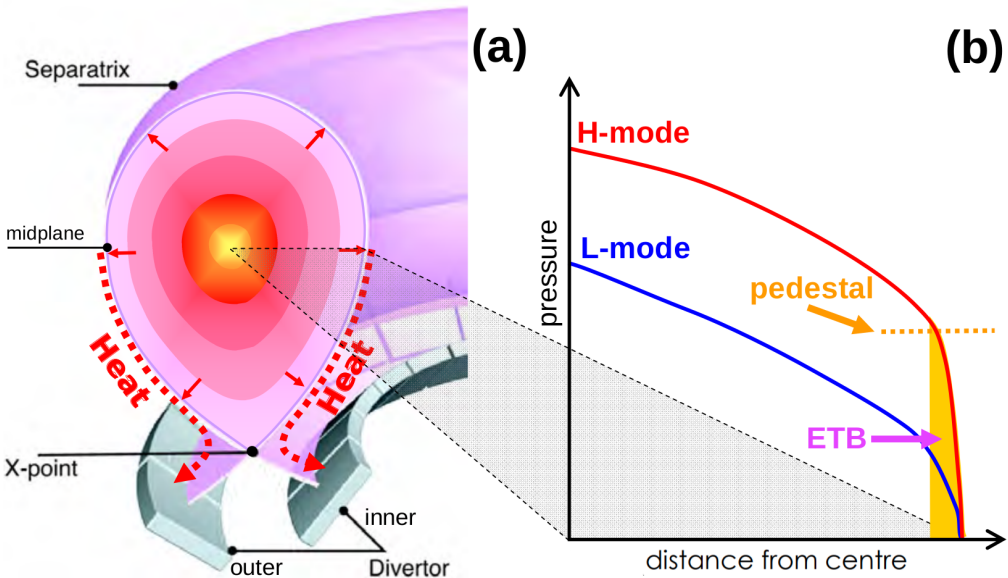


Figure 1.3: Schematic representation of a plasma confined in a diverted tokamak geometry (left), and of the H-mode pedestal (right). Heat (and particles) are transported out of the confined region, i.e., across the separatrix, mainly by turbulent and neoclassical transport. The concepts of *pedestal* and *edge transport barrier* are also shown. Figure reproduced from Ref. [22].

During H-mode operation, a strong suppression of turbulent transport exists in the plasma edge; specifically, in the last few centimeters of confined plasma. This edge region is called the *edge transport barrier* (ETB), and it is shown in fig. 1.3 (right). Very large pressure gradients develop across the ETB, and a so-called

*pedestal* is formed. The gradients in the rest of the confined plasma remain roughly constant between L- and H-mode due to profile stiffness [23] and, as such, the core pressure is rigidly increased with respect to L-mode core profiles. The core pressure is effectively increased by the pedestal height (denoted by the orange arrow in fig. 1.3). Associated to the large gradients that form in the edge of the confined region, a strong neoclassical bootstrap current is also generated (not shown).

### 1.3 Macroscopic edge instabilities

Resulting from large pressure gradients and strong current densities in the edge of the confined region, certain macroscopic instabilities can become excited. Two edge localised instabilities are of particular importance for the work described in this thesis. Large pressure gradients excite *ballooning modes*, which have short wavelengths in the poloidal direction and are poloidally localised to the outboard side of the plasma, called the Low Field Side (LFS). Additionally, large edge current density (and gradient) can excite so-called *external kink (peeling) modes*, which have longer wavelengths in the poloidal direction and are poloidally localised to the top and bottom of the confined plasma. Using a Fourier representation to describe these instabilities results in characteristic poloidal and toroidal mode numbers,  $m$  and  $n$  respectively. The mode numbers can be related to the safety factor on the ‘rational surfaces’ where modes are excited as  $q = m/n$ . Ballooning modes are characterised by large toroidal mode numbers ( $n \gtrsim 10$ ), and peeling modes by low toroidal mode numbers ( $n \lesssim 5$ ). Under the right circumstances, these two instabilities can become coupled and give rise to *peeling-balloonning modes* [24, 25].

#### 1.3.1 Type-I edge localised modes (ELMs)

The coupled peeling-balloonning modes have successfully been used to theoretically describe quasi-periodic events that take place under normal H-mode operation. Said events have been called type-I *edge localised modes*, or ELMs<sup>3</sup> [26]. Several review papers on the topic can be found in Refs. [27–33]. Type-I ELMs cause a significant reduction of the pedestal pressure and of the edge current density in fast timescales (hundreds of  $\mu\text{s}$ ) because plasma is ejected outwards from the confined region. In these timescales, each type-I ELM expels roughly 5 – 15% of the plasma stored energy. A large fraction of the expelled energy is directed towards the divertor targets. The divertor heat loads associated to type-I ELMs are not a cause for concern in present-day tokamaks. However, extrapolations to ITER from an empirical scaling [34] indicate that high performance operation will very likely suffer from unbearably large (i.e., beyond the acceptable  $\sim 0.5 \text{ MJ/m}^2$  for ITER divertor materials [35]) ELM energy fluence to the divertor targets. As such, producing realistic and, eventually, predictive simulations of type-I ELMs could

---

<sup>3</sup>Other ELM types exist, and are covered in chapter 3.1.2

provide insight into what experimental conditions would lead to tolerable divertor heat loads.

Single ELM crash simulations have been performed with several codes, by using initial equilibria that are unstable to peeling-balloon modes, and are described in chapter 3. However, an important requirement to produce realistic simulations of type-I ELMs is to simulate ELM cycles and not single ELM crashes. The reason is that the seed perturbations that give rise to a type-I ELM cannot be self-consistently modelled if only one ELM crash is simulated [36]. In this work, first simulations of type-I ELM cycles are presented, which have been published in Ref. [37]. All simulations presented in this thesis have been performed with the JOREK code, which is described in the next chapter. Indeed, the importance of considering multiple ELMs is highlighted by noting that the first simulated ELM crash is different from the subsequent, self-similar, ELMs.

### 1.3.2 ELM control and small/no ELM regimes

Achieving reliable H-mode operation in the absence of large type-I ELMs is possible by applying mitigation or suppression schemes, or by operating in small/no ELM regimes. Examples of the latter include Quiescent H-mode (QH-mode), I-mode, enhanced D-alpha H-mode (EDA H-mode), grassy ELMs, and quasi-continuous exhaust regime (QCE regime) [38]. An incomplete list of mitigation or suppression schemes includes the application of magnetic perturbation (MP) coils to modify the pedestal structure, and the excitation of ELMs at frequencies larger than the natural ELM frequency by vertical kicks or cryogenic pellet injection [39]. However, such regimes have been sustained only in limited operational spaces, and it remains uncertain whether ITER will be able to achieve the small/no ELM regimes or to adequately suppress/mitigate ELMs. Therefore, it is of interest to validate existing codes against experiments and to predictively assess which schemes could work for ITER.

The QCE regime (previously referred to as type-II ELMs or, more generically, small ELMs), appears in ASDEX Upgrade (AUG) and in the *tokamak à configuration variable* (TCV) with a magnetic configuration featuring high triangularity and closeness to double null together with a high separatrix density [41]. Triangularity is defined as  $\delta = (d_u + d_l)/2a$ , where  $d_{u,l}$  are depicted in fig. 1.4; closeness to double null is described by a small separation between primary and secondary separatrices<sup>4</sup> measured at the outer midplane,  $\Delta r_{sep}$ .

A quasi-continuous regulation of the pedestal is present during the QCE regime, such that no type-I ELMs appear. The mechanism(s) that stop the plasma from exhibiting type-I ELMs are not yet entirely clear. Ballooning modes localised near the separatrix are thought to be responsible [42]. In this thesis, simulations with remarkably similar features as those characteristic of the QCE regime are reported. In said simulations, resistive peeling-balloon modes localised very near the sepa-

---

<sup>4</sup>Unless specified otherwise, separatrix refers to the primary separatrix.

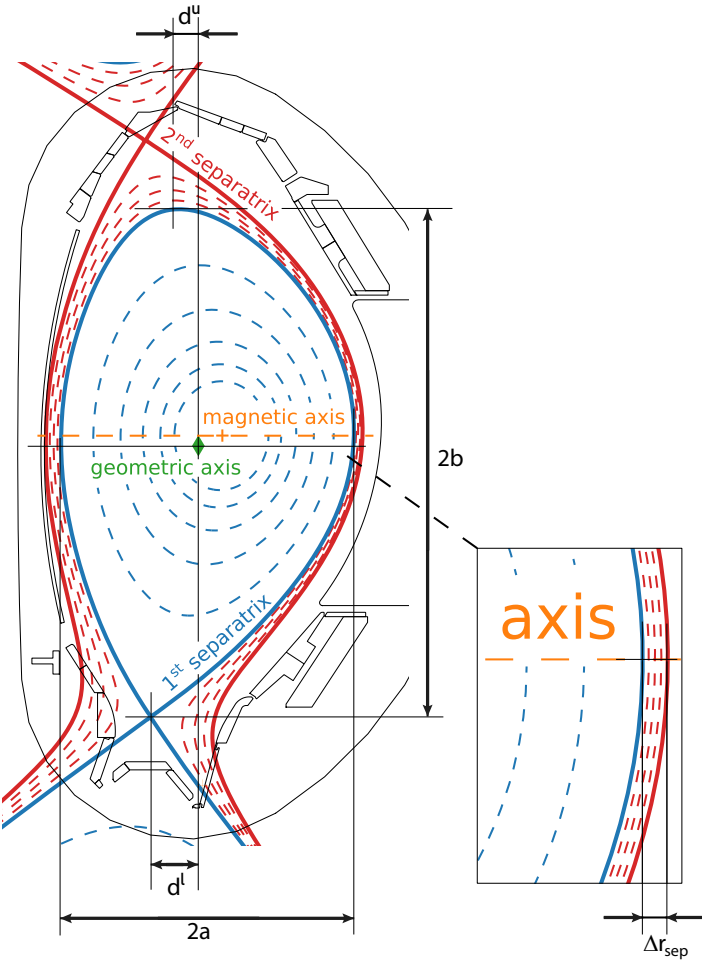


Figure 1.4: Magnetic equilibrium from an AUG discharge with a configuration close to double null. The concepts of geometric and magnetic axis, first and second separatrix, lower and upper triangularity ( $\delta_l = d^l/a$  and  $\delta_u = d^u/a$ , respectively), elongation ( $\kappa = b/a$ ), and the distance between the two separatrices at the outer midplane ( $\Delta r_{sep}$ ) are depicted. Figure reproduced from Ref. [40].

ratrix are present. These modes increase and decrease in amplitude without a clear periodic behaviour, and are identified as the responsible mechanism for regulating the pedestal below type-I ELM unstable conditions. Qualitatively similar to experiments, increasing the heating power in the simulations stabilises the resistive peeling-balloonning modes and type-I ELMs become excited.

Finally, pellet-ELM triggering, one of the ELM mitigation methods mentioned above, is also investigated in this work. Deuterium pellets of two different sizes are injected at different time points during the simulated pedestal build-up, but before an ELM crash spontaneously appears. It is then possible to compare the pellet-triggered ELMs to the spontaneous ELM in terms of the dominant perturbations

and non-linear dynamics. Using this approach, the pellet-ELM triggering lag-time observed experimentally in metal walled tokamaks<sup>5</sup> was obtained in simulations for the first time [45]. The comparison of the simulated pellet-triggered ELMs and spontaneous ELMs is presented in Chapter 6, and has been submitted to *Plasma Physics and Controlled Fusion*. A corresponding pre-print can be found in Ref. [46].

## 1.4 Thesis structure

This thesis is organised as follows. The second chapter describes magnetohydrodynamic (MHD) theory and the JOREK code which is used to produce all the simulations presented in this thesis. Chapter 3 presents relevant experimental findings and previous modelling work.

Simulations of peeling-balloonning modes that constantly regulate the pedestal below a type-I ELM unstable condition, i.e., small ELMs, are shown in Chapter 4. Thereafter, Chapter 5 presents published results of type-I ELM cycles simulated with JOREK by enforcing the pedestal build-up (from Ref. [37]). A comparison between spontaneous type-I ELMs and ELMs triggered by cryogenic deuterium pellet injection is presented in Chapter 6. Finally, conclusions and plans for future work are provided in Chapter 7.

---

<sup>5</sup>After an ELM crash, a finite amount of time has to pass in order to trigger an ELM through pellet injection. This is the pellet-ELM triggering lag-time, which has been observed in metal-walled tokamaks, but not with carbon walls [43, 44].



## 2 Physical model and the JOREK code

All simulations presented in this work are performed with the reduced MHD model within the JOREK code [47–50]. This chapter is devoted to describing the assumptions that need to be made in order to arrive at the reduced MHD equations. First, in section 2.1 the derivation of the single fluid MHD equations is described. Section 2.2 is devoted to the specific case of tokamak devices and the different simplifications that can be made to MHD in order to describe specific features of plasmas inside tokamaks. Different instabilities that may arise in the edge of tokamak plasmas are described in section 2.3. Finally, section 2.4 details the main characteristics of the JOREK code.

### 2.1 Derivation of magnetohydrodynamics (MHD) equations

This section roughly follows Refs. [15, 51–54]. The most detailed description of plasma dynamics comes from the Boltzmann equation applied to each species present in the plasma (ions and electrons). The Boltzmann equation describes the time-evolving probability distribution function  $f_\alpha$  of the species  $\alpha$ . It states that in the absence of collisions between particles, the total time derivative of  $f_\alpha$  is zero. The probability distribution function is a function of time, position, and velocity:  $f_\alpha = f(t, \mathbf{x}, \mathbf{u})$ . Using the chain rule, Boltzmann equation becomes

$$\frac{df_\alpha}{dt} = \frac{\partial f_\alpha}{\partial t} + \mathbf{u} \cdot \frac{\partial f_\alpha}{\partial \mathbf{x}} + \frac{\mathbf{F}_\alpha}{m_\alpha} \cdot \frac{\partial f_\alpha}{\partial \mathbf{u}} = \left( \frac{\partial f_\alpha}{\partial t} \right)_{\text{collisions}}. \quad (2.1)$$

In the equation above, the force acting on a given particle of species  $\alpha$  is the Lorentz force,  $\mathbf{F}_\alpha = q_\alpha(\mathbf{E} + \mathbf{u} \times \mathbf{B})$  where  $q_\alpha$  is the electric charge of said species. For magnetic confinement fusion (MCF), the gravitational force is neglected because it is much weaker than the electromagnetic forces. The above equation is only valid in spatial scales larger than the gradient scale lengths and longer than the Debye length  $\lambda_D$ , i.e., scales where the long-range electrostatic interaction between single particles is shielded by the surrounding oppositely charged particles.

Other than the collision operator in eqn. (2.1), the expressions for  $\mathbf{E}$  and  $\mathbf{B}$  are required to form a closed system of equations. The latter come from Maxwell's equations (2.2)-(2.5), where  $\sigma$  is the volumetric charge density,  $\mathbf{J}$  the current density, and  $c$ ,  $\epsilon_0$  and  $\mu_0$  are the speed of light, permittivity and magnetic permeability in vacuum, respectively. Ionised plasmas of interest to MCF are quasi-neutral, which means that  $\sigma = 0$  for any volume greater than a Debye sphere. The temporal

variations to the electric field in Ampère's law, eqn. (2.5), may be neglected for non-relativistic plasmas [55].

$$\nabla \cdot \mathbf{E} = \sigma/\epsilon_0 = 0, \quad (2.2)$$

$$\nabla \cdot \mathbf{B} = 0, \quad (2.3)$$

$$\nabla \times \mathbf{E} = \frac{\partial \mathbf{B}}{\partial t}, \quad (2.4)$$

$$\nabla \times \mathbf{B} = \mu_0 \mathbf{J} + \frac{1}{c^2} \frac{\partial \mathbf{E}}{\partial t} = \mu_0 \mathbf{J}. \quad (2.5)$$

Numerical solutions for these coupled equations (eqns. (2.1)-(2.5)) applied to MCF plasma carry significant computational cost. Therefore, reducing the system of equations (while at the same time understanding the physical effects that are being neglected) leads to models which appropriately describe certain aspects of the physical processes involved, and which carry less computational expenses.

In order to study large-scale phenomena taking place in MCF devices, it is useful to reduce the above system of equations to a 'fluid' model. To do so, the system is formulated in terms of moments of the Boltzmann equation, i.e., multiplying eqn. (2.1) by different powers of  $\mathbf{u}_\alpha$  :  $(1, m_\alpha \mathbf{u}_\alpha, m_\alpha u_\alpha^2, \dots)$  and integrating over the entire velocity space. Such approximation is valid as long as the reduced model considers

- time scales which are long with respect to microscopic particle motion (inverse collision frequencies, inverse electron plasma frequency, inverse electron cyclotron frequency), and
- spatial scales which are larger than  $\lambda_D$  and larger than the gradient scale length.

The three lowest order moments of the distribution function are the *number density*,  $n_\alpha$ , the *fluid velocity*,  $\mathbf{v}_\alpha$ , and the *pressure tensor*,  $\overline{P}_\alpha$ , of species  $\alpha$ . The expressions for these three quantities are shown below.

$$\begin{aligned} n_\alpha &= \int f_\alpha d^3 u_\alpha \\ \mathbf{v}_\alpha &= \frac{1}{n_\alpha} \int f_\alpha \mathbf{u}_\alpha d^3 u_\alpha \\ \overline{P}_\alpha &= \int m_\alpha f_\alpha (\mathbf{u}_\alpha - \mathbf{v}_\alpha) \otimes (\mathbf{u}_\alpha - \mathbf{v}_\alpha) d^3 u_\alpha \end{aligned}$$

In terms of the quantities defined above, taking the zeroth moment of eqn. (2.1) results in the continuity equation (2.6), where  $\rho_\alpha = m_\alpha n_\alpha$  is the mass density of species  $\alpha$ , and describes the conservation of particles in the absence of diffusion,

sources and sinks. However, knowledge of the species' fluid velocity to form a closed system of equations. Similarly, taking the first moment of eqn. (2.1) results in the momentum conservation equation (2.7), where  $q_\alpha$  is the electric charge,  $\sigma_\alpha = q_\alpha n_\alpha$  is the charge density,  $\mathbf{J}_\alpha = q_\alpha n_\alpha \mathbf{v}_\alpha$  is the current density of species  $\alpha$ , and  $\mathbf{R}_\alpha$  is the friction coefficient that comes from the collision term. But knowledge of the species' pressure tensor is needed to close the system of equations. Finally, eqn. (2.8) is obtained by taking the second moment of the Boltzmann equation, and it is the energy density equation for the fluid of species  $\alpha$ . The heat flux density is  $\mathbf{q}_\alpha$ , and the energy exchange between species is denoted by  $Q_{\Delta_\alpha}$ .

$$\frac{\partial \rho_\alpha}{\partial t} + \nabla \cdot (\rho_\alpha \mathbf{v}_\alpha) = 0 \quad (2.6)$$

$$\frac{\partial(\rho_\alpha \mathbf{v}_\alpha)}{\partial t} + \nabla \cdot (\rho_\alpha \mathbf{v}_\alpha \otimes \mathbf{v}_\alpha) + \nabla \cdot \bar{\mathbf{P}}_\alpha - \sigma_\alpha \mathbf{E} - \mathbf{J}_\alpha \times \mathbf{B} = \mathbf{R}_\alpha \quad (2.7)$$

$$\frac{\partial(\rho_\alpha \varepsilon_\alpha)}{\partial t} + \nabla \cdot (\rho_\alpha \mathbf{v}_\alpha \varepsilon_\alpha) + \nabla \cdot \mathbf{q}_\alpha + \nabla \cdot (\bar{\mathbf{P}}_\alpha \cdot \mathbf{v}_\alpha) - \sigma_\alpha \mathbf{E} \cdot \mathbf{v}_\alpha = \mathbf{R}_\alpha \cdot \mathbf{v}_\alpha + Q_{\Delta_\alpha} \quad (2.8)$$

The heat flux density, appearing in eqn. (2.8), is a third order moment of the distribution function of species  $\alpha$ . An equation describing the heat flux density is required in order to close the system. Such equation could be obtained by taking the third order moment of eqn. (2.1), but a similar problem would arise. Namely, the equation for the  $n^{\text{th}}$  moment of  $f_\alpha$  requires knowledge of the  $n^{\text{th}} + 1$  moment. This is known as the closure problem (see, for example, [54]). The closure problem makes it impossible to find a closed system of equations by only considering the solutions of the higher order moments of  $f_\alpha$ . An appropriate closure should be determined to solve this problem. Different closures are sensible for different problems. In this thesis, the adiabatic pressure close will be used.

Considering eqns. (2.6)-(2.8) separately for ions and electrons leads to the two-fluid model. For the two-fluid model, the friction coefficients are  $\mathbf{R}_i = -\mathbf{R}_e = \mathbf{R}$ , and the energy exchange terms satisfy  $Q_{\Delta_i} + Q_{\Delta_e} = 0$ . It is possible to further simplify the system by considering a single fluid model. To do so, the two-fluid equations are combined. The single fluid is described by the mass density  $\rho = \rho_i + \rho_e$ , momentum  $\rho \mathbf{v} = \rho_i \mathbf{v}_i + \rho_e \mathbf{v}_e$ , charge density  $\sigma = q_i n_i + q_e n_e$ , current density  $\mathbf{J} = q_i n_i \mathbf{v}_i - q_e n_e \mathbf{v}_e$ , and by the pressure tensor  $\bar{\mathbf{P}} = \bar{\mathbf{P}}_i + \bar{\mathbf{P}}_e$ . The latter may be decomposed into the isotropic pressure  $p = p_i + p_e$  and the stress tensor  $\bar{\Pi} = \bar{\Pi}_i + \bar{\Pi}_e$ , where  $\bar{\Pi}_\alpha = \bar{\mathbf{P}}_\alpha - p_\alpha \bar{\mathbf{I}}$ , and  $\bar{\mathbf{I}}$  is the identity tensor.

To arrive at the single fluid equations, first the continuity equations of the ions and electrons are summed. The same is done for the momentum equations. The system is simplified by noting that the ion mass is much larger than the electron mass, and neglecting terms of  $\mathcal{O}(m_e/m_i)$ . The resulting single fluid continuity and momentum equations are eqns. (2.9) and (2.10), where the pressure tensor is divided into the isotropic pressure tensor and the stress tensor.

$$\frac{\partial \rho}{\partial t} + \nabla \cdot (\rho \mathbf{v}) = 0 \quad (2.9)$$

$$\rho \frac{\partial \mathbf{v}}{\partial t} + \rho \mathbf{v} \cdot \nabla \mathbf{v} + \nabla p = \mathbf{J} \times \mathbf{B} - \nabla \cdot \bar{\Pi} \quad (2.10)$$

Given that plasmas in MCF behave roughly like an ideal gas, the adiabatic pressure equation is often used to close the single fluid MHD equations [54]. The adiabatic pressure equation is eqn. (2.11), where  $\gamma = 5/3$  is the ratio of specific heats for ideal gases. Note that eqn. (2.11) only provides a closure for the isotropic component of the pressure tensor. There are also different closures for the anisotropic component of  $\bar{P}$ . The choice used in JOREK will be addressed in section 2.4. Using the adiabatic pressure equation means that eqn. 2.8 does not have to be solved to close the system. The pressure equation may also be expressed as an equation for the single fluid temperature,  $T = T_i + T_e$ , since the single fluid pressure is  $p = \rho T$ .

$$\begin{aligned} \frac{d}{dt} \left( \frac{p}{\rho^\gamma} \right) &= 0 \\ \frac{\partial p}{\partial t} + \mathbf{v} \cdot \nabla p + \gamma p \nabla \cdot \mathbf{v} &= 0 \end{aligned} \quad (2.11)$$

The coupling between the fluid dynamics and the electromagnetic fields is obtained through Ohm's law, eqn. (2.12), where  $\eta$  is the plasma resistivity.

$$\mathbf{E} = \eta \mathbf{J} - \mathbf{v} \times \mathbf{B} \quad (2.12)$$

The single fluid MHD model is then defined by the set of equations below, eqns. (2.13)-(2.19), which are commonly referred to as *full MHD*. For realistic tokamak conditions, the full MHD equations may be solved numerically by various non-linear MHD codes, e.g., JOREK [56], NIMROD [57], and MEGA [58]. Nevertheless, depending on the problem being considered it may be possible to make certain reductions to the full MHD equations without loosing physical insight. One of these reductions in particular will be described in section 2.2.4. The terms in blue are restricted to the so-called *resistive MHD*. The terms in black describe ideal MHD, which is further described in section 2.2.2.

$$\frac{\partial \rho}{\partial t} + \nabla \cdot (\rho \mathbf{v}) = 0 \quad (2.13)$$

$$\rho \frac{\partial \mathbf{v}}{\partial t} + \rho \mathbf{v} \cdot \nabla \mathbf{v} + \nabla p = \mathbf{J} \times \mathbf{B} - \nabla \cdot \Pi \quad (2.14)$$

$$\frac{\partial p}{\partial t} + \mathbf{v} \cdot \nabla p + \gamma p \nabla \cdot \mathbf{v} = 0 \quad (2.15)$$

$$\nabla \times \mathbf{E} = \frac{\partial \mathbf{B}}{\partial t} \quad (2.16)$$

$$\mathbf{E} = \eta \mathbf{J} - \mathbf{v} \times \mathbf{B} \quad (2.17)$$

$$\nabla \times \mathbf{B} = \mu_0 \mathbf{J} \quad (2.18)$$

$$\nabla \cdot \mathbf{B} = 0 \quad (2.19)$$

The next section describes the application of the above equations to tokamak plasma physics. Single fluid MHD codes devoted to studying tokamaks frequently go beyond the single fluid MHD equations defined above. Some of the extensions to said equations that are used in the JOREK code are described in section 2.4.

## 2.2 MHD for magnetic confinement

This section deals with the application of single fluid MHD to describe the behaviour of plasma inside tokamak devices. An appropriate coordinate system is detailed in 2.2.1. Later, section 2.2.2 describes ideal MHD and the *frozen-in flux* condition. Section 2.2.3 describes the well-known Grad-Shafranov equilibrium equation. Reduced and extended MHD are described in sections 2.2.4 and 2.2.5, respectively. Finally, section 2.2.6 describes physical effects that are missing from MHD as well as the region of validity of MHD (in terms of spatial and temporal scales).

### 2.2.1 Coordinate system

There exist many coordinate systems that are adequate for the study of plasma behaviour inside tokamak devices. For the purpose of this work, cylindrical coordinates  $(\mathbf{R}, Z, \phi)$  will be used and are shown in fig. 2.1. Toroidal and poloidal planes are parallel to the  $\mathbf{R} - \phi$  and  $\mathbf{R} - Z$  planes, respectively. A Cartesian vector in this coordinate system is  $\mathbf{r} = (R \cos \phi, R \sin \phi, Z)$ , and the unit vectors are

$$\begin{aligned} \hat{\mathbf{R}} &= d\mathbf{r}/dR/|d\mathbf{r}/dR| = (\cos \phi, \sin \phi, 0), \\ \hat{\mathbf{Z}} &= d\mathbf{r}/dZ/|d\mathbf{r}/dZ| = (0, 0, 1), \text{ and} \\ \hat{\phi} &= d\mathbf{r}/d\phi/|d\mathbf{r}/d\phi| = (-\sin \phi, \cos \phi, 0). \end{aligned}$$

For the most part, the toroidal magnetic field  $\mathbf{B}_{\text{tor}}$  in tokamaks is produced by a set of toroidal field coils, and it can be described as  $\mathbf{B}_{\text{tor}} = B_{\text{tor}} \hat{\phi}$ . The poloidal

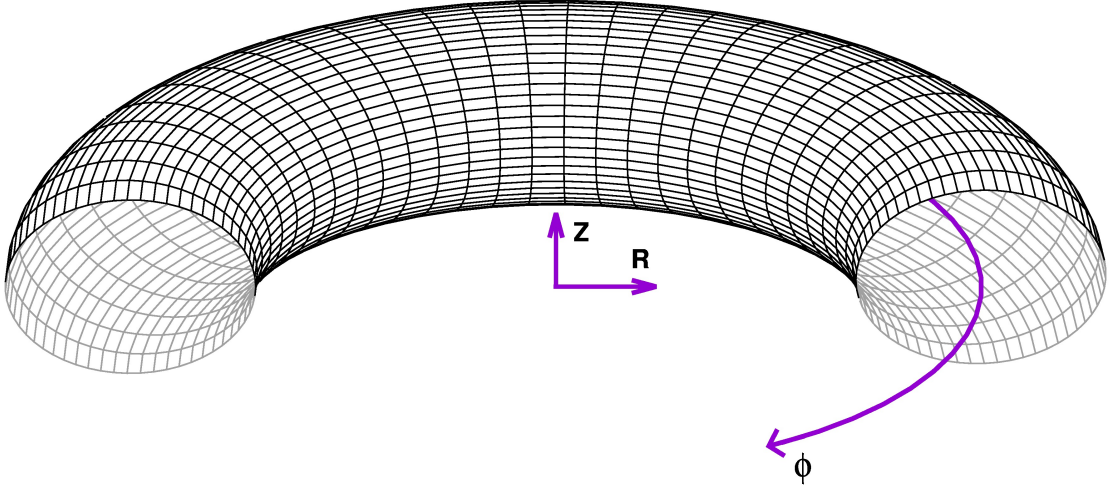


Figure 2.1: Cylindrical coordinates ( $\mathbf{R}, \mathbf{Z}, \phi$ ) in toroidal geometry. Planes that are parallel to the  $\mathbf{R}-\phi$  plane are called toroidal planes and planes that are orthogonal to  $\phi$  are called poloidal planes.

magnetic field  $\mathbf{B}_{\text{pol}}$  is generated by an electric current flowing along the toroidal direction and by poloidal field coils. The poloidal magnetic field can be described as  $\mathbf{B}_{\text{pol}} = B_R \hat{\mathbf{R}} + B_Z \hat{\mathbf{Z}}$ .

The flux of the magnetic field across a surface that lies on the toroidal plane ( $\mathcal{S}_{\text{pol}}$  in fig. 2.2) is called the poloidal magnetic flux  $\psi$ , and it is defined as eqn. (2.20) for the tokamak geometry. **Surfaces with a constant poloidal magnetic flux are called flux surfaces.** Closed flux surfaces are found inside the confined region, and open flux surfaces are found outside the confined region. The Last Closed Flux Surface (LCFS) is called the separatrix. The poloidal flux  $\psi$  is regularly used as a radial coordinate because (when properly normalised) it is equal to 0 at the magnetic axis and equal to 1 at the separatrix.

$$\Psi = \int_{\mathcal{S}_{\text{pol}}} \mathbf{B} \cdot d\mathbf{S} \quad \text{--> total flux}$$

$$\psi(R, Z) = -\frac{1}{2\pi} \Psi = -\int_0^R \mathbf{B}(R, Z) \cdot \hat{\mathbf{Z}} R dR \quad (2.20)$$

The equation for the poloidal magnetic flux may be used to express  $\mathbf{B}_Z$  in terms of  $\psi$  by the fundamental theorem of calculus. An expression for  $\mathbf{B}_R$  in terms of  $\psi$  can also be found by considering  $\nabla \cdot \mathbf{B} = 0$  and the axial symmetry with respect

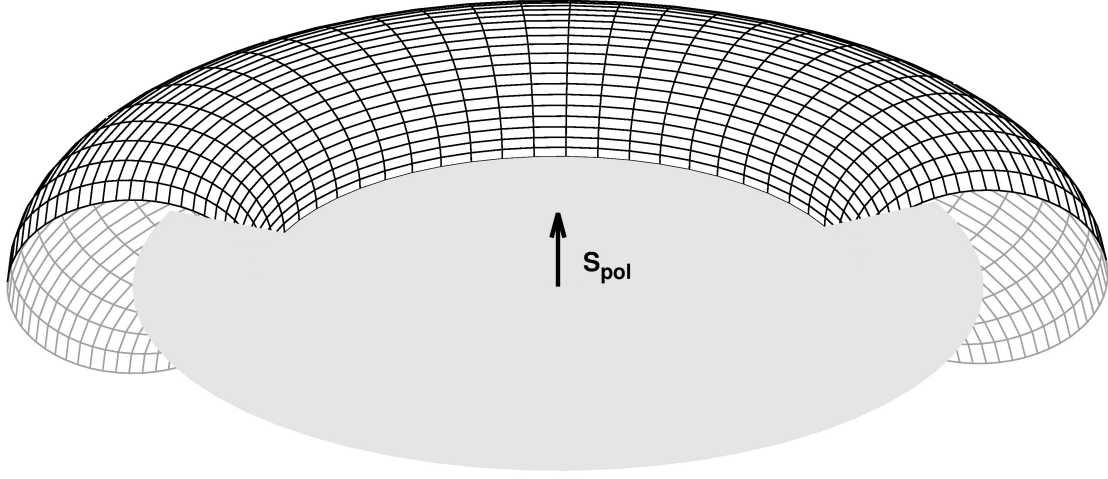


Figure 2.2: The magnetic flux through the surface  $S_{\text{pol}}$  is called the poloidal magnetic flux, and it is used as a radial coordinate.

to the toroidal direction, i.e.,  $\partial_\phi = 0$ . The equations for  $B_R$  and  $B_Z$  are

$$\begin{aligned}\mathbf{B}_R(R, Z) &= \frac{1}{R} \partial_Z \psi(R, Z) \hat{\mathbf{R}} \\ \mathbf{B}_Z(R, Z) &= -\frac{1}{R} \partial_R \psi(R, Z) \hat{\mathbf{Z}}\end{aligned}$$

A compact way to describe the magnetic field for toroidal geometry then is

$$\mathbf{B} = \nabla \psi \times \nabla \phi + F \nabla \phi, \quad (2.21)$$

where  $F$  is a function that can be used to describe the toroidal magnetic field, i.e.,  $\mathbf{B}_\phi = F/R\hat{\phi}$ . One important feature of such systems is that  $\mathbf{B} \cdot \nabla \psi = 0$ , which means that the magnetic field lines lie on surfaces of constant flux  $\psi$ .

The magnetic vector potential is directly related to the magnetic flux. To show this, the total magnetic field is written with the magnetic vector potential:  $\mathbf{B} = \nabla \times \mathbf{A}$ . Using the expression for the curl and, as done above, considering  $\partial_\phi = 0$ , the magnetic field is

$$\begin{aligned}\nabla \times \mathbf{A} &= \left(-\frac{1}{R} \partial_\phi A_Z + \partial_Z A_\phi\right) \hat{\mathbf{R}} + \frac{1}{R} \left(-\partial_R(RA_\phi) + \partial_\phi A_R\right) \hat{\mathbf{Z}} + \left(-\partial_Z A_R + \partial_R A_Z\right) \hat{\phi} \\ &= \partial_Z A_\phi \hat{\mathbf{R}} - \frac{1}{R} \partial_R(RA_\phi) \hat{\mathbf{Z}} + \left(-\partial_Z A_R + \partial_R A_Z\right) \hat{\phi}.\end{aligned}$$

Considering only the poloidal component, a direct relation between  $\psi$  and the toroidal component of the vector potential is defined with eqn. (2.22).

$$(\nabla \times \mathbf{A})_{\text{pol}} = \frac{1}{R} \partial_Z (RA_\phi) \hat{\mathbf{R}} - \frac{1}{R} \partial_R (RA_\phi) \hat{\mathbf{Z}}$$

$$\psi = RA_\phi \quad (2.22)$$

### 2.2.2 Ideal MHD – infinitely conducting plasma

Achieving a plasma configuration which is in equilibrium and stable is a fundamental requirement for a fusion reactor. The full MHD equations can be simplified to study what properties need to be satisfied in order to produce stable plasma configurations. This is the realm of ideal MHD, which assumes the plasma to be an infinitely conducting fluid, i.e., zero resistivity, which modifies Ohm's law to

$$\mathbf{E} = -\mathbf{v} \times \mathbf{B}.$$

The assumption of zero resistivity is motivated by the fact that MCF plasmas are extremely good electrical conductors. Ideal MHD further neglects the stress tensor in the single fluid momentum eqn. (2.14).

An important feature of the ideal MHD model is that it forbids certain physical processes to take place. In particular, the magnetic flux across any surface  $\mathbf{S}$  (moving with the plasma at a velocity  $\mathbf{v}$ ),

$$\Psi = \int_S \mathbf{B} \cdot d\mathbf{S},$$

must be conserved at all times. This is called the *frozen-in flux* condition. A simple proof of the *frozen-in flux* condition is detailed below.

The temporal change of the magnetic flux across the surface  $\mathbf{S}$  is comprised of two parts. First from the change of the magnetic field in time ( $\partial_t \mathbf{B}$ ), and second from the change of the contour of the co-moving surface  $\partial\mathbf{S}$  in a time  $dt$  ( $\mathbf{v} \times d\mathbf{l}$ , where  $d\mathbf{l}$  is an element of  $\partial\mathbf{S}$ ). The equation for the change of the magnetic flux is

$$\frac{d\Psi}{dt} = \int_S \frac{\partial \mathbf{B}}{\partial t} \cdot d\mathbf{S} + \oint_{\partial S} \overbrace{\mathbf{B} \cdot (\mathbf{v} \times d\mathbf{l})}^{=-(\mathbf{v} \times \mathbf{B}) \cdot d\mathbf{l}}.$$

Using Ampère's law (eqn. (2.18)) for the first term in the right hand side to express it in terms of the electric field, and Stokes theorem for the second term to express it as a surface integral,

$$\frac{d\Psi}{dt} = \int_S -\nabla \times \mathbf{E} \cdot d\mathbf{S} - \int_S \nabla \times (\mathbf{v} \times \mathbf{B}) \cdot d\mathbf{S}.$$

Finally, considering the ideal MHD Ohm's law, the change in flux is shown to be zero,

$$\frac{d\Psi}{dt} = - \int_S \nabla \times (\mathbf{E} + \mathbf{v} \times \mathbf{B}) \cdot d\mathbf{S} = 0.$$

The flux conservation implies that physical phenomena that break magnetic field lines, i.e., magnetic reconnection, cannot be described by ideal MHD. However, such physical processes (tearing modes, sawtooth crashes, and edge localised modes) are ubiquitous to magnetically confined plasma, and a model that allows magnetic reconnection is required to study them. One such model is resistive MHD, which will be further described in 2.2.4. Ideal MHD will be mentioned again in section 2.3 since it is commonly used as a powerful tool to assess whether the plasma is stable against certain (ideal) instabilities.

### 2.2.3 Plasma equilibrium – Grad-Shafranov equation

An extremely valuable application of ideal MHD is related to MHD equilibria. The MHD equilibrium equations arise by considering time-independent ideal MHD equations with static conditions ( $\mathbf{v} = \mathbf{0}$ ). This results in a modified momentum equation,

$$\nabla p = \mathbf{J} \times \mathbf{B}, \quad (2.23)$$

the divergence-less magnetic field (eqn. (2.19)), and the regular Ampère's law (eqn. (2.18)). Equation (2.23) essentially means that in order to obtain magnetohydrodynamic equilibrium it is necessary to balance the pressure gradient force and the magnetic force  $\mathbf{J} \times \mathbf{B}$ . Equation (2.23) is aptly named the static *force balance equation*. Expressing the force balance equation for the tokamak case results in the well-known Grad-Shafranov equation [59, 60].

The magnetic field and the current density may be written as

$$\begin{aligned} \mathbf{B} &= \mathbf{B}_{\text{pol}} + B_\phi \hat{\phi} = \nabla \times \mathbf{A}, \\ \mu_0 \mathbf{J} &= \mu_0 \left( \mathbf{J}_{\text{pol}} + j_\phi \hat{\phi} \right) = \nabla \times \mathbf{B}. \end{aligned}$$

We previously showed that the toroidal component of the magnetic vector potential is related to the magnetic flux by eqn. (2.22) ( $\psi = RA_\phi$ ). Similarly, a scalar function  $F$  related to the toroidal magnetic field ( $F = RB_\phi$ ) can be used to express the poloidal current density. Therefore, the following expressions of magnetic field and current density may be used.

$$\begin{aligned} \mathbf{B} &= \mathbf{B}_{\text{pol}} + B_\phi \hat{\phi} = \nabla \psi \times \nabla \phi + B_\phi \hat{\phi}, \\ \mu_0 \mathbf{J} &= \mu_0 \left( \mathbf{J}_{\text{pol}} + j_\phi \hat{\phi} \right) = \nabla F \times \nabla \phi + \mu_0 j_\phi \hat{\phi}. \end{aligned}$$

And substituting these expressions into the static force balance equation, and using

the vector identity  $\mathbf{A} \times (\mathbf{B} \times \mathbf{C}) = \mathbf{B}(\mathbf{A} \cdot \mathbf{C}) - \mathbf{C}(\mathbf{A} \cdot \mathbf{B})$  leads to

$$\begin{aligned}\nabla p &= \mathbf{J}_{\text{pol}} \times \mathbf{B}_\phi + \mathbf{J}_\phi \times \mathbf{B}_{\text{pol}} \\ &= -\mathbf{B}_\phi \times (\nabla F/\mu_0 \times \nabla \phi) + \mathbf{J}_\phi \times (\nabla \psi \times \nabla \phi) \\ &= -\nabla F/\mu_0 (\mathbf{B}_\phi \cdot \nabla \phi) + \nabla \phi (B_\phi \hat{\phi} \cdot \nabla F/\mu_0) + \nabla \psi (\mathbf{J}_\phi \cdot \nabla \phi) - \nabla \phi (j_\phi \hat{\phi} \cdot \nabla \psi) \\ &= -\frac{B_\phi}{\mu_0 R} \nabla F + \frac{j_\phi}{R} \nabla \psi.\end{aligned}\tag{2.24}$$

From eqn. (2.23), it can be seen that  $\mathbf{B} \cdot \nabla p = 0$ , which means that pressure is a flux function, i.e.,  $p = p(\psi)$ . Similarly,  $\mathbf{J} \cdot \nabla p = (\nabla p \times \nabla F) \cdot \nabla \phi = 0$  means that  $F = F(\psi)$  is also a flux function. Consequently,  $\nabla F(\psi) = dF/d\psi \nabla \psi$  and  $\nabla p(\psi) = dp/d\psi \nabla \psi$  and, therefore, eqn. (2.24) then may be expressed as

$$\frac{dp}{d\psi} \nabla \psi = -\frac{F}{\mu_0 R^2} \frac{dF}{d\psi} \nabla \psi + \frac{j_\phi}{R} \nabla \psi.$$

The above equation may be written purely in terms of  $p$ ,  $F$ , and  $\psi$  by making use of Ampère's law to write the toroidal current density in terms of  $\psi$ . To do so, it is necessary to insert  $\mathbf{B} = (B_R, B_Z, B_\phi)$  into the toroidal component of Ampère's law,

$$\begin{aligned}\mu_0 j_\phi &= \partial_R B_Z - \partial_Z B_R \\ &= \partial_Z (-R^{-1} \partial_Z \psi) - \partial_R (R^{-1} \partial_R \psi) \\ &= -R^{-1} [\partial_Z^2 + R \partial_R (R^{-1} \partial_R)] \psi \\ &= -R^{-1} \Delta^* \psi.\end{aligned}$$

Where the  $\Delta^*$  operator corresponds to the *Grad-Shafranov* differential operator, and it is defined as  $\Delta^* = R^2 \nabla \cdot (R^{-2} \nabla_\perp)$ , where  $\nabla_\perp = \hat{\mathbf{R}} \partial_R + \hat{\mathbf{Z}} \partial_Z$  is the gradient in the poloidal plane. Hence the toroidal current can be written as

$$\mathbf{J}_\phi = -\frac{1}{\mu_0 R} \Delta^* \psi \hat{\phi}.$$

And the force balance equation can then be written as

$$\mu_0 R^2 \frac{dp}{d\psi} + F \frac{dF}{d\psi} + \Delta^* \psi = 0,\tag{2.25}$$

which is called the *Grad-Shafranov* equation.

### 2.2.4 Reduced MHD

As it was mentioned at the end of section 2.1, solving the full MHD equations for realistic tokamak conditions is a costly endeavour. Ideal MHD reduces the complexity of the full MHD equations, and it is an excellent tool to study the equilibrium and stability of plasma. However, the assumption made of zero plasma resistivity is not realistic even though it is very small in MCF plasmas. Mainly because introducing resistivity permits magnetic reconnection to take place. In order to consider a resistive plasma and, at the same time, reduce the system of equations, reduced MHD models have been developed [53, 61, 62]. Reduced MHD simplifies the system of equations by eliminating the fast magnetosonic wave from the system. This may be done with an ordering-based approach, or with an ansatz-based approach. The reduced MHD model used in the JOREK code relies on the latter and, therefore, it will be expanded upon in this section. A detailed description of the reduced MHD model implemented in JOREK may be found in section 2 of Ref. [50].

The ansatz-based reduced MHD considers two ansatzes. Firstly by considering the toroidal component of the magnetic field to be fixed in time. This choice removes one variable from the full MHD system of equations which, by itself, reduces the complexity of the problem. A stationary toroidal magnetic field also eliminates the fast magnetosonic waves from the system, which reduces the fastest time scale in the system. This choice, however, limits the applicability of reduced MHD. For instance, internal kink modes at non-zero pressure cannot be realistically described [56, 63]. The magnetic field may then be expressed by replacing the scalar variable  $F$  of eqn. (2.21) with a constant  $F_0$

$$\mathbf{B} = \nabla\psi \times \nabla\phi + F_0 \nabla\phi. \quad (2.26)$$

The constant for the toroidal magnetic field is  $F_0 = B_{\text{axis}}R_{\text{axis}}$ . This ansatz obviously restricts the time-varying magnetic vector potential to  $\mathbf{A} = \psi \nabla\phi$  since any time-varying radial or vertical component of  $\mathbf{A}$  would lead to a time-varying  $B_\phi$ . It does not, however, mean that poloidal currents are completely dropped. Only their effect onto the toroidal magnetic field is neglected.

The second ansatz for the reduced MHD model in question deals with the plasma velocity. From Faraday's law, the electric field may be expressed as

$$\mathbf{E} = -\nabla\Phi - \partial_t \mathbf{A}.$$

Introducing the first ansatz into the above expression means that the electric field is constrained to be

$$\mathbf{E} = -\nabla\Phi - \partial_t \psi \hat{\phi}.$$

Substituting the electric field by using Ohm's law but neglecting resistivity, and taking the cross product with  $\nabla\phi$ , the following expression is obtained

$$(\mathbf{v} \times \mathbf{B}) \times \nabla\phi = \nabla\Phi \times \nabla\phi + \partial_t \psi \nabla\phi \times \hat{\phi}.$$

Considering the velocity as  $\mathbf{v} = \mathbf{v}_{\text{pol}} + v_{\parallel} \mathbf{B}$ , the above equation can be rewritten as

$$\begin{aligned} (\mathbf{v}_{\text{pol}} \times \mathbf{B}_{\phi}) \times \nabla \phi &= \nabla \Phi \times \nabla \phi, \\ (\mathbf{v}_{\text{pol}} \times (F_0 \nabla \phi)) \times \nabla \phi &= \nabla \Phi \times \nabla \phi, \\ -(\mathbf{v}_{\text{pol}} \underbrace{(\nabla \phi \cdot F_0 \nabla \phi)}_{F_0 R^2} - F_0 \nabla \phi \underbrace{(\nabla \phi \cdot \mathbf{v}_{\text{pol}})}_{\mathbf{v}_{\text{pol}}}) &= \nabla \Phi \times \nabla \phi, \\ \mathbf{v}_{\text{pol}} &= -R^2 \nabla u \times \nabla \phi, \end{aligned}$$

where  $u = \Phi/F_0$ . The resulting ansatz for the velocity, which must then be substituted into the full MHD equations, is then

$$\mathbf{v} = -R^2 \nabla u \times \nabla \phi + v_{\parallel} \mathbf{B}. \quad (2.27)$$

The reduced MHD model described here is obtained by substituting eqns. (2.26) and (2.27) into the full MHD equations ((2.13)-(2.19)), as shown in detail in Ref. [52].

### 2.2.5 Extended MHD

The ansatz for the velocity in reduced MHD (eqn (2.27)) can be more intuitively understood as assigning the fluid velocity to the plasma ExB velocity ( $\mathbf{v}_{\text{ExB}} = \frac{\mathbf{E} \times \mathbf{B}}{B^2}$ ) together with the velocity along the magnetic field lines, i.e.,  $\mathbf{v} = \mathbf{v}_{\text{ExB}} + v_{\parallel} \mathbf{B}$ . This velocity expression may be modified to include other relevant effects. For instance, it is possible to consider the two-fluid effect of diamagnetic drifts<sup>1</sup> by expressing the ion velocity as

$$\mathbf{v}_i = \underbrace{-R^2 \nabla u \times \nabla \phi}_{\text{ion diamagnetic velocity}} - \frac{\delta^* R^2}{\rho} \nabla p_i \times \nabla \phi + v_{\parallel} \mathbf{B}, \quad (2.28)$$

where  $\rho$  is the plasma density,  $\nabla p_i$  is the ion pressure, and the diamagnetic coefficient  $\delta^* = m_i/(eF_0)$  with  $m_i$  the ion mass and  $e$  the fundamental electric charge. The diamagnetic drift is a fluid drift and not a guiding centre drift, meaning that particles are not actually displaced by it. In the H-mode pedestal, the pressure gradient is large, and the pressure gradient-driven diamagnetic drift becomes comparable in amplitude to the  $v_{\text{ExB}}$  drift. Therefore, it must be considered. In the H-mode pedestal, the  $E_r$  (which directly sets the ExB velocity) is described by a large well that is roughly proportional to  $(en_i)^{-1} \nabla p_i$  due to neutral friction losses (for more details, the reader is directed to section 2.2.1 in Ref. [64]). In the reduced MHD JOREK model, the radial electric field well in the pedestal region is obtained only when diamagnetic effects are included.

---

<sup>1</sup>The name ‘diamagnetic’ comes from the fact that the electrical current associated to the ion and electron diamagnetic velocities,  $\mathbf{j}^* \equiv -en(\mathbf{v}_e^* - \mathbf{v}_i^*) = -(\nabla p \times \mathbf{B})/B^2$ , acts to reduce the magnetic field. The ion diamagnetic velocity,  $v_i^*$ , is roughly equal, but opposite, to the electron diamagnetic velocity,  $v_e^*$ .

Other terms may be further included in the ansatz for the velocity. Neoclassical flows, or the polarisation drift, for instance, may be included in this way. For the purpose of this work, the only additional term considered in the velocity ansatz is the ion diamagnetic velocity. It has been observed in previous work that neglecting diamagnetic effects does not allow to recover cyclical dynamics of (unrealistically high repetition frequency) ELMs [65]. The work detailed in this thesis shows that including the diamagnetic effects allows to simulate type-I ELM cycles when fully realistic plasma parameters are taken into consideration [37].

Another important physical effect that takes place in the pedestal of H-mode plasmas is the temporal evolution of the edge bootstrap current density. This is a neoclassical effect that occurs due to inhomogeneous density, temperature, and pressure profiles in toroidal geometry [11]. Taking Faraday's law (eqn. (2.16)), it is possible to write

$$\mathbf{E} = -\nabla\Phi - \partial_t\psi\hat{\phi} + \alpha_L\nabla\phi,$$

where  $\alpha_L$  is a loop voltage that may be freely introduced since  $\nabla \times (\alpha_L\nabla\phi) = 0$ . Introducing Ohm's law (eqn. (2.17)) leads to

$$\begin{aligned} \eta\mathbf{J} - \mathbf{v} \times \mathbf{B} &= -\nabla\Phi - \partial_t\psi\hat{\phi} + \alpha_L\nabla\phi, \\ \eta\mathbf{J} - F_0\nabla_{\text{pol}}u - R[\psi, u]\nabla\psi &= -\nabla\Phi - \partial_t\psi\hat{\phi} + \alpha_L\nabla\phi, \end{aligned} \quad (2.29)$$

where the  $\mathbf{v} \times \mathbf{B}$  term, expressed with the Poisson bracket  $[A, B] = \nabla\psi \cdot (\nabla A \times \nabla B)$ , is given by

$$\begin{aligned} \mathbf{v} \times \mathbf{B} &= (-R^2\nabla u \times \nabla\phi) \times (\nabla\psi \times \nabla\phi + F_0\nabla\phi), \\ &= -R^2(\nabla u \times \nabla\phi) \times (\nabla\psi \times \nabla\phi) + F_0R^2\nabla\phi \times (\nabla u \times \nabla\phi), \\ &= -R^2 \left[ \nabla\psi \left( \cancel{(\nabla u \times \nabla\phi) \cdot \nabla\phi} \right) - \nabla\phi \left( (\nabla u \times \nabla\phi) \cdot \nabla\psi \right) \right] \\ &\quad + F_0\nabla u - R^2F_0\nabla\phi(\nabla\phi \cdot \nabla u), \\ &= R^2\nabla\phi \left( (\nabla\psi \times \nabla u) \cdot \nabla\phi \right) + \underbrace{F_0\nabla u - F_0\hat{\phi}(\hat{\phi} \cdot \nabla u)}_{=F_0\nabla_{\text{pol}}u}, \\ \mathbf{v} \times \mathbf{B} &= F_0\nabla_{\text{pol}}u + R[\psi, u]\nabla\phi. \end{aligned}$$

Rearranging eqn. (2.29), expressing the electrostatic potential as  $\Phi = F_0u$ , substituting the loop voltage term with a current source term ( $\mathbf{J}_0 = \alpha_L/\eta\nabla\phi$ ), and considering only the toroidal component leads to the following expression for the induction equation

$$\partial_t\psi = R[\psi, u] - \eta(j_\phi - j_{\phi,0}) - F_0\partial_\phi u. \quad (2.30)$$

The current density source term may then be used to maintain an approximately constant current profile. In a tokamak plasma there are density, temperature, and

pressure gradients. These gradients in toroidal geometry produce a bootstrap current density, such that the confined plasma current density always has a component related to said bootstrap current density and an Ohmic component ( $j_\phi = j_\Omega + j_{\text{bs}}$ ). If density, temperature, and pressure gradients are varying in time, it is evidently necessary to account for the corresponding variation in the bootstrap current density. In order to consider this dynamical effect, it is possible to change the bootstrap contribution to the current density source term, i.e.,  $j_{\phi,0}(t) = j_{\Omega,0} + j_{\text{bs},0}(t)$ . An appropriate expression for the time-evolving bootstrap current density contribution to the source term can be inexpensively obtained through analytical expressions that have been fitted to results from kinetic simulations, e.g., the Sauter equations [66, 67].

There are several further extensions that can be implemented to the single fluid full (or reduced) MHD equations. For example, physics of radiation, energetic particles, turbulent and neoclassical transport, finite Larmor radius effects, plasma-wall interactions, among others may be included with varying levels of detail.

### 2.2.6 What else is missing in MHD?

The main mechanisms that cause heat and particle fluxes across closed magnetic field lines are turbulent and neoclassical transport. In fact, the density and temperature gradients measured in the confined plasma are a direct consequence of the balance between said transport mechanisms and the heat and particle sources. The H-mode pedestal region is more complicated because ion-scale turbulence is largely suppressed in the pedestal region and because the ionisation of neutrals takes place in this region. Therefore, the ion (density and temperature) gradients are determined by the remnant ion-scale turbulent transport, neoclassical transport, and the sources. The electron gradients are still mostly determined by the electron-scale turbulence, neoclassical transport (which is less significant for electrons than for ions), and the sources. Ultimately, however, the pedestal gradients cannot grow unconstrained because large-scale MHD instabilities (typically ELMs) become excited and cause a relaxation of the pedestal region.

In order to directly account for turbulent and neoclassical transport in the entire confined region, it would be necessary to run expensive simulations that consider the dynamical effect of micro-instabilities. Similarly, to properly consider the sources, in particular the particle source, a kinetic treatment is required for the neutral particles. However, it is very computationally expensive to run such simulations for the time-scales relevant to type-I ELM cycles ( $\sim 10$  ms). A common approach to circumvent this problem is to introduce *ad hoc* heat and particle diffusion coefficients that cause heat and particle fluxes across magnetic flux surfaces, which mimic the unresolved turbulent and neoclassical transport channels, and simplified source terms. To include the *ad hoc* diffusion and sources,  $\nabla \cdot (D_\perp \nabla_\perp \rho) + S_\rho$  and  $\nabla \cdot (\kappa_\perp \nabla_\perp T) + S_p$  are added to the right hand sides of eqns. (2.13) and (2.15), respectively. For H-mode plasmas, the diffusion coefficients  $D_\perp$  and  $\kappa_\perp$  depend on the radial location  $\psi$ . In particular, they are characterised by a well (edge trans-

port barrier) in the pedestal region, in order to represent the strong suppression of ion-scale turbulence. Heat transport along magnetic field lines is also present in tokamaks, and it is a very fast process for both ions and electrons because they are free to move along, but not across, magnetic field lines. This discrepancy between the parallel and perpendicular particle dynamics leads to an important anisotropy in the heat diffusion coefficients,  $\kappa_{\parallel}/\kappa_{\perp} \sim 10^8 \dots 10^{10}$ . The parallel heat diffusion coefficient is temperature dependent and it follows the  $T^{5/2}$  Spitzer-Härm dependency [68]. It may be introduced by also adding  $\nabla \cdot (\kappa_{\parallel} \nabla_{\parallel} T)$  to eqn. (2.15).

## 2.3 MHD edge instabilities

The previous section gave an overview of tokamak-centric MHD. Ideal MHD was described in section 2.2.2 as an appropriate tool to study the stability of tokamak equilibria. In particular, that is the realm of linear ideal MHD stability analysis, which is described in this section. The considerations presented in this section closely follow those from Refs. [15, 55].

For a system in equilibrium, introducing a small perturbation can result in different outcomes. In particular, a system in equilibrium may be stable, meta-stable, and unstable. A small perturbation introduced in a stable system will cause small oscillations, but if it is introduced in an unstable system it will become amplified. Meta-stable systems may oscillate or amplify initial perturbations, e.g., depending on the amplitude of the initial perturbation. Bowling pins are an example of meta-stable systems in that a gentle push will make them wobble, but a stronger push will tip them over.

The linearisation of the ideal MHD equations (black terms of eqns. (2.13)-(2.19)) is performed by considering a small initial spatial displacement  $\boldsymbol{\xi}(\mathbf{x})$  and doing a series expansion up to first order. For simplicity, the velocity of the equilibrium state is assumed to be  $\mathbf{v}_0 = \mathbf{0}$ . The velocity of the perturbation is  $\tilde{\mathbf{v}} = \partial \boldsymbol{\xi} / \partial t$ , and it is a first order term. The density is separated into an equilibrium component and a first order perturbation ( $\rho = \rho_0 + \tilde{\rho}$ ). The continuity equation for the perturbed density reads

$$\partial_t \tilde{\rho} + \nabla \cdot (\rho_0 \partial_t \boldsymbol{\xi}) = 0 \quad \Rightarrow \quad \tilde{\rho} = -\nabla \cdot (\rho_0 \boldsymbol{\xi}).$$

The pressure equation (eqn. (2.11)) for the perturbed pressure  $\tilde{p}$  reads

$$\partial_t \tilde{p} + \partial_t \boldsymbol{\xi} \cdot \nabla p_0 + \gamma p_0 \nabla \cdot \partial_t \boldsymbol{\xi} = 0 \quad \Rightarrow \quad \tilde{p} = -\boldsymbol{\xi} \cdot \nabla p_0 - \gamma p_0 \nabla \cdot \boldsymbol{\xi}.$$

Separating the magnetic field into an equilibrium ( $\mathbf{B}_0 + \tilde{\mathbf{B}}$ ), using the perturbed velocity for ideal Ohm's law ( $\tilde{\mathbf{E}} = -\tilde{\mathbf{v}} \times \mathbf{B}_0$ ), and combining it with Faraday's law results in an expression for the perturbed magnetic field

$$\partial_t \tilde{\mathbf{B}} = \nabla \times (-\partial_t \boldsymbol{\xi} \times \mathbf{B}_0) \quad \Rightarrow \quad \tilde{\mathbf{B}} = -\nabla \times (\boldsymbol{\xi} \times \mathbf{B}_0). \quad (2.31)$$

Separating the equilibrium and perturbed current density as  $\mathbf{J}_0 + \tilde{\mathbf{J}}$ , the linearised momentum equation (eqn. (2.14)) can be written as

$$\rho_0 \partial_t \tilde{\mathbf{v}} = \mathbf{J}_0 \times \tilde{\mathbf{B}} + \tilde{\mathbf{J}} \times \mathbf{B}_0 - \nabla \tilde{p}.$$

Note that this eliminates the non-linear term  $\rho \mathbf{v} \cdot \nabla \mathbf{v}$  through ordering arguments (because the lowest order term would be  $\rho_0 \tilde{\mathbf{v}} \cdot \nabla \tilde{\mathbf{v}}$  which is considered a second order term). Using the above expressions for the perturbed velocity and pressure, and writing the equilibrium and perturbed current density as  $\mu_0 \mathbf{J}_0 = \nabla \times \mathbf{B}_0$  and  $\mu_0 \tilde{\mathbf{J}} = \nabla \times \tilde{\mathbf{B}}$  respectively, leads to

$$\rho_0 \partial_t^2 \boldsymbol{\xi} = \frac{1}{\mu_0} (\nabla \times \mathbf{B}_0) \times \tilde{\mathbf{B}} + \frac{1}{\mu_0} (\nabla \times \tilde{\mathbf{B}}) \times \mathbf{B}_0 + \nabla (\gamma p_0 \nabla \cdot \boldsymbol{\xi} + \boldsymbol{\xi} \cdot \nabla p_0).$$

The above equation is a linear partial differential equation for  $\boldsymbol{\xi}$  since  $\tilde{\mathbf{B}}$  may be expressed in terms of  $\boldsymbol{\xi}$  through eqn. (2.31), and it can be written with the ideal MHD force operator  $\mathbf{F}(\boldsymbol{\xi})$ :

$$\rho_0 \partial_t^2 \boldsymbol{\xi} = \mathbf{F}(\boldsymbol{\xi})$$

Representing the displacement vector through a Fourier series as

$$\boldsymbol{\xi}(\mathbf{x}, t) = \sum_{n=-\infty}^{\infty} \boldsymbol{\xi}_n(\mathbf{x}) e^{-i\omega_n t},$$

means that the linear partial differential equation for  $\boldsymbol{\xi}$  results in a generalised eigenvalue problem

$$-\omega^2 \rho_0 \boldsymbol{\xi} = \mathbf{F}(\boldsymbol{\xi}).$$

If  $\omega^2 > 0$ , the system is stable, and if  $\omega^2 < 0$  the system is unstable<sup>2</sup>. Even with the simplifications detailed in this section, solving for the eigenvalues is not a trivial task, and for most cases requires numerical solutions. However, physical insight may be extracted by considering the work required to displace the system

$$\delta W(\boldsymbol{\xi}) = \frac{1}{2} \omega^2 \int \rho_0 |\boldsymbol{\xi}|^2 dV = -\frac{1}{2} \int \boldsymbol{\xi}^* \cdot \mathbf{F}(\boldsymbol{\xi}) dV.$$

The integral  $\int \rho_0 |\boldsymbol{\xi}|^2 dV$  is always positive and, therefore, the sign of  $\delta W$  is determined by  $\omega^2$ . This means, of course, that positive  $\delta W$  are stable systems, and negative  $\delta W$  represent unstable systems. For MCF, it is of interest to consider plasma surrounded by a vacuum region enclosed by a conducting wall. If a perfectly conducting wall is considered, the displacement vector at the wall must be zero and, therefore, no work is done  $\delta W_{\text{wall}} = 0$ . Additionally, the magnetic field

---

<sup>2</sup>This is true only if the eigenvalues  $\omega^2$  are real, which is guaranteed if  $\mathbf{F}(\boldsymbol{\xi})$  is a self-adjoint operator. It is shown in Ref. [55] that in ideal MHD  $\mathbf{F}(\boldsymbol{\xi})$  is self-adjoint.

perpendicular to the wall must be zero, and all quantities outside of the wall must also vanish. The integral  $-1/2 \int \boldsymbol{\xi}^* \mathbf{F}(\boldsymbol{\xi}) dV$  may be separated into three regions. The bulk plasma  $\delta W_F$ , a vacuum region surrounding the bulk plasma  $\delta W_V$ , and a surface integral related to the interface between the two regions  $\delta W_S$ . The contribution from the vacuum region is always positive. If we assume that there are no discrete jumps between the bulk plasma and the vacuum region,  $\delta W_S = 0$ . This leaves the bulk plasma, or fluid, component  $\delta W_F$  which is

$$\delta W_F = \frac{1}{2} \int_{\text{Fluid}} \boldsymbol{\xi}^* \cdot \left( -\mathbf{J}_0 \times \tilde{\mathbf{B}} - \frac{1}{\mu_0} (\nabla \times \tilde{\mathbf{B}}) \times \mathbf{B}_0 - \nabla (\gamma p_0 \nabla \cdot \boldsymbol{\xi} + \boldsymbol{\xi} \cdot \nabla p_0) \right) dV.$$

It is possible to rearrange the terms in the integral into a more *intuitive form*

$$\begin{aligned} \delta W_F = \frac{1}{2} \int_{\text{Fluid}} & \left( \frac{|\tilde{\mathbf{B}}|^2}{\mu_0} + \frac{B_0^2}{\mu_0} |\nabla \cdot \boldsymbol{\xi}_\perp + 2\boldsymbol{\xi}_\perp \cdot \boldsymbol{\kappa}|^2 + \gamma p_0 |\nabla \cdot \boldsymbol{\xi}|^2 \right. \\ & \left. - 2(\boldsymbol{\xi}_\perp \cdot \nabla p_0)(\boldsymbol{\kappa} \cdot \boldsymbol{\xi}_\perp^*) - \frac{j_{0\parallel}}{B_0} (\boldsymbol{\xi}_\perp^* \times \mathbf{B}_0) \cdot \tilde{\mathbf{B}} \right) dV. \end{aligned} \quad (2.32)$$

The curvature vector  $\boldsymbol{\kappa}$  is defined as  $\boldsymbol{\kappa} = (\mathbf{b} \cdot \nabla) \mathbf{b}$  with  $\mathbf{b} = \mathbf{B}/B$ , the displacement vector has been decomposed into parts parallel and perpendicular to the equilibrium magnetic field  $\boldsymbol{\xi} = \boldsymbol{\xi}_\perp + \xi_\parallel \mathbf{b}$ , and the same was done for the current density.

The above expression for  $\delta W_F$  is known as the *intuitive form* because it is easy to identify the stabilising and destabilising agents. In particular, the first three terms are always stabilising, and the last two terms can be negative (and potentially destabilising). If the amplitude of either of the last two terms is large enough, the system will become unstable. The stabilising terms are related to the shear Alfvén wave (energy necessary to bend magnetic field lines), compressional Alfvén wave (energy necessary to compress magnetic field lines), and sound wave (energy necessary to compress the plasma), respectively. The fact that these terms are stabilising can be understood by noting that bending and compressing the magnetic field and compressing the plasma requires energy; energy that would otherwise be free to amplify the perturbation. Finally, the last two terms are negative and correspond to pressure gradient-driven instabilities and current-driven instabilities.

### 2.3.1 Classification of ideal MHD instabilities

Ideal MHD instabilities may be classified in terms of their general structure and in terms of the drive of the instabilities. The drive for the instability, as mentioned before, can be the pressure gradient and/or the current density parallel to the magnetic field. In terms of their general structure, modes can be internal or external. Considering a plasma surrounded by a vacuum region, internal modes (or fixed boundary modes) do not perturb the interface between the plasma and the vacuum, i.e.,  $\delta W_V = \delta W_S = 0$ . Consequently, for internal modes it is only required to

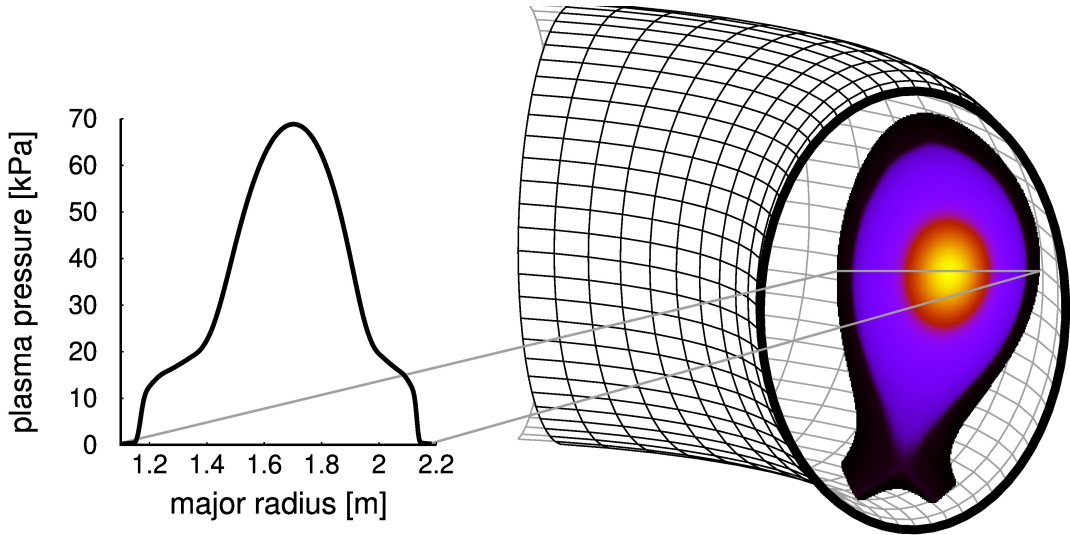


Figure 2.3: Pressure profile for the line cut-out along the horizontal line that crosses the magnetic axis,  $Z = Z_{\text{axis}}$ . A colour map for the plasma pressure is also shown in the right hand side.

consider  $\delta W_F$  since the vacuum term and the surface terms are both unperturbed. On the other hand, external modes (or free boundary modes) cause a displacement of the equilibrium plasma-vacuum interface. Therefore, it is necessary to consider the bulk plasma, surface, and vacuum contributions to  $\delta W$  when assessing the stability of external modes.

The term  $-2(\boldsymbol{\xi}_\perp \cdot \nabla p_0)(\boldsymbol{\kappa} \cdot \boldsymbol{\xi}_\perp^*)$  in eqn. (2.32) is associated with pressure gradient-driven instabilities. Pressure gradient-driven modes can exist in the absence of current density flowing parallel to the magnetic field lines because static force balance ( $\nabla p = \mathbf{J} \times \mathbf{B}$ ) implies that  $\nabla p \propto \mathbf{J}_\perp$ . However, these may destabilise the system only when the pressure gradient is parallel to the curvature vector. For a tokamak,  $\boldsymbol{\kappa}$  always points inwards and, under normal circumstances,  $\nabla p$  always points to the plasma core (magnetic axis). The toroidal magnetic field decays with increasing major radius. Therefore, for a poloidal cross section like the one shown in fig. 2.3, the region to the left of the magnetic axis is dubbed the high field side (HFS), and the region to the right is called the low field side (LFS). The pressure gradient points in the  $+\hat{\mathbf{R}}$  direction on the HFS and in the  $-\hat{\mathbf{R}}$  direction on the LFS. On the other hand, throughout the plasma volume  $\boldsymbol{\kappa}$  points in the  $-\hat{\mathbf{R}}$  direction. This means that, under normal circumstances,  $\nabla p$ -driven modes are destabilised on the LFS. Due to this, the LFS has been named ‘bad’ curvature region and the HFS ‘good’ curvature region. Pellets injected on the HFS can transiently lead to a local pressure gradient pointing in the  $-\hat{\mathbf{R}}$  direction in the good curvature region, therefore allowing for the destabilisation of  $\nabla p$ -driven modes. Such events are studied in chapter 6.

Toroidal and poloidal mode numbers are frequently used in the classification of different MHD instabilities. These can be understood by representing the displacement vector in the following way

$$\boldsymbol{\xi}(r, \theta, \phi, t) = \sum_{m=-\infty}^{\infty} \sum_{n=-\infty}^{\infty} \boldsymbol{\xi}_{mn}(r) e^{i(m\theta - n\phi)}.$$

Where  $\phi$  and  $\theta$  are the toroidal and poloidal angles. The toroidal and poloidal mode numbers are  $n$  and  $m$ , respectively. They are related to the safety factor in rational surfaces as  $q = m/n$ .

### 2.3.2 Pressure gradient-driven modes

The two main types of  $\nabla p$ -driven instabilities are interchange modes and ballooning modes. Interchange instabilities are internal modes characterised by long wavelengths parallel to  $\mathbf{B}$ , small wavelengths perpendicular to  $\mathbf{B}$  (large toroidal mode number), and do not cause bending of magnetic field lines. Due to the small perpendicular wavelengths, interchange modes are highly localised to a given flux surface. They are roughly constant along field lines and can be stabilised if the magnetic field lines are sheared (change direction in neighbouring flux surfaces). For tokamaks, the region confined inside the separatrix is usually stable to interchange modes [15]. Similarly, ballooning modes also have long parallel wavelengths and short perpendicular wavelengths (large  $n$ ) but they, in contrast to interchange instabilities, exhibit non-negligible variations along magnetic field lines. In particular, the variation along  $\mathbf{B}$  allows neighbouring perturbations to interact such that the perturbations cancel on the good curvature region, but they become concentrated in the bad curvature region, as depicted in fig. 2.4 (left). This characteristic of ballooning modes makes them more susceptible to being destabilised. Nevertheless, the field line bending required to concentrate the perturbations is a stabilising feature and, if the modes become too localised, can cause the ballooning mode to become completely stabilised. This happens for the so-called *infinite-n* ballooning modes because they are perfectly localised to a given flux surface. Plasma inside the separatrix is often susceptible to the excitation of ballooning modes. Of particular interest for the physics studied in this dissertation, ballooning modes are excited at the edge of H-mode plasmas due to the large associated pressure gradient. They typically have high toroidal mode numbers ( $n \approx [10 \dots 30]$ ) and play a crucial role in the physics of ELMs.

### 2.3.3 Current-driven modes

Current-driven instabilities obtain free energy from the term  $-j_{0\parallel} (\boldsymbol{\xi}_\perp^* \times \mathbf{B}_0) \cdot \tilde{\mathbf{B}}$ . In general, current-driven modes have long parallel wavelengths and perpendicular wavelengths longer than  $\nabla p$ -driven modes. They may be classified as kink modes

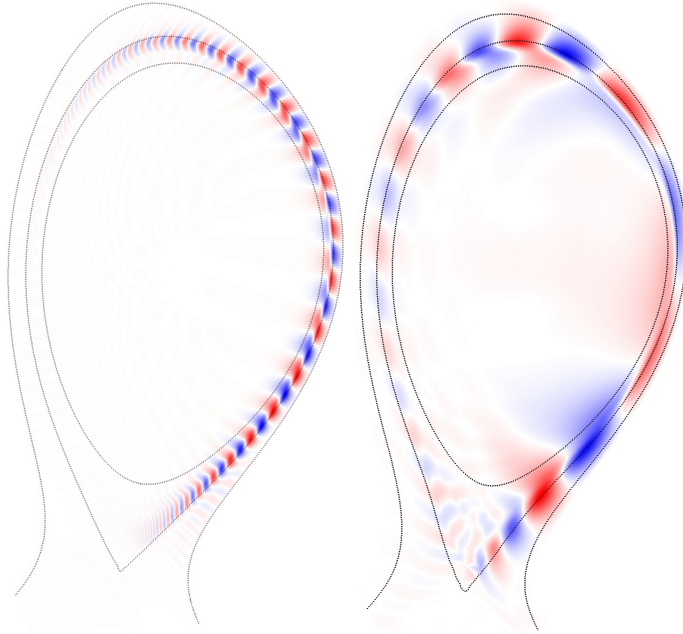


Figure 2.4: Structure of pressure gradient-driven ballooning modes with  $n = 12$  (left), and of current (density)-driven external kink (peeling) modes with  $n = 2$  (right). Three flux surfaces at  $\psi_N = 0.9, 1.0$ , and  $1.1$  are defined with dashed lines.

and tearing modes. The latter break magnetic field lines and, therefore, are resistive instabilities. The driving term is the parallel current density (or its radial derivative) and it may excite instabilities even in the absence of plasma pressure, for example certain external kink modes, which can lead to catastrophic termination of plasma discharges (disruptions). Internal kink instabilities require non-zero pressure to become destabilised. In tokamaks, the internal kink becomes excited when  $q \lesssim 1$  for toroidal and poloidal mode numbers  $n = m = 1$ , and produces ‘sawtooth oscillations’. An external kink mode that requires non-zero plasma pressure to become destabilised is the peeling mode. However, the pressure gradient has a stabilising effect onto peeling modes. The peeling mode is an external kink mode that is localised to the edge of the confined region. The driving term of peeling modes is finite current density at the separatrix and/or the radial gradient of the parallel current density that is locally increased at the edge of H-mode plasmas due to the pressure gradient-driven bootstrap current density  $j_{bs}$  [47]. Typically, peeling modes have low toroidal mode numbers ( $n \leq 5$ ) and they, like edge ballooning modes, are important for the destabilisation of type-I ELMs. Figure 2.4(right) shows the structure of a peeling mode of toroidal mode number  $n = 2$ . In fact, peeling modes couple with ballooning modes at intermediary toroidal mode numbers  $n \approx [5 \dots 10]$ . These coupled peeling-balloonning (PB) modes are considered to be the key instabilities dominating the physics of type-I ELMs.

### 2.3.4 Stability of non-stationary plasmas

Neglecting plasma flows in the stability analysis cannot be generally physically justified, but it allows for ‘simple’ analytical expressions like eqn. (2.32) that help understanding the physical mechanisms that underlie MHD stability. However, in order to assess the stability of tokamak equilibria, it is important to understand the role of plasma flows. In particular, to study the H-mode edge pedestal, it is necessary to include (at least) the ExB velocity and the diamagnetic velocity because the pressure gradient is large in the pedestal<sup>3</sup> [37, 65]. The role of plasma flows onto the stability of ideal MHD edge instabilities is a subject of active study and it is addressed via linear and non-linear numerical simulations. Recently, the de/stabilising influence of toroidal rotation, which can be non-negligible in the plasma edge due to torque input, e.g., by neutral beam injection (NBI), has also received attention [69].

Experimentally, it has been observed that the edge radial electric field is determined by the radial gradient of the main ion pressure gradient [64, 70]. Namely,  $E_r$  in the H-mode edge is primarily set by the pressure gradient term on the radial force balance equation,  $E_r = (n_i q_i)^{-1} \partial_r p_i - v_{\theta,i} B_\phi + v_{\phi,i} B_\theta$ . As a result, the ion fluid is approximately at rest, i.e.,  $v_i = v_{\text{ExB}} + v_i^* \sim 0$ . The influence of the diamagnetic flows and of the radial electric field shear have been reported as stabilising agents. The stabilising effect of the diamagnetic flows onto ideal MHD modes (with stationary growth rate  $\gamma_{\text{MHD}}$ ) manages to suppress said modes if

$$\omega_i^* = m \frac{\delta^* \nabla p_i}{\rho_i} \gtrsim \frac{1}{2} \gamma_{\text{MHD}}.$$

Here  $m$  is the poloidal mode number,  $\rho_i$  and  $p_i$  are the main ion mass density and pressure, respectively, and  $\delta^* = m_i/(eF_0)$  as defined in section 2.2.5 [71–73]. Given that high-n ballooning modes have high poloidal mode numbers, the influence of diamagnetic stabilisation is of significant importance. Similarly, intermediary-n PB modes can also become stabilised by considering diamagnetic effects. It is fundamental to include diamagnetic effects when performing non-linear ELM simulations in order to properly account for the stability of high-n ballooning modes and intermediary-n coupled PB modes.

ELM simulations that do not include the two-fluid diamagnetic effect host unrealistic plasma dynamics because the stabilising effects of the diamagnetic drifts and of  $E_r$  (and of its shear) are missing. In such cases, the end of the ELM crash cannot be properly defined and, therefore, the duration of the event is not in line with experimental observations. On the other hand, including diamagnetic effects leads to more realistic dynamics [65], as shown in chapter 4. The reduced MHD JOREK model does not fulfill the radial force balance equation if the pressure gradient-driven term in the ion velocity is not included.

---

<sup>3</sup>Depending on the size of the machine involved, finite-Larmor-radius modifications to the plasma velocity may need to be taken into consideration as well.

## 2.4 JOREK

The present section is devoted to briefly describing the initial-value non-linear extended MHD code JOREK used to produce the simulations detailed in this dissertation. The JOREK code is regularly used to produce simulations of large-scale instabilities occurring in tokamaks in limiter and divertor geometries. It was first used to study edge localised external kink (peeling) modes [47], and it was subsequently applied to the study of coupled peeling-balloonning modes, thought to be responsible for type-I ELMs [48]. After these applications, the code was extended to simulate ELM control mechanisms like the plasma response to resonant magnetic perturbations (RMPs) [74], cryogenic deuterium pellet injection [75, 76], and vertical kicks [77]. Afterwards, the code has been (and continues to be) applied to study core MHD modes and, in particular, to study disruption physics [78–80]. JOREK is accurate to 2<sup>nd</sup> order in time and to 4<sup>th</sup> order in space. The code has evolved significantly from its original form, and a thorough review of the physics models, numerical methods, verification and benchmark efforts, and the various applications can be found in Ref. [50]. In the following, the temporal discretisation is described in section 2.4.1. The spatial discretisation in the poloidal and toroidal directions are then detailed in section 2.4.2. The code includes a reduced MHD model (that may be used with and without several extensions, e.g., diamagnetic effects) and a full MHD model. Only the reduced MHD model was used in the realisation of this dissertation and, together with the relevant extended physical effects, is described in section 2.4.3. Recently, the validity of reduced MHD for the study of edge localised instabilities like ballooning modes has been bolstered by comparing reduced MHD results to the full MHD version of JOREK [56].

### 2.4.1 Temporal discretisation

JOREK uses a fully implicit time stepping scheme and, in the early stages of development, required inverting a large sparse matrix in every time step. Performing such matrix inversion for each time step carries significant computational cost and caused limitations of the achievable toroidal resolution for a given simulation. Said cost and resolution limitation were reduced by means of an iterative GMRES solver [81]. Appropriately resolving simulations of type-I ELMs requires multiple toroidal mode numbers to be included in the simulation and, therefore, the iterative solver is a key feature of the JOREK code.

The implicit time stepping scheme, although computationally demanding, comes with intrinsic advantages over explicit schemes. For explicit schemes, the size of the time step,  $\delta t$ , is restricted to be below the CFL condition, which decreases with increasing grid resolution. Implicit time stepping schemes, on the other hand, are stable regardless of the time step. However, arbitrarily large time steps can lead to inaccurate results if the chosen time steps are larger than the physical phenomena of interest require.

JOREK is well suited to the study of type-I ELM cycles from the point of view

of the temporal discretisation used. Namely, type-I ELM cycles have a strong time scale separation since the physical effects related to the fast ELM crash are of the order of the Alfvén time ( $\tau_A \sim \mu\text{s}$ )<sup>4</sup> are much faster than the time between ELMs  $1/f_{\text{ELM}} \sim 10$  ms. During the ELM crash, the time step  $\delta t$  must be of the order of  $\tau_A$ , but after the ELM crash is over  $\delta t$  can be substantially increased to decrease the simulation run time without loosing accuracy.

#### 2.4.2 Spatial discretisation

The JOREK code is based on a finite element method that ensures  $G^1$  continuity<sup>5</sup> throughout the simulation domain (except for flux-surface aligned grids in the vicinity of special topological points like the magnetic O- and X-points). In particular, JOREK achieves such properties by using cubic Bézier finite elements. An important feature of the finite element method used in JOREK is that it uses an isoparametric representation, which means that the coordinates  $(R, Z)$  are obtained by the same order of interpolation as the unknowns [49]. Having continuity of the variables and their first derivatives is important for the stability of the system. The spatial discretisation in the poloidal plane is realised on a 2D grid, which can be a polar grid or a flux-surface aligned grid and both are shown in fig. 2.5. JOREK is also able to handle flux-surface aligned grids that host two magnetic X-points [82]. The flux-surface aligned grid with a single magnetic X-point is used for all the simulations presented in this dissertation. For such grids, the simulation domain is divided into three regions. First, the confined region that lies inside the separatrix and it is comprised of closed flux surfaces. Second, the scrape-off layer that lies outside the separatrix. And third, the private flux region that is located underneath the X-point. The latter two regions are comprised of open flux surfaces that start and end in simplified divertor targets. There are two types of computational boundaries. Namely, one that is aligned to the field lines and another that is perpendicular to the field lines (the simplified divertor targets).

In the toroidal direction, JOREK makes use of a Fourier representation to perform the discretisation. Simulations may be run axisymmetrically by considering only a single poloidal plane (i.e., a single toroidal mode  $n = 0$ ) and any variation in the toroidal direction is removed ( $\partial_\phi \equiv 0$ ) or non-axisymmetrically. In order to simulate MHD instabilities, the plasma must be treated non-axisymmetrically. Due to the Fourier representation, the user is able to select (with some constraints), which toroidal mode numbers are to be included in a given simulation. To produce non-linear simulations, the  $n = 0$  mode together with the non-axisymmetric toroidal mode numbers desired are included. However, the selected toroidal modes

<sup>4</sup>The Alfvén time is  $\tau_A = a\sqrt{\mu_0\rho_i}/B$  where  $a$  is the minor radius,  $\mu_0 = 4\pi \times 10^{-7} \text{ N/A}^2$  is the vacuum permeability,  $\rho_i$  is the ion mass density, and  $B$  is the magnetic field strength. For ASDEX Upgrade,  $a = 0.5 \text{ m}$ , typical parameters at the magnetic axis are  $\rho_i = 2 \times 10^{-7} \text{ kg/m}^2$  and  $B = 2.5 \text{ T}$ , which leads to  $\tau_A \sim 0.1 \mu\text{s}$ .

<sup>5</sup>A surface in the poloidal plane with  $G^1$  continuity ensures continuity of a given variable  $v$ , and of the spatial derivatives  $\partial_R v$  and  $\partial_Z v$ .

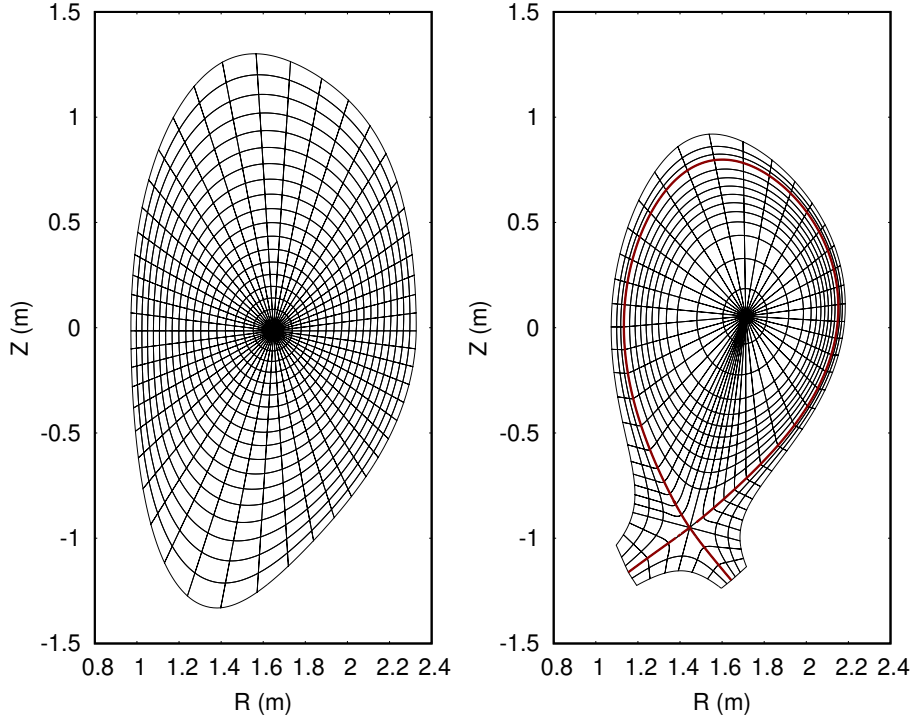


Figure 2.5: Polar grid (left) and flux-surface aligned grid with the magnetic separatrix in dark-red colour (right). The flux-surface aligned grid is comprised of three sections, the region comprised of closed flux surfaces and the regions comprised of open flux surfaces are divided into the private flux region directly below the magnetic X-point and the scrape-off layer. The boundary of the open field line regions are either a field-aligned boundary or a boundary intersecting with the flux surfaces. The grid resolution in these plots has been reduced to show the features of the grids.

must have a certain periodicity  $n_{\text{period}}$ . A periodicity of  $n_{\text{period}} = 1$  is analogous to simulating an entire tokamak, of 2 a half-tokamak, of 3 a third of a tokamak, and so forth. While there is flexibility regarding the set of toroidal mode numbers to be included in a given simulation, a user must choose an adequate set of  $n$  that achieves convergence of the physical phenomena relevant for the simulation. The correct choice of toroidal resolution depends on the physical effects that will be simulated. For example, realistically simulating (2, 1) tearing modes will not require including high toroidal mode numbers and including  $n = 0, 1, 2, \dots, 5$  might be sufficient to resolve the relevant non-linear dynamics. In contrast, simulating high- $n$  ballooning modes typically requires a higher toroidal resolution.

### 2.4.3 Governing equations

The present section details the equations that govern the reduced MHD model used for the simulations presented in this thesis. The model and its equations closely follow the reduced MHD equations described in section 2.2.4, i.e., inserting the ansatzes of eqns. (2.26) and (2.27) into the full MHD equations ((2.13)-(2.19)):

$$\frac{\partial \rho}{\partial t} = -\nabla \cdot (\rho \mathbf{v}) + \nabla \cdot (D_{\perp} \nabla_{\perp} \rho) + D_{\text{hyp}} \nabla^4 \rho + S_{\rho} \quad (2.33)$$

$$\rho \frac{\partial \mathbf{v}_{\text{pol}}}{\partial t} = -\rho(\mathbf{v} \cdot \nabla) \mathbf{v}_{\text{pol}} - \nabla_{\text{pol}} p + (\mathbf{J} \times \mathbf{B})_{\text{pol}} + \mu \nabla^2 \mathbf{v}_{\text{pol}} + \mu_{\text{hyp}} \nabla^4 \mathbf{v}_{\text{pol}} - \mathbf{v}_{\text{pol}} S_{\rho} + S_{v_{\parallel}} \mathbf{b}_{\text{pol}} \quad (2.34)$$

$$\rho \frac{\partial v_{\parallel}}{\partial t} = -\rho(\mathbf{v} \cdot \nabla) v_{\parallel} - \nabla_{\parallel} p + \mu_{\parallel} \nabla^2 v_{\parallel} + \mu_{\parallel, \text{hyp}} \nabla^4 v_{\parallel} - v_{\parallel} S_{\rho} + S_{v_{\parallel}} \quad (2.35)$$

$$\frac{\partial p}{\partial t} = -\mathbf{v} \cdot \nabla p - \gamma p \nabla \cdot \mathbf{v} + \nabla \cdot (\kappa_{\perp} \nabla_{\perp} T + \kappa_{\parallel} \nabla_{\parallel} T) + S_p \quad (2.36)$$

$$\frac{\partial \psi}{\partial t} = R[\psi, u] - F_0 \partial_{\phi} u + \eta(j - j_0 - (j_{\text{BS}} - j_{\text{BS},0})) + \eta_{\text{hyp}} \nabla^2 j \quad (2.37)$$

The momentum equation results in two equations because it is projected onto the poloidal plane and onto the direction parallel to the magnetic field. A few additional considerations are required to arrive at the JOREK reduced MHD equations shown above. In particular, stationary particle and heat sources<sup>6</sup> are included that are used to maintain the initial plasma profiles or tailor them to a reach desired profile, e.g., build-up the edge pedestal. A parallel velocity source is also included in order to account for sources of parallel momentum, e.g., neutral beam injection (NBI). Heat and particle diffusion is included, and it is used to mimic the transport processes that go beyond MHD as detailed in section 2.2.6, e.g., turbulent transport. The stress tensor is approximated as an isotropic tensor such that the corresponding expression in the momentum equation is related to the poloidal and parallel dynamic plasma viscosity  $\mu$  and  $\mu_{\parallel}$ , respectively. A current source term is included in the induction equation to avoid Ohmic decay and, therefore, helps keep the initial current density profile  $j_0$  constant. A current source term that depends on analytical expressions for the initial and instantaneous bootstrap current contributions ( $j_{\text{BS},0}$  and  $j_{\text{BS}}$ , respectively) is also included. Hyper-diffusive terms ( $\eta_{\text{hyp}}$ ,  $\mu_{\parallel, \text{hyp}}$ , and  $\mu_{\text{hyp}}$ ) are available for numerical stability.

The JOREK toroidal current density is related to the physical toroidal current density as  $j = -R j_{\phi}$ , and it is defined by an additional equation  $j = \Delta^* \psi$ , where  $\Delta^*$  is the Grad-Shafranov differential operator defined in section 2.2.3. Finally, the toroidal component of the ExB vorticity is also added as a variable,  $\omega = \nabla \cdot \nabla_{\text{pol}} u$ , where  $\nabla_{\text{pol}} = \nabla - \hat{\phi} R^{-1} \partial_{\phi}$ . The JOREK variables are, in the order of the above equations,

---

<sup>6</sup>Note that  $S_{\rho}$  in reality depends on time-dynamical processes such as the ionisation of neutrals coming from gas and impurity puffing, pellet ablation, and plasma-wall interactions.

- the mass density  $\rho$ ,
- the velocity stream function  $u$  which is directly related to the electrostatic potential as  $\Phi = F_0 u$ , and it satisfies  $\mathbf{v}_{\text{ExB}} = -R^2 \nabla u \times \nabla \phi$ ,
- the parallel velocity  $v_{\parallel}$ ,
- the single fluid temperature  $T$ ,
- the poloidal flux  $\psi$ ,
- the toroidal current density  $j = -R j_{\phi}$ ,
- and the vorticity  $\omega$ .

The poloidal viscosity, toroidal resistivity, and the parallel heat diffusivity can be chosen to be spatially constant or temperature dependent with the following expressions

$$\mu(T) = \mu_0 \left( \frac{T}{T_0} \right)^{3/2}, \quad \eta(T) = \eta_0 \left( \frac{T}{T_0} \right)^{3/2}, \text{ and} \quad \kappa_{\parallel}(T) = \kappa_{\parallel,0} \left( \frac{T}{T_0} \right)^{5/2}.$$

The subscript 0 denotes the value at the magnetic axis, and the values for viscosity, resistivity, and parallel heat diffusivity at the magnetic axis are input parameters set by the user.  $\kappa_{\parallel}$  has a Spitzer-Härm temperature dependence, and the central value may be set accordingly [83]. The resistivity follows a Spitzer temperature dependence, and the viscosity as well in order to maintain a roughly constant magnetic Prandtl number throughout the simulation domain. The central value for the resistivity should be determined from the Spitzer expression plus a neoclassical correction [66, 67]. The neoclassical correction is required because the Spitzer expression is strictly valid only for cylindrical plasmas. In toroidal geometry, trapped particles cannot respond freely to an applied electric field and, therefore, neoclassical corrections dependent on the trapped particle fraction and on  $\varepsilon (= r/R)$  are necessary to determine the correct value of the resistivity. In particular, larger fraction of trapped particles results in larger resistivity. These corrections play a minor role near the magnetic axis, but a much more substantial role near the plasma edge. An even more accurate expression is dependent on the main ion charge  $Z$  and on  $Z_{\text{eff}} (= \sum_i n_i Z_i^2 / n_e)$  [11].

An important feature of JOREK is that it accurately captures the strong anisotropy between parallel and perpendicular heat diffusion,  $\kappa_{\parallel}/\kappa_{\perp} \sim 10^{8...10}$  [84]. The perpendicular diffusion coefficients depend on the radial distance from the magnetic axis,  $D_{\perp}(\psi_N)$  and  $\kappa_{\perp}(\psi_N)$ , where

$$\psi_N = \frac{\psi - \psi_{\text{axis}}}{\psi_{\text{bnd}} - \psi_{\text{axis}}} \tag{2.38}$$

is the normalised poloidal flux and  $\psi_{\text{axis}}$  and  $\psi_{\text{bnd}}$  are the values of  $\psi$  at the magnetic axis and at the last closed flux surface, respectively. The heat and particle

sources are chosen to either maintain the initial profiles constant when performing an axisymmetric simulation, or to cause a desired axisymmetric evolution of the initial profiles. For example, to achieve pedestal build-up or to maintain H-mode profiles, perpendicular diffusion coefficients should have a deep well in the edge region, which would represent the edge transport barrier, qualitatively shown in fig. 2.6. It is emphasised that these profiles are user-defined as *ad-hoc* diffusion and sources.

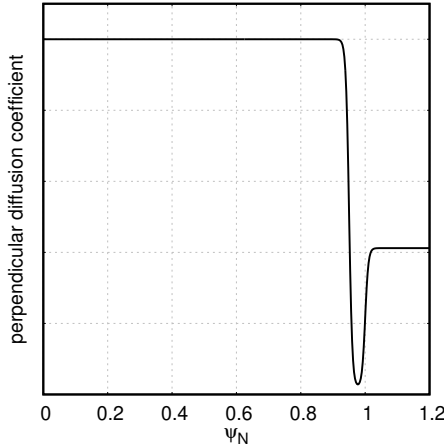


Figure 2.6: Qualitative profile of perpendicular diffusion coefficients characterised by an edge transport barrier to host a density/temperature pedestal. The magnetic axis is at  $\psi_N = 0$  and the separatrix is at  $\psi_N = 1$ .

JOREK allows for some flexibility with respect to the boundary conditions (BCs). For the simulations presented in this dissertation, Dirichlet (fixed) BCs are used for  $\psi$ ,  $u$ ,  $j$ , and  $\omega$  throughout the boundary. Fixed boundary conditions for the magnetic flux is equivalent to stating that the plasma is surrounded by an ideally conducting wall located at the computational boundary. For  $\rho$  and  $T$ , Dirichlet BCs are applied throughout the boundary except at the divertor tiles. At the divertor tiles, no BC is enforced for the plasma density and temperature, and Bohm BCs are used such that  $v_{\parallel}$  is set to the local sound speed. If sheath BCs are applied, which may be easily set by the user, a BC for the plasma temperature gradient at the divertor targets is enforced such that the Stangeby sheath heat flux equals the MHD heat flux [85],

$$\mathbf{q} \cdot \hat{\mathbf{n}} \equiv \left( \frac{\rho}{2} \mathbf{v} \cdot \mathbf{v} + \frac{\gamma}{\gamma - 1} \rho T \right) \mathbf{v} \cdot \hat{\mathbf{n}} - \frac{\kappa_{\perp} \nabla_{\perp} T + \kappa_{\parallel} \nabla_{\parallel} T}{\gamma - 1} \cdot \hat{\mathbf{n}} = \gamma_{sh} \rho T_e \mathbf{v} \cdot \hat{\mathbf{n}}, \quad (2.39)$$

where  $\hat{\mathbf{n}}$  is the normal unit vector to the boundary (the divertor tiles),  $T_e$  is the electron temperature (which for the single fluid model considered may be obtained as  $T_e = T_i = T/2$ ), and  $\gamma_{sh}$  is the sheath transmission factor. Unless specified otherwise, sheath boundary conditions are not used for the simulations presented in this dissertation.



## 3 Overview of experiments and MHD simulations

This chapter attempts to provide an overview of the experimental conditions relevant for this work. To begin with, several physical characteristics of the high-confinement mode (H-mode) and some of the observed edge instabilities are described in section 3.1. Baseline conditions in H-mode plasmas are prone to periodic events dubbed type-I edge localised modes (ELMs). Section 3.2 describes the different phases relevant for the type-I ELM cycle. The state-of-the-art in terms of ELM simulations is then provided in section 3.3. Lastly, section 3.4 details the features of an operational regime observed in ASDEX Upgrade and TCV (tokamak à configuration variable) that is dominated by so-called ‘small ELMs’ and recently named quasi-continuous exhaust (QCE) scenario.

### 3.1 High confinement mode (H-mode)

The high confinement mode was discovered in 1982 in the ASDEX tokamak in Garching near Munich, Germany [17]. The relevant observation was that in the diverted magnetic geometry, applying sufficient heating power leads to a bifurcation in the plasma behaviour at the edge of the confined region. Said bifurcation resulted in an operational regime with roughly twice the central pressure and energy confinement time. This represented a significant breakthrough for the magnetic confinement fusion community. Thereafter, the previous ‘normal’ operational regime was named L-mode (for low confinement). The threshold heating power required to transition from L- to H-mode,  $P_{LH}$ , is primarily dependent on the plasma density, toroidal magnetic field, and the surface area of the last closed flux surface [86].

The reason behind the improvement in confinement is a significant reduction in the radially outward turbulent (also called anomalous) transport in the plasma edge. Prior to entering H-mode, in L-mode operation, turbulence in the plasma edge represents the main transport channel for heat and particles. This is reflected in low density and temperature (and pressure) gradients at the edge of the confined region, as shown with the black pressure profile in fig. 3.1 (left). Upon entry to H-mode, however, this transport channel disappears and, therefore, heat and particles become accumulated and form a so-called *pedestal* across a few centimeters (this region is called the edge transport barrier, or ETB). The ETB is then associated to a local increase of the density and temperature and to their associated gradients in the plasma edge. This local increase of density and temperature at the plasma

edge (often referred to as pedestal top) translates to a proportionate increase of the core values of density and temperature as can be seen in fig. 3.1.

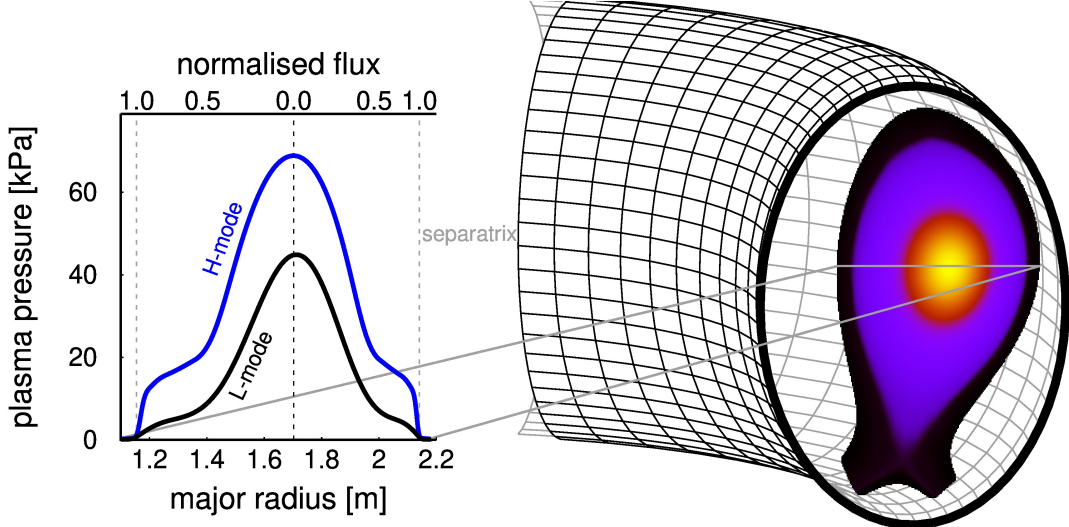


Figure 3.1: Schematic representation of pressure profiles for L-mode and H-mode across the midplane,  $Z = Z_{\text{axis}}$  (left). A colour map corresponding to the H-mode plasma pressure is also shown in the right hand side.

### 3.1.1 Role of the radial electric field

The most widely accepted theory that attempts to explain the physical processes that permit entry into H-mode is based on the Biglari-Diamond-Terry (BDT) paradigm of suppression of turbulent transport by sheared ExB flow [20, 87, 88]. In a few words, this paradigm posits that sufficiently sheared ExB flow leads to a decorrelation, and ultimately suppression, of certain turbulent instabilities. Indeed it has been observed that the edge radial electric field becomes more negative at the time of the L-H transition, which shows support for said theory. The radial electric field and its shear are also known to stabilise macroscopic MHD instabilities like high-n ballooning modes, as described in section 2.3.4. The mechanism (or the combination of mechanisms) that leads to the formation of the sheared radial electric field directly before entry into H-mode is a topic of active study. It has been observed that the  $E_r$  well located at the pedestal during H-mode operation roughly corresponds to the ‘neoclassical’ estimate  $E_{r,\text{neo}} \approx (en_i)^{-1} \nabla p_i$ , where  $p_i$  and  $n_i$  are the ion pressure and density, respectively [70]. A thorough review of the different theories for the L-H transition and of the mechanisms that may generate the sheared radial electric field can be found in Ref. [89].

The reduced turbulent transport in the plasma edge associated to H-mode operation leads to a local increase of density and temperature, but this is not an

unconstrained increase. In L-mode, the gradient-limiting micro-turbulence induces approximately constant heat and particle fluxes. On the other hand, in H-mode, the outward heat and particle fluxes are a combination of constant transport from the remnant anomalous transport and transient instabilities. The latter consists of short periods of time that repetitively cause greatly enhanced transport. The physical mechanisms that limit the edge density and temperature gradients in H-mode are macroscopic MHD instabilities instead of the microscopic turbulence that limit them in L-mode. Indeed, upon entry to H-mode, quasi-periodic events that expel heat and particles outwards from the confined region were observed. These events were already reported in Ref. [17] and were later called edge localised modes (ELMs) [26].

### 3.1.2 Type-I ELMs and other ELM types

The repetition frequency of ELMs varies in the range  $f_{\text{ELM}} \approx 1 - 10^3$  Hz. In general terms, ELMs are comprised of two distinct phases: the inter-ELM phase or recovery phase, and the ELM crash phase. The latter is a short lived phase roughly lasting  $t_{\text{ELM}} \sim 0.1 - 3$  ms, and it is characterised by large transient heat and particle fluxes that cause a collapse of the edge density and temperature pedestals, and of the large associated bootstrap current density. The duration of the inter-ELM phase relates to the time required for the pedestal to return to its pre-ELM (crash) conditions, i.e.  $\tau_{\text{ped}} \sim 1/f_{\text{ELM}}$ , and it is associated to heat and particle fluxes lower than those observed in L-mode discharges. Historically, ELMs became classified depending on their size (the energy that each ELM expels) and how the ELM repetition frequency responds to a change in the applied heating power. The classification separated ELMs into the three main types listed below [27, 28].

- **Type-I ELMs** have directly proportional ELM repetition frequency and applied heating power,  $f_{\text{ELM}} \propto P_{\text{heat}}$ . The relative ELM size,  $\Delta W_{\text{ELM}}/W_{\text{pre-ELM}}$  where  $\Delta W_{\text{ELM}}$  is the energy lost per ELM and  $W_{\text{pre-ELM}}$  is the pre-ELM stored energy, is the largest among all ELM types and it ranges between 5 – 15%. Associated to the large ELM sizes, type-I ELMs cause high transient heat loads to the divertor targets, which are a cause for concern for large tokamaks like ITER [90]. This type of ELM has been understood in the framework of the peeling-balloonning model, which has proven successful in estimating linear stability properties of type-I ELMs [24, 25, 91]. A more complete description of type-I ELMs is provided in section 3.2.
- **Type-II ELMs** cannot be classified in terms of the ELM repetition frequency response to a change in the applied heating power. In fact, it is somewhat ambiguous to talk about type-II ELM repetition frequency because type-II ELMs often do not show a well defined periodic behaviour and, instead, there is a quasi-continuous exhaust of heat and particles. Additionally, no large transient heat load like those associated to type-I ELMs are observed. This type of ELM has also been called grassy or (high density) small ELMs [92, 93].

A thorough review of small and no-ELM regimes can be found in Ref. [94]. Small ELMs at high density have been observed in AUG at high triangularity and closeness to double null [42, 95, 96]. More details onto the small ELMs observed in AUG (recently named *quasi-continuous exhaust* (QCE) regime) are found in section 3.4.

- **Type-III ELMs** are characterised by decreasing their repetition frequency when the heating power is increased,  $f_{\text{ELM}} \propto 1/P_{\text{heat}}$ . In comparison to type-I ELMs, these have a larger  $f_{\text{ELM}}$  and lower relative ELM sizes. This type of ELM appears both at low and at high pedestal densities, but always below a critical edge temperature. It is believed that the underlying instabilities that govern type-III ELMs are resistive MHD instabilities. Type-III ELMs appear either at low density with heating powers close to the L-H power threshold,  $P_{\text{heat}} \approx P_{\text{LH}}$ , or with high heating power at large densities. At low density, type-III ELMs disappear when the heating power exceeds a threshold  $P_{\text{type-I}}$ . At high heating power, a type-I ELM My H-mode may give rise to type-III ELMs if the plasma density is sufficiently increased [97].

The pedestal collisionality<sup>1</sup> plays an important role for MHD instabilities because the bootstrap current is strongly dependent on  $\nu_{e,\text{ped}}^*$ . Concretely, low (but not arbitrarily low)  $\nu_{e,\text{ped}}^*$  is related to large bootstrap current density fractions, and high  $\nu_{e,\text{ped}}^*$  is related to low  $j_{\text{bs}}$  fractions. It has been observed that low collisionality is related to large type-I ELM energy losses, which is of particular concern for future machines like ITER that are poised to operate at low pedestal collisionality [98].

### 3.1.3 Naturally ELM-free regimes

Due to the risks posed by type-I ELMs, and to the restricted operational spaces of ELM My H-mode operation with good confinement properties but without (or with mitigated/suppressed) type-I ELMs, H-mode operation without ELMs is an active research topic. Indeed a few ELM-free H-mode regimes have been obtained in various machines around the world. Such ELM-free regimes may be classified into three categories: Quiescent H-mode (QH-mode), improved energy confinement mode (I-mode), and high collisionality regimes with enhanced recycling. It could be said that these ELM-free regimes (and the quasi-continuous exhaust scenario further described in section 3.4) share some commonalities with L-mode in that there is a roughly constant transport mechanism that regulates the gradients at the edge region. For QH-mode, the mechanism is an  $n = 1$  mode called edge harmonic oscillation (EHO). I-mode features high energy confinement (like H-mode), but has poor particle confinement (like L-mode). The underlying transport mechanism is believed to be a non-linear coupling between the so-called weakly coherent mode

---

<sup>1</sup>Collisionality is the ratio between the electron-ion collision frequency to the trapped particles bounce frequency. It is defined in Ref. [66] as  $\nu_e^* = 6.921 \times 10^{-18} R q n_e Z_{\text{eff}} \ln \Lambda_e / (\varepsilon^{3/2} T_e^2)$ , where  $q$  is the safety factor,  $\varepsilon = r/R$  is the inverse aspect ratio, and  $\ln \Lambda_e = 31.3 - \ln(\sqrt{n_e}/T_e)$  is the Coulomb logarithm.

(WCO) localised at the plasma edge and geodesic acoustic modes. Finally, the enhanced recycling regimes, like the EDA H-mode in Alcator C-mod or the stationary ELM-free H-mode in AUG, are believed to be regulated by edge electromagnetic quasi-coherent modes [99, 100]. More details onto these ELM-free operation regimes may be found in Refs. [38, 94].

### 3.1.4 ELM mitigated or suppressed regimes

In addition to naturally ELM-free regimes, type-I ELMs may be mitigated (and even suppressed) by applying known ELM-control mechanisms [39, 101]. The following presents an incomplete list of such mechanisms

- **Application of resonant magnetic perturbations (RMPs)** is the primary ELM mitigation/suppression method for ITER. It consists of applying magnetic perturbations in order to avoid the plasma pedestal from crossing the type-I ELM stability threshold. The access conditions for an ELM-mitigated or ELM-suppressed H-mode in ITER are not yet understood because ITER-relevant densities and pedestal collisionalities cannot be simultaneously achieved in present-day tokamaks. Figure 3.2 shows the access conditions to ELM suppression and it highlights the fact that it is unclear whether it will be possible to completely avoid type-I ELMs in ITER solely with the use of RMPs.

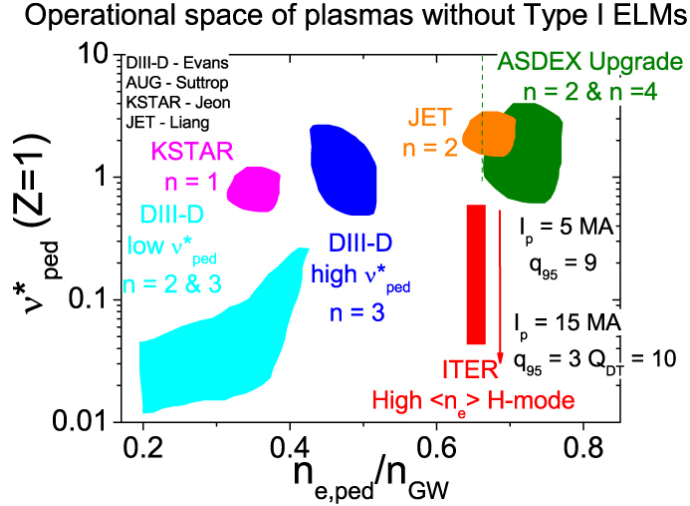


Figure 3.2: Access conditions for plasmas without ELMs through the application of magnetic perturbations. The red region corresponds to ITER-relevant densities and collisionalities, which cannot be simultaneously achieved in present-day tokamaks. Figure reproduced from [101].

- **Pellet pacing** is foreseen as one of two main ELM mitigation methods for ITER, which will have ELM frequencies on the order of  $f_{\text{ELM}} \sim (1, 10)$  Hz [101].

The underlying mechanism for pellet pacing is the controlled increase of the ELM repetition frequency, as it has been observed that the power lost due to ELMs corresponds to roughly 20 to 40% of the applied input power  $P$ ,

$$\frac{\Delta W_{\text{ELM}} \times f_{\text{ELM}}}{P} = 0.2 - 0.4.$$

Namely, the ELM size is inversely proportional to the ELM repetition frequency. The successful application of pellet pacing as an ELM control mechanism additionally relies on the relationship between the ELM size and the area over which the ELM-related energy is deposited (wetted area,  $A_{\text{ELM}}$ ). And it also relies on being able to control  $f_{\text{ELM}}$  above certain minimum values.

An unfavourable relation between the ELM size and  $A_{\text{ELM}}$  has been observed, and poses concerns about the applicability of pellet pacing as an ELM-control mechanism for ITER [102]. Additionally, it has been observed that it is not possible to pace ELMs through pellet injection at arbitrarily large frequency in AUG with tungsten (AUG-W) as first-wall material [44] and in JET with the ITER-like-wall (JET-ILW)<sup>2</sup> [43]. These two observations are worrisome in terms of the applicability of pellet ELM pacing as an ELM control scheme for ITER. However, pellet pacing is foreseen as an option for controlling the ELM frequency in low plasma current experiments which may be prone to impurity accumulation.

Pellet-triggered ELMs, including the lag-time required to trigger an ELM following a spontaneous or pellet-triggered ELM that has been observed in AUG-W [44], have been simulated with the JOREK code, and it is suggested that the mechanism responsible for the ELM triggering is a localised increase of the plasma pressure, which excites ballooning modes [46, 76, 103].

- **Vertical kicks**, or jogging, is an ELM pacing method with which ELMs are triggered by bouncing the plasma up and down. This ELM control method has been achieved in several tokamaks and has been simulated with the free-boundary code JOREK-STARWALL [77]. Said simulations shed light onto the triggering mechanism: a vertical kick caused an increase in the pedestal toroidal current due to a compression of the confined plasma, and the increased edge current density is likely responsible for triggering the ELM. Kicks are considered as a fall-back option to avoid impurity accumulation in low plasma current experiments in ITER by pacing ELMs at a sufficiently large repetition frequency.

Type-III ELMs have also been considered as a potential mitigation system, but have been associated with bad plasma confinement. Therefore, it appears that operation with type-III ELMs is not a suitable alternative for ITER. The following section provides further details regarding type-I ELMs and the type-I ELM cycle.

---

<sup>2</sup>ILW refers to tungsten divertor tiles and beryllium for the rest of the plasma facing components.

## 3.2 The type-I ELM cycle

As described above, type-I ELMs are quasi-periodic MHD instabilities that are characterised by a repetition frequency proportional to the input heating power. This type of ELM is associated with large heat and particle losses and are a cause for concern in ITER [90]. Presently, it is generally accepted that type-I ELMs are the result of a coupling between two ideal MHD instabilities—ballooning modes and external kink (peeling) modes (the so-called PB model) [24, 25, 91]. However, some experiments at high fuelling rates and high heating powers in JET-ILW do not seem to adhere to the PB model and, therefore, point to additional physical mechanisms which are important to the dynamics of type-I ELMs [104, 105].

The type-I ELM cycle may be divided into an ELM crash phase and an inter-ELM phase. The duration of the ELM crash phase shows variations throughout different tokamaks and ranges anywhere between  $\tau_{\text{ELM}} \sim 200 \mu\text{s}$  up to a few milliseconds [106–108]. The inter-ELM phase duration varies from as fast as a few milliseconds (in small or medium-sized machines with high heating power) up to a few tenths of a second (for large machines with  $P_{\text{heat}} \approx P_{\text{type-I}}$ ). The present section describes three different phases (shown in fig. 3.3a) that comprise the inter-ELM phase in subsections 3.2.1–3.2.3, and then the ELM crash phase in subsection 3.2.4.

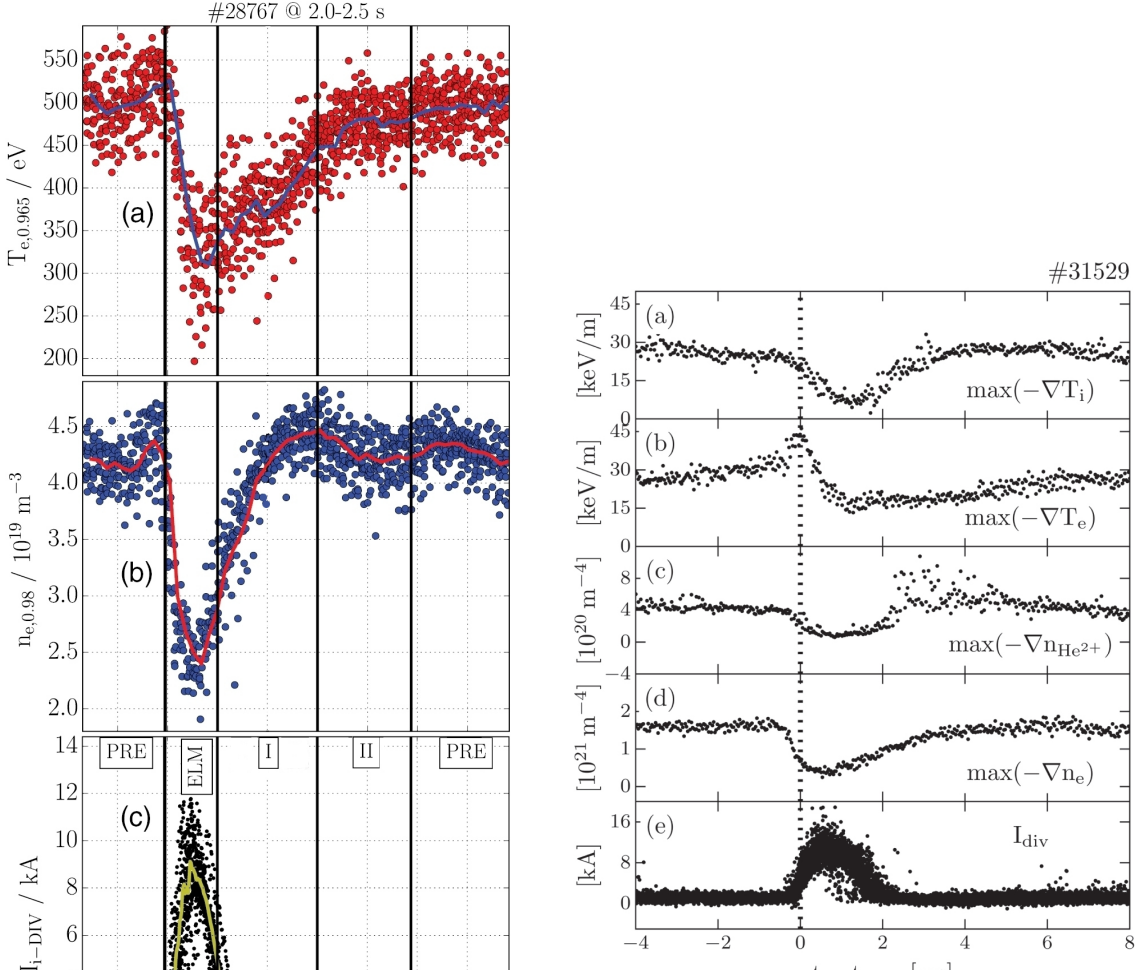
A general description of the type-I ELM cycle, arbitrarily taking the end of the ELM crash as a starting point, is provided below. The different phases of the type-I ELM cycle are detailed by making use of figs. 3.3a and 3.3b, which qualitatively show the evolution of the pedestal electron temperature and density (fig. 3.3a), and of  $T_i$ ,  $T_e$ , and  $n_e$  maximum gradients (fig. 3.3b) synchronised throughout several ELM cycles. The ELMs used for the above-mentioned figures have low repetition frequency,  $f_{\text{ELM}} \approx 50$  and 85 Hz, respectively.

### 3.2.1 Phase I: $\nabla n_e$ and $\nabla T_i$ saturation

The ion and electron pedestal density, temperature, and pressure (and their gradients) start from values well below the peeling-balloonning stability boundary. The ion and electron pedestals then begin to grow in height and width. Near the end of this early pedestal build-up phase, the electron density and the ion temperature (and their respective edge gradients) saturate [110]. Together with the increase of  $n_e$ ,  $T_i$ , and their respective gradients, the radial electric field increases; within the error bars it increases as  $E_{r,\text{neo}} \approx (en_i)^{-1}\nabla p_i$  and, therefore, saturates in the same time as  $n_e$  and  $T_i$  [110]. The electron temperature and its gradient, however, continue to increase [111–114]. At the very beginning of this inter-ELM phase, no activity is observed in terms of density and magnetic fluctuations [109, 113, 115, 116]. However, as the pedestal develops, medium/low-frequency ( $f \leq 50$  kHz) oscillations in the magnetic signals with intermediary toroidal mode numbers  $n \approx 5 \dots 8$  have been detected, e.g., in AUG [109] and in KSTAR [117].

This first inter-ELM phase ends when  $n_e$  and  $T_i$  (and  $\max(\nabla n_e)$  and  $\max(\nabla T_i)$ ) saturate to roughly their pre-ELM values ( $t - t_{\text{ELM}} \approx 6$  ms in fig. 3.3a and 4 ms in

### 3 Overview of experiments and MHD simulations



(a) The pedestal top electron temperature (a) and density (b), and the divertor shunt current (c) of 25 different (low-repetition frequency) ELMs in the same AUG discharge (#28767) synchronized to  $t_{\text{ELM}}$ , together with smoothed signals. Figure modified from Ref. [109].

(b) Data of several ELMs from AUG discharge (#31529) synchronised to the rise of the divertor shunt current. The maximum gradient of the ion temperature (a), electron temperature (b), helium ( $\text{He}^{2+}$ ) impurity density (c), and electron density (d), and the divertor shunt current (e). The build-up time of the electron density and the ion temperature gradients appear to be roughly the same, but the evolution of the maximum electron temperature gradient appears to be slower. Figure reproduced from Ref. [110].

Figure 3.3

fig. 3.3b). The actual duration of each phase within the inter-ELM is dependent on several aspects, e.g., heating power, collisionality, and gas puff. Indeed, it appears that the occurrence of the medium/low-frequency modes correlates to the saturated

growth of the ion temperature and the electron density.

### 3.2.2 Phase II: $\nabla T_e$ saturation

In this phase, the intermediary-n modes with medium/low frequencies ( $f \approx 50$  kHz) that had started to appear at the end of the early build-up phase persist. These appear to cause some outwards transport associated with modulations of the  $n_e$  pedestal about its pre-ELM value, and are located in the steep pressure gradient region [109, 113]. Nearing the end of this late pedestal build-up phase, high-frequency fluctuations ( $f \approx 250$  kHz) with toroidal mode numbers of  $n \approx 8 \dots 14$  are observed [109, 113, 116], and it has been postulated that non-linear interactions are partly responsible for their onset [118]. In AUG, the appearance of modes with low-frequency ( $f \approx 4 - 12$  kHz) and high toroidal mode number ( $n \approx 13, 14$ ) has also been linked to this phase [119]. Together with the appearance of the high-frequency, high-n modes,  $T_e$  and  $\max(\nabla T_e)$  reach their pre-ELM values and stop growing further. The fact that two different sets of modes are related to the saturation of the ion temperature and to the electron temperature indicates that different mechanisms are at play in terms of the inter-ELM ion and electron channels.

### 3.2.3 Pre-ELM phase: constant gradients and pedestal widening

At the beginning of the pre-ELM phase, the ion and electron maximum gradients often have saturated to the values that they will, on average, hold throughout the entire phase until the ELM crash. This so-called clamping of the edge gradient is accompanied by a continued widening of the pedestal that results in an increase of the pedestal top. The duration of the pre-ELM phase varies significantly between different discharges in a given tokamak and between different tokamaks. It is presently unknown what exactly governs the duration of the pre-ELM phase. Additionally, it is unclear why the ELM does not become excited immediately when the pedestals steepen to the pre-ELM values.

Low-frequency magnetic precursors that live for  $\sim 0.2 - 2.0$  ms have been detected in COMPASS-D ( $n \approx 4 \dots 6$ ) [120], AUG ( $n \approx 2 \dots 10$ ) [109, 121–124], JT-60U [125], and JET ( $n \approx 2 \dots 4$ ) [115]. It is thought that these low-frequency fluctuations are coupled peeling-balloonning modes and precursors to the non-linear ELM crash [126, 127]. In addition to the low-frequency precursors, medium- and high-frequency magnetic fluctuations ( $f \approx 70 - 300$  kHz) with larger toroidal mode numbers ( $n \approx 8 \dots 16$ ) are also often observed in several machines [109, 113, 115, 116, 119, 127].

Properly understanding how the pedestal grows between ELMs is a topic of active discussion and deals with a plethora of physical effects ranging from the de/stabilisation of different micro-instabilities to the penetration (and ionisation) of neutral particles [128–130]. The width of the pedestal right before the ELM crash appears to be approximately correlated to the pedestal top normalised electron pressure,  $\beta_{p,\text{ped}}^{0.5} = 2\mu_0 p_{p,\text{ped}}^{0.5}/\langle B_{\text{pol}} \rangle$ , in DIII-D [131, 132], JT-60U [133], JET,

and AUG [134]. The observed scaling would point to the destabilisation of kinetic ballooning modes (KBMs) as an important ingredient in setting the pedestal width, as posited by the EPED1 model [135], but definite evidence for the effect of KBMs onto the pedestal width is yet to be found and the pedestal top beta poloidal scaling is not always present [136].

As the pre-ELM phase nears its end, the high-frequency magnetic fluctuations mentioned before appear to fade away while the low-frequency fluctuations persist. This indicates that the latter could be ELM precursors and, as such, partly responsible for the ELM triggering mechanism [33, 109, 127]. However, said low-frequency precursors are not always directly observed either because they are not always present or because their growth is sometimes too fast to be captured. This phase abruptly ends as the ELM crash begins to take place.

### 3.2.4 ELM crash

During the pre-ELM phase, the edge profiles slowly cross the peeling-balloonning stability boundary due to a widening and/or steepening of the pedestal. The rise time of an MHD instability that becomes destabilised by driving the plasma across the stability boundary is estimated as  $\tau \sim \tau_A^{2/3} \tau_{\text{ped}}^{1/3}$  [137], where  $\tau_A$  is the Alfvén time and  $\tau_{\text{ped}} \sim 1/f_{\text{ELM}}$  is the time required to rebuild the pedestal. This results in typical rise times of several tens of microseconds [36]. As the destabilised PB modes reach large amplitudes, energy transport from the confined region to the scrape-off layer (SOL), and ultimately to the divertor targets, through conduction and/or convection starts to become significant. In particular, the relative energy losses (with respect to the pre-ELM stored energy,  $W_{\text{pre-ELM}}$ ) observed for type-I ELM crashes are in the order of  $\Delta W_{\text{ELM}}/W_{\text{pre-ELM}} \approx 5 - 15\%$  typically in short periods of time ( $\sim 0.1 - 3.0$  ms) [106, 138]. As energy is flushed out of the confined region due to the ELM crash, the pedestal relaxes and, therefore, the drive for PB modes is eliminated. At the same time, the radial electric field (and its stabilising influence on high-n ballooning modes) is drastically reduced to values close to L-mode conditions, but within the error bars,  $E_r$  is roughly equal to  $E_{r,\text{neo}} \sim \nabla p_i/n_i$  even during and after the ELM crash [110].

During the ELM crash, the dominant toroidal mode numbers obtained from the analysis of edge magnetic fluctuations are often observed to be low-n modes, e.g.,  $n = 1$  in TCV [139] and  $n \approx 2 - 5$  in AUG [109, 140], however higher toroidal mode numbers have also been reported to be dominant during the ELM crash [33, 129]. Associated to the ELM crash, filamentary structures aligned to the magnetic field appear and are expelled from the confined region to the SOL while carrying large fractions of the convected ELM energy (convection dominated ELMs have small  $\Delta T_e \equiv T_{e,\text{pre-ELM}} - T_{e,\text{post-ELM}}$  and large  $\Delta n_e$ ) [138, 141]. The conductive losses due to an ELM crash are related to ergodisation of the edge region (dominant conductive ELMs have large  $\Delta T_e$  and small  $\Delta n_e$ ) [98, 142]. The ergodisation of the plasma edge opens a fast transport channel through parallel heat diffusion via

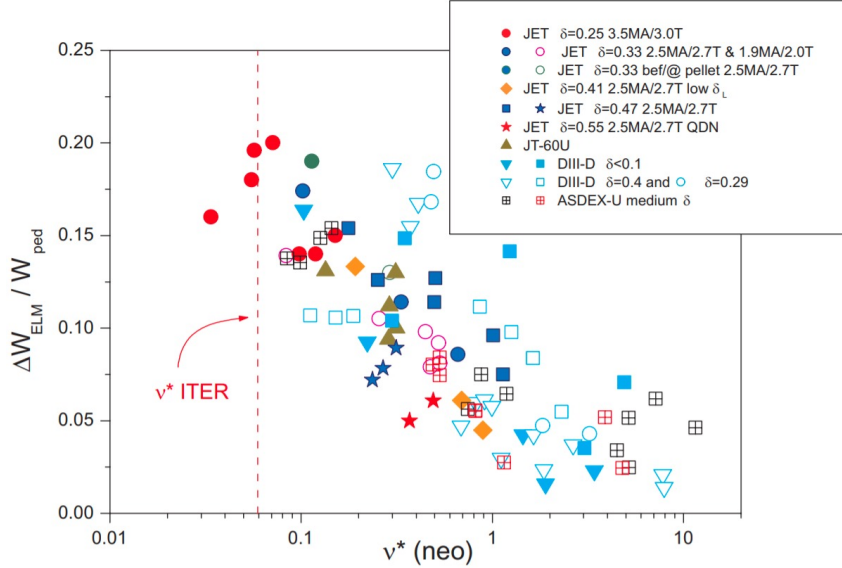


Figure 3.4: Relative ELM size scaling with respect to the electron collisionality in the pedestal during the pre-ELM phase. The ELM size increases with decreasing pedestal top collisionality across tokamaks of different sizes. ITER will operate at low pedestal top collisionality and, thus, type-I ELMs are expected to be large. Figure reproduced from Ref. [98]

magnetic field lines that begin in the pedestal and end in the divertor targets. It has been observed that increasing the pedestal density reduces the conductive losses. Convective losses, on the other hand, do not show any clear dependence with density [143]. This implies that conduction-dominated ELMs, i.e., ELMs at high densities, typically have smaller sizes. Considering additionally the influence of the pedestal temperature on the ELM losses, a clear trend of increasing ELM size with decreasing pedestal collisionality is present, as shown in fig. 3.4 (recall that  $\nu_{e,ped}^* \propto n_e/T_e^2$ ) [98].

The ELM size scaling with the pedestal collisionality shows that large ELMs are to be expected for ITER-relevant collisionalities. This observation alone is a cause for concern in terms of type-I ELMs H-mode operation in ITER because most of the energy expelled by the ELM ultimately arrives at the divertor plates which can tolerate only a limited amount of energy fluence, e.g.,  $0.3 \text{ MJ/m}^2$  for ITER divertor materials [35, 144, 145]. The rise time of the heat flux to the divertor targets can be approximated with the ion sound speed in the pedestal and the connection length from the midplane to the divertor targets,  $\tau_{\parallel} \sim L_{\parallel}/c_s$  where  $c_s \sim \sqrt{T_i/m_i}$  is the local ion sound speed and  $L_{\parallel}$  is the connection length [98, 146]. The energy deposition has been found to be asymmetric in terms of the inner and outer divertor targets. In discharges where the ion  $\mathbf{B} \times \nabla B$  points towards the active X-point, more energy arrives in the inner target than in the outer target, and vice-versa

when the ion  $\mathbf{B} \times \nabla B$  points away from the active X-point<sup>3</sup> [148, 149]. The ELM energy fluence limit emphasises the fact that ELM size is not necessarily the most important factor in terms of tolerating the transient heat loads produced by ELMs. An ELM depositing large amounts of energy over a long period of time and across a large area may be more tolerable than a smaller ELM that deposits its energy in a much shorter time and in a very small area. Estimates of the uncontrolled type-I ELM energy fluence in ITER at  $I_p = 15$  MA with a fusion power amplification factor of  $Q = 10$  are well above the tolerable energy fluence and would allow only a few high performance discharges before unacceptable levels of cracking, melting, or erosion of the plasma facing components (PFCs) takes place [35, 90, 101]. An empirical scaling for the parallel ELM energy fluence in terms of relative ELM size  $\Delta E_{\text{ELM}}$ , pedestal density (in  $10^{19} \text{ m}^{-3}$ ) and temperature (in keV), and geometric major radius,  $R_{\text{geo}}$ , is described by eqn. 3.1 and the extrapolation to ITER at full and half-current operation are shown in fig. 3.5 [90].

$$\varepsilon_{\parallel} \left( \frac{MJ}{m^2} \right) = (0.28 \pm 0.14) \frac{MJ}{m^2} \times n_{e,\text{ped}}^{0.75 \pm 0.15} T_{e,\text{ped}}^{0.98 \pm 0.1} \times \Delta E_{\text{ELM}}^{0.52 \pm 0.16} \times R_{\text{geo}}^{1 \pm 0.4} \quad (3.1)$$

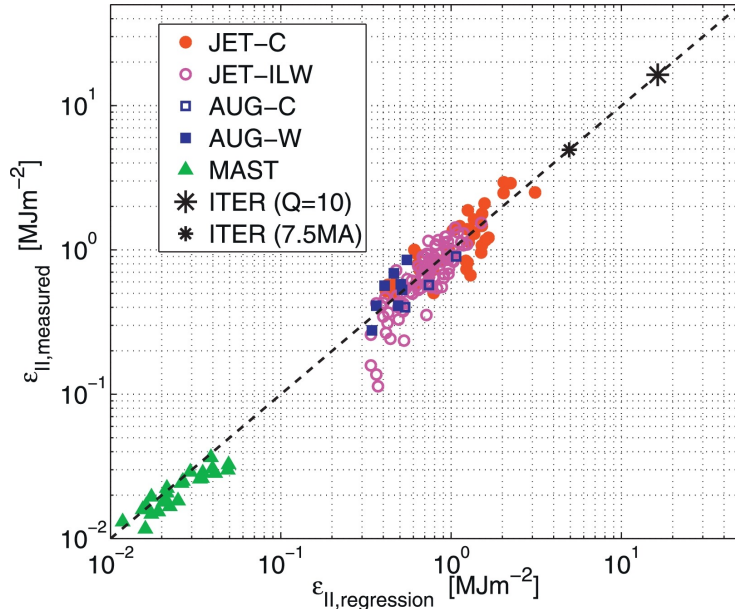


Figure 3.5: Parallel ELM energy fluence scaling with fitted data and extrapolation to ITER high performance operation,  $Q = 10$ :  $(I_p, B_{\text{tor}}) = (15 \text{ MA}, 5.3 \text{ T})$  and half-field/half-current operation (7.5 MA, 2.65 T). Figure reproduced from Ref. [90]

<sup>3</sup>The direction of the ion  $\mathbf{B} \times \nabla B$  is seen to influence the LH power threshold, and it facilitates access to the I-mode regime described above [147].

### 3.3 Simulations of ELMs

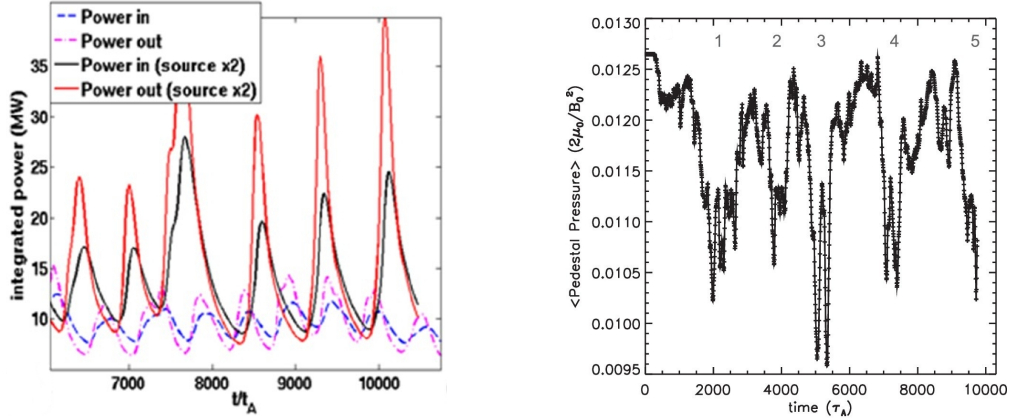
In light of the uncertainties remaining in terms of ELM fluence in ITER, numerical simulations of ELMs became an active research topic since the turn of the century. Linear ideal MHD simulations have been able to accurately estimate the maximum achievable pedestal pressure gradients before the ELM onset, but the ELM losses cannot be studied this way. Non-linear simulations are required in order to investigate the ELM dynamics, and have been produced by several codes worldwide: BOUT++ [150, 151], GEM [152], JOREK [47, 153], M3D [154], and NIMROD [155]. Detailed reviews of ELM simulations can be found in section 6 of Ref. [32], in Ref. [156] and, in great depth, in Ref. [36]. The field of non-linear simulations of ELMs has evolved significantly since then (2015). By that time, ELM simulations were always initialised from unstable (to ideal peeling-balloonning modes) initial conditions, and no simulations of multiple type-I ELMs in X-point geometry had been reported. Ref. [36] emphasised that achieving multiple type-I ELM simulations was fundamental in order to produce predictive simulations of type-I ELM energy losses.

Since 2015, repetitive ELMs with very large repetition frequencies ( $f_{\text{ELM}} \approx 3 \text{ kHz}$ ) were simulated with the JOREK code at unrealistically high plasma resistivity in X-point geometry [65, 157]. For said simulations, an inverse relationship between ELM repetition frequency and applied heating power was found, as shown in fig. 3.6a, indicating that the ELMs simulated were more likely type-III ELMs. Additionally, simulations from the BOUT++ code reported to have simulated ELM cycles with high repetition frequencies in a JET-like circular geometry [158]. The crashes of the pedestal pressure caused by five simulated ELMs with an averaged repetition frequency around  $f_{\text{ELM}} \approx 1.5 \text{ kHz}$  are shown in fig. 3.6b.

Important progress in quantitatively validating ELM simulations in JET-ILW with the JOREK code was reported in Ref. [153]. Other than reproducing important experimental observations, like the inverse scaling of relative ELM size with pedestal collisionality, it highlighted the importance of simulating multiple ELMs in the path to producing predictive simulations. In particular, it showed that non-linear coupling between modes with different toroidal mode numbers is not adequately reproduced in the most violent phase of the ELM crash. The build-up of a stable pedestal at fixed width showed the destabilisation of PB modes and the subsequent appearance of an ELM crash. Significant differences between ELMs simulated with unstable initial conditions and with stable initial conditions plus pedestal build up, which can be seen in fig. 3.7, brought into evidence the critical importance of simulating the crossing of the PB stability boundary and, ultimately, simulating multiple ELMs. It should be noted that the ELM crash from fig. 3.7(b) hosts what appears to be an  $n = 15$  precursor. And said simulation leads to significantly larger ELM size and peak heat flux incident on the divertor, with respect to the simulation with unstable initial conditions, fig. 3.7(a). Finally, it is worth mentioning that through the pedestal build up detailed above, another ELM crash

### 3 Overview of experiments and MHD simulations

---



(a) Inner and outer divertor incident power for nominal (dashed lines) and double heating powers (solid lines) from JOREK simulations. The scenario with nominal heating power has a higher ELM repetition frequency than the case with twice the heating power. Figure modified from Ref. [157].

(b) Temporal evolution of the normalised pedestal pressure (at  $\psi_N = 0.6$ ) through 5 ‘ELM crashes’ from a BOUT++ simulation. In these simulations, the ELM repetition frequency ( $f_{\text{ELM}} \approx 1.5 \text{ kHz}$ ) appears to be too high for type-I ELMs. Figure modified from Ref. [158]

Figure 3.6

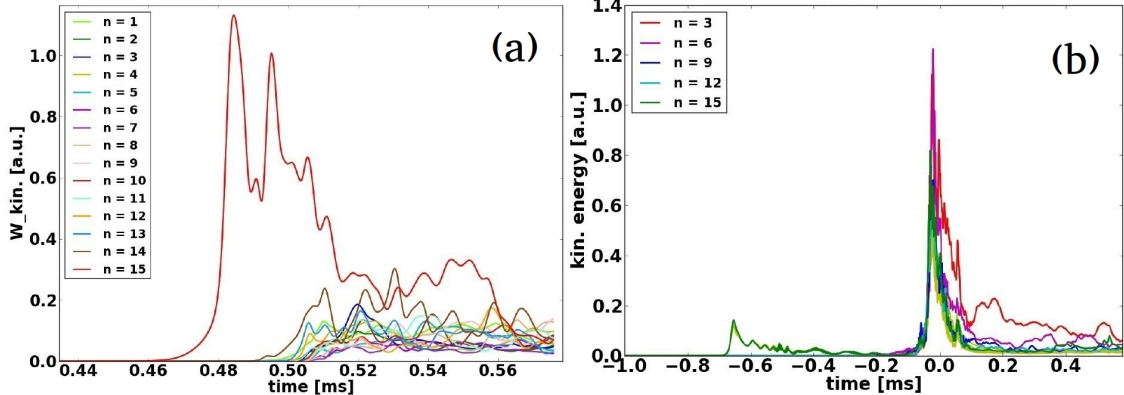


Figure 3.7: Two ELM crashes with (a) unstable initial conditions and (b) stable initial conditions plus pedestal evolution at fixed pedestal width. The importance of simulating how the pedestal crosses the PB stability boundary is highlighted in the increased amount of non-linear coupling observed for the ELM crash in (b). Figure modified from Ref. [153].

is obtained roughly 1.5 ms after the first ELM crash (not shown). If the heating power is increased, the second crash appears at an earlier time, therefore indicating that type-I ELMs are being simulated.

Natural ELM simulations have seen progress with the BOUT++ code in the Chinese tokamak EAST [159], and with NIMROD by considering the current evo-

lution, but not the plasma pressure (therefore eliminating any ballooning modes) in NSTX/NSTX-U geometries [160]. Significant progress has been reported in terms of natural ELMs with the JOREK code. Simulations for the Korean tokamak, KSTAR, have been performed with JOREK, which reproduced peeling-balloonning inter-ELM modes with toroidal mode numbers in experimentally-relevant ranges [161]. The inter-ELM modes were observed after the appearance (and decay) of an ELM crash simulated from initially unstable conditions. The toroidal mode spectrum of an ELM crash in AUG was compared between simulations and experimental observations and found the ranges of dominant mode numbers during the ELM crash to be consistent between simulations and experiments [109, 162].

From the simulations in Ref. [109], the transport of tungsten due to the ELM crash was studied with a full-orbit kinetic model implemented in JOREK [163]. It was reported that tungsten impurities travel both from the confined region outwards and from the SOL inwards. The influence of the ELM crash onto the dynamics of neutrals (ELM burn through) has been recently studied with a neutrals fluid model in predictive simulations for the MAST-U tokamak with the Super-X divertor under detached conditions<sup>4</sup> with JOREK [164], and for ITER [165].

There has been significant progress in simulations of several ELM mitigation and suppression methods in the recent years. With the JOREK code, important advances have been made in terms of simulating the mitigation/suppression of large ELMs through the application of magnetic perturbations in ASDEX Upgrade [166], KSTAR [167], and ITER [168, 169]. Simulating the ELM suppression with the application of RMP fields has also been reported with the M3D-C1 code [170, 171]. The TM1 code has also been used to study ELM suppression with RMPs in circular geometry for low- $\nu^*$  plasmas [172, 173]. Simulations of the triggering of ELMs through pellet injection has also progressed in recent years. Very recently, first simulations with the BOUT++ code [174], and also with the M3D-C1 code [175–177] have been performed. Additionally, pellet-triggered ELM simulations with the JOREK code have become more realistic, and have managed to recover the experimentally-observed lag-time that is required to trigger an ELM through pellet injection after an ELM crash [46, 103, 178]. The effect of vertical kicks onto ELMs has also been studied with the BOUT++ code in the HL-2A tokamak [159] and with JOREK-STARWALL [179] for ITER [77].

Simulations of small ELMs with good confinement (described experimentally in the following section) in the EAST tokamak have been reported with the BOUT++ code [180] (and the corresponding supplementary material). The ELM-free regime known as QH-mode has been successfully simulated with JOREK for DIII-D and ITER and the role of the edge harmonic oscillation (EHO) in sustaining the QH-mode was recovered [181]. The importance of the stabilising effect of ExB flow shear on high-n ballooning modes and destabilising effect on low-n kink-peeling modes

---

<sup>4</sup>Detachment refers to conditions with low pressure and temperature and high neutrals and main ion density near the divertor targets. It is favourable in terms of handling power fluxes from the confined region (be it continuous or transient).

is discussed as an important factor in accessing QH-mode, and it predicts that an ITER  $Q_{DT} = 10$  plasma would have sufficiently large current to destabilise low- $n$  kink-peeling modes and lead to QH-mode. Simulations of QH-mode with NIMROD have also been reported for the DIII-D tokamak and the dynamics of the EHO are investigated [182, 183]. Lastly, BOUT++ simulations of the ExB shear effect onto low- $n$  peeling modes in circular cross-section plasmas show a destabilising role that may be related to the formation and saturation of the EHO during QH-mode [184].

### 3.4 Small ELMs and QCE at ASDEX Upgrade (AUG)

Naturally ELM-free operation as an alternative for type-I ELMs H-mode was briefly outlined in subsection 3.1.3. Another approach to avoid type-I ELMs are operational scenarios with small ELMs. One such scenario that keeps favourable high-confinement properties is the *quasi-continuous exhaust* (QCE) regime depicted in fig. 3.8. It requires high separatrix density and is close to a magnetic double null (DN) configuration; it is further described in subsection 3.4.1. In single null, small ELMs also appear at sufficiently high separatrix density even with a magnetic single null configuration as detailed in subsection 3.4.2.

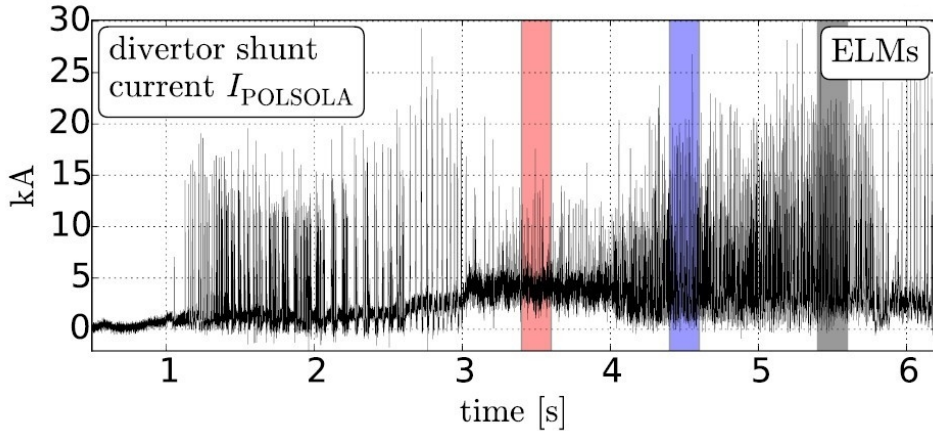


Figure 3.8: Outer divertor shunt current, which serves as ELM monitor, during AUG discharge #34462 that shows three relevant phases. A phase dominated by small ELMs (red), one with mixed small ELMs and type-I ELMs (blue), and one dominated by type-I ELMs (black). The QCE regime corresponds to the red phase. Figure modified from Ref. [42]

#### 3.4.1 QCE regime

The QCE regime is posited to be an attractive scenario for ITER because it completely avoids type-I ELMs while maintaining good confinement properties. Another favourable property of this regime is that it deposits the expelled energy in a

broader area than observed in the inter type-I ELM phase [185]. This regime has strict access conditions and it is being actively developed in TCV and AUG [41, 42] in order to improve its understanding and, eventually, determine whether it could be reproduced in ITER.

Small ELMs operate as a cross-field transport mechanism that flushes heat and particles out of the confined region such that the pedestal cannot develop to a point where type-I ELMs are excited. Despite the absence of type-I ELMs, it cannot be definitively ruled out that small ELMs become excited by edge pedestals that are below the ideal PB stability boundary [42]. The appearance of small ELMs is accompanied by the appearance of broadband (magnetic, density, and temperature) fluctuations with frequencies ranging from 30 to 50 kHz, which are not precursors [41, 96]. The important ingredients for maintaining the QCE regime are high separatrix density ( $n_{e,\text{sep}}/n_{\text{GW}} \gtrsim 0.3$ , where  $n_{\text{GW}} = I_p/(\pi a^2)$  is the Greenwald density in  $10^{20} \text{ m}^{-3}$  by considering the plasma current in MA and the minor radius in m) and closeness to double null (which is often accompanied by high triangularity) [41, 42, 95]. At the required high  $n_{e,\text{sep}}$ , the separatrix collisionality must also be high because there is little variation of the separatrix temperature for a given device ( $T_{e,\text{sep}} \approx 100 \text{ eV}$  for H-modes in AUG [186]) [85]. In existing tokamaks, high  $\nu_{\text{sep}}^*$  implies also high pedestal collisionality because the temperature cannot increase arbitrarily due to the excitation of ELMs. Nevertheless, ITER (which can reach higher pedestal top temperatures) is expected to operate with simultaneously high  $\nu_{\text{sep}}^*$  and low  $\nu_{\text{ped}}^*$ . Such conditions cannot be simultaneously achieved in present day machines and, therefore, uncertainties exist on whether or not ITER could achieve the QCE regime [42].

### 3.4.2 Small ELMs with bad confinement

With a single null magnetic configuration at low triangularity, high density operation may suffer from low confinement. In an H-mode discharge, if the density is high enough, there can be a degradation of confinement that ultimately leads to a back transition to L-mode (H-mode density limit  $n_e \lesssim n_{\text{GW}}$ ), or a disruptive density limit ( $n_e \sim n_{\text{GW}}$ ) [9]. The latter is not relevant for the present work, but the former is discussed below.

For H-mode density limited (HDL) discharges, the back transition from H- to L-mode has been studied in depth. As the separatrix density is increased (by increasing the gas puff rate), filamentary transport also increases [187, 188] and can lead to a flattening of the pressure gradient which, in turn, causes a reduction of the edge radial electric field<sup>5</sup> that causes the back transition to L-mode [187]. Recently, a correlation has been observed between ballooning stability at the separatrix and the onset of the HDL in AUG [34] and in JET-ILW [189]. In this context, the

---

<sup>5</sup>The radial electric field well in the pedestal region associated to the edge transport barrier roughly follows the ‘neoclassical’ radial electric field,  $E_{r,\text{neo}} \approx (en_i)^{-1} \nabla p_i$  [70]

deterioration of the H-mode confinement and, ultimately, the breakdown of the H-mode are explained by an excess of cross-field transport caused by small ELMs located near the separatrix.

## 4 Small ELMs at low triangularity

As described at the end of the previous chapter, in section 3.4, it is presently hypothesised that small ELMs are ballooning modes and/or high-n peeling-balloonning modes that are located at, or very near, the magnetic separatrix. This chapter describes JOREK simulations at high separatrix density ( $n_{e,\text{sep}}/n_{\text{GW}} \approx 0.4$ ) that reproduce several key experimental observations of small ELMs in the ASDEX Upgrade tokamak, e.g., the  $30 - 50$  kHz fluctuations observed in the magnetic signals, and the transition to a type-I ELMy H-mode when the heating power is increased or the separatrix density is decreased. In the simulations presented in this chapter, resistive (peeling-)ballooning modes near the separatrix are identified as the main transport mechanism responsible for the quasi-continuous exhaust from the confined region to the divertors. The chapter is organised as follows, section 4.1 describes the simulation set-up and the axisymmetric evolution, i.e., the pedestal build-up in the absence of any perturbations, which is imposed with diffusion coefficients and sources. Section 4.2 describes the MHD activity that develops in non-axisymmetric simulations. Thereafter, in section 4.3, two different paths that lead to a type-I ELMy H-mode are described and an explanation is provided as to what is the mechanism that allows the transition. Finally, conclusions are provided in section 4.4.

Some results in this chapter have been presented in international conferences [190, 191].

### 4.1 Simulation set-up

Unlike previous ELM simulations to date (excluding Ref. [153]), initial conditions which are stable to ideal peeling-balloonning modes are considered. These initial conditions are obtained from an equilibrium reconstruction of a post-ELM phase in AUG discharge #33616 at roughly 7 s with the CLISTE code [192]. The magnetic field at the magnetic axis for these simulations (and all simulations presented in this thesis) is 2.5 T, and the plasma pressure is  $I_p = 0.8$  MA. The discharge was characterised by a lower single null magnetic configuration with low triangularity  $\delta_{\text{av}} = 0.29$  and with the ion  $\mathbf{B} \times \nabla B$  direction pointing towards the active X-point.

The outboard midplane initial profiles of the electron density, plasma temperature and pressure, and toroidal current density are shown in fig. 4.1. The plasma temperature,  $T$ , is the sum of the ion and electron temperature. The ion and electron temperatures are further assumed to be equal. The toroidal current density

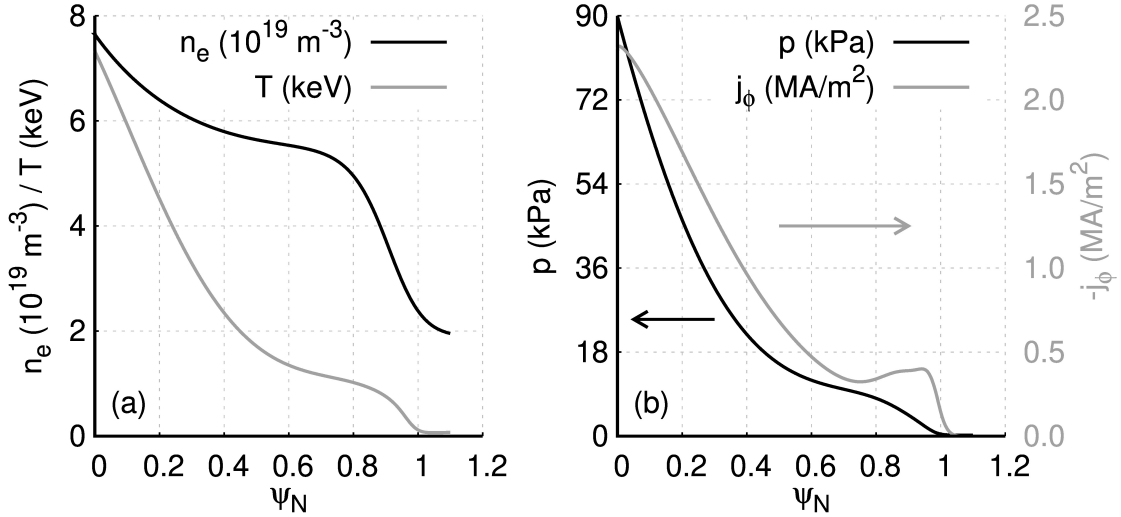


Figure 4.1: Initial conditions for the electron density and plasma temperature ( $T = T_e + T_i$ ) (a), and plasma pressure ( $p = p_e + p_i$ ) and toroidal current density (b) in the outboard midplane.

is comprised of an Ohmic contribution together with a Pfirsch-Schlüter current<sup>1</sup> contribution and a bootstrap current contribution. The latter is only a small contribution due to the small steepness of the pressure profile. The pedestal at this stage is not unstable to ideal peeling-balloonning modes, and needs to steepen in order to excite type-I ELMs.

The grid used for the simulations presented in this chapter is aligned to the flux surfaces and it is comprised of 138 points in the radial direction (120 points in the confined region and 18 in the scrape-off layer) and 354 in the poloidal direction. For the axisymmetric build-up, only one poloidal plane is considered, and for the non-axisymmetric simulations 32 poloidal planes are used in order to simulate the toroidal mode numbers  $n = 0, 2, 4, \dots, 12$  (and 64 planes for  $n = 0, 2, 4, \dots, 20$ ). The central resistivity that is used for the simulations presented in this chapter (unless specified otherwise) is  $\eta = 6.6 \times 10^{-8} \Omega\text{m}$ . This value is larger than the actual resistivity in the centre ( $\eta_{\text{Spitzer}} \approx 2.1 \times 10^{-9} \Omega\text{m}$ ) and increases with decreasing temperature as it follows the Spitzer temperature dependency,  $T^{-3/2}$ . Due to neoclassical alterations, and the effect of  $Z_{\text{eff}}$  which increases from the core to the edge, the resistivity in the pedestal lies within the error bars of the experimental value. For all cases, the viscosity is chosen such that at the pedestal top the magnetic Prandtl number is set to unity. The realistic parallel heat diffusion in the pedestal region of AUG may be estimated with the Spitzer-Härm expression,

<sup>1</sup>The Pfirsch-Schlüter current is a force-free current, i.e., parallel to  $\mathbf{B}$ , which has opposite signs in the inboard and outboard sides. Performing a flux-surface average over the Pfirsch-Schlüter results in  $\langle \mathbf{J}_{\text{PS}} \cdot \mathbf{B} \rangle = 0$  [11]. Consequently, the flux-surface averaged toroidal current density is only composed of the Ohmic current and the pressure gradient-driven bootstrap current.

$\chi_{\parallel, \text{SH}} = 3.6 \times 10^{29} T_{e,[\text{keV}]}^{5/2} / n_{e,[\text{m}^{-3}]}^{} [193]$ . For a plasma temperature of 1 keV and density of  $5 \times 10^{19} \text{ m}^{-3}$ , i.e., roughly corresponding to  $\psi_N \approx 0.8$  in the post-ELM equilibrium shown in fig. 4.1,  $\chi_{\parallel, \text{SH}} \approx 1.27 \times 10^9 \text{ m}^2/\text{s}$ . For the simulations presented in this chapter, unless specified otherwise, at 1 keV of plasma temperature ( $T_e = 0.5 \text{ keV}$ ), the parallel heat diffusion is  $0.09 \times 10^9 \text{ m}^2/\text{s}$ , i.e., roughly 14 times lower than the Spitzer-Härm value.

### 4.1.1 Axisymmetric pedestal build-up

Together with the post-ELM equilibrium reconstruction of AUG discharge #33616, a pre-ELM reconstruction is used, which has a bootstrap current density constraint on the resulting profiles, i.e., the resulting current density profile is constrained from information on the steepness of the density, temperature, and pressure profiles [194]. Through the linear ideal MHD stability analysis code MISHKA, the pre-ELM profiles are known to be unstable to ideal peeling-balloonning modes. The approach used to evolve the post-ELM profiles (fig. 4.1) is to use stationary diffusion coefficients and sources to build-up towards the pre-ELM pedestal conditions. The pedestal build-up is performed at fixed pedestal width because the diffusion coefficient profiles and the source profiles are chosen to be stationary throughout the simulation run-time. Adaptive diffusion coefficients and sources would require including several key physical effects that are beyond the scope of MHD, and which will be investigated in future work. As the pedestal density and temperature evolve due to the imposed diffusion and sources, the radial electric field and the current density become driven by the steepening of the profiles. Figure 4.2 shows the time evolution of the outboard midplane pedestal electron density, plasma temperature, radial electric field, and the flux-surface averaged toroidal current density. The colours of the profiles change gradually from purple to blue with increasing time as shown in the colour bar on top of the figure. The evolution is shown for the first four milliseconds of simulation time every 0.2 ms. The profile shape changes quickly in the first 0.5 ms as clearly observed in the plots for the density and radial electric field. The  $E_r$  in the pedestal region is roughly  $E_{r,\text{neo}} \approx (\nabla p_i) / (en_i)$ , and  $j_\phi$  evolution is determined by a Sauter bootstrap current module in JOREK (described and used first in [153]).

### 4.1.2 Bootstrap current density source

In JOREK, the analytical expression for the Sauter bootstrap current density, which uses the pressure, density, and temperature gradients as input is used to determine a current density source. The results obtained from JOREK are compared to the Sauter bootstrap current density model in ASTRA [195]. The bootstrap current density model in ASTRA is different from the JOREK model only in that it considers the neoclassical expression for the resistivity. The ASTRA simulations were run by Clemente Angioni with the JOREK density and temperature profiles at different

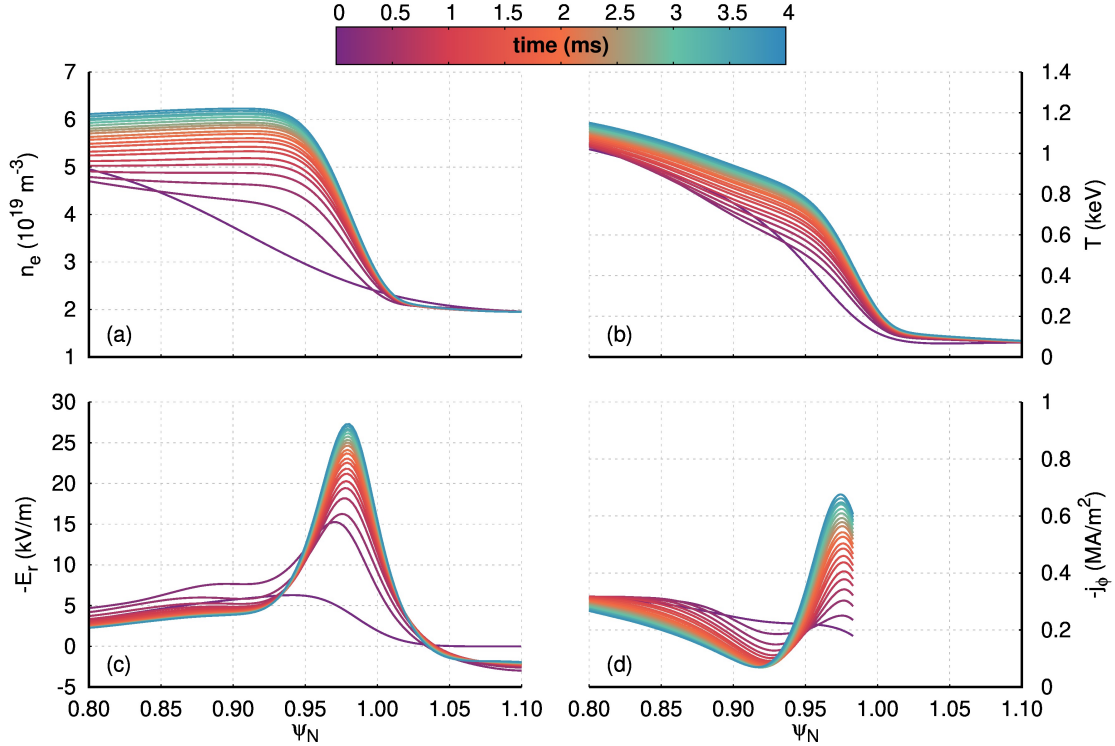


Figure 4.2: Outboard midplane pedestal profiles of electron density (a), plasma temperature (b), radial electric field (c), and flux-surface averaged toroidal current density (d) during the imposed pedestal build-up. The first millisecond is defined by a strong steepening of the pedestal, and the pedestal top grows progressively at a fixed gradient.

times (and the initial profile of the current density) as input. The resulting flux-surface averaged profiles of the current density are shown in fig. 4.3. The JOREK bootstrap current density seems to under predict the ASTRA results. For this reason, the JOREK bootstrap current density source is scaled up by a factor of 2 for all the simulations presented in this thesis. A more consistent bootstrap current density source implementation to the JOREK code is considered as an important topic for future work.

#### 4.1.3 Limitations of the present approach

Experimentally, turbulent and neoclassical transport evolve in time as profiles change. However, these dynamics are not considered with the present approach. Indeed, these changes in transport would determine how exactly the pedestal width evolves. In that sense, in order to produce an accurate pedestal build-up, including the pedestal widening, it is necessary to run neoclassical and gyro-kinetic (or even kinetic) simulations to determine the evolving turbulent and neoclassical transport

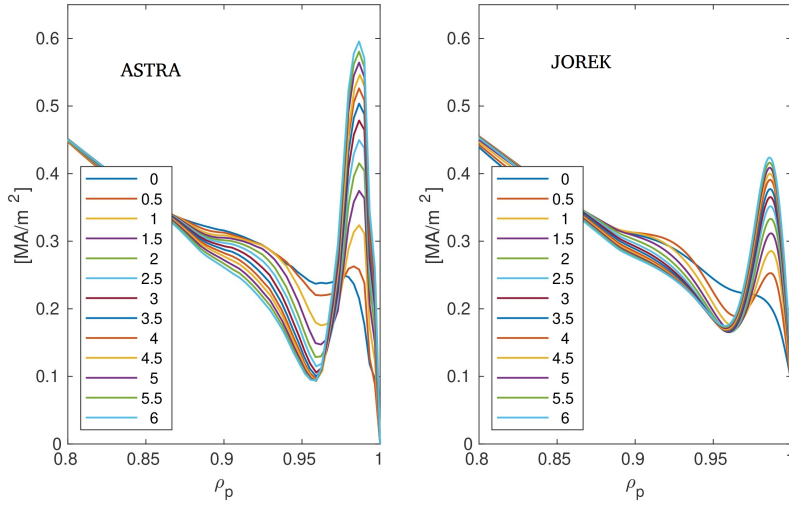


Figure 4.3: Flux-surface averaged toroidal current density evolving during the imposed pedestal build-up at a fixed gradient calculated with the Sauter bootstrap current density model in ASTRA (left) and with JOREK (right).

throughout the simulation time. This represents not only an extremely costly endeavour, but also would require significant efforts in terms of code development, which lie well beyond the scope of the present work.

The ion and electron species can be approximated to have the same temperatures and densities in the pedestal region, but in reality these behave in distinct ways due to the large difference in their respective masses. All such effects are neglected in the present simulations because these are performed in the single fluid version of the JOREK code. However, a two temperature model has been developed and it will be used in the future to understand the effect of such temperature separation in ELM physics. Another important physical effect that cannot be considered under the present approach is that of the penetration of neutral particles onto the confined region. The ensuing ionisation of the neutral particles has important consequences on the particle fuelling that should be considered for a given simulation. These fuelling effects, in turn, directly influence the density (and ultimately temperature) profiles in the pedestal. Ongoing efforts are underway that permit JOREK simulations to consider such effects either by a kinetic treatment [165] and a fluid treatment [164] of the neutral particles.

## 4.2 Non-axisymmetric simulations

The pedestal build-up shown in fig. 4.2 does not cross the ideal peeling-balloonning boundary in the time shown. However, non-ideal instabilities can still become excited due to the finite resistivity used in JOREK. A simulation which includes the toroidal mode numbers  $n = 0, 2, 4, \dots, 12$  is performed. After a brief time of stability,  $\sim 0.2$  ms, the steepened pedestals that are not unstable to ideal PB instabilities, begin to excite high- $n$  peeling-balloonning modes with predominant balloonning features. The initial growth phase is started by an  $n = 12$  mode in these simulation and closely followed by the growth of the  $n = 10$  mode. The growth rates of these modes are very similar, roughly  $\gamma_{n=10,12} \approx 5 \cdot 10^4$ /s. With simulations at higher toroidal resolution that include the toroidal mode numbers  $n = 0, 2, 4, \dots, 20$ , it has been confirmed that indeed the fastest growing mode is the  $n = 12$  and the higher toroidal harmonics grow at a lower rate. These  $n > 12$  modes do not seem to alter how the profiles evolve non-linearly, but they do modify the non-linear interactions between modes with different toroidal mode numbers.

The linear phase of the two simulations at different resolutions are shown in fig. 4.4(a) and (b), which show the magnetic energies of the  $n \neq 0$  modes. The time frame between the first vertical black line and the vertical purple line denotes the linear phase. The time between the latter and the second vertical black line denotes the early non-linear phase, during which quadratic non-linear mode coupling takes place. For example, the  $n = 2$  and 4 modes become driven by the  $n = 12$  and 10 and the  $n = 12$  and 8 modes, respectively. The non-linear mode coupling that gives rise to the excitation of linearly stable modes has been described in JOREK simulations from Ref. [196]. During the linear phase, the non-axisymmetric modes collectively form a peeling-balloonning structure with predominant balloonning features. The density, temperature, and magnetic flux perturbations at 0.4 ms are shown in fig. 4.5. The flux surfaces at  $\psi_N = 0.95, 1.00, 1.05, 1.10$  are also shown in thin black lines. It is observed that the PB modes are localised very close to the separatrix. The modes are observed to rotate in the electron diamagnetic direction (upwards from the outer midplane). The upcoming subsection is devoted to studying the velocity at which the modes rotate during the early linear phase.

### 4.2.1 Linear growth phase – mode velocity

Considering how the peak of the modes in fig. 4.5 move with time it is possible to determine their poloidal velocity at a given radial location. The perturbation shown in the aforementioned figure is the result of perturbations with different toroidal mode numbers, e.g., the magnetic flux fluctuation is defined as

$$\tilde{\psi} = \sum_{n>0}^{n_{\max}} \psi_n = \psi - \psi_{n=0},$$

where  $n$  is the toroidal mode number. Figure 4.6 shows the  $\psi_N = 0.92$  and 0.99 flux surfaces together with the colour coded arc length,  $s$ , calculated from the inboard

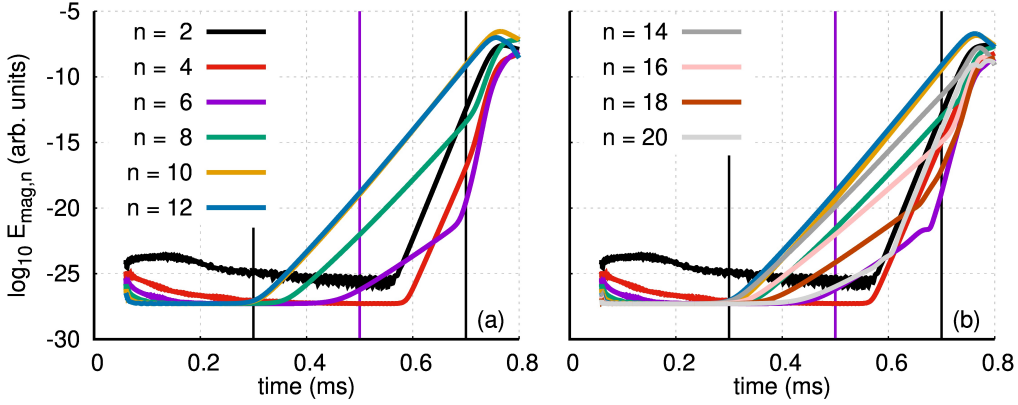


Figure 4.4: Magnetic energies of the non-axisymmetric modes in logarithmic scale in the first 0.8 milliseconds of simulation time. (a) shows the simulation with  $n = 0, 2, 4, \dots, 12$  and (b) shows the simulation with  $n = 0, 2, 4, \dots, 20$ . This comparison shows that the dominant mode numbers in the linear phase are  $n = 10$  and  $12$  in both cases.

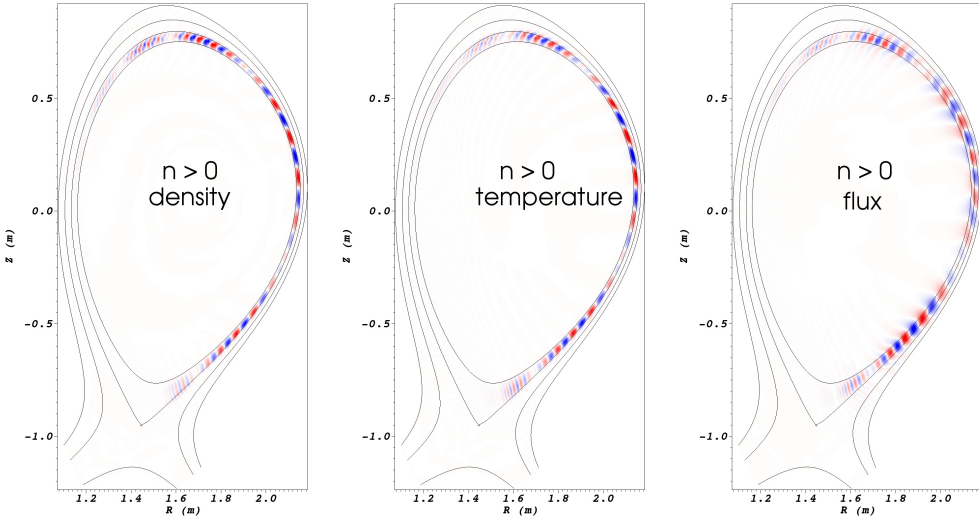


Figure 4.5: Density, temperature, and magnetic flux non-axisymmetric perturbations ( $n > 0$ ) from the simulation with  $n = 0, 2, 4, \dots, 12$  at 0.4 ms. The peeling-balloonning structure with dominant ballooning characteristics (i.e., more localised to the LFS) can be observed in both plots. Flux surfaces at  $\psi_N = 0.95, 1.00, 1.05$ , and  $1.10$  are shown with gray lines.

midplane (a) and the  $\psi_n$  perturbation for the different toroidal mode numbers (b)-(g) at  $t = 0.5$  ms. The  $n \geq 8$  mode amplitudes dominate in the LFS indicating their ballooning nature while the modes with lower  $n$  do not have a coherent structure

(the  $n = 6$  already has a coherent structure, but its amplitude is too small to be observed in fig. 4.6(e)).

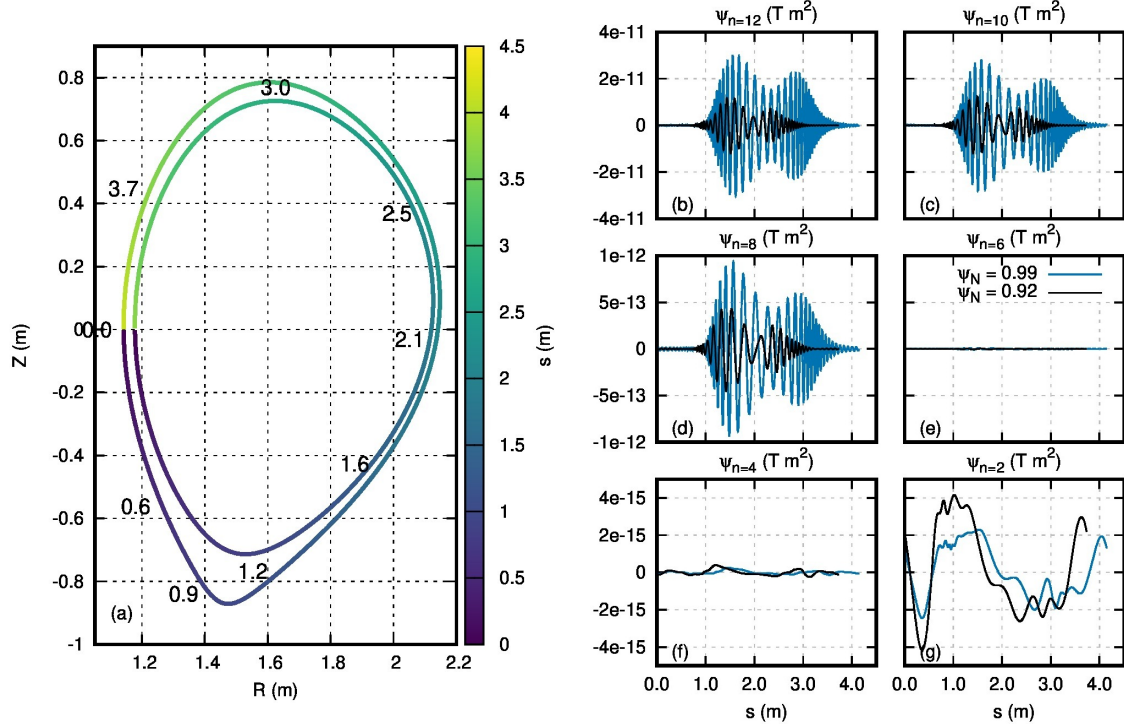


Figure 4.6: (a) Flux surfaces of  $\psi_N = 0.92$  and  $0.99$  with their corresponding colour coded arc lengths. (b)-(g) The variation of the poloidal magnetic flux perturbations along the arc length for the different toroidal mode numbers. The magnetic flux perturbations for  $n = 2$  and  $4$  do not have any coherent structures as they are linearly stable to the profiles at this point in time ( $t = 0.5$  ms).

Taking the distance travelled by the peaks of fig. 4.6(b)-(e) in a small time, it is possible to determine the poloidal velocity of the different modes. This results in a poloidal mode velocity that varies along the arc length. Using the normalised arc length ( $s/\max(s)$ ), the poloidal mode velocity for the linearly unstable modes,  $n = 6, 8, 10, 12$ , in  $\psi_N = 0.92$  and  $0.99$  is shown in fig. 4.7. The poloidal mode velocity for all linearly unstable modes peaks roughly at the outer midplane (normalised arc length of  $\sim 0.5$ ). The overall maxima of the perturbations is located at  $\psi_N = 0.98$ , and the mode velocity does not show large variation between  $\psi_N = 0.92$  and  $1.00$ .

The poloidal velocity of a mode may be used to attempt to identify the nature of the mode. In particular, from Ref. [197], ideal and resistive ballooning mode rotation velocities in the laboratory frame have been identified as

$$\text{Resistive : } v_{\text{mode},\text{pol}} = v_{\text{ExB}} + v_{\parallel,\text{pol}}, \quad (4.1)$$

$$\text{Ideal : } v_{\text{mode},\text{pol}} = v_{\text{ExB}} + v_{\parallel,\text{pol}} + v_i^*/2, \quad (4.2)$$

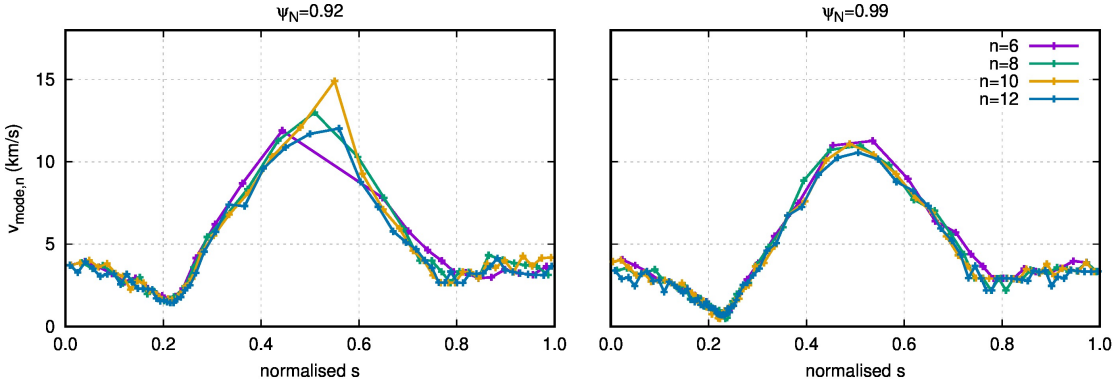


Figure 4.7: Poloidal mode velocity for the different linearly unstable modes at  $t = 0.5$  ms at  $\psi_N = 0.92$  (left) and  $\psi_N = 0.99$  (right).

where  $v_i^* = \nabla p_i / (en_e B)$  is the ion diamagnetic velocity, and  $v_{\parallel, \text{pol}}$  is the poloidal projection of the parallel velocity. At 0.5 ms of simulation time, eqn. 4.1 results in a poloidal velocity of approximately  $-10$  km/s in the maximum gradient region ( $\text{normalised } s \approx 0.45$ ), where the negative sign denotes motion in the electron diamagnetic direction (vertically upwards from the outer midplane). On the other hand, eqn. 4.2 results in a poloidal velocity of  $\sim -4$  km/s. Comparing these two, it would appear that the mode velocity of the linearly unstable  $n = 6, 8, 10, 12$  modes are closer to the resistive ballooning modes than to ideal ballooning modes. Further support to the identification of these modes as resistive ballooning modes comes from the fact that their growth rates become larger by increasing the resistivity (at constant magnetic Prandtl number). Similarly, by reducing the resistivity, the growth rates of the unstable modes decrease. Therefore, the unstable high- $n$  modes unstable in the present simulations are characterised as resistive ballooning modes.

#### 4.2.2 Importance of extended MHD

Simulations without the diamagnetic effects have been performed in order to understand the influence onto the underlying instabilities described in the previous section. This is done for simulations with only one toroidal harmonic present,  $n = 8$ , and for different applied heating powers. It is observed that the simulations that include  $v_i^*$  have fundamentally different non-axisymmetric dynamics with respect to the simulations that neglect the diamagnetic effects. Figure 4.8 shows the evolution of the  $n = 8$  magnetic energy in logarithmic scale of (a) simulations with and (b) without diamagnetic effects at four different values of  $P_{\text{heat}}$ .

Increasing heating power causes a steepening of the temperature and, therefore, of the pressure at the plasma edge. For the simulations that include diamagnetic effects, the edge radial electric field well at the pedestal becomes deeper with steeper pressure profiles. In said simulations, the high- $n$  ballooning modes become stabilised by the diamagnetic drift together with the  $E_r$  (and its shear) [71–73]. For

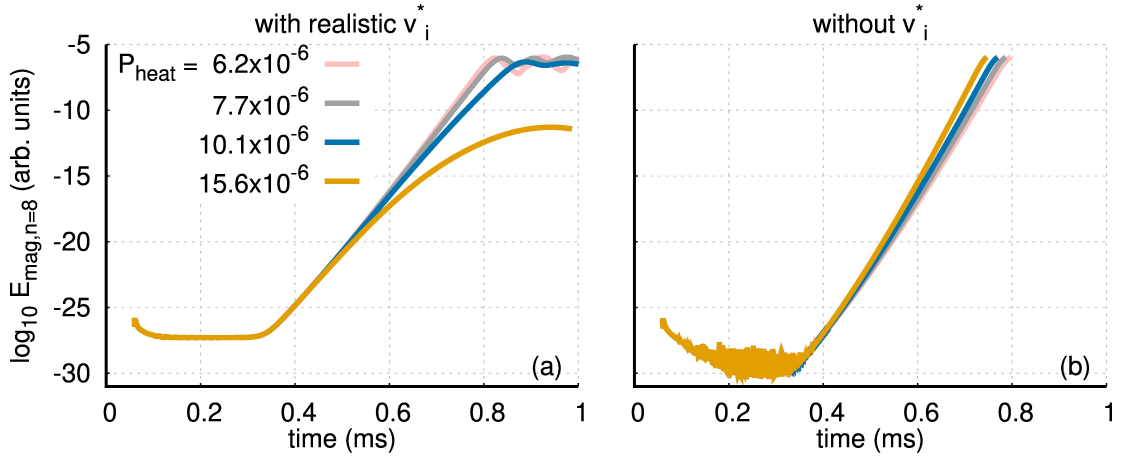


Figure 4.8: Evolution of  $E_{\text{mag},n=8}$  for simulations with (a) and without (b) the inclusion of ion pressure gradient-driven diamagnetic flows. Four different input heating powers are considered. Therefore, eight single toroidal mode number simulations are shown. Increasing heating power in simulations that include diamagnetic flows shows an important stabilisation of the  $n = 8$  peeling-balloonning mode. When neglecting the diamagnetic effects, on the other hand, increasing heating power causes the unstable PB mode to grow even faster due to the steeper pressure profiles.

the simulations without diamagnetic effects the pedestal steepens, but  $E_r$  does not change. In fig. 4.8(a) and (b), the heating power is changed at  $t = 0.33$  ms in all different simulations. The simulations that consider diamagnetic effects observe  $\gamma_{n=8}$  to decrease as the heating power is increased. On the other hand, the simulations that neglect diamagnetic effects result in an increase of  $\gamma_{n=8}$  with increasing heating power. The results presented in this section emphasise the importance of including the diamagnetic flows.

As mentioned at the beginning of this section (4.2), the pedestal at these stages is stable to ideal peeling-balloonning modes. Higher pedestal pressure and/or edge current densities are required in order to reach a type-I ELM unstable scenario. The access to a type-I ELM unstable scenario appears to be closed without the inclusion of the two-fluid diamagnetic effects. Indeed this result was previously reported in Ref. [65] in the context of obtaining repetitive ELM cycle simulations, and was extended as a requirement to simulate type-I ELM cycles in Ref. [37]. The following sections are devoted to the non-linear study of non-ideal (resistive) peeling-balloonning modes in the presence of diamagnetic effects.

### 4.2.3 Non-linear phase

For the simulation that includes  $n = 0, 2, 4, \dots, 12$ , i.e., figure 4.4(a), the magnetic and kinetic energies of the non-axisymmetric modes is shown in fig. 4.9 in linear scale for 10 ms of simulation time (a) and (c) and in logarithmic scale for the first 2 ms (b) and (d).

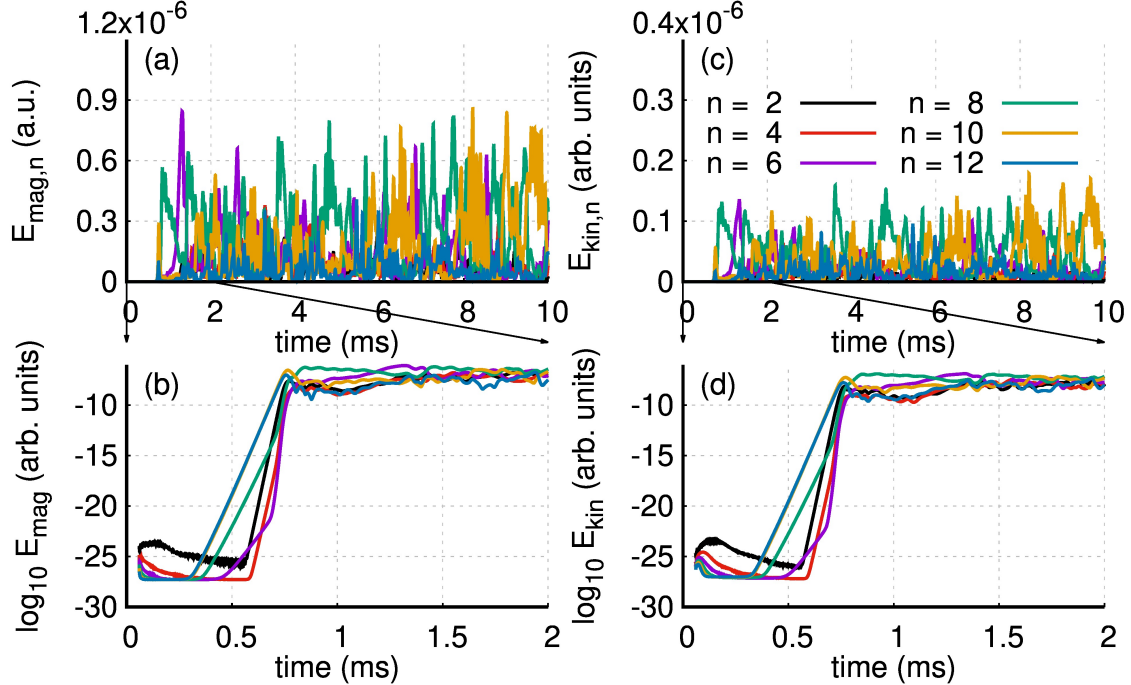


Figure 4.9: Magnetic and kinetic energies of the non-axisymmetric modes in linear scale for 10 ms of simulation time (top) and in logarithmic scale for the first 2 ms of simulation time during which the linear growth phase takes place.

The linear growth phase gives way to the early non-linear growth phase until the amplitude of the perturbations becomes large with respect to the background plasma, at which point the non-linear phase begins. During the latter, a dynamic interplay between growing and decaying instabilities and the background plasma determines the instantaneous profiles observed in the simulations. Due to the persisting PB modes and the lack of a clear cyclical dynamics, the dynamics observed are dubbed peeling-balloonning turbulence.

#### 4.2.4 Filamentary transport

The non-axisymmetric time evolution of the  $\phi = 0$  midplane pressure gradient and the inner/outer divertor incident power are shown in fig. 4.10(a) and (b), respectively, for 10 ms of simulation time. The incident power is defined as

$$P_{\text{div}} = \int_0^{2\pi} \int_{s_0}^{s_{\max}} q(t, s, \phi) R ds d\phi,$$

where  $q(t, s, \phi)$  is the heat flux at a given time in the divertor location  $s$  at the toroidal angle  $\phi$ , and  $R$  is the major radius. The noisy colour map indicates that the pressure gradient and, therefore, the pressure profile in the outermost edge of the plasma is rapidly fluctuating. The corresponding fluctuations are governed by the non-axisymmetric modes that regulate the pedestal to fluctuate about a mean value, i.e., the PB turbulence. Figure 4.11 shows the outer midplane pressure with a logarithmic scale for a reduced time window of 0.4 ms, which is chosen between 4.8 and 5.2 ms, in order to show the dynamics of what appears to be filamentary structures travelling outwards from slightly inside the separatrix (roughly 2 cm). The y-axis is the major radius, and the separatrix position is represented with a white line. The plasma blobs that travel outwards correspond to non-ideal PB modes that are aligned to the magnetic fields and are moving in the electron diamagnetic direction.

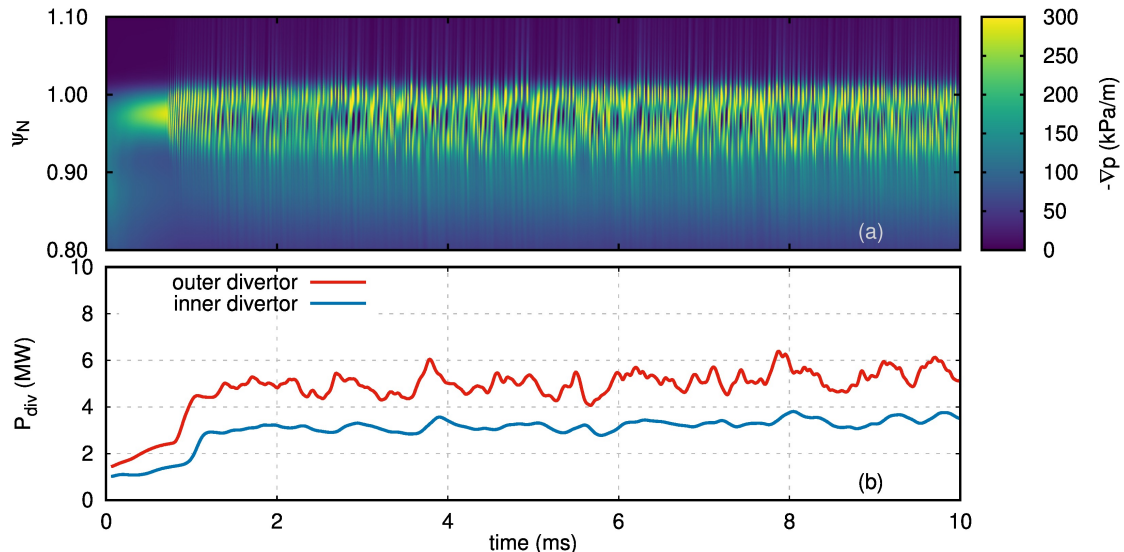


Figure 4.10: Time evolving outer midplane edge pressure gradient at  $\phi = 0$  in colour scale (a), and inner/outer divertor incident power (b). The varying pressure profile is caused by quasi-continuous outward transport created by non-ideal peeling ballooning modes.

Non-ideal (resistive) peeling ballooning modes that are destabilised below the ideal PB stability boundary regulate the pressure gradient about  $-250$  kPa/m.

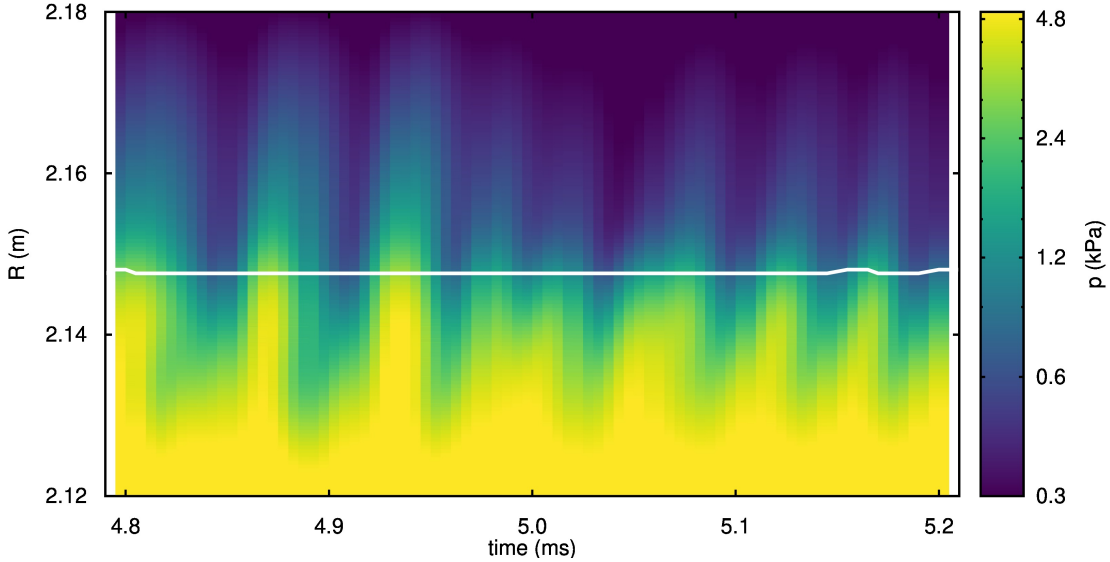


Figure 4.11: Time evolving outer midplane edge pressure at  $\phi = 0$  in logarithmic scale.  
Plasma blobs travelling outwards are aligned to the magnetic field lines.

This is made clearer with pressure and pressure gradient profiles taken in the representative time frame of [4 – 6] ms together with averaged profiles in black shown in fig. 4.12(a) and (b). As mentioned before, the peeling-ballooning modes do not behave in a cyclical fashion, but cause a quasi-continuous power deposition in the inner and outer divertor targets, as shown in fig. 4.10(b).

The fluctuating profile in the last  $\sim 7\%$  of the confined region is clearly visible in fig. 4.12(a). It shows how the non-ideal PB modes regulate the pedestal in such a way that the steepness of the profiles cannot grow to large values. This is why these simulations feature only small ELMs and not a mixed regime with small ELMs and type-I ELMs. Taking the time-varying temperature fluctuations at a single point in the steep gradient region in the outer midplane,  $(R, Z) = (2.14, 0.06)$ , a spectrogram is performed. As a result, a dominant frequency in the range of 20 – 40 kHz is found, as can be observed in fig. 4.13. A type-II ELMMy H-mode in AUG with high triangularity and close to double null reported in Ref. [96] was described as having an electron pressure gradient oscillating about  $\sim 150$  kPa/m. The oscillating  $\nabla p_e$  was reportedly caused by MHD modes which were associated with electromagnetic fluctuations observed in a wide radial extent peaking in a frequency range of 30 – 50 kHz. Both observations hint at qualitative similarities to the simulation results described in this section. Nevertheless, it must be noted that the present simulations were performed in a different magnetic configuration, i.e., low triangularity and far from double null. Therefore, dedicated comparisons need to be performed in order to produce quantitative comparisons between experiments and simulations. In particular, such comparisons will have to focus on variations of the plasma shape.

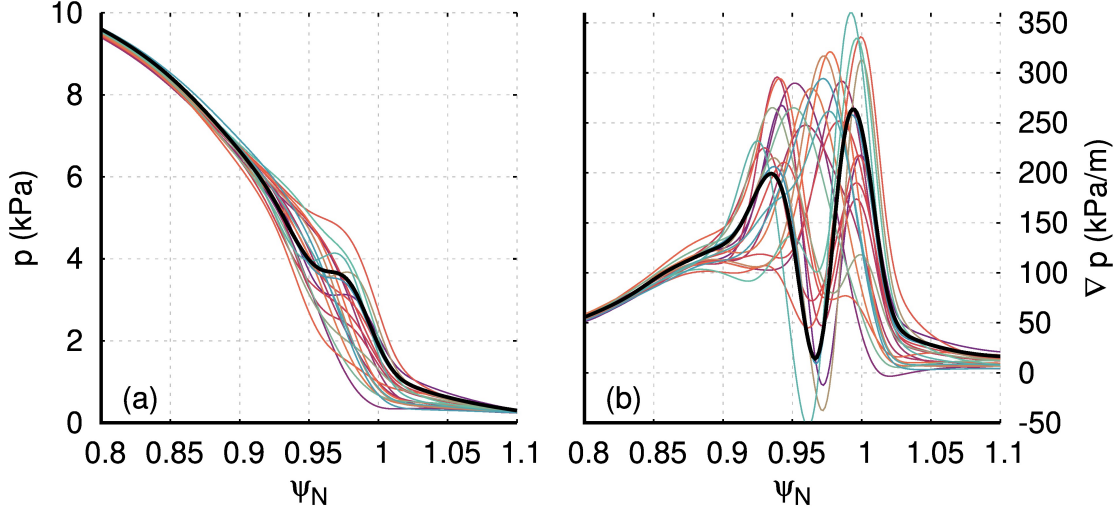


Figure 4.12: Pressure (a) and pressure gradient (b) profiles in the time window 4 – 6 ms together with a time-averaged profile in black. The time-averaged profile shows a ‘staircase’ structure with a large pressure gradient in the vicinity of the separatrix.

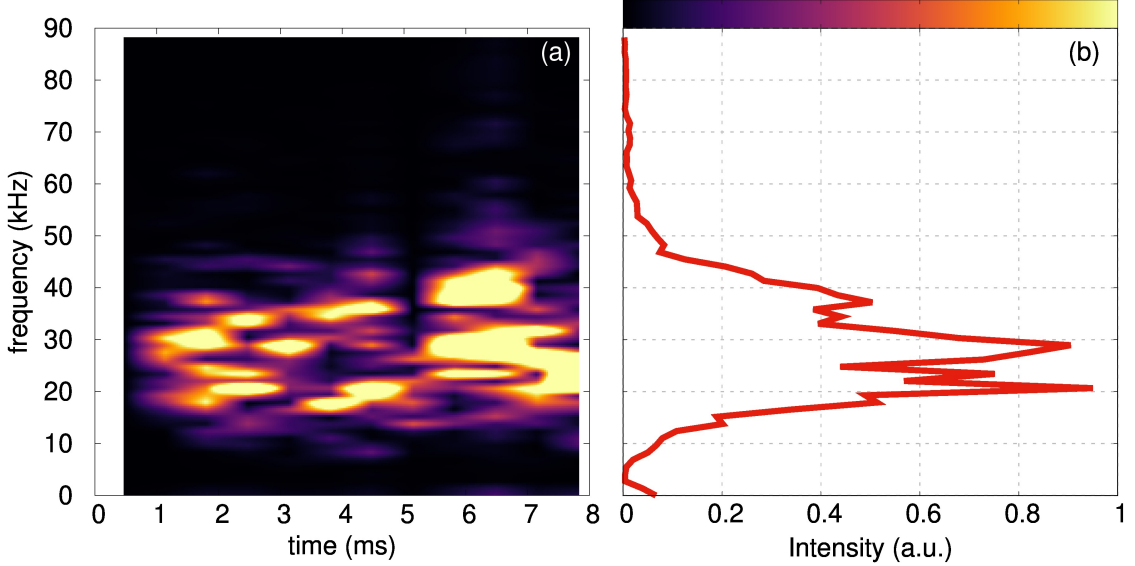


Figure 4.13: Time evolving (a) and averaged (b) frequency spectrogram of the temperature fluctuations in  $(R, Z) = (2.14, 0.06)$ . Dominant frequencies in the range 20 – 40 kHz can be observed in both cases.

#### 4.2.5 Divertor heat deposition

To show the quasi-continuous exhaust caused by the non-ideal peeling-ballooning modes excited near the separatrix, the electron temperature at the inner and outer

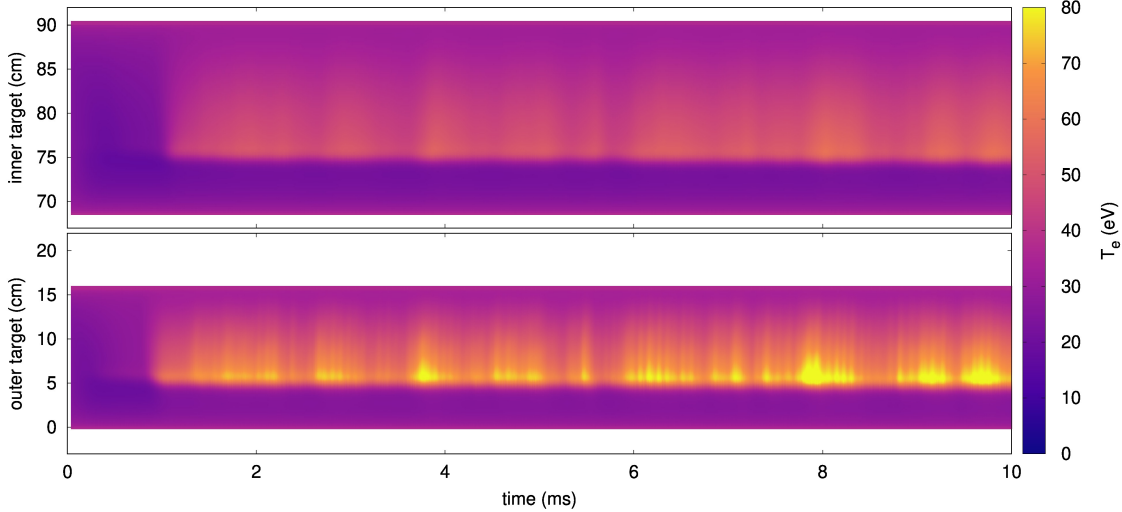


Figure 4.14: Time evolution of the inner (a) and outer (b) target electron temperature ( $T_e = T/2$ ) caused by the non-ideal peeling-balloonning modes excited at the very edge of the plasma. The inner target has a lower temperature than the outer target as well as a lower incident power.

divertor targets is plotted in fig. 4.14(a) and (b), respectively. The target electron temperature is considered to be half of the plasma temperature and it is plotted for 10 ms of simulation time. The inner divertor target has a lower target temperature than the outer divertor. Similarly, the incident power to the inner divertor is lower than to the outer divertor, as seen in fig. 4.10(b). There is a slight increase in the maximum target temperature (particularly visible in the outer target) as time progresses. This is due to the chosen heat source in the confined region which slowly increases the thermal energy content inside the separatrix. The heat deposition does not show significant variations in the toroidal direction at any given time point. In other words, the heat deposition is roughly axisymmetric. It is important to note that the present simulations used only a simplified SOL transport model and, as such, the obtained heat distribution between targets will not necessarily reflect experimental observations.

### 4.3 Two simple paths to type-I ELMs

In small ELM experiments, sufficiently increasing the heating power causes the plasma to transition from ‘pure’ small ELMs to a mixed regime and ultimately to a ‘pure’ type-I ELMy H-mode. Based on the simulations presented in the previous section, the heating power is increased to corroborate whether or not access to type-I ELMy H-mode was feasible. This path to type-I ELMs is described in section 4.3.1. Indeed, type-I ELMs are achieved by sufficiently increasing the heating power with respect to the simulations presented in the previous sections. Increasing

heating power causes the edge temperature (and its gradient) to increase, which, in turn, causes the pressure gradient and the diamagnetic drifts to grow larger. The stabilising influence of the diamagnetic effects and of  $E_r$  (and its shear) onto high-n (peeling-)ballooning modes becomes stronger and eventually completely stabilises them. At this point, the small ELM regime gives way to a type-I ELMy H-mode. The transition from the small ELM regime to a type-I ELMy H-mode can also take place by sufficiently decreasing the separatrix density. Section 4.3.2 describes how decreasing  $n_{e,\text{sep}}$ , with respect to the pure small ELM simulations, manages to completely stabilise the non-ideal peeling-balloonning modes and gives way to a type-I ELMy H-mode. The decreasing separatrix density prompts two important stabilising effects to take place: faster plasma flows since  $v_i^*$  and  $v_{\text{ExB}}$  are  $\propto 1/n_i$  and a larger bootstrap current density.

### 4.3.1 Increasing heating power – stronger radial electric field

The nominal heating power in JOREK units is  $6.2 \times 10^{-6}$  (equivalent to  $\approx 13$  MW) and it was applied in the simulations shown in section 4.2. The magnetic energies of the non-axisymmetric perturbations for the first 7 ms of said simulation are shown in fig. 4.15(a). In the subsequent sub-figures, the heating power is progressively increased<sup>2</sup> in small steps (from the beginning of the simulation). In fig. 4.15(b), the non-linear behaviour does not show much differences. However, in the next figure, a transient phase where the  $n = 8$  mode hosts most of the total non-axisymmetric energy,  $\Sigma_{n>0}E_{\text{mag},n}$ , is present. For this case with  $P_{\text{heat}} \approx 6.4 \times 10^{-6}$  ( $\approx 13.5$  MW), the non-ideal PB modes become stabilised after roughly 10 ms. And in figs. 4.15(d) and (e),  $\Sigma_{n>0}E_{\text{mag},n}$  is reduced until complete stabilisation.

To further understand what governs the transition from small ELMs to type-I ELMs, the radial electric field at the outboard midplane is averaged between 1.0 – 2.0 ms and it is shown in figs. 4.16(a)-(e). An interesting observation is that the three scenarios where the small ELMs become stabilised (c)-(e) have deeper radial electric field wells than the two cases that sustain the small ELMs (a) and (b). It is worth pointing out that even for the lowest heating power, the instantaneous radial electric field profiles at the outer midplane are often deeper than  $E_r \sim -15$  kV/m, a representative value which has been associated to the L-H transition in AUG [198, 199]. This can be seen in fig. 4.16(a), which shows in gray the instantaneous profiles used to obtain the time-averaged profile (black). The scans with and without diamagnetic effects shown in section 4.2.2 together with the observations presented so far in this section indicate that small ELMs can be completely stabilised with a sufficiently deep radial electric field well.

In order to directly show the transition from small ELMs to type-I ELMs, the heating power of the simulation described in section 4.2 is increased at 5.6 ms of

---

<sup>2</sup>The excess heating power is always applied in the vicinity of the pedestal, such that the effect of the faster pedestal evolution can be rapidly determined. Depositing the excess heating power in the core produces the same results, but in a longer time scale as the excess heat needs to diffuse from the core to the pedestal top.

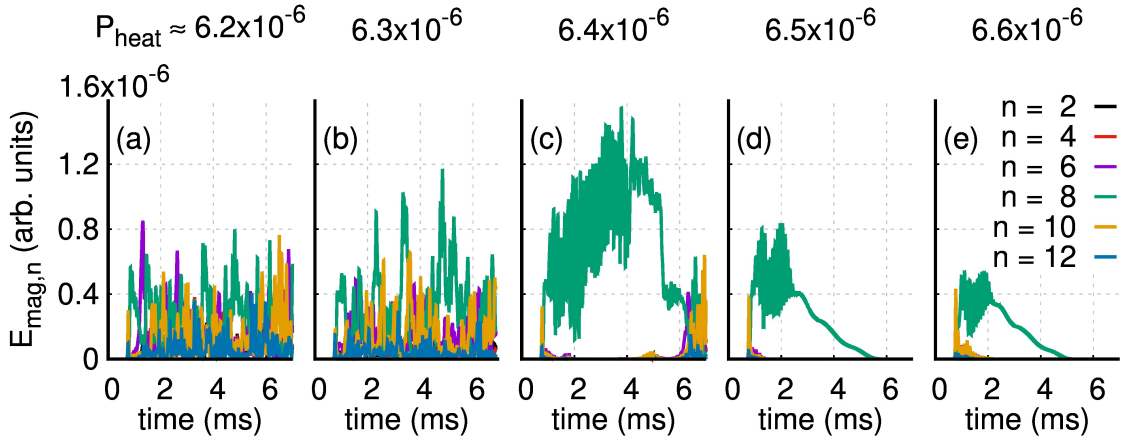


Figure 4.15: Magnetic energies of the non-axisymmetric perturbations for five different values of input heating power. The applied heating power increases progressively from (a) ( $\approx 13.0$  MW) to (e) ( $\approx 13.9$  MW). As a result of the increasing heating power, the magnetic energies of the  $n > 0$  perturbations become weaker.

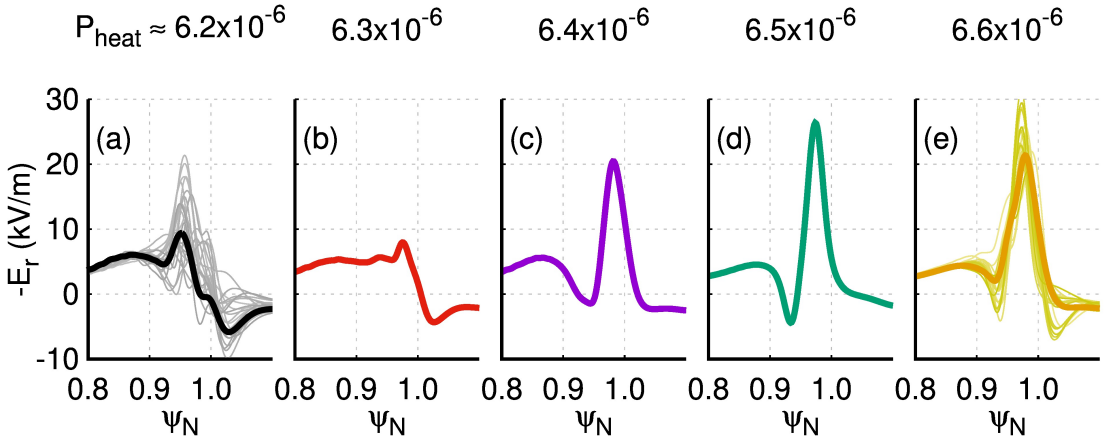


Figure 4.16: Time-averaged profiles of the outboard midplane radial electric field for five different values of input heating power. The applied heating power increases progressively from (a) ( $\approx 13.0$  MW) to (e) ( $\approx 13.9$  MW).

simulation time. The increase is from  $\sim 6.2 \times 10^{-6}$  to  $\sim 6.6 \times 10^{-6}$  in JOREK units. Resulting from the heating power increase, the non-ideal PB modes start to weaken in amplitude and their radial extent starts to reduce. This process takes roughly 4 ms to complete and, thereafter, a steeper pedestal is allowed to form. Ultimately, the steepening pedestal crosses the ideal PB stability boundary and a type-I ELM with dominant toroidal mode numbers  $n = 2$  and  $4$  is excited. The process described in this paragraph can be evidenced in fig. 4.17(a) and (b), which respectively show the outboard midplane pressure gradient and the power incident on the inner and outer divertors. At  $t \approx 12$  ms, the parallel heat conductivity

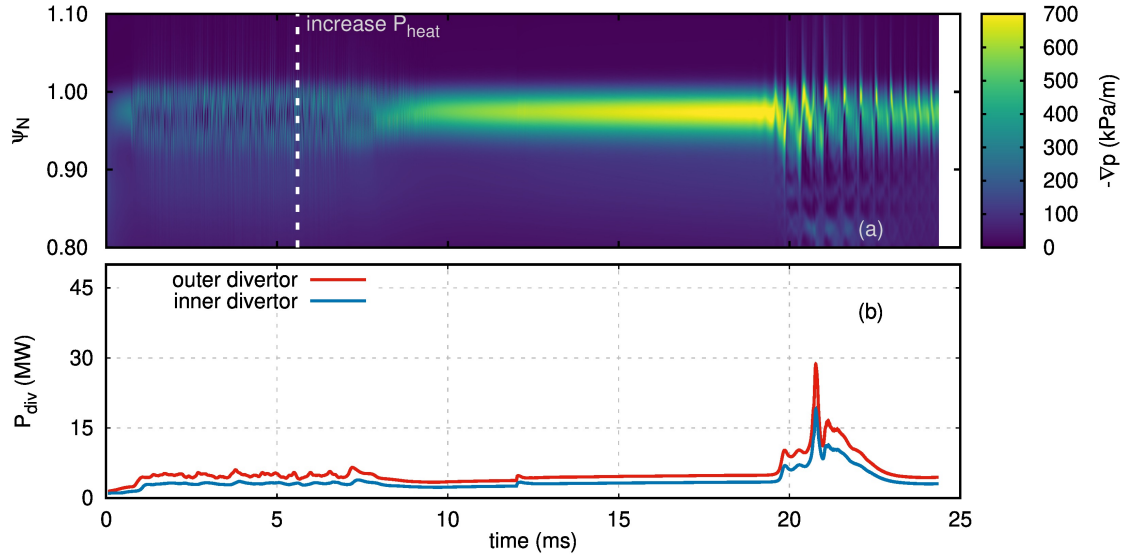


Figure 4.17: Time evolution of the outboard midplane pressure gradient at  $\phi = 0$  (a) upon increasing the heating power at 5.6 ms. And the power incident on the inner and outer divertor targets (b) resulting from small ELMs ( $t < 10$  ms) and from a type-I ELM ( $t \gtrsim 19$  ms).

is increased roughly to the Spitzer-Härm values (for  $T_e = 0.5$  keV and  $n_e = 5 \times 10^{19} \text{ m}^{-3}$ ,  $\chi_{\parallel} = 1.16 \times 10^9 \text{ m}^2/\text{s} \approx \chi_{\parallel,\text{SH}}$ ). The incident power that reaches the divertor targets is transiently increased in significant proportions when the type-I ELM crash appears. The small ELMs cause much weaker heat fluxes to the divertor targets. To directly show the influence of the increased heating power onto the non-ideal PB modes that cause small ELMs, the plasma pressure in real space together with the position of the separatrix are plotted for a restricted time frame between 5 and 10 ms in fig. 4.18. The expelled filaments after the heating power increase seem to have smaller amplitudes and they travel for shorter distances. They eventually disappear completely.

The transition from a regime dominated by small ELMs caused by non-ideal peeling-balloonning modes towards a type-I ELM is obtained by suddenly increasing the input heating power in small ELM simulations. The small ELMs start to weaken and the filaments formed by the small ELMs are gradually reduced in amplitude until disappearing completely. The pedestal top pressure rises with increasing  $P_{\text{heat}}$  due to the pedestal top temperature increase; the pedestal top density remains unchanged in the first few milliseconds after the heating power was increased—it only starts rising when the particle transport by small ELMs becomes significantly reduced. Additionally, due to the larger pressure gradient, the radial electric field well at the plasma edge deepens, and the bootstrap current density starts to rise. Taking one millisecond time-averages, the outer midplane profiles are tracked during the pure small ELMs phase (from 2.6 ms until 5.6 ms) and during the transition

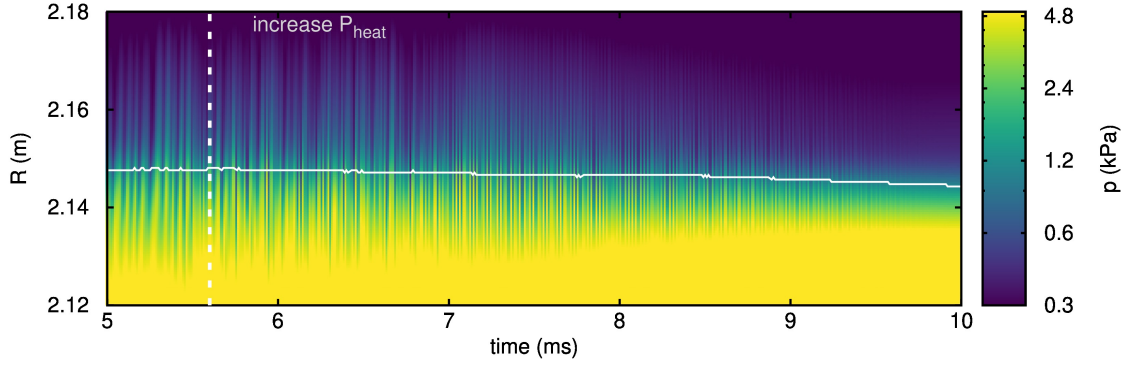


Figure 4.18: Time evolution of the outboard midplane pressure at  $\phi = 0$  (a) upon increasing the heating power at 5.6 ms. The filaments expelled from the confined region become weaker when the heating power is increased. They ultimately completely disappear and the pedestal is able to grow further.

phase where the non-ideal PB modes start to disappear (from 5.6 ms to 9.6 ms) and are plotted in fig. 4.19.

Three time-averaged profiles correspond to the original small ELM phase and show a constant pedestal top pressure, a weak radial electric field at the edge, and low toroidal current density. On the other hand, the four profiles at higher heating power show systematically higher pedestal top pressure, deeper  $E_r$  well, and a broader and larger edge current density. The last time-averaged profiles in gray, with the largest pedestal top value,  $\min(E_r) \approx -28$  kV/m and a high toroidal current density, is taken during a phase that mostly has suppressed the non-ideal PB modes. The destabilising effect of the increased  $\nabla p$  is tied to the stabilising effects of the deepening of the  $E_r$  well and of the toroidal current density. The additional stabilising effect of the edge resistivity decreasing as the pedestal top temperature increases is also important at this stage. Therefore, the disappearance of the non-ideal PB modes appears to be due to the  $E_r$  deepening,  $-j_\phi$  increasing, and the decreasing local  $\eta$  despite the increasing destabilising effect of  $\nabla p$ .

### 4.3.2 Decreasing separatrix density

The previous section detailed the bifurcation from a small ELM-dominant regime to a type-I ELM by means of increasing the heating power. Another path towards type-I ELMs, starting from a small ELM regime, is to decrease the separatrix density. In the experiment, this can be achieved by reducing, or completely removing, the particle source given by a gas puff (replacing the particle flux by means of cryogenic deuterium pellet injection can keep the density profiles fixed). As a result of the reduced edge density source, the separatrix density decreases. Resulting from the lower separatrix density, the pressure gradient is lowered, and it is overall shifted slightly inwards—such response of the pressure profile position is also observed in experiments [200, 201]. However, many physical effects related

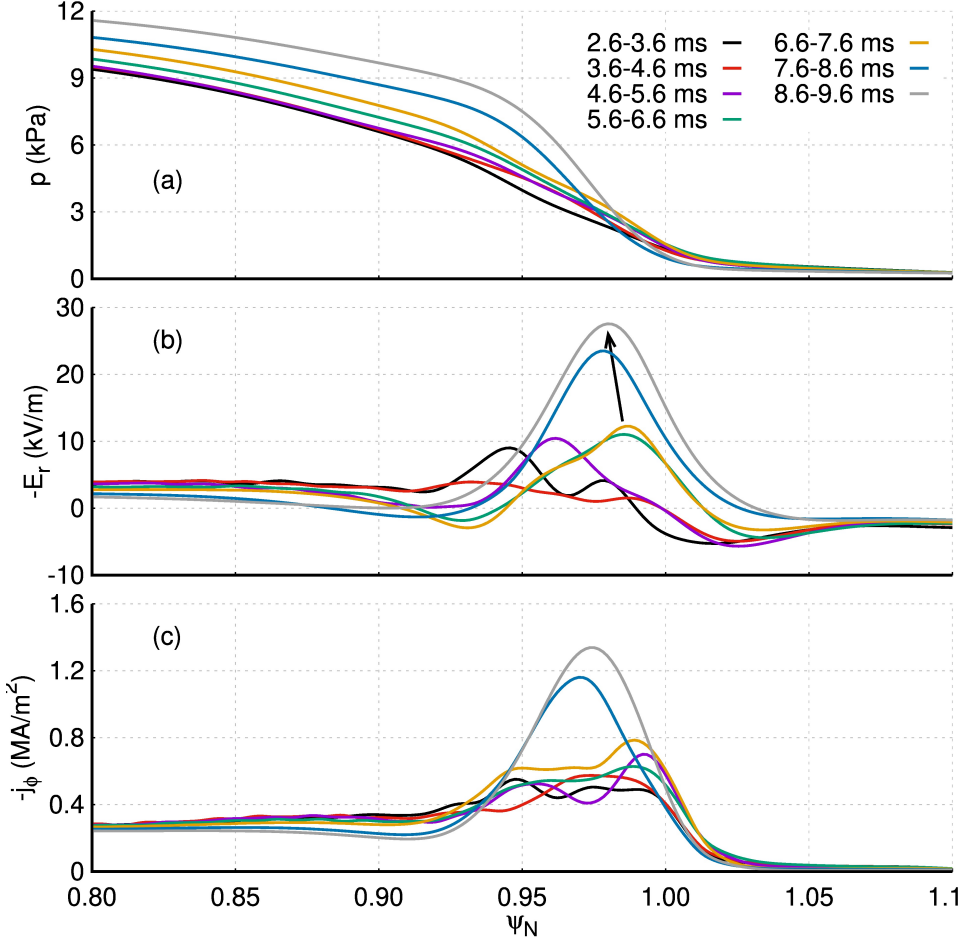


Figure 4.19: Evolution of the time-averaged outboard midplane pressure (a), radial electric field (b), and toroidal current density (c) at  $\phi = 0$ . The time averaging is done for one millisecond intervals. The three time-averaged profiles before the heating power is increased have a shallow  $E_r$ , and the four profiles after  $P_{\text{heat}}$  increases show a systematic deepening of the  $E_r$  well, as indicated by the black arrow.

to the pedestal position (particularly neutrals penetration) are not included in the JOREK model used for these simulations and, therefore, the qualitative agreement will likely not translate to a quantitative agreement at this stage. The decrease of separatrix density (at fixed pedestal top density) also causes a deeper radial electric field well (because  $E_r \propto 1/n_e$ ) and a larger bootstrap current density (because the density gradient increases).

Decreasing the edge particle source in the simulations leads to a reduced separatrix density. This is done to start a new axisymmetric simulation and the non-zero toroidal modes are included after 0.1 ms (exactly the same time as the small ELM simulations described in section 4.2). The magnetic energies of the two cases are

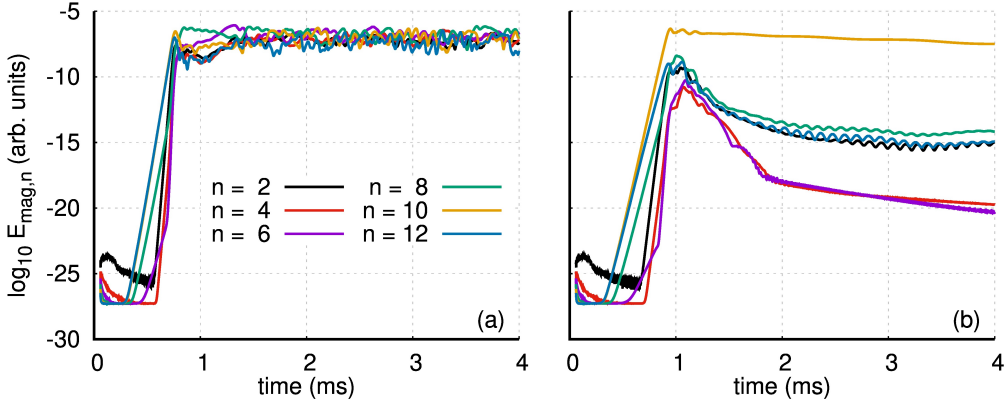


Figure 4.20: Magnetic energies of the non-axisymmetric modes in logarithmic scale in the first 4 milliseconds of simulation time for (a) small ELMs at high  $n_{\text{sep}} (\sim 3 \times 10^{19} \text{ m}^{-3})$  and (b) their response to lower separatrix density ( $\sim 2 \times 10^{19} \text{ m}^{-3}$ ).

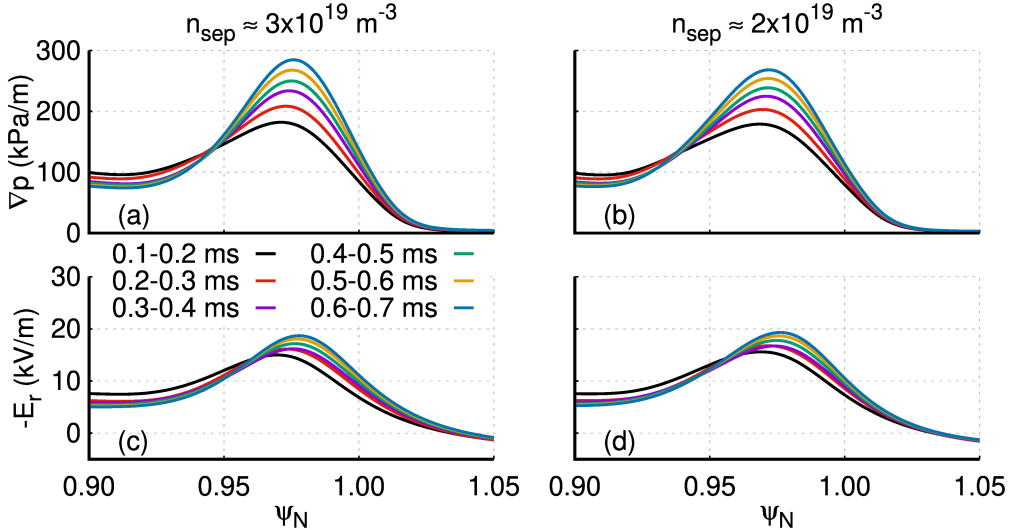


Figure 4.21: Time-averaged outboard midplane profiles of the pressure gradient and  $E_r$  during the linear growth phase for nominal separatrix density (a) and (c), and for lower separatrix density (b) and (d).

shown in fig. 4.20. The linear phases are similar between the two cases, with growing  $n = 8, 10, 12$  high- $n$  (peeling-)ballooning modes. But the simulation with low  $n_{\text{sep}}$  (b) deviates as the  $n < 10$  and  $n = 12$  become completely stabilised, and the  $n = 10$  only reaches small amplitudes and does not affect the  $n = 0$  background. The stabilisation of the modes with higher toroidal mode numbers leads to a single toroidal mode number with very small amplitude that does not cause any changes to the background plasma.

The simulation at lower separatrix density, fig 4.20(b), sees the pedestal evolve, but it was not continued until a type-I ELM is reached to save computing time. Time-averaged outer midplane profiles of the pressure gradient and radial electric field are displayed in fig. 4.21 for the small ELMs (a) and (c), and for the lowered separatrix density case (b) and (d). The profiles are averaged over 0.1 ms during the linear growth phase, < 0.7 ms. The lower  $n_{\text{sep}}$  causes an inward shift of  $\nabla p$  and, particularly, a smaller pressure gradient in the vicinity of the separatrix. It additionally allows for a deeper  $E_r$  well and an increase of the bootstrap current density (not shown). Diminishing the destabilising influence of the large  $\nabla p$  near the separatrix together with the stabilising influence of the deeper  $E_r$  and the higher  $-j_\phi$  cause the small ELMs to become completely stabilised.

With a slower pedestal top temperature growth, but still at low separatrix density, it is possible to recover the quasi-continuous transport caused by small ELMs. The slower temperature recovery implies that the pressure recovery is also slowed down with respect to the previously described simulations at lower  $n_{\text{sep}}$ . The non-axisymmetric modes are initialised at 0.1 ms and the high-n modes start growing quickly. After the linear growth phase, non-linear coupling takes place and ultimately, a fully non-linear phase becomes established. This can be seen (in comparison to the nominal small ELM simulations) in the time-evolving magnetic energies of the  $n > 0$  modes of fig. 4.22 (a) and (b). The small ELMs at low separatrix density and slower pedestal temperature recovery are sustained with even lower pressure gradients than those shown in fig. 4.21(b) and, therefore, are a strong indication that the role of resistivity (which increases with decreasing temperature) is a key parameter for the dynamical evolution of the underlying non-ideal peeling-balloonning modes. Neoclassical effects and  $Z_{\text{eff}}$  modify the resistivity and are not included in the JOREK expression. Therefore, improving the resistivity model used in JOREK is also important for future work regarding small ELM dynamics.

## 4.4 Conclusions

H-mode operation without large type-I ELMs is an imperative requirement for ITER in high-performance conditions. To this purpose, naturally ELM-free H-modes and ELM mitigated/suppressed regimes are considered and actively researched. In AUG, one such alternative under investigation is the quasi-continuous exhaust (QCE) regime. The QCE regime can be operated completely without type-I ELMs. The pedestal is limited by small ELMs, which quasi-continuously expel heat and particles from the confined region. It is presently unclear whether or not such regime can be operated in ITER. Simulations performed with JOREK, which show several key features of small ELMs have been presented in this chapter. Non-ideal peeling-balloonning modes near the separatrix are identified as the possible transport mechanism underlying such small ELMs.

Modelling the pedestal build-up at fixed pedestal width, with stationary diffusion coefficients and sources, non-ideal peeling-balloonning modes that regulate the

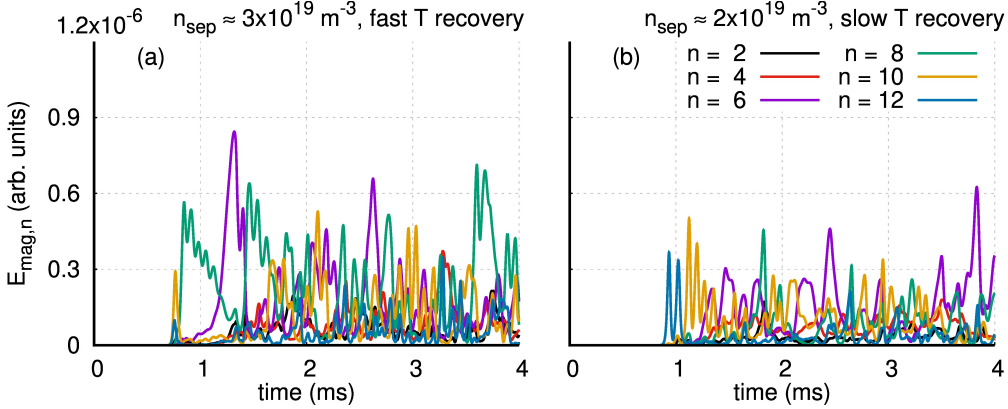


Figure 4.22: Magnetic energies of the non-axisymmetric modes in the first 4 milliseconds of simulation time for (a) small ELMs at high  $n_{sep} (\approx 3 \times 10^{19} \text{ m}^{-3})$  and (b) small ELMs at lower separatrix density ( $\approx 2 \times 10^{19} \text{ m}^{-3}$ ) but slower pedestal temperature recovery.

pedestal below the ideal PB stability boundary are observed under appropriate conditions. The non-ideal nature of such PB modes is determined by the fact that they appear below the ideal PB stability boundary and because their growth rates are largely reduced/enhanced by decreasing/increasing resistivity. The necessary conditions to sustain sufficient outwards transport by small ELMs is primarily determined by the separatrix density and the input heating power. In particular, simulations with high  $n_{e,sep}$  and low heating power observe phases (longer than 10 ms) with quasi-continuous outwards transport that prevent the pedestal from reaching a type-I ELM unstable scenario.

An important ingredient required in order to properly produce simulations of these non-ideal PB modes is the inclusion of diamagnetic effects, which (in the simulations) cause the radial electric field well to develop in the pedestal region. In the absence of diamagnetic effects, it is not possible to stabilise the small ELMs by increasing the heating power. In contrast, when diamagnetic effects are included, the small ELMs become completely stabilised and the plasma state moves to a type-I ELMy H-mode by increasing  $P_{heat}$ . Similarly, decreasing the separatrix density completely stabilises the small ELMs if diamagnetic effects are included. Another important effect that should be included when modelling these instabilities is the bootstrap current density because it has a stabilising influence onto ballooning modes and high-n peeling-balloonning modes. At the moment, JOREK evolves the bootstrap current density through the Sauter formula [66, 67]. However, the Sauter expression is known to be inaccurate depending on the parameter regime, particularly at high collisionality [202]. Therefore, an improvement of the bootstrap current density source in JOREK will be required in order to realistically move forward. Finally, it is observed that the influence of resistivity plays a pivotal role in the dynamics of the non-ideal PB modes that underlie small ELMs. The simplified

resistivity with only Spitzer temperature dependency used in JOREK would have to be improved to include the influence of neoclassical effects and effective main ion charge greater than unity. Doing so could also allow to study ELM-mitigation through impurity seeding with JOREK.

# 5 Type-I ELMs

This chapter describes first of a kind simulations of type-I ELM cycles in realistic X-point geometry. Most of the results shown here have been published [37].

The simulation set-up necessary to obtain the cyclical simulations of ELMs is presented in section 5.1. It is closely related to the simulation set-up used to simulate the small ELMs related to the QCE regime shown in the previous chapter, but with higher applied heating power. The resulting non-axisymmetric activity ensued by linearly destabilising low-n peeling-balloonning modes (precursors), as the pressure gradient and the edge current density increase, is described for the first ELM crash in section 5.2. The destabilisation of the low-n PB modes drives the modes with larger toroidal mode numbers through three-wave non-linear interactions.

A description of the cyclical dynamics of the simulated ELMs, together with the influence of the seed perturbations, is then presented in section 5.3. The response of the ELM repetition frequency with respect to a modified heating power and, separately, to a change in the scrape off layer (SOL) density are also detailed. The altered SOL density results in an inward shift of the density pedestal, and it can be related to a change of the gas fuelling rate. The observed response of the ELM repetition frequency is qualitatively consistent with experimental observations.

As a result of the growing non-axisymmetric activity, the magnetic fields at the edge of the confined region get perturbed from the original configuration with nested closed flux surfaces. Eventually, this leads to the generation of ergodic magnetic topology through magnetic reconnection. The non-linear stability of peeling-balloonning modes is modified by the ergodic magnetic fields and reduced plasma flows in a way that explosive, i.e., faster than exponential, growth is obtained. This electromagnetic triggering mechanism denotes the non-linear onset of the ELM crash, and it is further described in section 5.4. The last section provides conclusions and insights for future work.

## 5.1 Simulation set-up

The simulation is set-up in the same way as the small ELM simulations presented in the previous chapter, in section 4.1. Namely, the pedestal build-up at constant pedestal width is imposed through stationary heat and particle diffusion and sources. The only difference is an increase of the injected heating power, from  $P_{\text{heat}} = 6.2 \times 10^{-6}$  to  $6.6 \times 10^{-6}$  in JOREK units (equivalent to  $\approx 13.0$  MW and  $\approx 13.9$  MW, respectively), and the choice of realistic (Spitzer-Härm) parallel heat diffusion coefficient. Note that the additional heating power is applied directly at

the pedestal top region. The former represents a small increase of the heating power ( $\sim 6.5\%$ ). As discussed in the previous chapter, the larger heating power causes the temperature pedestal to rise in a faster time scale. This causes the pressure pedestal to also rise faster and, consequently, the radial electric field and edge current density to also increase in faster time scales. As a direct result of these changes, the non-ideal (resistive) peeling-balloonning modes present in the simulations described for  $P_{\text{heat}} = 6.2 \times 10^{-6}$  (in section 4.2) become completely stabilised.

In the absence of the peeling-balloonning turbulence, the edge pressure gradient and current density can rise to a point where a peeling-balloonning stability boundary is crossed. The next section describes the ensuing growth of the linearly unstable modes, and the non-linear mode coupling that allows for linearly stable modes to become driven.

It is reiterated at this stage that the pedestal build-up considered for these simulations is only a simplified model. The pedestal top increases without the pedestal width changing in time. Several ingredients are not present in the simulated build-up that are known to be present in the experiment. However, the physical processes that dominate said effects are not included in the MHD model considered for the present simulations. For example, the particle source used for the simulations constitutes a stationary profile, but in reality it is a time-dynamical source that is governed by the ionisation of neutral particles. In order to model such physics, a kinetic description of the neutrals is most accurate, but a fluid approach can also be used. The JOREK code has been recently adapted, and it is now possible to investigate such effects with a neutrals fluid model [164, 165]. A kinetic particle framework within JOREK [203] makes it possible to account for kinetic neutrals. In addition, anomalous transport is a time-varying effect that is crudely approximated with stationary diffusion coefficients in order to simulate the pedestal build-up. As the pedestal evolves, the local gradients change and, therefore, the gradient-driven micro-turbulence becomes significantly affected. Not only does the drive for instabilities in the edge region change through the ELM cycle, but also the stabilising influence of increasingly sheared ExB and diamagnetic flows. Reference [204] provides an overview of turbulent dynamics present in the pedestal during the inter-ELM pedestal build-up. A more consistent treatment would require kinetic or gyro-kinetic simulations to be performed at different time points during the pedestal build-up, and returning the results to modify the diffusion coefficients used in the JOREK simulation. However, (gyro-)kinetic simulations in the H-mode edge region are notoriously difficult to carry out and are very demanding in terms of computational resources [205–207]. Reduced models (physics-based [208] and/or with properly trained neural networks [209]) to account for turbulent transport can certainly be helpful in circumventing this problem. Such efforts, however, are beyond the scope of the present work, and would first require significant development, validation, and verification to be carried out.

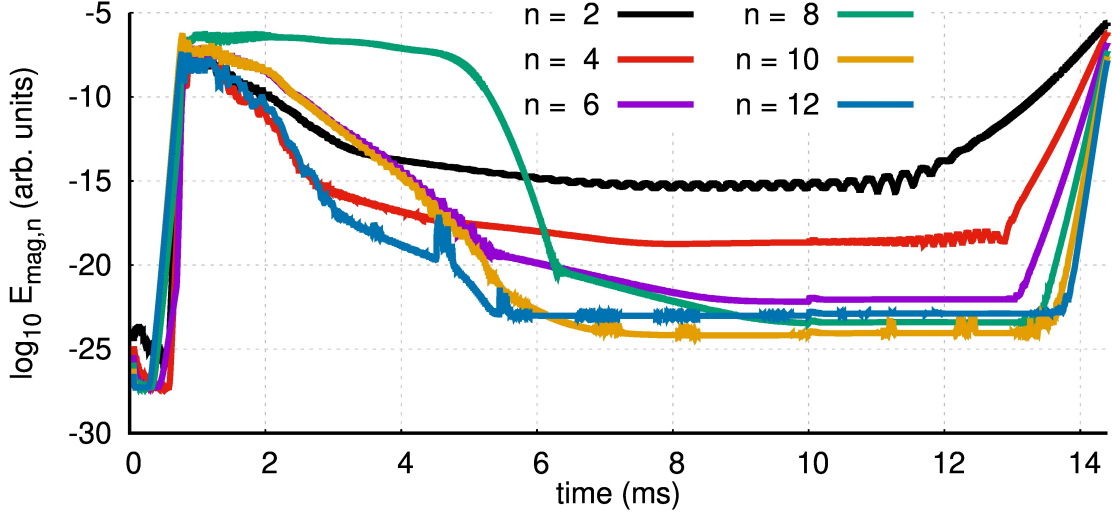


Figure 5.1: Magnetic energies of the non-axisymmetric modes ( $n = 2, 4, \dots, 12$ ) in logarithmic scale for 14.4 milliseconds of simulation time.

## 5.2 Non-axisymmetric linear and early non-linear evolution

The toroidal mode numbers chosen for the present simulations are  $n = 0, 2, 4, \dots, 12$ . This choice is made for two reasons. The first reason is that the plasma core is unstable to a 2/1 tearing mode, and it could interfere with the ELM cyclical dynamics. The tearing mode is unrelated to the ELMs. Neglecting the  $n = 1$  mode from the simulations circumvents this problem. The second reason deals with the cost of the present simulations. Because the ELM crash and the inter-ELM phase occur in vastly different time scales ( $\sim 0.1 \mu\text{s}$  and  $\sim 10 \text{ ms}$ ), constraining the number of toroidal mode numbers reduces the, already large, computational expense required to run such simulations. When the peeling-balloonning boundary is crossed, the linearly unstable modes are  $n = 2$  and  $3$ , but through simulations with  $n_{\text{period}} = 1$  (not included here) it is observed that the  $n = 1$  is strongly subdominant. Simulations with a periodicity of  $n_{\text{period}} = 3$  have also been performed, but the cyclical dynamics and the triggering mechanism remain unaffected and, therefore, said simulations are not shown here.

The magnetic energies of the non-axisymmetric modes ( $n \neq 0$ ) are shown in fig. 5.1 for 14.4 ms of simulation time. There are three main stages in the plotted time window. In the first stage of the simulation,  $t \lesssim 6 \text{ ms}$ , resistive peeling-balloonning modes are destabilised and quickly suppressed by the strong stabilising influence of the growing  $E_r$  well. The dynamics of these resistive instabilities is not of interest for the present study, and it was covered in the previous chapter. The amplitude of these modes is very low, even for  $n = 8$  which is the strongest mode in this phase, and the pedestal build-up continues. At  $t \approx 10 \text{ ms}$ , the heat conductivity is increased to realistic (Spitzer-Härm) values. The second phase is described

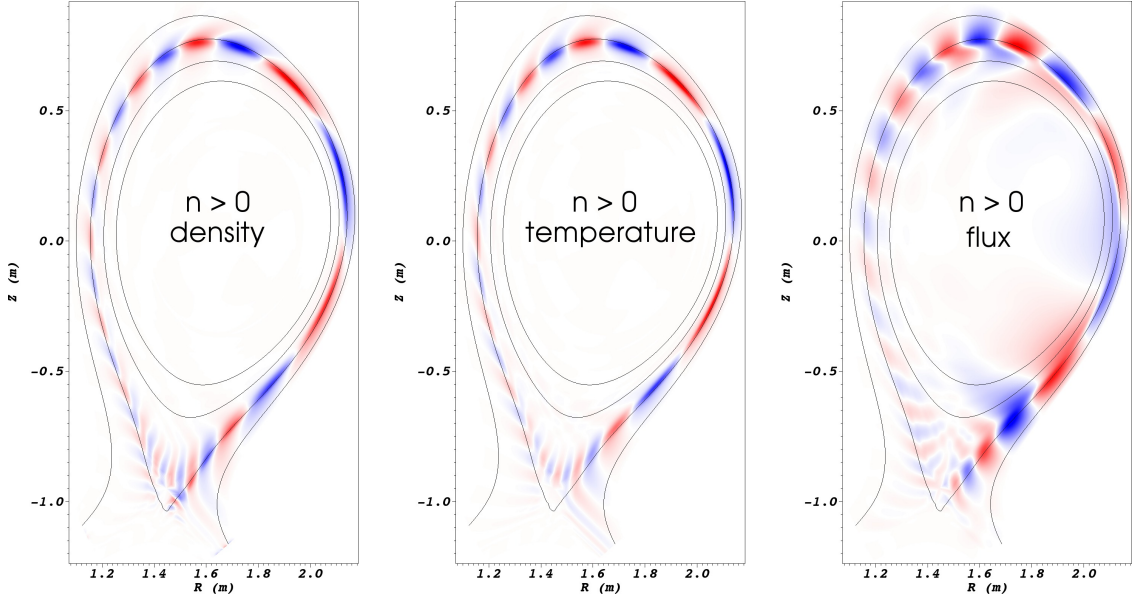


Figure 5.2: Density, temperature, and magnetic flux perturbations at 12.5 ms. The peeling-balloonning structure with dominant peeling characteristics can be observed. Black lines denoting the flux surfaces  $\psi_N = 0.8, 0.9, 1.0, 1.1$  are also included.

by stable modes with very small amplitudes and small oscillations,  $t \sim 6 - 12$  ms. During this time, the pedestal is linearly stable to ideal peeling-balloonning modes.

The phase with stable modes ends when  $n = 2$  becomes linearly destabilised by the large edge current density and pressure gradient. The structure of the mode has a dominant external kink (peeling) component, as can be seen in fig. 5.2. The linearly unstable mode peaks in amplitude in the outer 5% of the confined region. The last phase pictured in fig. 5.1 ends at 14.4 ms. This last phase is the linear growth phase that precedes the onset of a type-I ELM crash.

### 5.2.1 Early non-linear growth phase – mode coupling

After reaching a sufficiently high amplitude, the low frequency  $n = 2$  perturbation couples with itself to drive an  $n = 2 + 2 = 4$  mode via three-wave interactions [196]. Thereafter, these two modes drive the  $n = 2 + 4 = 6$  mode, and so forth. During the early non-linear phase (approximately from 12 to 13 ms), the growth rate of the driven modes is roughly the added growth rate of the driving modes. For example, the growth rate of  $n = 4$  is twice the growth rate of  $n = 2$ . As a result, the fastest growing mode (during the early non-linear phase) in these simulations will always be the mode with the largest toroidal mode number, i.e.,  $n = 12$  for the present simulations. Nevertheless, this does not imply a dominant role for said high- $n$  mode.

There is also non-linear mode coupling taking place from high- $n$  to low- $n$  modes,

and one could think that it is therefore necessary to include infinitely high-n modes. Fortunately, however, that is not the case for three main reasons. First, the strength of the non-linear coupling depends on the product between the square root of the energy of the driving modes. The coupling strength for high-n modes  $n = 12$  and  $10$  to drive the  $n = 2$  mode depends on  $\sqrt{E_{n=12}}\sqrt{E_{n=10}}$ , which is small compared to the energy of the  $n = 2$  mode. Consequently, in this case the non-linear mode coupling from high-n to low-n modes is much weaker than the coupling from low-n to high-n. The second reason why it is not necessary to include infinitely high-n modes is that the early non-linear growth phase ends as soon as the total perturbation manages to alter the background plasma and, therefore, affects the instability drive (i.e., the pressure gradient and the current density and its gradient). The third reason is that modes with larger toroidal mode numbers are more easily stabilised by the diamagnetic and ExB drifts. That being said, including only low-n modes leads to unrealistic dynamics. For example, the simulation described so far, with  $n = 0, 2, 4, \dots, 12$ , features a sharp ELM crash with a distinct end; however, including fewer toroidal mode numbers shows an ELM event that continues to expel heat and particles from the plasma and, as such, does not have a distinct end.

The modes that grow during this early non-linear phase are identified as low frequency precursors. Precursor activity of such characteristics has been identified in several tokamaks [109, 210–215]. An example from the AUG discharge that was used for the post-ELM initial conditions of the present simulations, shot #33616, is shown in fig. 5.3. The figure displays an ELM-synchronised spectrum of the magnetic perturbations measured with Mirnov coils in the LFS. The magnetic signals are averaged over 53 type-I ELMs. To do so, the signals are shifted such that  $t - t_{\text{ELM}} = 0$ , where  $t_{\text{ELM}}$  denotes the start time of the ELM. A dashed red box indicates precursors that precede the ELM crash at  $f \lesssim 140$  kHz. These increase in amplitude as the ELM approaches. The high-frequency perturbations that are also visible in fig. 5.3 are thought to be gradient-limiting micro-turbulence related to the widening of the pedestal during the inter-ELM phase [113, 116, 118, 216]. These high frequency modes are not present in the simulations presented in this work, potentially indicating that these modes cannot be captured with the used MHD model.

The growth rate of the simulated low frequency, low-n precursors in the simulations increases with time, which is expected when the plasma is slowly driven across an instability boundary [217]. Concomitant with the increase in amplitude of the low-n precursors from the simulations, the divertor incident power is also observed to moderately increase (prior to the violent ELM crash). This observation is qualitatively in agreement with experimental observations of slow (lasting  $\gtrsim 1$  ms) increases of the divertor incident power prior to the ELM crash [218]. Said low-frequency precursors are not always directly observed either because they are not always present or because their growth is sometimes too fast to be captured.

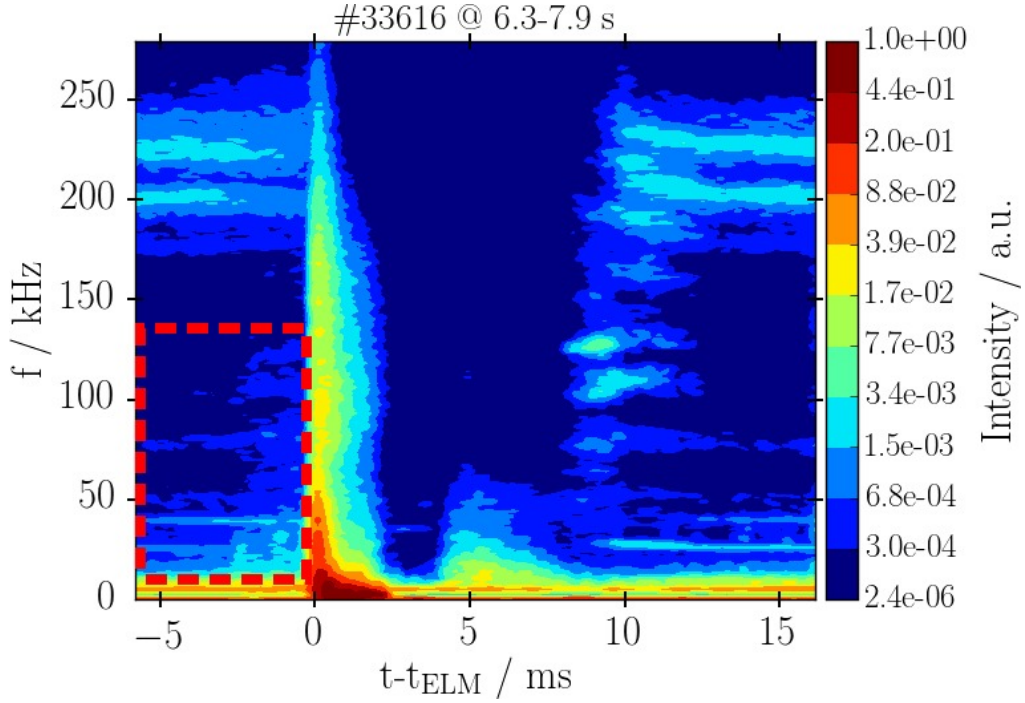


Figure 5.3: AUG shot #33616 from 6.3 to 7.9 s is in type-I ELMy H-mode. Spectrogram of magnetic pick-up coils measuring magnetic fluctuations from 53 ELMs and synchronised to each ELM start time ( $t - t_{\text{ELM}} = 0$ ). Low frequency, low- $n$ , precursors grow before the ELM onset.

### 5.3 Type-I ELM cycles

During the early non-linear phase, the  $n \neq 0$  modes interact with each other, but not with the  $n = 0$  background. It ends when the precursors reach a sufficiently large amplitude ( $\delta n_e/n_e \sim 1$ ). Thereafter, a non-linear phase that features interactions between  $n \neq 0$  modes and the  $n = 0$  axisymmetric background is observed. The latter leads to a strong collapse of the edge pedestal caused by the ELM crash. The non-linear mechanisms that lead to the ELM onset are described in section 5.4. The present section describes the cyclical dynamics of the simulated ELMs. The magnetic energies of the non-axisymmetric modes (in linear and logarithmic scales), and the power incident onto the inner and outer divertor targets are shown in figs. 5.4(a), (b), and (c), respectively.

For the first ELM, the end of the early non-linear phase happens roughly at 14 ms, and the precursor phase begins. The  $n = 2$  and 4 modes modify the background plasma in sub-ms time scales. As a result of the non-linear interaction between the precursors and the background plasma, the precursor phase ends and the onset of the first ELM crash takes place (at  $t \approx 15$  ms). The ELM crash lasts roughly  $\sim 1.5$  ms for the first ELM. The dominant toroidal modes during the ELM crash are  $n = 2$  and 4, which is consistent with experimental observations at AUG [211].

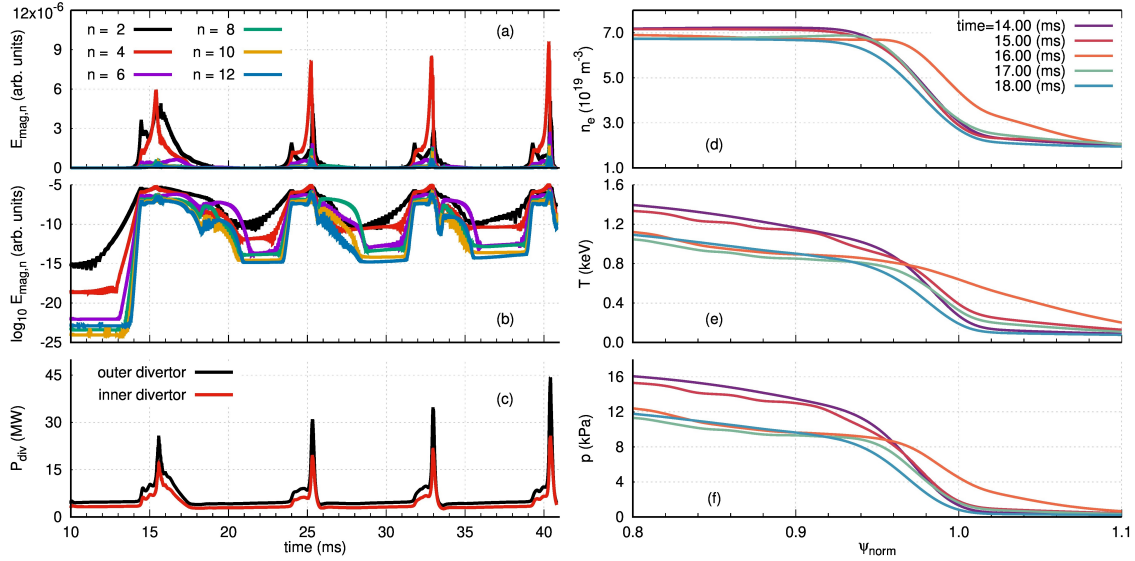


Figure 5.4: Magnetic energy of the non-axisymmetric perturbations in linear (a) and logarithmic (b) scales. The energies of the perturbations increase and decrease in each ELM crash. The inner/outer divertor incident power (c) is shown throughout four ELMs simulated in sequence. Five time slices are chosen to show how the density (d), temperature ( $T = T_e + T_i$ ) (e), and pressure (f) profiles at the outboard midplane look before, during, and after the first ELM.

Resulting from the ELM crash, the (density, temperature, and pressure) pedestals become significantly reduced, as shown in figs. 5.4(d)-(f).

### 5.3.1 ELM crash and inter-ELM activity

The evolution of the density, temperature, and pressure at the outer midplane is shown in figs. 5.4(d)-(f). It can be seen that the reduction in the density is small in comparison with the decrease of the temperature pedestal. The effect of the precursors onto the confined plasma can be evidenced in the profiles at 15 ms because there are corrugations of the temperature and pressure profiles that are absent at 14 ms. During the ELM crash (at  $t = 16$  ms), plasma filaments, which cause the increase in density and pressure observed in figs. 5.4(d) and (f), are expelled. At the same time, the temperature increases significantly in the outermost flux surfaces ( $\psi_N \gtrsim 0.97$ ), but decreases inside of  $\psi_N \approx 0.97$  up to  $\psi_N \approx 0.5$ . Said behaviour is characteristic of the ion temperature profile evolution during the ELM crash, as reported in Ref. [110]. In the following time slices ( $t = 17$  and 18 ms), the density profile shows only a moderate reduction below the pre-ELM state, while the temperature profile has relaxed significantly below its pre-ELM state.

The first ELM crash expels roughly 11% of the stored thermal energy. In contrast, the subsequent ELMs expel approximately 7% of the pre-ELM stored thermal

energy. The absolute and relative ELM sizes for all four type-I ELMs are shown in figs. 5.5(a) and (b), respectively. The pre-ELM stored thermal energy increases (from the second to the fourth pre-ELM state) because the central temperature monotonically increases slightly in the simulations as time progresses. This has to do with the stationary sources and diffusion. The duration of the ELM (as defined by an increase in divertor incident power above a given threshold) is also different between the first ELM and the subsequent ELMs. The first ELM lasts longer than the subsequent ELMs as can be inferred from figs. 5.4(a) and (c), and is directly visible in fig. 5.5(c). The reason why the first ELM is different from the subsequent ELMs will be detailed in the next subsection.

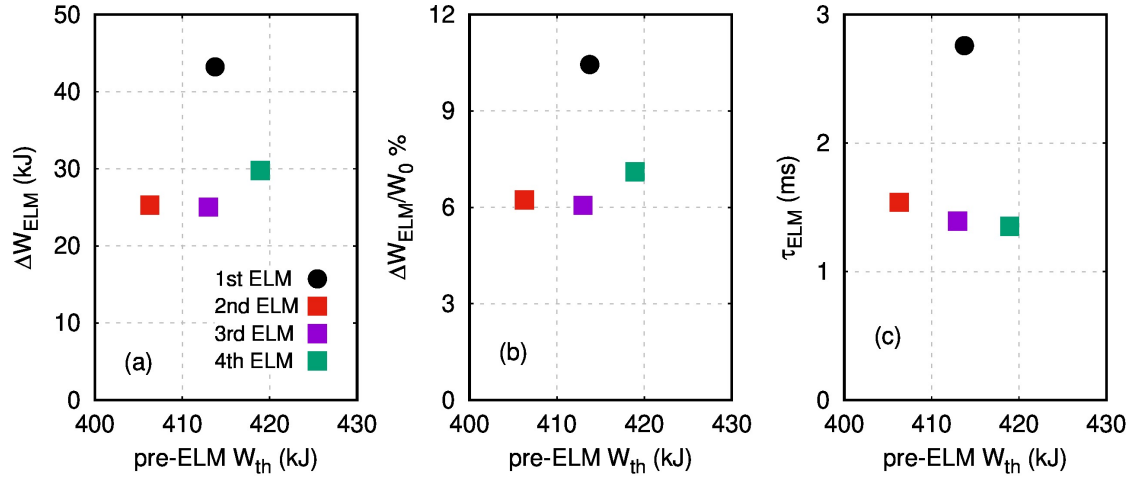


Figure 5.5: Absolute ELM size (a), ELM size relative to the pre-ELM stored thermal energy (b), and duration of the increased divertor incident power as a measure of the ELM duration (c) for the four consecutive type-I ELMs. The first ELM crash has longer duration, and larger absolute and relative ELM size.

After the end of the ELM crash ( $t \approx 18$  ms for the first ELM), the pressure gradient is considerably smaller than the pre-ELM  $\nabla p$ , but it excites medium-n peeling-balloonning modes (as can be seen in fig. 5.4(b) at  $t \approx 18 \dots 21$  ms for the first ELM crash). Inter-ELM modes with comparable toroidal mode numbers (between 5 and 8) have been reported in experiments from AUG [211] and KSTAR [117]. The latter have additionally been simulated with JOREK [161]. The simulated inter-ELM modes of medium-n become suppressed by the diamagnetic and ExB drifts. As these inter-ELM modes become suppressed, the magnetic energies of the non-axisymmetric perturbations decrease significantly, with respect to their amplitudes during the ELM crash.

### 5.3.2 Seed perturbations

After the medium-n inter-ELM modes are suppressed, the energies of the non-axisymmetric perturbations remain up to 10 orders of magnitude larger than their

amplitudes before the first ELM crash. Recall that before the first ELM crash the seed perturbations are somewhat arbitrary. This difference between  $E_{\text{mag},n>0}$  before and after the ELM crash is very important. Experimentally, and in the simulations, the post-ELM conditions of the  $n \neq 0$  modes are not arbitrary; they retain some information (amplitudes and/or structures) from the previous ELM crash.

The seed perturbations for the first ELM crash are arbitrary (they have to be for any initial value code like JOREK) while those for the subsequent ELMs are consistent with the prior existence of an ELM crash. This constitutes the main reason for the first ELM crash being different from the subsequent ELMs. The most important differences are the ELM size and the duration of the ELM crash, which can be seen in fig. 5.5. These differences appear because the seed perturbations (which are destabilised when  $\nabla p$  and  $j$  become large enough to excite PB modes and, at the same time, to overcome the stabilising influence of  $v_{\text{ExB}}$  and its shear) require a finite amount of time to grow. The time required for the seed perturbations to grow to sufficiently large amplitudes and modify the background plasma differs between arbitrary and self-consistent seed perturbations,  $t_{\text{arb.}}$  and  $t_{\text{s.c.}}$  respectively. For the simulations shown here,  $t_{\text{arb.}} > t_{\text{s.c.}}$  and, therefore, the pre-ELM profiles exhibit higher pedestals for the arbitrary seed perturbations (first ELM) compared to the self-consistent cases (subsequent ELMs).

Due to the stationary sources and diffusion used to model the pedestal build-up, the first time the precursors become excited ( $t \approx 12$  ms) the pedestal features slightly different profiles than the subsequent times it happens ( $t \approx 22, 29$ , or  $38$  ms). An additional simulation is performed to confirm the hypothesis that the differences in the ELM sizes and duration come from the seed perturbations, and not from differences in the pedestal profiles between the first ELM and the subsequent ELMs. The non-axisymmetric modes of the original simulation are set all to zero at  $t = 28.3$  ms, and are immediately re-introduced at noise-level amplitudes (as was done in the beginning of the simulation). The evolving magnetic energies of these  $n > 0$  modes are shown in fig. 5.6 in thick lines together with the magnetic energies of the original modes in thin lines. The new case with arbitrary seed perturbations also shows  $t_{\text{arb.}} > t_{\text{s.c.}}$ . The pre-ELM profiles for the case with arbitrary perturbations has (artificially) higher pedestals than the case with the self-consistent seed, thereby emphasising the importance of simulating ELMs with self-consistent seed perturbations.

The differences in ELM size and duration between the first ELM and the subsequent ELMs is reminiscent of so-called ‘giant’ ELMs. Giant ELMs appear after ELM-free phases during which the confined energy increases, and they are characterised by larger ELM sizes and longer ELM duration, with respect to the subsequent ELMs [219–222]. Since giant ELMs take place after an ELM-free phase, the seed perturbations that give rise to the giant ELM should be weaker than the seed perturbations for a regular type-I ELM<sup>1</sup>. In light of the differences between

---

<sup>1</sup>The seed perturbations for a given ELM can be comprised of remnant MHD activity (e.g., from a previous ELM crash) and inter-ELM modes of MHD or turbulent nature. With the present set-up

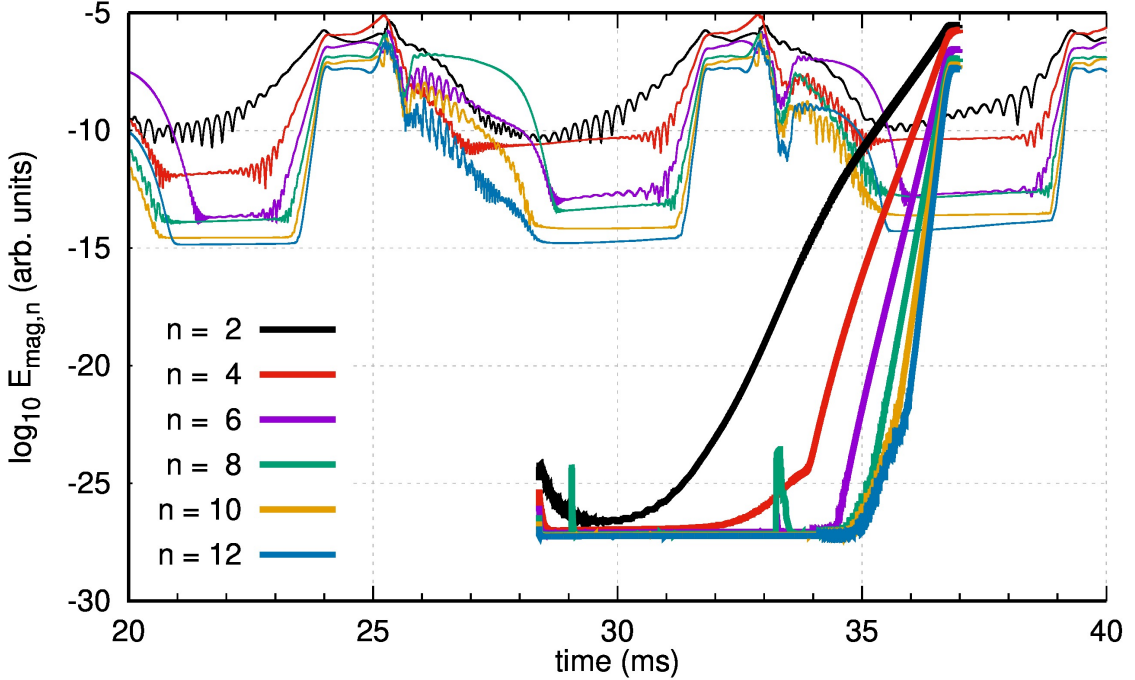


Figure 5.6: Magnetic energies of the  $n > 0$  modes from the base simulation (with thin coloured lines), and from a simulation that eliminates the perturbations at  $t = 28.3$  ms and immediately re-introduces arbitrary perturbations at noise-level amplitudes. As a result, the ELM is significantly delayed and it takes place at a considerably larger pedestal pressure, thus emphasising the importance for multi ELM-cycle simulations for predictive modelling.

the first ELM and the next ELMs, only the latter will be further analysed in the remainder of this chapter.

### 5.3.3 Heating power dependency

The most important characteristics of type-I ELMs are the large ELM sizes and the direct dependency between input heating power and ELM repetition frequency [28]. It has already been shown that the simulated ELMs presented in this chapter can be considered type-I ELMs in terms of the ELM size. In order to confirm that the simulations are indeed type-I ELMs the heating power is changed to probe how the ELM repetition frequency,  $f_{\text{ELM}}$ , changes.

In the simulations, the time scale at which the pressure gradient increases is determined by the imposed stationary diffusion coefficients, particle source, and heating power applied. In the experiment, however, the build-up of the pedestal is given by the anomalous and neoclassical transport, the applied heating power,

---

only the MHD activity can be modelled, and any direct or indirect interaction between the MHD modes and turbulent micro-instabilities cannot be considered.

and the ionisation of neutral particles mainly from fuelling sources and recycling, all of which evolve in time together with the profiles. Accounting for all such dynamical effects in a realistic way goes well beyond the scope of the present work. Nevertheless, the heating power scan is produced in order to confirm whether or not the simulated ELMs are indeed type-I ELMs.

Immediately after the end of the second ELM crash, at  $t = 25.6$  ms, the heating power is suddenly reduced by roughly 15%. As a result, the pedestal build-up is slowed down and, therefore, the peeling-balloonning precursors become excited later in time, with respect to those for the base simulation. Ultimately, this means that the ELM crash takes place at a later point in time for the case with reduced heating power, and that the ELM repetition frequency is decreased. For the base simulations,  $f_{\text{ELM}} \approx 120$  Hz, and for the simulations with reduced heating power,  $f_{\text{ELM}} \approx 87$  Hz. The magnetic energies of the non-axisymmetric modes for each simulation are shown in figs. 5.7(a) and (b), respectively. From the figures, it is possible to observe that  $E_{\text{mag},n>0}$  are larger for the base simulation than for the simulation with lower heating power. Additionally, the pre-ELM pedestal top pressure is also lower for the case with decreased heating power. The observed direct dependency between the ELM repetition frequency and the heating power provide support to the identification of the simulated ELMs as type-I ELMs.

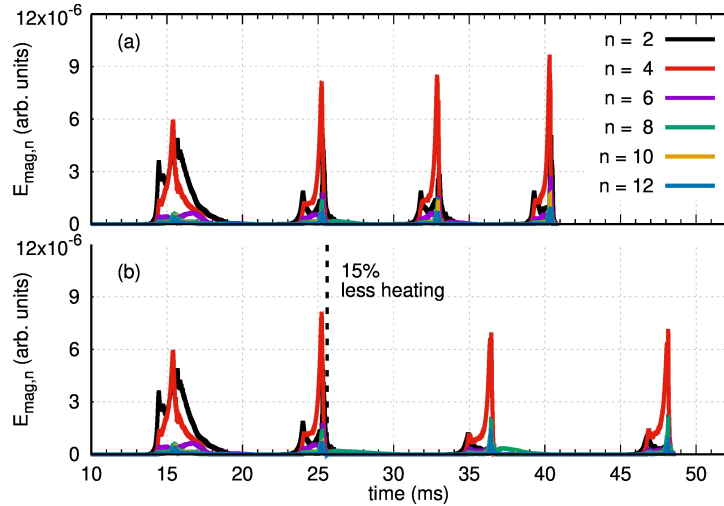


Figure 5.7: Magnetic energies of the  $n > 0$  modes for the base simulation (a), and for a simulation that reduces the input heating power by 15% at  $t = 25.6$  ms. The base simulation is only run until  $t = 40.9$  ms.

### 5.3.4 Varying the scrape-off layer density

Another change performed with respect to the base simulation is to decrease the far SOL density. In the base simulation, the far SOL density is  $n_{e,\text{far-SOL}} \approx 2.0 \times 10^{19} \text{ m}^{-3}$ , and in the modified simulation it is forced down towards  $0.2 \times 10^{19} \text{ m}^{-3}$ . This change may be thought of as reducing the gas fuelling rate. In those terms, type-I ELM My H-mode plasmas are observed to increase  $f_{\text{ELM}}$  together with the fuelling rate in experiments. This happens until a type-III ELM My H-mode is obtained (at high fuelling rates) at high densities [223]. The magnetic energies of the non-axisymmetric modes for the base simulation and for the simulation with 10% of the far SOL density are shown in figs. 5.8(a) and (b), respectively. A very clear reduction of the ELM frequency is obtained with this ‘decrease of the fuelling rate’, which is qualitatively consistent with experiments.

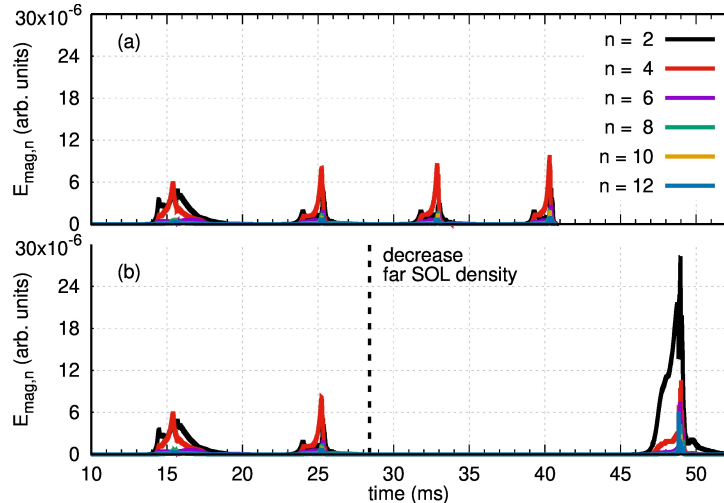


Figure 5.8: Magnetic energies of the  $n > 0$  modes for the base simulation (a), and for a simulation that reduces the far SOL density by 90% at  $t = 28.4$  ms. The base simulation is only ran until  $t = 40.9$  ms.

Together with the significant decrease of  $f_{\text{ELM}}$ , there is a rigid decrease of the pedestal density, but the pedestal temperature and pressure increase. The plasma is stable from the time when the far SOL density was decreased, 28.4 ms, until  $t \approx 45$  ms when an  $n = 2$  peeling-ballooning precursor is destabilised. The differences between the pre-ELM profiles for the base simulation and for the simulation with lower far SOL density are shown in figs. 5.9(a)-(f). The longer inter-ELM duration and the larger pedestal pressure, achieved when reducing the far SOL density, are related to larger stabilising contributions from the faster plasma flows (recall that  $E_r \sim \nabla p_i / n_i$ ), the larger toroidal current density, fig. 5.9(e), and from the inward shift of the pedestal density [200, 201]. The combination of these stabilising effects allows the pedestal to remain stable for a longer period of time. During this time, the pedestal top temperature and pressure continue to increase until the

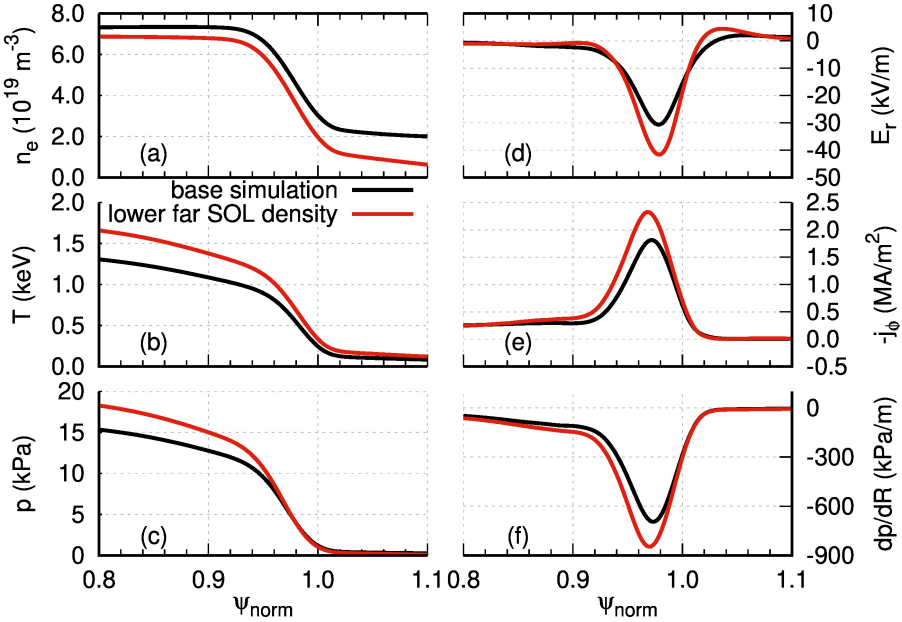


Figure 5.9: Pre-ELM profiles at the outboard midplane for the base simulation and for a simulation that reduces the far SOL density by 90% at  $t = 28.4$  ms. The profiles of density (a), temperature (b), pressure (c), radial electric field (d), toroidal current density (e), and pressure gradient (f) are depicted. The pre-ELM profiles for the base simulation are at  $t = 31.0$  ms, and for the simulation with modified far SOL density at  $t = 47.0$  ms

$n = 2$  peeling-ballooning precursor is excited, which prompts the non-linear ELM onset (at  $t \approx 48$  ms).

## 5.4 ELM triggering mechanism

The peeling-ballooning precursors that precede all simulated type-I ELMs described in this chapter are observed to be responsible for the non-linear onset of the ELM crash. Figure 5.10 shows the sum of the magnetic energies for all the non-axisymmetric modes present during the third ELM from the simulation with nominal heating power and far SOL density. The precursor phase is comprised of three phases. First, an early non-linear phase, where  $n \neq 0$  modes only interact with one-another ( $t \lesssim 31.8$  ms). Second, a brief non-linear saturation phase ( $t \lesssim 32.2$  ms) where the non-axisymmetric modes interact additionally with the  $n = 0$  background plasma. And an explosive (i.e., faster than exponential) growth phase ( $t \lesssim 32.8$  ms) that is referred to as the non-linear ELM onset. The faster than exponential growth during the non-linear ELM onset is depicted by including an exponential and a faster than exponential fitting function in fig. 5.10. The latter shows an adequate fit to the simulation data.

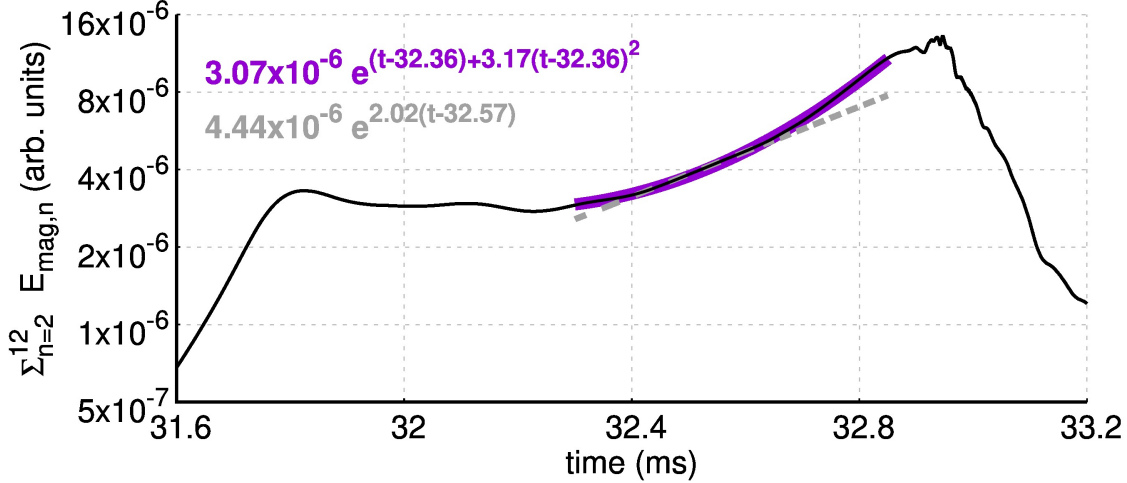


Figure 5.10: Sum of the magnetic energies for all non-axisymmetric modes,  $\sum_{n=2}^{12} E_{\text{mag},n}$ , in the third ELM crash of the simulation with nominal heating power. The precursor phase,  $31.6 \text{ ms} \lesssim t \lesssim 32.8 \text{ ms}$ , starts when the axisymmetric background first becomes altered by the non-axisymmetric modes, and ends when the ELM crash begins.

#### 5.4.1 The role of resistivity – magnetic reconnection

The mechanism that underlies the explosive onset relies on the presence of reconnection of magnetic field lines (which takes place due to non-zero resistivity), and on the resulting separation of time scales between the non-linear evolution of the pressure gradient and the plasma flows. As the precursor amplitude becomes sufficiently large ( $\delta n_e/n_e \sim 1$ ), magnetic reconnection begins to take place in the plasma edge. The increasingly ergodic magnetic field causes a gradual decrease of the pressure gradient at the plasma edge, which can be seen in fig. 5.11(g). Concomitant with this reduction of  $\nabla p$ , the plasma flow slows down in even faster time scales<sup>2</sup>. Figure 5.11(a) shows the Poincaré map of a near-axisymmetric magnetic field throughout the edge region. In the next Poincaré map, one millisecond later, the edge region has become altered due to the non-linear interaction between the non-axisymmetric precursor activity and the axisymmetric background plasma.

#### 5.4.2 Heat and particle transport in stochastic magnetic fields

The ergodic magnetic topology that is prompted during the precursor phase connects flux surfaces located at different radial positions. This, in turn, substantially increases radial diffusion from parallel heat diffusion. As a result, the temperature gradient is rapidly widened and flattened across  $\psi_N \approx [0.92 - 1.00]$ . These changes

<sup>2</sup>It is worth pointing out that the initial stages of the non-linear precursor phase becomes shortened in simulations that include more toroidal mode numbers. However, the fact that the plasma flows slow down faster than  $\nabla p$  remains always present.

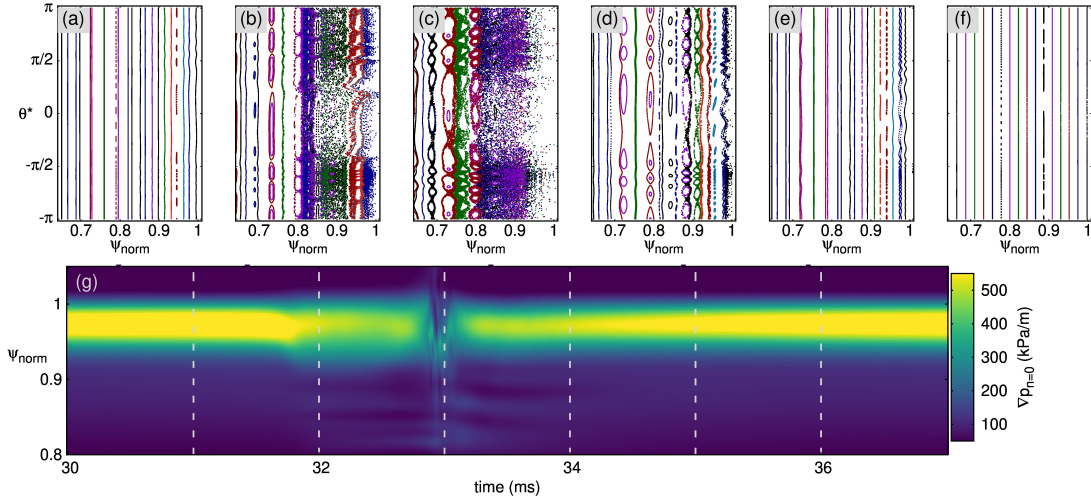


Figure 5.11: Precursor phase, ELM crash, and post-ELM phase showing six Poincaré plots every 1 ms from  $31 - 35$  ms (a)-(f), and the axisymmetric pressure gradient at the outboard midplane (g). The precursor activity starts at  $\sim 31.8$  ms and lasts roughly 1 ms. The poloidal coordinate,  $\theta^*$  equal to 0 at the outboard midplane and  $-\pi/2$  at the magnetic x-point is used.

to the temperature profile translate to  $\nabla p$ , as can be observed in fig. 5.11(g). Diffusion due to ergodic magnetic fields affects the temperature (and its gradient) in a faster time scale than the density (and its gradient) [11]. As a result, the pressure gradient decreases faster than the density. In addition, the radial electric field decreases slower than  $\nabla p$ , as can be seen through the ratio  $E_r/\nabla p$  in fig. 5.12. The current density, which is the second destabilising term, changes in a slower time scale (slower than  $\nabla p$ ) through current diffusion.

The gradual decrease of  $\nabla p$  and  $j$  caused by the precursor activity may seem stabilising at first glance because lower  $\nabla p$  and  $j$  in the pedestal are, from the linear MHD picture, further away from the PB stability boundary. Nevertheless, given that the stabilising effect of the plasma flows decreases faster than  $\nabla p$  and  $j$ , which are destabilising, the non-linear ELM onset is able to occur. The simulation results presented here suggest that the ELM onset is governed by non-linear processes. The monotonic decrease of the ratio  $E_r/\nabla p$  during the precursor phase (labelled in fig. 5.12) implies that the peeling-balloonning modes become less restricted by the stabilising influence of  $E_r$ . Ultimately, this decreasing stabilising effect allows the progressively faster growth of the non-axisymmetric modes and result in the ELM crash. Simultaneously, there is a localised increase of  $\nabla p$  in the simulations due to the precursor activity, and it drives the plasma further into the unstable regime. These effects are self-amplifying [224] and lead to the explosive growth of the perturbations. The effects of the local increase in  $\nabla p$  and of the separation of time scales between stabilising ( $E_r$ ) and destabilising ( $\nabla p$  and  $j$ ) terms play an important role in terms of the non-linear ELM onset. Recent experimental work

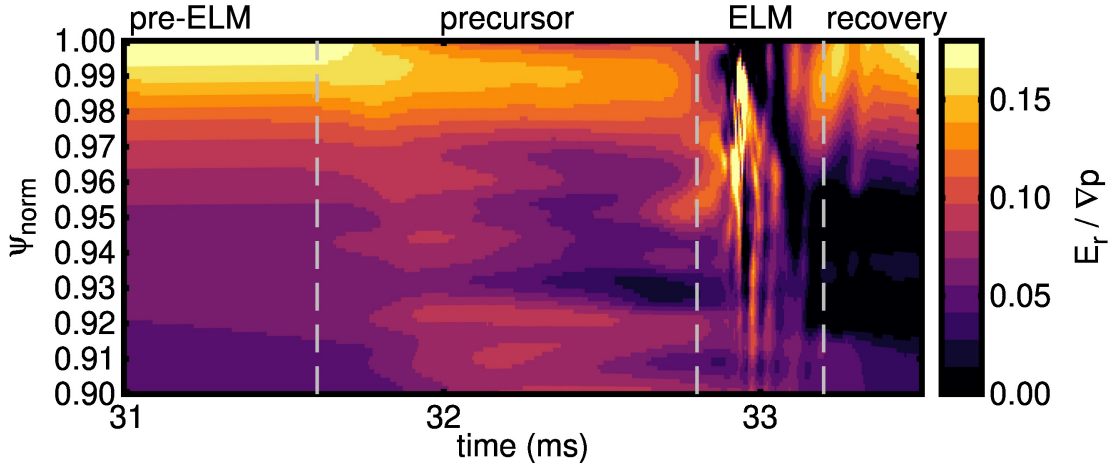


Figure 5.12: Precursor phase, ELM crash, and post-ELM recovery phase showing the ratio between the axisymmetric  $E_r/\nabla p$  at the outboard midplane. The precursor activity starts at  $\sim 31.8$  ms and lasts roughly 1 ms.

from the DIII-D tokamak appears to provide evidence of the non-linear nature of the ELM onset [225].

The explosive growth of peeling-balloonning modes causes the ergodic region to penetrate further inwards, as can be seen between figs. 5.11(b) and (c). The ELM crash is characterised with losses from convective and conductive channels, and it occurs in sub-ms time scales, which are directly comparable to type-I ELMs in experiments [226]. Once the ELM crash phase is finalised, the inter-ELM recovery phase begins. During the inter-ELM phase, the remnant MHD activity from the ELM crash together with medium-n peeling-balloonning modes cause corrugations to the edge magnetic topology, which can be observed in fig. 5.11(d). As described in section 5.3.1, the inter-ELM modes are excited by the pressure gradient and become suppressed as  $E_r$  increases.

It is important to reiterate the fact that the duration of the precursor phase is shortened in simulations that include higher toroidal mode numbers. However, the separation of time scales between the destabilising terms ( $\nabla p$  and  $j$ ) and the stabilising plasma flow (quantified through  $E_r$ ) is also present in said simulations with higher toroidal resolution such that the qualitative observations remain unaffected. The faster time scales obtained with the increased toroidal resolution obviously imply that high toroidal resolution is required in order to quantitatively validate the simulations against experimental results in the future. Code optimisations will allow to do full simulations of several ELM crashes with higher toroidal resolution at different plasma parameters and magnetic configurations. Some simulations with increased toroidal resolution are included in the next chapter.

## 5.5 Conclusions

The simulations presented in this chapter have been published in Ref. [37], and represent the first simulations of type-I ELM cycles in X-point geometry. One important result reported in this chapter is the differences (particularly in terms of the ELM size and duration) between the first ELM crash and the subsequent ELMs. The differences are shown to be related to the seed perturbations that grow to cause the ELM crash. Namely, the arbitrary seed perturbations used to produce the first ELM crash are related to a larger ELM size and a longer duration of the ELM crash with respect to the subsequent ELMs that are borne out of self-consistent seed perturbations. Experimentally, the seed perturbations for type-I ELMs are determined by the remnant MHD activity from the last ELM crash and any potential interplay between said remnant MHD activity, inter-ELM modes, and turbulent micro-instabilities. This result highlights the importance of simulating full ELM cycles in order to predictively assess their impact, e.g., for ITER.

Another important result is the identification of a non-linear electromagnetic mechanism that gives rise to the ELM crash. Peeling-balloonning modes that precede the ELM crash, and are called precursors, cause magnetic reconnection at the edge of the confined region. Such non-linear interaction between the axisymmetric background plasma and the non-axisymmetric modes causes a decrease of the destabilising pressure gradient and current density. In a faster time scale, however, the radial electric field is also reduced. As a result, the stabilising effect of the plasma flows decreases and, together with localised increases of  $\nabla p$  that can locally destabilise high-n peeling-balloonning modes, give way to the explosive ELM onset.

For the simulations reported in this chapter, a single fluid model with two-fluid extensions (diamagnetic drifts) was used. Transport across magnetic field lines due to parallel heat diffusion becomes significantly enhanced in the presence of ergodic magnetic topology. However, ions and electrons have different parallel heat diffusion coefficients. Such two-fluid effect is not included, but may have an influence onto the non-linear ELM onset; the duration of the precursor phase could be altered by taking such effect into account. Experimentally, it has been observed that the inter-ELM recovery of the electron channel is different from the ion channel [110]. Consequently, separating the ion and electron temperatures is foreseen for future work. The cross-field transport of heat and particles in the pedestal is determined from turbulent micro-instabilities and neoclassical effects, and cannot be realistically represented with stationary diffusion coefficients. In that sense, the present simulations consider a simplified pedestal build-up that has to be improved for future predictive simulations of type-I ELM cycles. The ionisation of neutral particles, coming primarily from gas fuelling or recycling, also represents a dynamical effect that is neglected in the present simulations. The influence of such effects can be studied in the future using a fluid neutrals model in JOREK [164, 165] and a kinetic neutrals model accessible now due to the recent development of a kinetic particle module [203].

The simulated type-I ELMs show good agreement with respect to experimental observations in terms of the dominant toroidal mode numbers during the ELM crash ( $n = 2 \dots 4$ ) [211]. Increasing the toroidal resolution maintains the dominant toroidal mode numbers and keeps the same non-linear electromagnetic mechanism for the ELM onset, but shortens the duration of the precursor phase. Additionally, the type-I ELM repetition frequency is observed to decrease when the heating power is reduced in the simulations, as expected for type-I ELMs [28]. The set-up used to simulate type-I ELM cycles presented in this chapter (i.e., by considering how the pedestal crosses the peeling-balloonning boundary) has been used to simulate the triggering of ELMs through the injection of cryogenic deuterium pellets by Ref. [45], as will be discussed in the next chapter.

# 6 Pellet-triggered ELMs

This chapter describes a comparison between JOREK [48–50] simulations of spontaneous ELMs (similar to those shown in the previous chapter) and pellet-triggered ELMs in ASDEX Upgrade (AUG). The spontaneous ELMs were performed as part of this thesis. The triggered ELMs were performed by Shimpei Futatani based on the set-up established for type-I ELM cycles described in the previous chapter and include, for the first time, the effect of the ion pressure gradient-driven diamagnetic flows in pellet-ELM simulations. The approach was to model the injection of cryogenic deuterium pellets at different time points during the pedestal build-up from the previous chapter. A detailed description of the non-axisymmetric activity that is prompted as a result of the pellet injection at different time points is described in Ref. [45]. In particular, the pellet-triggering lag-time that is characteristic of metal-walled tokamaks [43, 44] was qualitatively reproduced in simulations for the first time. Additionally, a direct comparison of the spontaneous and pellet-triggered ELM simulations has been performed as part of this thesis and has been accepted for publication [46].

The present chapter closely follows Ref. [46] and is arranged as follows. A brief introduction of pellet-ELM triggering is detailed in section 6.1. The approach used in JOREK to treat the pellet and the pellet ablation are found in section 6.2. Afterwards, section 6.3 describes the set-up for the pellet-triggered ELM simulations; the spontaneous ELM simulation set-up was described in the previous chapter. A description of individual spontaneous and pellet-triggered ELMs, including a comparison in terms of heat loads to the divertor targets and of the mode structures present, are provided in section 6.4. Several spontaneous and pellet-triggered ELMs are then compared in section 6.5 in terms of relative and absolute energy losses, toroidal mode spectra, and heat fluxes to the divertors. The chapter ends with an outlook to future work and conclusions for this study.

## 6.1 Introduction

Empirical extrapolations to ITER indicate that uncontrolled type-I ELMs would lead to an unacceptably short lifetime of the divertor targets [90, 101]. Several strategies are presently foreseen to mitigate or fully suppress type-I ELMs in ITER (small ELM scenarios like the one described in chapter 4, QH-mode [38], and active control methods with external resonant magnetic perturbations [227] or with pellet-ELM pacing [228, 229]). The operational space for the successful implementation of such mitigation/suppression techniques remains uncertain. For example,

it is possible that ELM control through magnetic perturbations will not be possible throughout a given discharge because of changes to the edge safety factor (particularly during plasma ramp-up and ramp-down). The access conditions of small/no-ELM regimes for ITER also remain uncertain. As such, pellet-ELM triggering is foreseen as a complementary approach/backup scheme and, in particular, it can be instrumental in avoiding impurity accumulation [101]. The idea behind pellet pacing as a mitigation method is motivated by the observation that smaller ELM sizes can be achieved at higher ELM frequencies ( $f_{\text{ELM}}$ ) [230], and it aims at increasing the ELM frequency to the pacing frequency,  $f_{\text{ELM}} \approx f_p$ . Experiments of pellet pacing have shown that it is possible to increase the ELM repetition frequency (beyond the natural ELM frequency) and to reduce the ELM size [228].

Experimental measurements in AUG-C (with a carbon wall) indicated that the pellet-induced seed perturbation was located near the maximum pressure gradient region of the pedestal at the time of triggering the ELM [231]. The generality of several important findings from AUG-C was confirmed in DIII-D [229] and JET [232]. Despite of significant experimental and modelling efforts, important questions remain open for the practical feasibility of pellet-ELM triggering as an ELM control method.

The maximum achievable frequency at which ELMs can be triggered is one open question that can be critical for the successful application of pellet pacing. Experiments in DIII-D have managed to increase the ELM frequency by 12 times the natural ELM repetition frequency,  $12 \times f_{\text{ELM}}^0$ , in a particular scenario [229]. The results obtained in the carbon-walled machine are indeed promising, but experiments in metal-walled machines (AUG with tungsten divertor and walls, and JET with tungsten divertor and beryllium walls) have shown a reduction in the maximum achievable pellet-ELM pacing frequency. Namely, it was observed that an ELM cannot be triggered right after a preceding ELM crash (spontaneous or triggered) has taken place [43, 44, 233]. The time during which an ELM cannot be triggered (by pellet injection) after an ELM crash is denoted pellet-triggering lag-time, or simply lag-time. Understanding the physical mechanisms that govern the lag-time is crucial for the successful conceptualisation of pellet pacing as an ELM control scheme (or as a method to avoid impurity accumulation) in ITER. The reason why the triggering of ELMs through pellet injection is different when the wall material is changed is not clear. However, it has been observed that the pedestal itself is slightly different between the two types of wall material; at equal pressures, metal-walled devices display a higher density and collisionality than carbon-walled machines [234]. Simulations from Ref. [45] have qualitatively reproduced the lag-time for the first time. A subset of said simulations (only pellet injections that triggered ELMs) was analysed in Ref. [46] and is presented in this chapter.

Another important question that remains open, with respect to pellet pacing as an ELM control mechanism, deals with the heat flux distribution onto the divertor targets. Achieving an increase of the ELM repetition frequency by a factor of, for example, 2 ( $f_{\text{ELM}} = 2f_{\text{ELM}}^0$ ) does not necessarily mean that the ELM energy fluence

will be similarly reduced. Experimental observations suggest that pellet-triggered ELMs deposit their associated energy onto a narrower area, denoted wetted area, than spontaneous ELMs [102]. Whether or not the beneficial impact of an increased  $f_{\text{ELM}}$  will be cancelled in ITER by a reduction of the wetted area can be predictively investigated in the future with non-linear extended MHD simulations.

This chapter presents JOREK simulations of pellet-triggered and spontaneous ELMs in AUG. The ELM simulations consider the same parameters and, therefore, are directly comparable. Pellets of two different sizes are injected at different times before a spontaneous ELM crash takes place, i.e., during an inter-ELM phase. The spontaneous ELM simulations follow the set-up described in the previous chapter and in Ref. [37]. The resistivity used in these simulations is within the error bars of the neoclassical resistivity. Similarly, the parallel heat diffusion coefficient is set to the realistic Spitzer-Härm values. The pedestal build-up is characterised by evolving edge gradients, and the evolving ion pressure gradient-driven diamagnetic flow and bootstrap current density are considered.

## 6.2 Pellet module in JOREK

As a pellet is injected into the plasma, it starts to ablate<sup>1</sup>, the ablated particles get ionised and act as a localised density source. To model the effect of injecting a pellet into the plasma, a pellet module can be used in JOREK. The physical effects related to the ablation of the pellet particles are not modelled with JOREK because it would be computationally too expensive<sup>2</sup>. The pellet module considers a localised volumetric density source that moves along the pellet trajectory and deposits the pellet particles to the plasma. The 3D source is localised to a narrow poloidal area, and it stretches along a toroidal arc that is defined by the user. The density source is adiabatic and, as such, no energy source/sink is related to it.

The number of particles that are deposited in the bulk plasma at a given time is determined with a neutral gas shielding model. The model depends on the instantaneous pellet size, local plasma temperature and density. The trajectory of the pellet is defined by a straight line, and it maintains a constant velocity throughout its lifetime (the pellet is stripped of all its particles at the time of full ablation). The assumption of constant velocity is supported by experimental observations in AUG [231]. For an in-depth description of the pellet module used, the reader is referred to Refs. [50, 76]. During the pellet ablation, the adiabatic volumetric density source causes a localised increase of the plasma density, which stretches along the magnetic field lines. As a direct result, the plasma temperature is decreased in the same volume, and the pressure remains constant. Nevertheless, parallel heat conduction causes the temperature in each flux surface to rapidly

---

<sup>1</sup>In this context, ablation refers to the physical processes responsible for the erosion of particles located in the surface of the pellet.

<sup>2</sup>The spatial scales relevant for the ablation process are much smaller than for the MHD instabilities, and the processes that govern the pellet ablation can only be described kinetically.

equilibrate (in a time scale defined by  $\tau_{\chi_{\parallel}} = (2\pi Rq)^2/\chi_{\parallel} \sim 0.1 \mu\text{s}$ ). The density plasmoid also becomes redistributed in a given flux surface, but in a slower time scale governed by parallel convection at the ion sound speed ( $\tau_s = 2\pi Rq/c_s \sim 1 \text{ ms}$ ). As a result of the temporal asymmetry between the redistribution of density and temperature in a flux surface, the plasma pressure observes a net increase in the volume defined by the density plasmoid. The excess pressure that results from the pellet ablation is associated with high pressure gradients. As such it can excite ballooning modes and, ultimately, lead to a pellet-triggered ELM.

### 6.2.1 Previous pellet-triggered ELM JOREK simulations

An overview of ELM simulations (with JOREK and other non-linear MHD codes) was provided in section 3.3. Pellet-triggered ELMs were first studied with JOREK by considering a localised stationary density source [75]. Later, simulations which used a density source moving along the pellet trajectory were used to study pellet-triggered ELMs in DIII-D [76]. The excitation of high- $n$  peeling-balloonning modes was determined to be always present in cases that showed ELMs triggered by pellet injection. More recently, a comparison between JOREK simulations of a spontaneous ELM and a pellet-triggered ELM in JET has been reported together with experimental comparisons [103]. For said simulations, the pellet was injected to an already unstable pedestal. However, the more interesting comparison is between a spontaneous ELMs and an ELM triggered by a pellet injected to a stable plasma because it represents a more realistic scenario in terms of pellet-ELM triggering as an ELM control method. Said comparison is the topic of the present chapter.

## 6.3 Simulation set-up and parameters

It was shown in the previous chapter (in 5.3.2) that the seed perturbations that act as initial conditions for a spontaneous ELM crash influence the ELM size and duration. The first three ELM crashes from the type-I ELM cycles shown in section 5.2 are compared against pellet-triggered ELMs in this chapter. Additional simulations of type-I ELM cycles with higher toroidal resolution were performed for this thesis, and were published in Ref. [46], are also included in the comparison. The set-up for the spontaneous ELMs was described in the previous chapter. To avoid unnecessary verbosity in the text, the spontaneous ELMs are labelled depending on the toroidal mode numbers present in the given simulation. Spontaneous ELMs have been simulated with different sets of toroidal mode numbers:  $n = 0, 2, 4, \dots, 12$ ,  $n = 0, 3, 6, \dots, 15$ ,  $n = 0, 3, 6, \dots, 18$ , and  $n = 0, 2, 4, \dots, 20$ . Using the periodicity ( $n_{\text{period}}$ ) and the highest toroidal mode number included in the simulation ( $n_{\text{max}}$ ), the naming scheme for the  $j^{\text{th}}$  spontaneous ELM in a series of ELM cycles is  $\text{Sp-}n_{\text{period}}n_{\text{max}}.j$  and will be used throughout the text. Density, temperature, and pressure profiles at the outboard midplane are shown in fig. 6.1 at four different times during the pedestal build-up. The label  $\text{Sp-}318.1$  is the

pre-ELM pedestal right before the onset of the first ELM crash from a simulation with  $n_{\text{period}} = 3$  and  $n_{\text{max}} = 18$ , and it corresponds to roughly 16 ms.

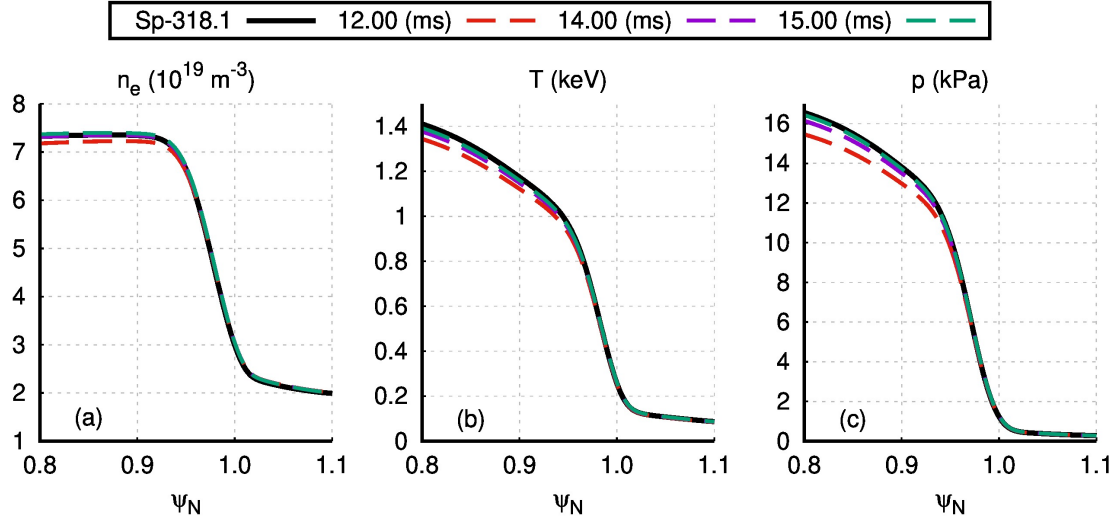


Figure 6.1: Density, temperature, and pressure profiles at the outer midplane right before the onset of an spontaneous ELM (full lines) and at the three different times where pellets are injected (dashed lines). Injection at earlier times is described in Ref. [45].

Spontaneous ELM simulations with  $n_{\text{period}} = 3$  and  $n_{\text{max}} = 24$  and 30 have also been produced. These are not included in the present comparisons because only the first ELM crash in the series was simulated due to the high computational costs. The simulations with  $n_{\text{max}} \geq 15$  are converged in terms of the temporal, toroidal and poloidal resolution<sup>3</sup>. The  $n_{\text{max}} = 12$  simulations, on the other hand, do not capture peak heat fluxes and integrated energy fluence accurately despite showing qualitatively identical dynamics compared to the simulations with higher resolution. For this reason, such simulations are not used in all the comparisons.

### 6.3.1 Pellet injection – sizes and trajectory

The pellet injection system in AUG is set to an injection angle of  $72^\circ$ , which is used to determine the pellet trajectory in the simulations (all simulations share the same pellet trajectory). Pellets with  $1.5 \times 10^{20}$ ,  $2.4 \times 10^{20}$ , and  $3.7 \times 10^{20}$  deuterium atoms, and injection velocities of  $v_p = 240, 560, 900$ , and  $1040$  m/s are possible<sup>4</sup>. For the simulations shown here, the pellet injection velocity is fixed to  $v_p = 560$  m/s. The pellet injection system includes a guide tube through which the accelerated pellet travels until reaching the scrape-off layer (SOL) and then the

<sup>3</sup>The relative error in the ELM-related energy losses between the first ELM crash simulated with  $n = 0, 3, 6, \dots, 18$  and  $n = 0, 3, 6, \dots, 30$  is approximately 4%.

<sup>4</sup>Not all combinations of pellet size and injection velocity are experimentally accessible.

confined plasma. Material is lost as the pellet travels through the guide tube, so a fraction of the original pellet content actually exit the guide tube. For a pellet injection velocity of 560 m/s, it has been observed that roughly half of the pellet content actually reaches the plasma [235]. For the simulations, pellets containing  $0.8 \times 10^{20}$  and  $1.5 \times 10^{20}$ D atoms, which can be compared with experimental pellets of  $\sim 1.6 \times 10^{20}$  and  $\sim 3.0 \times 10^{20}$ D atoms, respectively, are considered. Namely, the injected pellets have sizes that are experimentally relevant. For simplicity, throughout the text, the pellet with  $0.8 \times 10^{20}$ D atoms is referred to as the ‘small’ pellet, and the one with  $1.5 \times 10^{20}$ D is the ‘large’ pellet.

The surface area of the pellets depends on their particle content as constant particle density and a spherical shape are assumed for the pellets. A larger surface area is then related to a higher ablation rate. The large pellet is injected at 12 and 14 ms, which correspond to  $\sim 4$  and  $\sim 2$  ms before the spontaneous ELM onset. The small pellet is injected at 12, 14, and 15 ms. The toroidal mode numbers simulated for all the pellet-triggered ELMs was  $n = 0, 1, 2, \dots, 12$ . In order to model the pellet injection it is not possible to choose a periodicity different than unity because  $n = 1$  is generally the dominant mode number [76, 103]. The  $n = 12$  toroidal mode number is already strongly sub-dominant in these simulations, as can be seen in fig. 21 of Ref. [103], which justifies this choice. As it was done for the spontaneous ELMs, a naming convention is also used for the pellet-triggered ELMs. For an ELM triggered by a pellet containing  $1.5 \times 10^{20}$ D atoms injected at 14 ms (the case shown in fig. 6.2), the tag is **Tr-15-14ms**. A small pellet ( $0.8 \times 10^{20}$ D atoms) injected at 12 ms is **Tr-08-12ms**. It is reiterated that the pellet-triggered ELMs were simulated by Shimpei Futatani (Ref. [45]) based on the set-up described in the previous chapter.

Poloidal cross sections of the electron number density ( $n_e$ ) at the toroidal angle of pellet injection ( $\phi = 0$ ) at three different times are depicted in fig. 6.2 to show the influence of a large pellet injected into the plasma at 14 ms (i.e., **Tr-15-14ms**). The pellet trajectory is shown in black dashed lines and is the same for all cases. The first frame (left) shows the plasma at 14.06 ms, 60  $\mu$ s after the pellet is injected, when the pellet has crossed the separatrix and is located at a flux surface of  $\psi_{N,p} = 0.977$ . Other than the locally increased density due to the pellet, no observable deviations from the background plasma are visible. The pellet then excites an ELM at  $\sim 14.09$  ms; at that time, the pellet is located at  $\psi_{N,p} = 0.958$ . The middle and right plots in the figure show  $n_e$  during the ELM crash, at 14.22 ms and 14.38 ms, respectively. Strong perturbations ( $\delta n_e/n_e \sim 1$ ) are visible outside of the pellet location, i.e.,  $\psi_N > \psi_{N,p} (= 0.872)$  for the middle plot. It is worth mentioning that the MHD activity that is triggered due to the pellet injection causes particle losses from the confined region. Consequently, the total particles enclosed in the confined region after the time of full pellet ablation does not correspond exactly to the pre-injection content plus the number of particles in the pellet.

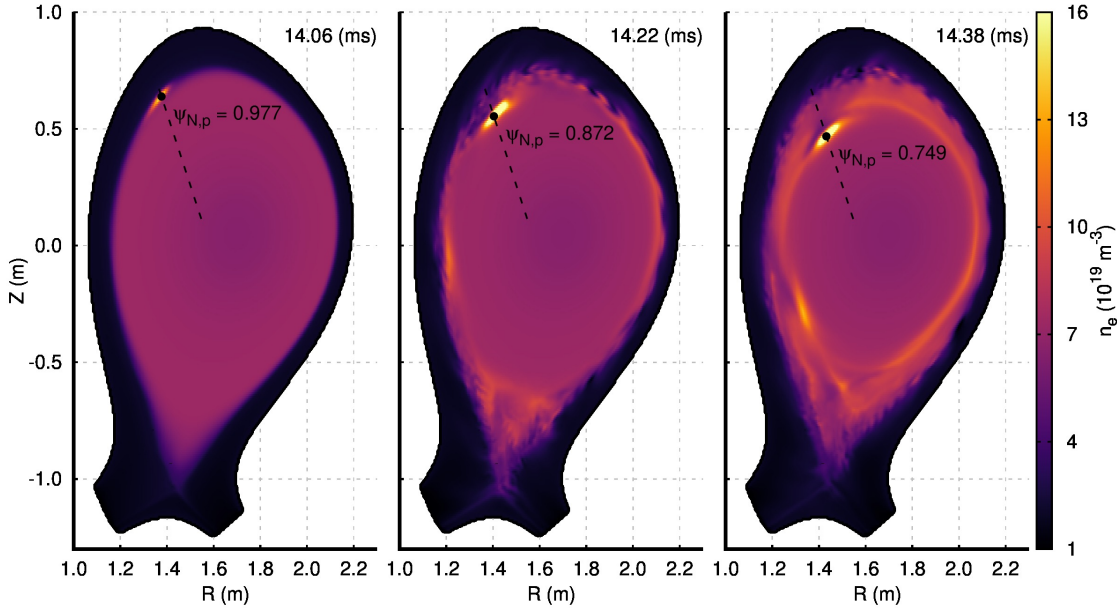


Figure 6.2: Poloidal cross sections of the density at 3 time points resulting from a large pellet injected at 14 ms. The density plasmoid moves along the pellet trajectory (dashed black line) is redistributed through parallel convection. The normalised flux at the pellet location for the different times are  $\psi_N = 0.977$ , 0.872, and 0.749.

## 6.4 Spontaneous and pellet-triggered ELMs

The time evolution of a spontaneous ELM (Sp-318.1) and of a pellet-triggered ELM (Tr-08-14ms) are shown in subsections 6.4.1 and 6.4.2, respectively. These representative ELM crashes of spontaneous and triggered nature are described in terms of the magnetic energies of the non-axisymmetric perturbations, divertor incident power, the pre- and post-ELM profiles, the magnetic topology before, during, and after the ELM, among other things. A comparison of the ELM energy fluence of Sp-318.1, Sp-318.2, and Tr-08-14ms is shown in subsection 6.4.3. Finally, the non-axisymmetric mode structures during the spontaneous and pellet-triggered ELM crashes are compared between in subsection 6.4.4. Section 6.5 then shows a systematic comparison between all spontaneous and pellet-triggered ELMs,

### 6.4.1 Spontaneous ELMs

A spontaneous ELM simulated with  $n = 0, 3, 6, \dots, 18$  is described in this section. In particular, the first ELM from a series of 3 ELMs is chosen, Sp-318.1. The pre-ELM density, temperature, and pressure profiles for this ELM crash are shown in figs. 6.1(a)-(c). The onset of Sp-318.1 takes place at  $\sim 16$  ms, as can be seen in fig. 6.3(a), which shows the evolution of the  $n \neq 0$  magnetic energies. Before

the ELM crash, the stored thermal energy is 421 kJ and is reduced to 388 kJ as a result of the ELM. That is, an ELM size of  $\Delta W_{\text{ELM}} = 33 \text{ kJ}$ , and a relative ELM size of  $\Delta E_{\text{ELM}} = \Delta W_{\text{ELM}}/W_{\text{pre-ELM}} \approx 7.8\%$ . Resulting from the ELM, the power incident onto the inner and outer divertor targets is sharply increased up to maximum values of  $22.2 \text{ MW/m}^2$  and  $43.8 \text{ MW/m}^2$ . The effect of the ELM crash onto the inner/outer divertor incident power and the maximum value of the pressure gradient (toroidally averaged value at the outer midplane) are shown in figs. 6.3(b) and (c), respectively.

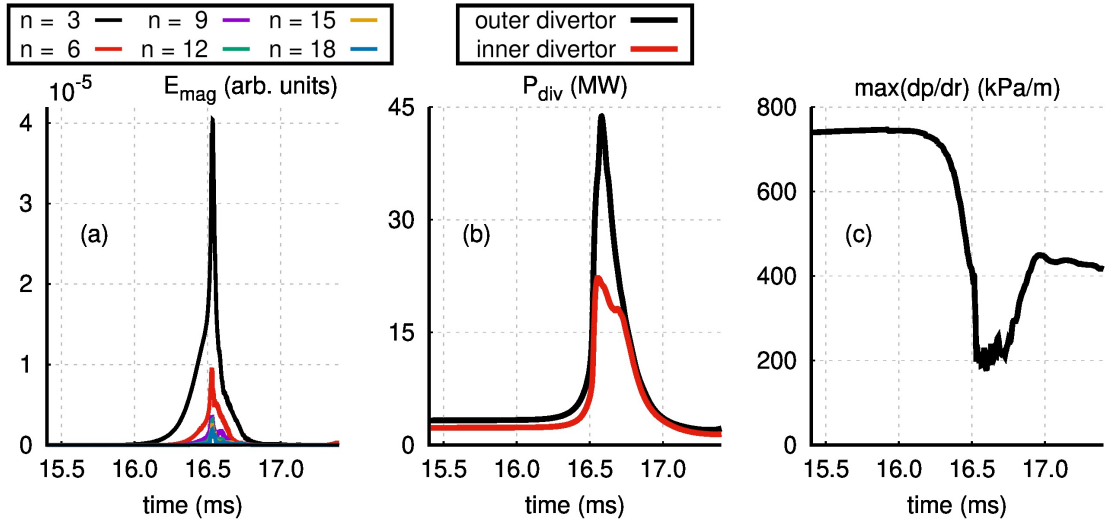


Figure 6.3: Temporal dynamics of Sp-318.1: magnetic energies of the non-axisymmetric perturbations (a), the power that is incident onto the inner and outer divertor targets (b), and the toroidally averaged outer midplane maximum pressure gradient (c). The temporal evolution is shown over 2 ms, and it spans from 15.4 to 17.4 ms.

The heat flux onto the divertor target is  $q(t, s, \phi)$ , where  $t$  is time,  $s$  is the target length and the toroidal angle is  $\phi$ . Integrating the heat flux over the divertor area determines the incident power,  $P_{\text{div}}$ . Experimentally, it is observed that during type-I ELMs there is power asymmetry between the power incident onto the inner and outer divertors. For single null magnetic configurations with the ion  $\mathbf{B} \times \nabla B$  drift pointing towards the active X-point (like the simulations shown here), the inner divertor receives more power than the outer divertor,  $P_{\text{div,in}} > P_{\text{div,out}}$  [236]. In simulations that do not include diamagnetic effects, the outer divertor receives almost all the energy expelled by the ELM [65]. In all the simulations presented in this chapter, the asymmetry is opposite to the experimental observations:  $P_{\text{div,out}} > P_{\text{div,in}}$ . The discrepancy in terms of the power asymmetry is not completely understood, but it could be related to the single fluid temperature, the simplified SOL model, or the temperature dependent viscosity used for the present simulations. Nonetheless, the simulations shown in this chapter qualitatively recover the experimental obser-

vation of the reduced wetted area between pellet-triggered ELMs and spontaneous ELMs.

The pressure gradient becomes affected by the precursors and thereafter it crashes rapidly due to the violent ELM crash. The two different phases can be seen in fig. 6.3(c) where the maximum LFS midplane pressure gradient (averaged toroidally) is shown: precursor phase  $t \approx (16.0, 16.5)$  ms and violent crash  $t \approx (16.5, 16.7)$  ms. After the ELM crash, there is a short recovery phase (until  $\sim 17.0$  ms) that is temporarily interrupted by the onset of medium-n peeling-balloonning inter-ELM modes (described in section 5.3.1). After this interruption in the  $\max(\nabla p)$  growth, the inter-ELM modes are suppressed, and the pedestal builds-up further (not shown). The pre- and post-ELM profiles of density, temperature, and pressure can be observed in fig. 6.4(a)-(c). One time point is chosen for the pre-ELM phase, and three time points for the post-ELM phase.

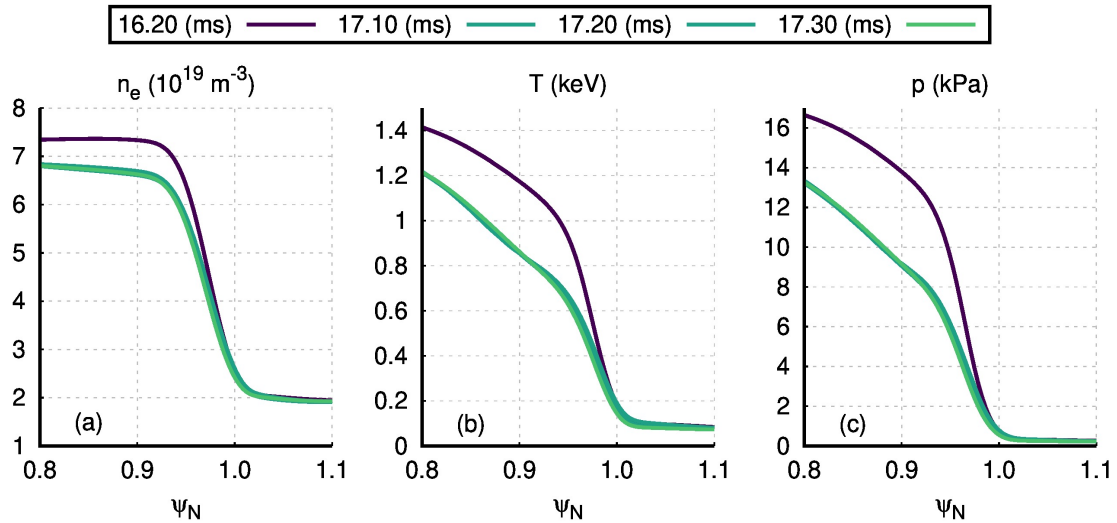


Figure 6.4: LFS midplane profiles of the density (a), temperature (b), and pressure(c) at a single toroidal angle before and after Sp-318.1. Only one time point is chosen for the pre-ELM phase and three for the post-ELM phase.

Figure 6.5 shows the magnetic topology during the ELM through Poincaré plots that cover the radial extent  $\psi_N = [0.8, 1.0]$  and the y-axis is the poloidal angle  $\theta^*$ , which is 0 at the midplane and increases(decreases) going counter-clockwise(clockwise). Seven time points are chosen with respect to the time of peak incident power to the outer divertor ( $t_0 = t_{\max(P_{\text{div,out}})}$ ). For Sp-318.1,  $t_0 = 16.57$  ms, and the chosen time points are equally spaced by 0.04 ms from  $t_0 - 0.22$  ms up to  $t_0 + 0.02$  ms. The procedure used to produce the Poincaré plots was to follow 400 magnetic field lines, with different initial positions (radially and poloidally), for 3000 toroidal turns each. A point is produced each time the magnetic field line crosses the  $\phi = 0$  plane. Field lines are plotted with different colours to visualise the ergodisation of the magnetic field by the ‘mixing of colours’.

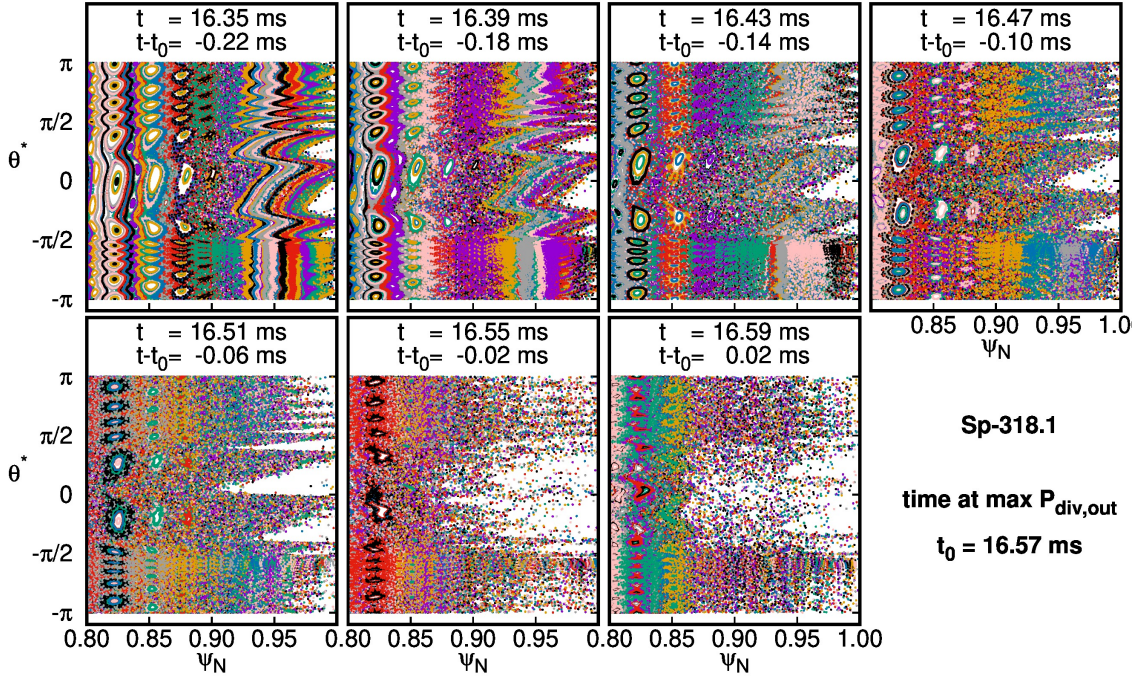


Figure 6.5: Poincaré plots for 7 different time points. The times are equidistant by 0.04 ms and are chosen with respect to the time of maximum power incident onto the outer divertor target,  $t_0 = 16.57$  ms. The influence of the precursors onto the edge magnetic topology can be seen even in the earliest time point (top left plot). The white region at the very edge relates to short connection length, and it penetrates further inward (until  $\psi_N \approx 0.87$  in the last two times) as a result of the ELM onset.

At  $t - t_0 = -0.22$  ms, the amplitude of the non-axisymmetric perturbations is already large, as can be observed in fig. 6.3(a), and from the magnetic field topology in the corresponding Poincaré plot. The significant deformation of the flux surfaces at the plasma edge ( $\psi_N \gtrsim 0.88$ ) induces cross-field transport due to parallel heat diffusion, as discussed in detail in section 5.4. Further inside,  $\psi_N \approx (0.8, 0.9)$ , magnetic islands at the rational surfaces  $q = 11/3, 12/3$ , and  $13/3$  can be observed. The amplitude of the perturbations increases in the next times (see top row in fig. 6.5) and, in turn, the ergodic topology penetrates further inside the confined region. In the last two time points, there is a large increase in the ergodic (white) region which is caused by the ELM crash. The field lines in the outermost 13% of the confined region reach the divertor with a short connection length, particularly in the LFS:  $\theta^* \approx (-\pi/2, \pi/2)$ .

The Poincaré plots feature elongated structures in the outer region. These structures cause a splitting of the strike lines that impinge onto the inner and outer divertors. The splitting of the main strike line into secondary strike lines is observed experimentally [236, 237]. At  $t_0 = t_{\max(P_{\text{div,out}})} = 16.57$  ms, the outer divertor heat

flux as a function of the toroidal angle and the target length is shown<sup>5</sup> in fig. 6.6. The splitting of the main strike line can be indirectly evidenced from the slanted secondary peaks in the heat flux profile that sweep from top to the bottom.

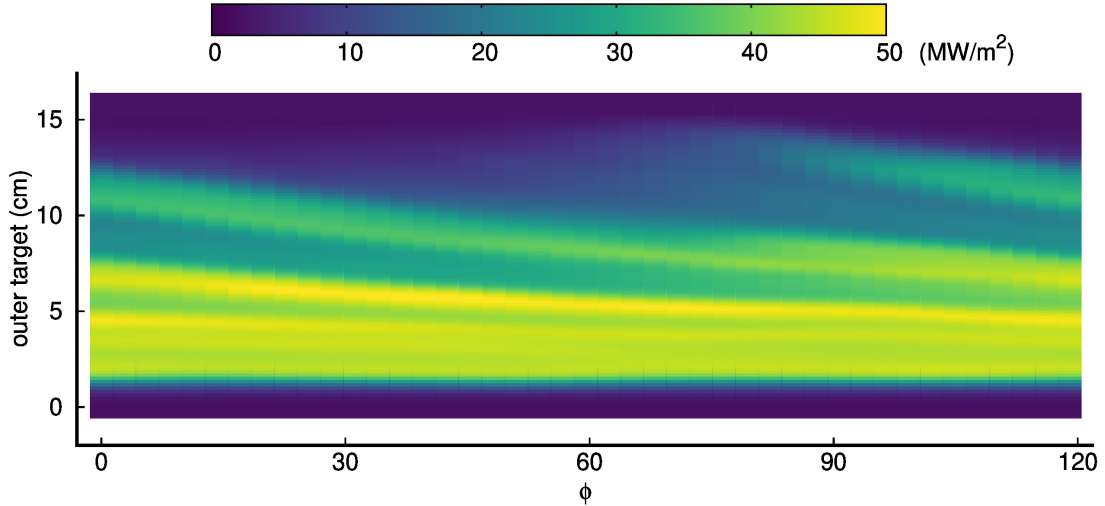


Figure 6.6: Heat flux impinging in the outer divertor at  $t_0 = 16.57$  ms for Sp-318.1. The footprint generated by several strike lines can be seen as distinct peaks. The wetted area of the heat flux profile at this time is  $A_{\text{wet}} \approx 0.95$  m $^2$ .

The area over which the heat flux is distributed can be quantified with the wetted area,

$$A_{\text{wet}} = \frac{\int_0^{2\pi} \int q(s, t = t_0) ds R d\phi}{\max(q(s, t = t_0))} = \frac{P_{\text{div}}(t = t_0)}{\max(q(s, t = t_0))}.$$

For Sp-318.1, the outer divertor wetted area is  $A_{\text{wet}} \approx 0.95$  m $^2$  at  $t_0$ . The wetted area that is obtained during the type-I ELM is directly influenced by the number of strike lines.

#### 6.4.2 Pellet-triggered ELMs

A pellet-triggered ELM is now described much in the same way as it was done for the spontaneous ELM Sp-318.1. The ELM that is described here is triggered by a small pellet (i.e., with  $0.8 \times 10^{20}$  D atoms) injected at 14 ms: Tr-08-14ms. The toroidal modes present in all the simulations with pellet injection are  $n = 0, 1, 2, \dots, 12$ . The  $n = 1$  has to be included in the pellet-triggered ELM simulations because it is the most energetic mode in such simulations [76, 178]. Immediately before the pellet is injected onto the plasma, the stored energy is 416 kJ. Tr-08-14ms expels roughly 18 kJ, which corresponds to a relative ELM size of  $\Delta E_{\text{ELM}} \approx 4.4\%$ , which is

<sup>5</sup>The range of  $\phi$  is restricted to  $\phi = [0 - 120]^\circ$  because this simulation has  $n_{\text{period}} = 3$ , i.e., one third of the tokamak.

smaller than the spontaneous ELM described before. The magnetic energies of the  $n \neq 0$  modes, the inner/outer divertor incident power, and the maximum pressure gradient (toroidally averaged), are shown in fig. 6.7(a)-(c). The same axes scales for all three quantities remains unchanged with respect to fig. 6.3, thus allowing for a direct comparison.

Resulting from the pellet injection, the  $n = 1$  mode is dominant, as is generally the case for simulations with pellet injection [76, 178], and which has also been observed experimentally [238]. Indeed, the  $n = 1$  energy increases when the pellet is injected, and the higher toroidal mode numbers start growing as a result. The high- $n$  modes growth is then accelerated by the excitation of ballooning modes both in the HFS and LFS. Figure 6.8 shows the pressure profile along the pellet trajectory for five different time points. The first time point is the time of injection. The next time point, 100  $\mu\text{s}$  later, shows a localised increase of pressure resulting from the pellet injection. The pellet and the local pressure increase, continue to penetrate further inwards with time. The ballooning modes at the HFS are excited directly by the localised plasmoid, which results in large  $\nabla p$  parallel to the curvature vector, which can be seen in fig. 6.8; in the absence of pellet injection  $\nabla p$  in the HFS is always anti-parallel to the curvature vector<sup>6</sup>. An ELM is triggered because of it, and it causes a fast collapse of the pressure pedestal and a sharp increase in the divertor incident power, as seen in figs. 6.7(c) and (b), respectively. The peak power that is incident onto the inner/outer divertors are 10.8 and 20.2 MW.

The pellet starts its trajectory at  $(R, Z) = (1.365, 0.674)$  m, which is outside the separatrix in  $\psi_N = 1.019$ . The radial position where  $\nabla p$  is maximised is  $\sim 4.5$  cm along the pellet trajectory, at  $\psi_N \approx 0.97$ . Given that the pellet injection velocity is  $v_p = 560$  m/s, 80  $\mu\text{s}$  are required for the pellet to reach  $\max(\nabla p)$ . The density, temperature, and pressure profiles right before the pellet is injected (13.8 ms) are plotted in fig. 6.9 together with post-ELM profiles for Tr-08-14ms and for two spontaneous ELMs: Sp-318.1 and Sp-318.2. The pellet location in terms of  $\psi_N$  at different times (equidistant by 40  $\mu\text{s}$ ) is also shown with blue arrows. The post-ELM density profiles observe a net increase after Tr-08-14ms due to the particle source related to the pellet ablation. The temperature and pressure pedestals, on the other hand, crash similarly to the spontaneous ELMs Sp-318.1 and Sp-318.2. The slightly higher post-ELM pressure pedestal of the pellet-triggered ELM, with respect to the spontaneous ELMs, is related to the higher density pedestal.

---

<sup>6</sup>Pressure gradient-driven instabilities require the pressure gradient and the curvature vector (which always points to the centre of the device) to be parallel in order to be destabilised, as explained in section 2.3

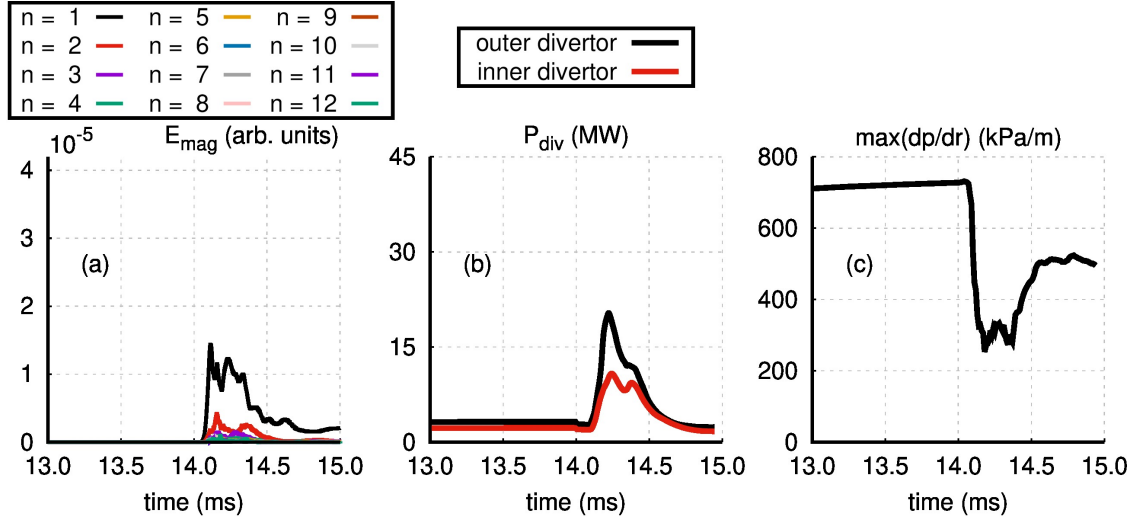


Figure 6.7: Temporal dynamics of Tr-08-14ms: magnetic energies of the non-axisymmetric perturbations (a), the power that is incident onto the inner and outer divertor targets (b), and the toroidally averaged outer midplane maximum pressure gradient (c). The temporal evolution is shown over 2 ms, and it spans from 13.0 to 15.0 ms in all three plots.

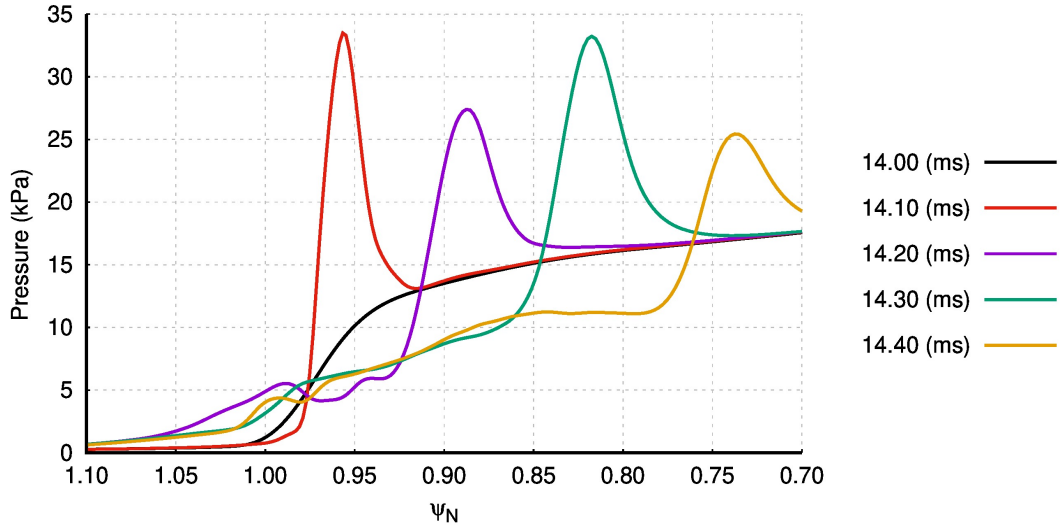


Figure 6.8: Profiles of the pressure along the pellet trajectory (in the toroidal angle of injection,  $\phi = 0$ ). The effect of the moving plasmoid onto the pressure profile is clear. The curvature vector is parallel to the pressure gradient at the right of the plasmoid. The pre-ELM profile is depleted by the ELM, which takes place roughly at  $t - t_{\text{inj}} = 0.1$  ms.

In direct comparison to fig. 6.5, Poincaré plots are produced for Tr-08-14ms for seven different times, and are shown in fig. 6.10. The time points are equidistant

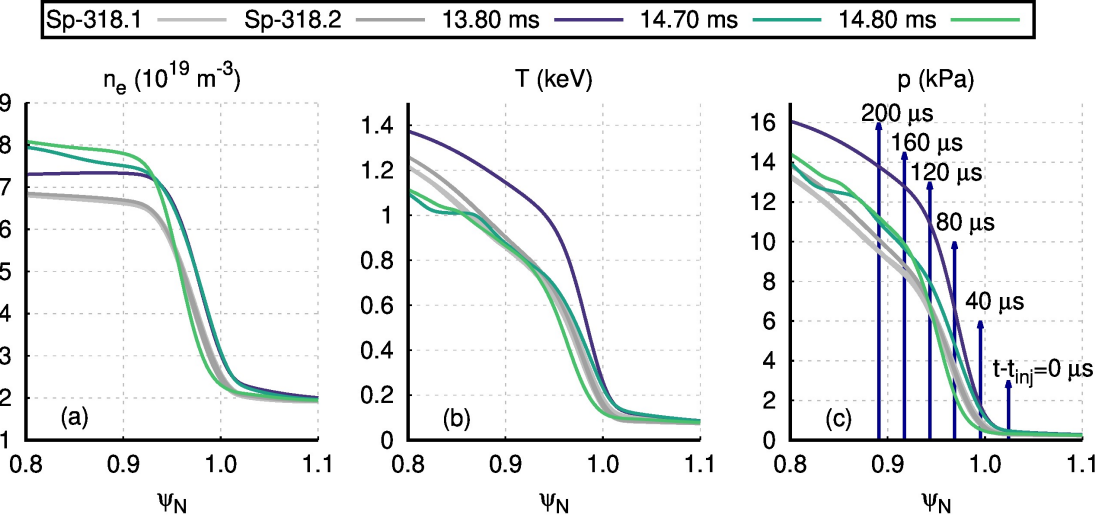


Figure 6.9: Pre- and post-ELM LFS midplane profiles of the density (a), temperature (b), and pressure (c) at  $\phi = 0$  for Tr-08-14ms. Post-ELM profiles from two spontaneous ELMs (Sp-318.1 and Sp-318.2) are shown. The pellet location (in terms of  $\psi_N$ ) is included in the pressure plot. The post-ELM density in the triggered ELM is higher to the spontaneous ELM because of the particle source coming from the pellet ablation.

by 0.04 ms, and are chosen with respect to  $t_0 = t_{\max(P_{\text{div,out}})} = 14.22$  ms in the same way described for Sp-318.1. The first time point corresponds to the time of pellet injection,  $t = 14.0$  ms. These figures visualise the magnetic topology changes resulting from the pellet injection. The first time slice shows a near-axisymmetric magnetic topology with field lines staying on their respective flux surfaces. In the next time slice, 0.04 ms later, the pellet has crossed the separatrix and it is located at  $\psi_N = 0.995$  (fig. 6.9(c)). The flux surfaces have not broken, but there is a slight deviation from axisymmetry, which is most pronounced at the outermost flux surfaces. At  $t - t_0 = -0.14$  ms, in the third frame, the pellet has reached  $\psi_N = 0.969$ . This frame is the last one that clearly shows the magnetic perturbation induced by the pellet, and not the combined effect of the pellet perturbation plus the excited MHD activity. From the separatrix until the pellet position, magnetic reconnection has begun to take place (as evidenced by the ‘mixing of colours’). In the fourth frame (top, right), the pellet has penetrated until  $\psi_N = 0.943$ , but it is not possible to differentiate any more between the pellet-induced perturbation and the MHD activity. It is evident that the region that features magnetic reconnection seeps further inward than the pellet position. At this point in time, the pedestal region (in particular in the LFS) features a short connection length to the divertors, and the confining magnetic field degrades even further in the next three time slices (as can be inferred from the increased white region).

Resulting from the pellet-triggered ELM, the expelled energy is deposited onto

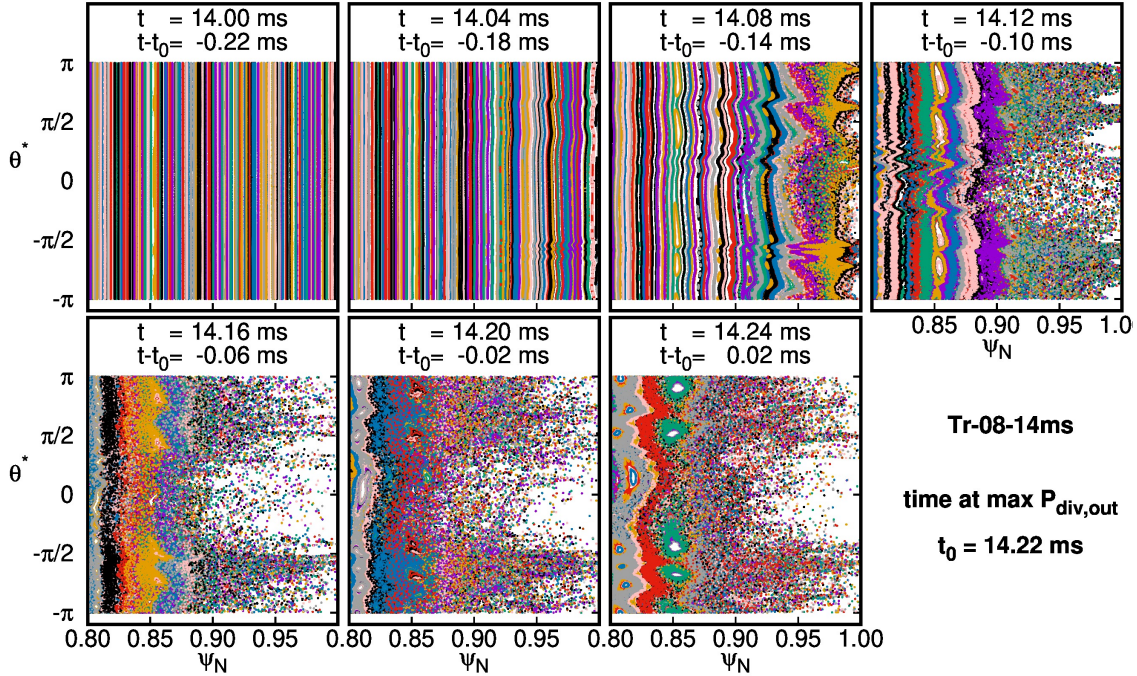


Figure 6.10: Poincaré plots for 7 different time points. The times are equidistant by 0.04 ms and are chosen with respect to  $t_0 = 14.22$  ms. Closed flux surfaces (top left) quickly degenerate as the pellet penetrates into the confined region. Between  $t = 0.08$  ms and 0.12 ms, the ELM onset takes place and there is clear evidence of reconnection taking place. The ergodic region penetrates further inward as the ELM crash develops (bottom row), and short connection length to the divertor targets is evidenced by the white region.

the inner and outer divertor targets in a non-axisymmetric pattern. In the same way as Sp-318.1 (and all the ELMs simulated for this study), less energy impinges onto the inner divertor than onto the outer divertor. The heat flux onto the outer divertor at  $t = t_0 = 14.22$  ms can be seen in fig. 6.11. In contrast to the heat flux deposition pattern from the spontaneous ELM (fig. 6.6), the peak heat flux from Tr-08-14ms is weaker, and there are only two stripes that display large heat fluxes. The main stripe is related to the primary strike-line (located at  $\sim 2$  cm), and the second stripe comes from a secondary strike-line that sweeps from top to bottom and is maximised roughly at  $240^\circ$ . The latter rotates slowly along  $\hat{\phi}$ , and it is characterised by an  $n = 1$  helical perturbation.

As a consequence from the fewer number of (secondary) strike-lines observed in the heat flux deposition pattern for Tr-08-14ms, with respect to Sp-318.1, the wetted area is reduced. In particular, the spontaneous ELM features  $A_{\text{wet}} \approx 0.95 \text{ m}^2$ , while the pellet-triggered ELM has a wetted area that is  $A_{\text{wet}} \approx 0.65 \text{ m}^2$ . Namely, there is a reduction of  $\sim 31\%$  in the wetted area by means of pellet injection. This simulation result is qualitatively consistent with pellet-triggered ELMs in experi-

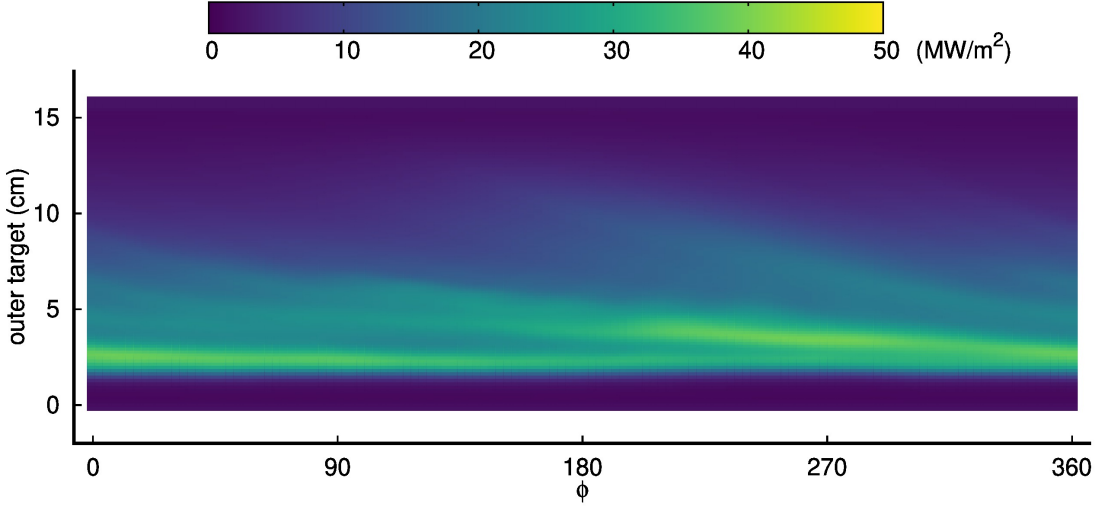


Figure 6.11: Heat flux impinging in the outer divertor at  $t_0 = 14.22$  ms for Tr-08-14ms. The footprint generated by mainly two strike lines can be seen as distinct peaks. The wetted area of the heat flux profile at this time is  $A_{\text{wet}} \approx 0.65$  m $^2$ : roughly 31% smaller than Sp-318.1. The peak heat flux is visibly smaller than Sp-318.1, shown in fig. 6.6.

ments [102]. Confirming whether this qualitative similarity translates to quantitative consistency with respect to experimental observations goes beyond the scope of the present work, but has to be determined before being able to conduct reliable predictive simulations.

#### 6.4.3 Comparison of Sp-318 and Tr-08-14ms

The instantaneous comparison of peak heat flux and wetted area between spontaneous and pellet-triggered ELMs does not tell the full story. Indeed, the time-integrated heat flux profile describes how the energy is deposited along the divertor targets during the ELM crashes. This quantity is the target energy fluence,

$$\varepsilon_{\text{target}}(s, \phi) = \int_{t_{\text{ELM}}} q(s, \phi, t) dt. \quad (6.1)$$

The integration is performed over the ELM duration,  $t_{\text{ELM}}$ . Figure 6.12 shows the resulting profiles for the outer divertor energy fluence in full black line for Tr-08-14ms, in full red line for Sp-318.1, and in pink line with squares for Sp-318.2. The latter corresponds to the second ELM crash in the simulation that includes  $n = 0, 3, 6, \dots, 18$ . The full lines correspond to the fluence profile in the toroidal angle  $\phi = 0$ , i.e., the toroidal position of pellet injection. The deviations from the full line describe the fluence at different toroidal angles, so the toroidal variation of the fluence. The peak fluence is larger for the spontaneous ELMs than for the pellet-triggered ELM. Two spontaneous ELMs are shown because the first ELM

crash that is simulated displays a higher ELM size than the next ELMs because of the seed perturbations, as described in the previous chapter (in 5.3.2). From the figure, it is also possible to directly observe the reduced wetted area between Tr-08-14ms and the spontaneous ELMs.

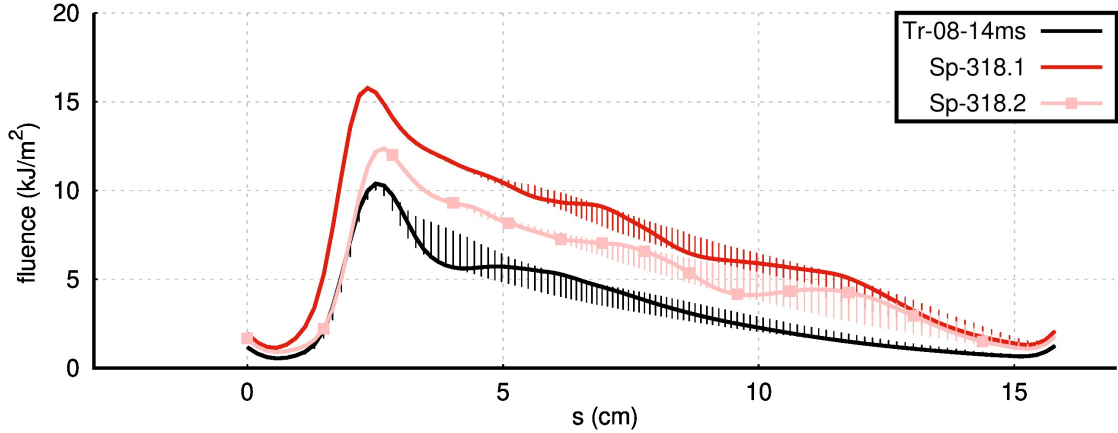


Figure 6.12: The ELM energy fluence for the outer divertor for three different ELMs: the pellet-triggered ELM Tr-08-14ms and the spontaneous ELMs Sp-318.1 and Sp-318.2. The spontaneous ELMs show a higher energy fluence throughout the target, but the pellet-triggered ELM is characterised by a narrower wetted area.

The reduced peak fluence that is observed between Tr-08-14ms and Sp-318.1 can be understood from the multi-machine scaling from Ref. [90]. The scaling fits the measured peak parallel energy fluence against an expression dependent on the relative ELM size, the pedestal density, temperature, and pressure, and the machine size (eqn. 3.1). For the present simulations, the machine size is unchanged and the pedestal density is also roughly the same between the triggered and the spontaneous ELMs (see fig. 6.1(a)). The pedestal temperature and pressure show minor differences (see the dashed red and black lines in fig. 6.1(b) and (c)). The main difference lies in the relative ELM size, which is  $\Delta E_{\text{ELM}} \approx 4.4\%$  for the pellet-triggered ELM and  $\Delta E_{\text{ELM}} \approx 7.8\%$  for the spontaneous ELM. The relative ELM size enters the scaling as  $\Delta E_{\text{ELM}}^{0.52}$ . If the peak fluence from Sp-318.1 ( $15.5 \frac{\text{kJ}}{\text{m}^2}$ ) is scaled by the different relative ELM sizes, the resulting peak fluence is  $15.5 \frac{\text{kJ}}{\text{m}^2} \left(\frac{4.4}{7.8}\right)^{0.52} \approx 11.5 \frac{\text{kJ}}{\text{m}^2}$ . This value is comparable, but slightly larger, to the peak fluence of Tr-08-14ms ( $10.4 \frac{\text{kJ}}{\text{m}^2}$ ). The smaller pedestal pressure and temperature at the time of pellet injection may explain the remaining difference. Following the above procedure above for Sp-318.2 results in a similarly small discrepancy,  $15.5 \frac{\text{kJ}}{\text{m}^2} \left(\frac{5.9}{7.8}\right)^{0.52} \approx 13.4 \frac{\text{kJ}}{\text{m}^2}$  while the actual peak fluence is  $13.7 \frac{\text{kJ}}{\text{m}^2}$ .

The instantaneous heat fluxes in the inner and outer divertors at the time of maximum  $P_{\text{div,out}}$  for Sp-318.1 and Tr-08-14ms are shown in figs. 6.13(a) at  $t = t_0 = 16.57$  ms and (b) at  $t = t_0 = 14.22$  ms, respectively. Poincaré plots in real

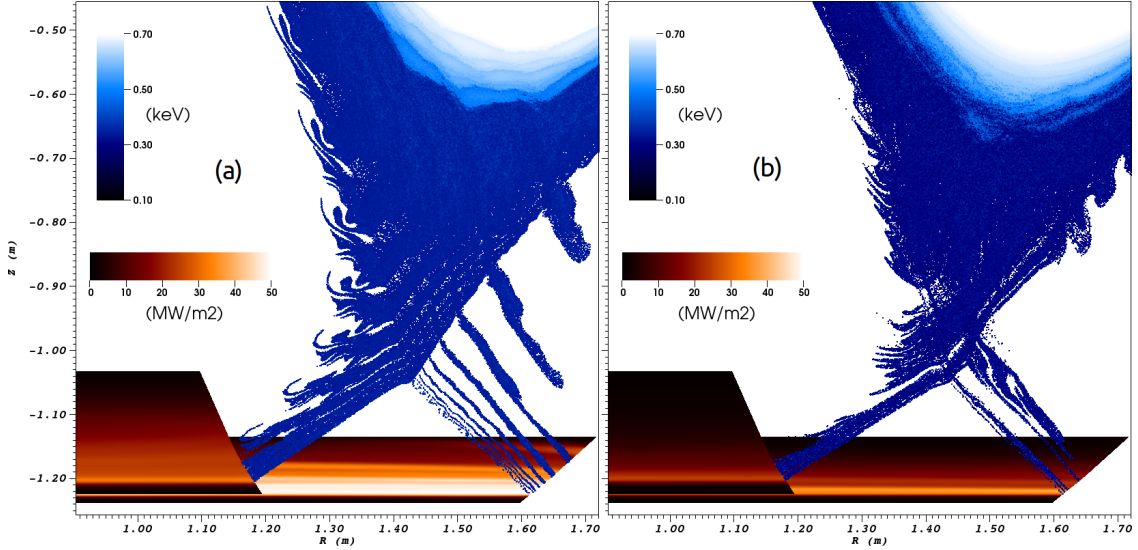


Figure 6.13: An example spontaneous ELM, Sp-318.1, (a) and pellet-triggered ELM, Tr-08-14ms, (b). Poincaré plots in real space characterise the non-axisymmetric magnetic topology at  $\phi = 0$ ; the colour scheme represents the plasma temperature at the initial position of the magnetic field lines that are traced to produce the plot. The heat flux impinging on the inner and outer divertor targets is also included. There are fewer secondary strike-lines for Tr-08-14ms than for Sp-318.1 resulting in different wetted areas. Figure modified from Ref. [46]

space are also included in each figure to portray the non-axisymmetric magnetic topology caused by the ELMs. The colour scale for the Poincaré plots represents the temperature at the initial position of the magnetic field lines. The larger heat flux for Sp-318.1 and the narrower deposition area for Tr-08-14ms are clearly visible. The structure of the magnetic field outside of the confined region (which generates the secondary strike lines) is visible in the Poincaré plot, and its influence is also evident in the divertor heat fluxes. Indeed it seems that the narrowing of the wetted area between the spontaneous ELM and the pellet-triggered ELM is directly related to the reduced number of secondary strike lines. In addition to this, a small difference in the temperature between the Sp-318.1 and Tr-08-14ms can be observed. This is an indication that the stochastic region reaches further inside during the spontaneous ELM crash.

#### 6.4.4 Mode structures

The non-axisymmetric mode structures for Sp-318.1 and Tr-08-14ms are shown in figs. 6.14(a)-(f) at the times of maximum outer divertor incident power,  $t_0 = 16.57$  ms and  $t_0 = 14.22$  ms, respectively. The mode structures are shown for three quantities: density ( $10^{20} / \text{m}^3$ ), poloidal magnetic flux (Wb), and plasma temperature

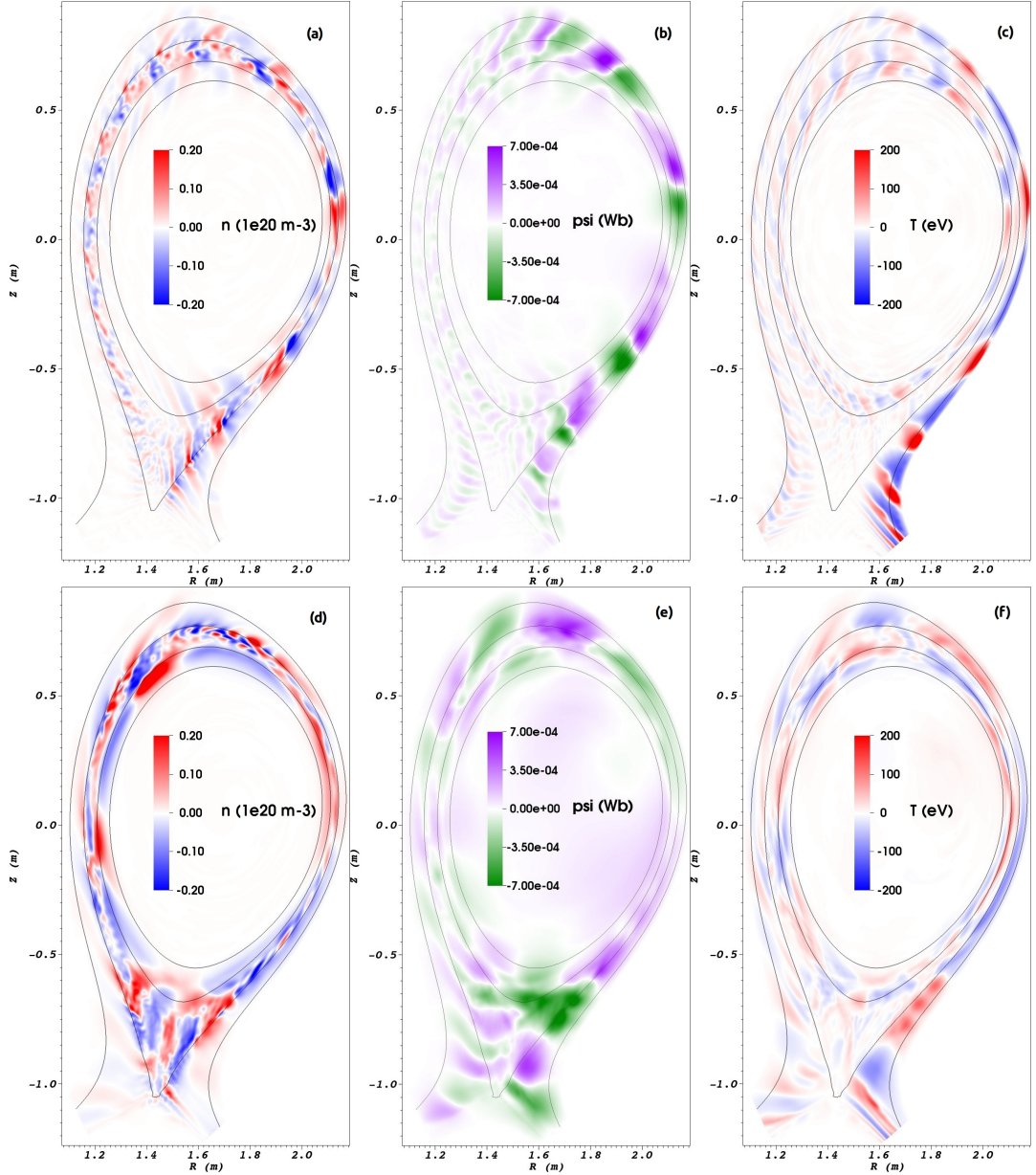


Figure 6.14: Non-axisymmetric perturbations of density, poloidal magnetic flux, and temperature for Sp-318.1 (a)-(c), and Tr-08-14ms (d)-(f), at  $t_0 = 16.57$  and  $t_0 = 14.22$  ms, respectively. Flux surfaces at  $\psi_N = 0.8, 0.9, 1.0$ , and  $1.1$  are shown with gray lines. Sp-318.1 display peeling-balloonning structures, while Tr-08-14ms feature the mix between the pellet-induced perturbation and PB modes excited because of it. The  $n \neq 0$  modes are larger for the triggered ELM than for the spontaneous ELM. Figure modified from Ref. [46].

(eV). The top row (a)-(c) shows the spontaneous ELM and the bottom row (d)-

(f) the pellet-triggered ELM; the colour scale is the same for the spontaneous and triggered ELMs. Flux surfaces at  $\psi_N = 0.8, 0.9, 1.0$ , and 1.1 are also contoured in gray. For the pellet-triggered ELMs, the dominant toroidal mode number is  $n = 1$  and it is a helical perturbation which is produced by the pellet injection. For the spontaneous ELM, it is the  $n = 3$  peeling-balloonning mode. This difference indicates that there are different and/or additional physical processes that govern the destabilisation of the two events and the non-linear dynamics that are present<sup>7</sup>. In JET, ELMs which are triggered by pellets are characterised with  $n = 1$  [238]. Experiments in AUG exhibit spontaneous ELMs with dominant toroidal mode number is the range  $n = 2 \dots 5$  [109]. It is encouraging that the simulations qualitatively match the experimental observations in terms of dominant  $n$ .

The  $n \neq 0$  perturbations for Sp-318.1, figs. 6.14(a)-(c), feature modes with a peeling-balloonning structure inside the separatrix. In all quantities (especially the poloidal magnetic flux), ballooning modes on the LFS can be distinguished. In addition, there are large fluctuations of the temperature in the SOL; these follow the structures observed in fig. 6.13(a). Tr-08-14ms displays different behaviour in terms of the spatial mode structures. It is possible to faintly distinguish peeling-balloonning structures; in particular in the density perturbations at the HFS between  $\psi_N = 0.9$  and 1.0. Unfortunately, discriminating between PB modes excited by the pellet and the large pellet-induced perturbation is not possible. Therefore, the absence of clear PB structures may either be because they are masked by the pellet-induced perturbation, or because pellet-triggered ELM hosts different perturbations.

There are more differences in the spatial structure of the modes of the spontaneous ELM and the pellet-triggered ELM. One such difference is the large density perturbation that is directly caused by the density source related to the pellet ablation process, fig. 6.14(d) vs. 6.14(a). In general, the density perturbations observed inside the confined region for Tr-08-14ms are larger than those for Sp-318.1. However, in the SOL the density perturbations are larger for the spontaneous ELM. In contrast to the density perturbations, the temperature perturbations are observed to be stronger for Sp-318.1 than for Tr-08-14ms. Finally, the X-point region is very different between the two ELMs: the density and flux perturbations are very large above the X-point for the pellet-triggered ELM, but they are weak for the spontaneous ELM.

## 6.5 Comparison between spontaneous and pellet-triggered ELM

This section compares important quantities between simulations of several pellet-triggered ELMs and spontaneous ELMs.

---

<sup>7</sup>The described differences in the mode structures between triggered ELMs and spontaneous ELMs remain unchanged in spontaneous ELM simulations that include the  $n = 1$  mode. Therefore indicating that the observed differences are not dependent on the toroidal mode numbers present in Sp-318.1.

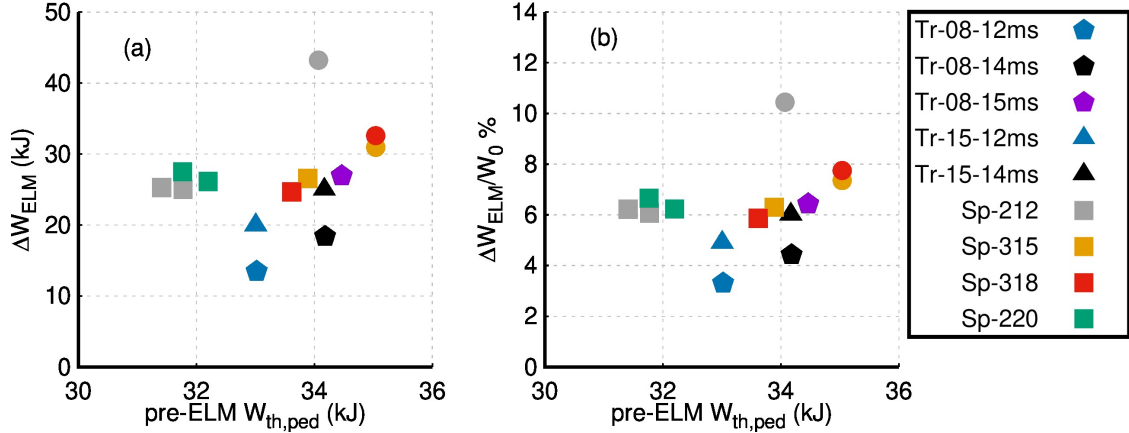


Figure 6.15: Simulations of spontaneous and pellet-triggered ELMs and their associated energy losses (a) and relative ELM size (b) vs. the pre-ELM pedestal stored energy. The spontaneous ELMs are represented with circles (for the first ELM in a given series) and with squares (for the subsequent ELMs). It can be seen that the first ELM in a given series, which are borne out of arbitrary seed perturbations, have larger sizes than the subsequent ELMs. Pellet-triggered ELMs, on the other hand, are represented with pentagons (for small pellets) and with triangles (for large pellets). Pellet injection appears to systematically reduce the ELM size when the pellets are injected early enough.

### 6.5.1 ELM-induced thermal energy losses

The ELM energy ( $\Delta W_{\text{ELM}}$ ), and the relative ELM size ( $\Delta E_{\text{ELM}}$ ) for the different pellet-triggered ELMs and spontaneous ELMs are shown in figs. 6.15(a) and (b), respectively. Pellets injected at 12 ms are coloured with blue, those injected at 14 ms in black and at 15 ms in purple. Small pellets ( $0.8 \times 10^{20}$ D atoms) are depicted with pentagons, and large pellets ( $1.5 \times 10^{20}$ D atoms) with triangles. The spontaneous ELMs are represented with different colours to distinguish the toroidal mode numbers that were present in the given simulations, e.g., red for the simulations with  $n = 0, 3, 6, \dots, 18$ . Additionally, the first ELM in a series is shown with coloured circles, while the subsequent ELMs are depicted with squares. The different symbols used to distinguish between the first ELM crash and the subsequent ELMs is chosen because the first ELM crashes are observed to be systematically larger than the next ELMs in a given series, as explained in the previous chapter (in 5.3.2) and in Ref. [37]. The spontaneous ELMs that are preceded by self-consistent seeds (squares) all have very similar sizes: their average absolute ELM size is  $\Delta W_{\text{ELM}} = 25.88 \pm 0.96$  kJ, and relative ELM size is  $\Delta E_{\text{ELM}} = 6.22 \pm 0.24\%$ .

For the pellet-triggered ELMs, the pre-ELM pedestal stored energy acts as a measure for the time of pellet injection. Because the pedestal build-up is simulated, the earliest pellet injection (12 ms in blue colour) is associated with a lower pedestal

stored energy than the latest pellet injection (15 ms in purple colour). The pellet-triggered ELMs are characterised by ELM sizes that monotonically increase as the injection time is closer to the onset of the spontaneous ELM (with increasing pedestal stored energy). For the small pellets (pentagons), only the injection at 15 ms results in similar absolute and relative ELM losses, with respect to the self-consistent spontaneous ELMs (squares). An increase in the pellet-triggered ELM size is observed with the injection of larger pellets (triangles). Indeed, the large pellet injected at 14 ms shows similar ELM size as the self-consistent spontaneous ELMs, while the small pellet injected at the same time features a smaller ELM size (roughly 30% smaller absolute ELM size).

The pellet-triggered ELM with the smallest size corresponds to a small pellet injected at 12 ms:  $\Delta W_{\text{ELM}} = 13.5 \text{ kJ}$ , which is roughly half of the average ELM size for the spontaneous ELMs. The differences in ELM size observed between the pellet-triggered ELMs and the spontaneous ELMs seem to qualitatively agree with experiments in AUG [44].

### 6.5.2 Toroidal mode spectrum

Figure 6.16 shows time-averaged spectra of the non-axisymmetric perturbations in terms of their toroidal mode numbers. Pellet-triggered ELMs are shown with lines and symbols: ELMs triggered by small pellets are symbolised with pentagons and triggered by large pellets with triangles. Spontaneous ELMs are depicted with full lines. The time averaging is done for 0.5 ms and it starts from 0.1 ms before the time of  $\max(\sum_{n>1}^{\text{n}_{\text{max}}} E_{\text{mag},n})$ .

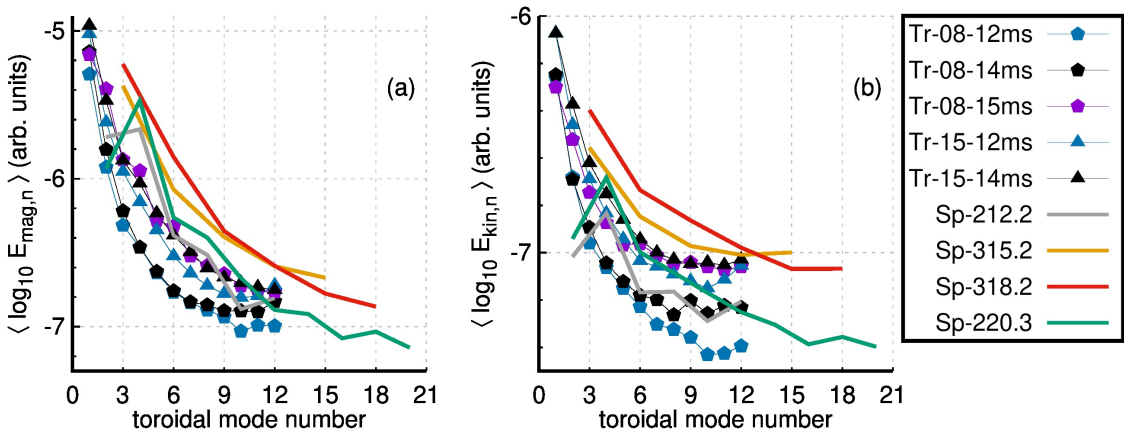


Figure 6.16: Time-averaged spectra of the magnetic (a) and kinetic (b) energies with respect to the toroidal mode numbers. Spontaneous ELMs are shown with full lines, and pellet-triggered ELMs with lines and symbols (pentagons for small pellets, and triangles for large pellets). The time averaging runs for 0.5 ms, and it starts at  $t - t(\max(\sum_{n>1}^{\text{n}_{\text{max}}} E_{\text{mag}})) = -0.1 \text{ ms}$ .

The dominant toroidal mode in the pellet-triggered ELM simulations corresponds

to the  $n = 1$  helical perturbation, which is qualitatively consistent with experiments [238] and with previous JOREK simulations [76, 178]. The energy of the modes then decreases for larger  $n$ , but after  $n \sim 8$  a ‘saturation’ is observed. This is because of the excitation of high- $n$  ballooning modes. For the presented spontaneous ELMs, low toroidal mode numbers are the most unstable ones  $n = 2, 3, 4$ , which is consistent with experimental measurements at AUG [109], however higher toroidal mode numbers have also been reported to be dominant during the ELM crash [33, 129]. The mode spectrum also shows decreasing energies for the modes with higher- $n$ , but the mechanism in this case is related to the non-linear drive from three-wave coupling [196]. It is worth mentioning that an additional spontaneous ELM simulation which includes  $n = 0, 1, 2, \dots, 19$  has the  $n = 3$  as the most unstable mode, and the  $n = 1$  is clearly sub-dominant.

The magnetic energies of the non-axisymmetric perturbations for the ELMs described in section 6.4 (Sp-318.1 and Tr-08-14ms) and Sp-318.2 are shown in figs. 6.17(a)-(c). The figure clearly demonstrates the differing dynamics between pellet-triggered ELM and the spontaneous ELMs. The precursor phase for Sp-318.1 and Sp-318.2 can be clearly observed up to one millisecond before the ELM crash. In contrast, the pellet-triggered ELM grows shortly after the pellet is injected ( $\sim 0.1$  ms). It is apparent that the magnetic energies decay in amplitude in a shorter time scale for the spontaneous ELMs than for Tr-08-14ms. The pellet-triggered ELM has a comparatively higher pedestal density after the end of the ELM crash (as can be seen in fig. 6.9). This causes the diamagnetic drift to be weaker in the post-ELM phase for Tr-08-14ms than for the spontaneous ELMs ( $v_i^* \sim 1/n_e$ ). Therefore, the related stabilising effect is weaker and allows the  $n \neq 0$  perturbations to maintain large amplitudes for longer times.

### 6.5.3 Heat flux and energy fluence comparison

Unmitigated type-I ELMs are predicted to cause intolerable heat loads to the divertor targets in ITER [90]. The feasibility of pellet pacing as a control method remains unclear. One remaining uncertainty deals with the heat loads related to pellet-triggered ELMs, as it has been experimentally observed that said heat loads are deposited over narrower regions than comparable spontaneous ELMs [102]. Choosing the time of maximum incident power onto the outer divertor,  $t_0 = t_{\max(P_{\text{div,out}})}$ , the divertor incident power onto the inner and outer divertors is shown in figs. 6.18(a) and (b) for several ELMs by shifting the time to  $t - t_0$ . The inner divertor receives less power than the outer divertor, which is inconsistent with experimental observations [236] most probably due to the single temperature model and/or to the simplified SOL modelling (temperature-dependent viscosity or the missing influence of neutrals). As mentioned before, spontaneous ELMs with low toroidal resolution result in unrealistically low incident power (compare Sp-212.2 and Sp-318.2) because of the longer precursor phase. For this reason, spontaneous ELMs simulated with  $n_{\max} < 15$  are neglected. Also, only the second (or third) ELMs in a series are plotted. An ELM triggered by a small pellet injected at 14 ms has been simulated

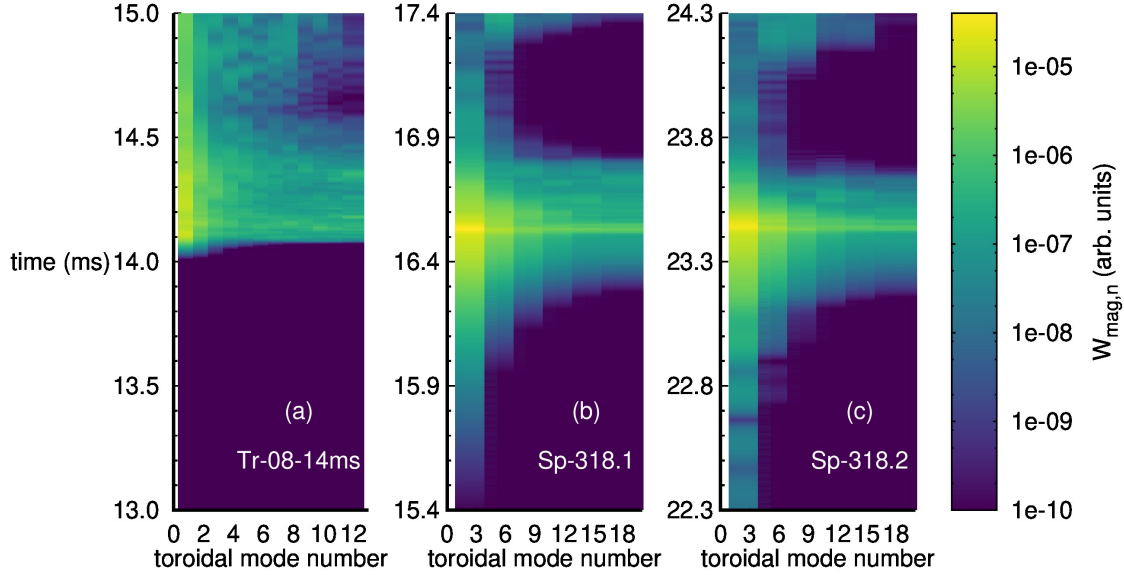


Figure 6.17: Magnetic energies of the non-axisymmetric perturbations of Tr-08-14ms (a) and Sp-318.1 (b). The y-axes, time in ms, correspond to the time ranges from fig. 6.7 and fig. 6.3, respectively. The colour scale is logarithmic.

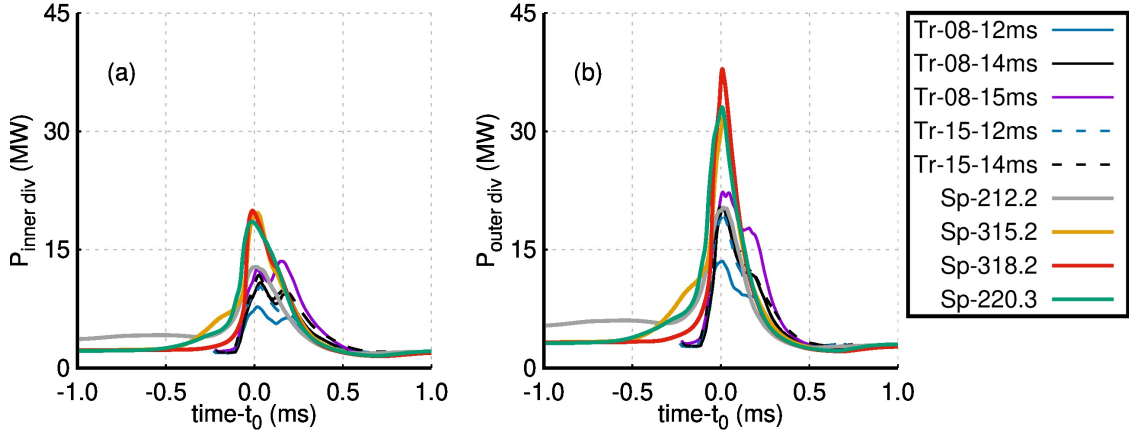


Figure 6.18: Incident power onto the inner (a) and outer (b) divertor targets for several spontaneous (gray, yellow, red, and green) and pellet-triggered ELMs (blue, black, and purple). Sp-212.2 has too little toroidal resolution and it does not converge. Therefore, it is neglected from the analysis. The pellet-triggered ELMs all show a reduction of the peak incident power (shown at  $t - t_0 = 0$  ms).

with higher toroidal resolution (up to  $n_{\max} = 18$ ), and it shows a slightly smaller peak divertor incident power (7%) with respect to Tr-08-14ms. Consequently, we consider the pellet-triggered ELMs shown in fig. 6.18 to be adequately converged.

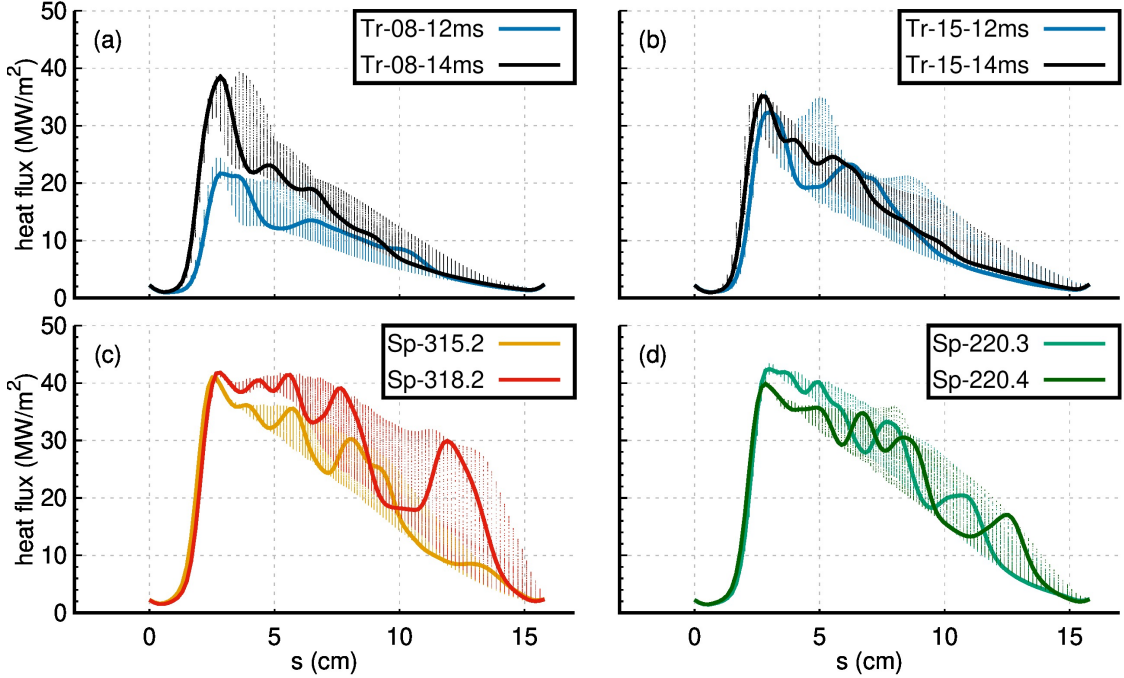


Figure 6.19: Heat flux profiles at the outer divertor at the time of maximum outer divertor incident power. ELMs triggered by small pellets (a) and large pellets (b) injected at 12 (blue) and 14 ms (black) are compared to spontaneous ELMs (c) and (d). The heat flux is deposited over a narrower area for pellet-triggered ELMs than for spontaneous ELMs.

Figure 6.18 shows that there is an important reduction in the peak divertor incident power when ELMs are triggered by pellets. It is also apparent that there is only a minor influence of the pellet size; only the small pellet injected at 12 ms differs in peak  $P_{\text{div}}$  with respect to the other pellet-triggered ELMs. The heat flux profiles on the outer divertor for several ELMs are shown in figs. 6.19(a)-(d) at  $t_0$ . Solid lines show the heat flux profile at  $\phi = 0$  (which is the pellet injection angle), and the small dots represent the heat flux at other toroidal angles. There are eight different ELMs represented; (a) and (b) show pellet-triggered ELMs with small and large pellets, respectively. (c) and (d) show spontaneous ELMs with  $n_{\text{period}} = 3$  and 2, respectively. All four examples of pellet-triggered ELMs show narrower heat deposition area when compared to the spontaneous ELMs, but similar peak heat fluxes. The non-axisymmetric features corresponding to the spontaneous ELMs are concentrated at  $s \gtrsim 5$  cm. For the pellet-triggered ELMs, on the other hand, there is non-axisymmetry in the heat flux even at the location of the primary strike-line ( $s \approx 3$  cm). These results qualitatively agree with experimental observations of the heat flux deposition patterns of pellet-triggered ELMs [102]. A systematic quantitative validation goes well beyond the scope of the present work.

Material limits are usually determined by the peak energy fluence, which is de-

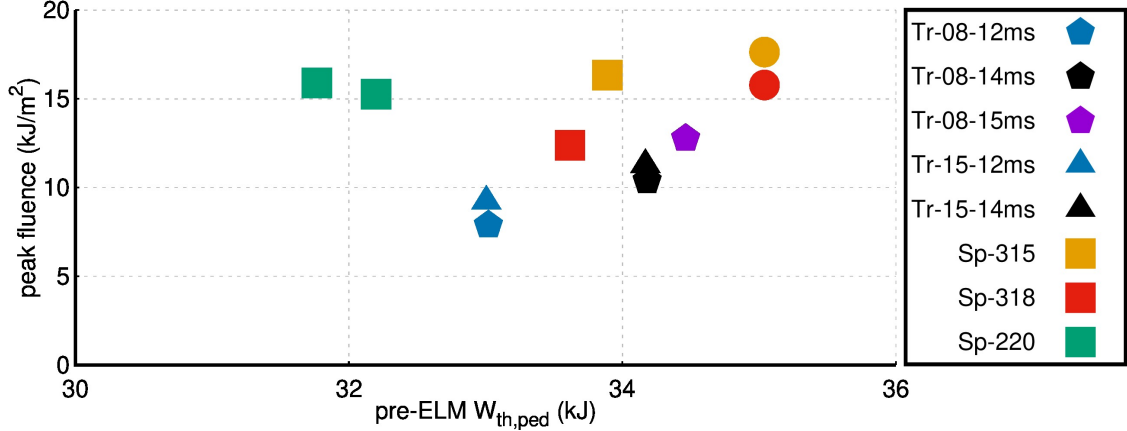


Figure 6.20: Simulations of spontaneous and pellet-triggered ELMs and their associated peak target fluence vs. the pre-ELM pedestal stored energy. The spontaneous ELMs are represented with circles (for the first ELM in a given series) and with squares (for the subsequent ELMs). The first ELM in a given series has higher peak fluence than the subsequent ELMs. Pellet-triggered ELMs are represented with pentagons (for small pellets) and with triangles (for large pellets). Pellet injection appears to systematically reduce the peak fluence when the pellets are injected early enough, but there is only a moderate decrease in the peak fluence between pellet-triggered ELMs and spontaneous ELMs.

terminated by the time integrated heat flux deposition profile. An example of this was shown for Sp-318.1, Sp-318.2, and Tr-08-14ms in fig. 6.12. The peak values of the target fluence for the various different ELMs (excluding Sp-212 because of the insufficient toroidal resolution) are plotted in fig. 6.20 with respect to the pre-ELM pedestal stored energy. The symbols correspond to those from fig. 6.15: ELMs triggered by small pellets with pentagons, by large pellets with triangles, and spontaneous ELMs with circles and squares (circles for the first ELM in a given series).

The peak target fluence of five pellet-triggered ELMs is shown in comparison to six spontaneous ELMs. Only one pellet-triggered ELM, Tr-08-15ms, shows larger peak target fluence than a spontaneous ELM (Sp-318.2). Among the pellet-triggered ELMs, Tr-08-15ms has the largest pre-ELM pedestal stored energy. The remaining pellet-triggered ELMs show a reduction of peak target fluence with respect to all spontaneous ELMs. Injecting a pellet at 12 ms results in the largest reduction of peak target fluence (Tr-08-12ms and Tr-15-12ms). There is only a small influence of pellet size onto the peak fluence. For the spontaneous ELMs, the peak fluence decreases between the first ELM in a series (circles) and the subsequent ELMs (squares), as shown already in fig. 6.12. The fact that the peak heat flux in fig. 6.19 is comparable between pellet-triggered ELMs and spontaneous ELMs may seem to be contradictory with the measured reduction in peak target fluence in

fig. 6.20. However, this is not the case because of the precursor phase, that is only present in the spontaneous ELMs, causes an increase of the peak fluence. The ELM duration ( $t_{\text{ELM}}$  in eqn. 6.1) is determined from the time at which  $P_{\text{div,out}}$  exceeds 3.4 MW until it returns to the same value.

## 6.6 Conclusions

The simulations presented in this chapter have been published in Ref. [46], and some of them in Ref. [45]. A comparison of pellet-triggered ELMs and spontaneous ELMs simulated with JOREK has been shown. The simulations of pellet injection were performed by Shimpei Futatani based on the type-I ELM cycles simulation set-up established as part of this thesis. The pellet injections are performed at different time points in the simulations of type-I ELM cycles presented in the previous chapter. Injecting pellets too early during the pedestal build-up fails to trigger ELMs [45]. This finding, which is qualitatively consistent with the pellet-triggering lag-time observed at AUG-W and JET-ILW, is an important step forward for the predictive assessment of pellet pacing as an ELM control method or as a scheme to prevent impurity accumulation. The pellet-triggered ELM simulations presented in this chapter considered two different sizes, both of which represent experimentally accessible sizes. The simulations included ExB and diamagnetic flows, but neglected higher order terms in the fluid velocity. The pedestal resistivity that was used for these simulations lies within the experimental error bars for the neoclassical resistivity. The parallel heat diffusion was set to realistic Spitzer-Härm values.

The non-linear dynamics of representative spontaneous and pellet-triggered ELMs were described in detail to show the differences and similarities observed. The absence of a precursor phase in the pellet-triggered ELMs is a fundamental difference between the two events. The triggered ELM becomes excited roughly 0.1 ms after the pellet injection, when the pellet perturbation is located near the maximum pressure gradient region. This result is consistent with experimental measurements from AUG [231]. The dominant mode numbers that are present during each type of ELM crash was also observed to differ from  $n = 1$  in the pellet-triggered ELMs to  $n = 2, 3, 4$  in the spontaneous ELMs. It has been observed that triggered ELMs have a dominant  $n = 1$  contribution in JET [238], and that spontaneous ELMs feature dominant  $n = 2 \dots 6$  during the ELM crash in AUG [109]. The  $n = 1$  perturbation in the pellet-triggered ELMs is directly related to the pellet injection, and it is a helical perturbation which is reflected in the heat flux profiles at the divertor tiles.

A single temperature description and a simplified SOL model were used, which reduces the complexity of the simulations, but neglects some physics relevant for the deposition of energy onto the divertor targets. Despite this simplification, qualitative agreement is found in terms of the experimentally observed narrowing of the wetted area of pellet-triggered ELMs with respect to spontaneous ELMs [102]. It is suggested that the narrower deposition area is related to a reduction in the number of secondary strike-lines. Indeed, the simulations show several strike-lines for the spontaneous ELMs together with a wide deposition area, while only one secondary strike-lines for the pellet-triggered ELMs. The singular secondary strike-line related to the pellet-triggered ELM is related to the  $n = 1$  helical perturbation.

A comparison of several pellet-triggered ELMs showed that the pellet size has

small influence onto the ELM size. Injecting a pellet earlier during the pedestal build-up leads to a smaller ELM size because of the lower pedestal stored energy. Several spontaneous ELMs are also included in the comparisons, and it is observed that pellet injection leads to smaller ELM sizes. However, if the pellet is injected too close to the onset of the spontaneous ELM, the ELM losses are comparable to the spontaneous ELM. The peak divertor incident power is also smaller for the cases with pellet injection with respect to the spontaneous ELMs. Finally, the peak target fluence is also smaller for pellet-triggered ELMs than for spontaneous ELMs. The largest reduction in peak fluence is obtained for pellets injected 4 ms before a spontaneous ELM is excited.

The first direct comparison of pellet-triggered ELM and spontaneous ELM simulations in AUG was presented in this chapter. Qualitative, and in some respects quantitative, agreement to the experiment was found in several important aspects like the dominant mode numbers during the respective ELM crashes, the reduction of ELM size when ELMs are triggered by means of pellet injection, and the corresponding narrowing of the wetted area. Future investigations onto pellet packing obtained by repetitive pellet injection are underway. Ultimately, quantitative comparisons between simulations and experiments must be performed.



## 7 Conclusions and Outlook

Edge instabilities in high-confinement mode (H-mode) plasmas have been studied via numerical simulations with the goal of improving the underlying physical mechanisms. A specific type of edge instability, *type-I edge localised modes* (type-I ELMs), could limit the lifetime of large tokamaks like ITER. Type-I ELMs have been theoretically understood as the coupling of two edge instabilities: current-driven peeling modes and pressure gradient-driven ballooning modes. Scenarios that do not host type-I ELMs, like the quasi-continuous exhaust (QCE) regime, and scenarios that mitigate their deleterious effects have been developed and experimentally tested. Nevertheless, their successful applicability in ITER, or other future machines, is not void of uncertainties. In that sense, achieving reliable simulations of ELMs in a predictive manner can provide valuable support for future experiments. Several key features of ELMs have been reproduced in simulations with various codes thus far. However, an important characteristic of type-I ELMs lies in their cyclical nature which, until now, had not been reproduced in numerical simulations.

Past simulations of ELMs were initialised with unstable plasma conditions (unstable to peeling-balloonning modes) and the cyclical dynamics of ELMs could not be obtained. In such simulations, the ELM-related energy and particle losses depend on how unstable the initial conditions are. Therefore, said approach cannot produce predictive simulations. In this thesis, a different approach was followed to understand how these instabilities behave when the stability boundary is crossed (as it happens in experiments). Namely, simulations start with stable initial conditions, and the pedestal build-up is simulated. During the build-up, the bootstrap current density evolution is accounted for in the simulations with a source term, and the stabilising effects of the  $E \times B$  and diamagnetic drifts are considered. With this approach, three main topics were investigated in the course of this work by considering realistic experimental parameters for the ASDEX Upgrade (AUG) tokamak:

- Small ELMs similar to those observed in the QCE regime (chapter 4),
- the cyclical dynamics of type-I ELMs (chapter 5), and
- the premature excitation of ELMs by deuterium pellet injection (chapter 6).

The non-linear extended MHD code JOREK (chapter 2) has been used for all the simulations presented in this thesis. The main results presented in this thesis are summarised in the following.

## 7.1 Resistive peeling-balloonning modes during the QCE regime

The QCE regime is a promising scenario that avoids type-I ELMs altogether while maintaining good confinement properties. The pedestal is limited below the type-I ELM threshold by small ELMs/peeling-balloonning turbulence, which quasi-continuously expel heat and particles from the confined region. As such, it might constitute an attractive operational scenario for ITER. However, it is presently unclear whether or not such regime can be achieved in ITER. Chapter 4, presents simulations that show several key characteristics of such small ELMs. Non-ideal (resistive) peeling-balloonning modes near the separatrix in the simulations present a transport mechanism that prevents the onset of type-I ELMs. These modes are hypothesised to be the transport mechanism that prevents the pedestal build-up towards type-I ELM crashes and thus might form the basis for accessing the QCE regime.

It is observed that the necessary conditions to sustain sufficient outwards transport by the resistive peeling-balloonning (PB) modes are primarily determined by the separatrix density and the input heating power. In particular, simulations with high  $n_{e,\text{sep}}$  and low heating power observe phases with quasi-continuous outwards transport that prevent the pedestal from reaching a type-I ELM unstable scenario. Sufficiently increasing the heating power stabilises the resistive PB modes and the plasma state moves to a type-I ELM My H-mode. Similarly, reducing the separatrix density completely stabilises the resistive PB modes and allows the pedestal to build-up towards a type-I ELM unstable scenario.

## 7.2 The importance of seed perturbations

Type-I ELM cycles have been simulated in realistic X-point geometry, for the first time, in the course of this thesis. This represents a significant step forward in terms of the predictive assessment of type-I ELMs in future machines like ITER, and will form the basis for predictive simulations of ELM control in the future. The multi-ELM simulations are presented in chapter 5 and the studies performed highlight the importance of seed perturbations onto the ELM dynamics. The simulated type-I ELMs show good quantitative agreement with respect to experimental observations in terms of the dominant toroidal mode numbers during the ELM crash ( $n = 2, 3, 4$ ), and good qualitative agreement in terms of ELM size and duration. Additionally, the dependence of the repetition frequency of the simulated ELMs with the imposed heating power is consistent with the one observed for type-I ELMs, i.e., the ELM repetition frequency increases(decreases) with increasing(decreasing) input heating power. Finally, two self-amplifying mechanisms are proposed to explain the explosive onset of the ELM crash (faster than exponential growth). Low- $n$  peeling-balloonning precursor modes (and their interaction with the background plasma) cause  $\nabla p$  to locally increase, but on average cause it to decrease. The precursors also induce a reduction of the stabilising plasma flows on a faster time scale than the global decrease of the destabilising pressure gradient and

current density. The combined influence of these local and global effects results in an explosive onset of the ELM crash.

The initial conditions for the non-axisymmetric perturbations are arbitrary at the beginning of any simulation. The first ELM crash grows out of arbitrary seed perturbations. After the first ELM crash, the non-axisymmetric perturbations retain some information from the ELM crash (structure and amplitude), which means that the seed perturbations for the second ELM crash are fundamentally different than those for the first ELM. This leads to important differences between the first ELM and the subsequent ELMs. In order to consider self-consistent seed perturbations, it is necessary to simulate more than one ELM, thus highlighting the importance of multi-ELM simulations for predictive purposes.

### 7.3 Pellet-triggered ELMs and spontaneous ELMs

A direct comparison between spontaneous ELMs and pellet-triggered ELMs was also produced as part of this thesis. This study was performed in collaboration with Shimpei Futatani, who performed the pellet-triggered ELM simulations by using the type-I ELM cycles simulation set-up established as part of this thesis. Analysis of results and, in particular, the comparisons to spontaneous ELM crashes were performed as part of this thesis. In contrast to spontaneous ELMs, pellet-triggered ELMs do not observe a precursor phase as they become rapidly excited within  $< 0.1$  ms from the time of injection. In qualitative agreement with experimental observations, the ELM is triggered when the pellet position roughly corresponds to the location of maximum pressure gradient. The dominant perturbation in the pellet-triggered ELM simulations is a helical perturbation related to the  $n = 1$  toroidal mode number, as it is also observed in experiments.

The pellet-triggered ELMs achieve a reduction in the ELM size, with respect to the spontaneous ELM counterparts, if they are excited early enough during the pedestal build-up, i.e., when less energy is stored in the confined region. The area over which the expelled energy is deposited (wetted area) becomes reduced by roughly 30% when ELMs are triggered. The simulation results suggest that the narrower wetted area for the triggered ELMs results from a reduction in the number of strike-lines that deviate from the primary strike-line during the ELM crash. For the spontaneous ELMs there are several secondary strike-lines and a wide deposition area, while the pellet-triggered ELMs display only one clear secondary strike-line related to the  $n = 1$  helical perturbation and a reduced wetted area.

ELMs were triggered with pellets of two different sizes, and the pellet size is observed to only weakly influence the ELM dynamics. The bigger pellets cause slightly larger ELM-related losses. The peak divertor incident power and the time integrated target fluence are lower for pellet-triggered ELMs than for spontaneous ELMs. The largest reductions are observed when ELMs are triggered earlier during the pedestal build-up, i.e., when less thermal energy is stored in the confined region. Qualitative, and in some respects quantitative, agreement with experimental

observations was obtained in several important aspects. For example, the dominant mode numbers during the respective ELM crashes, the reduction of ELM size when ELMs are triggered by means of pellet injection, and the corresponding narrowing of the wetted area.

## 7.4 Outlook

The results obtained in the course of this thesis advanced the state of the art for modelling edge localised modes in several ways. Simulations of type-I ELM cycles, resistive peeling-balloonning turbulence that might be the underlying phenomenon for the quasi-continuous exhaust (QCE) regime, and a consistent comparison between spontaneous ELMs and pellet-triggered ELMs were produced through the novel approach of simulating the pedestal build-up that has been established in this thesis. Said studies can, and should, be extended to further advance validation of the models with experiments and, eventually, provide insight to future experiments. The simulations presented in this thesis considered a single fluid model with extensions to consider two-fluid effects (diamagnetic drifts) and the evolving bootstrap current density through a source term. Future work should consider separate ion and electron temperatures because they can have an important effect onto the ELM dynamics. For example with respect to heat transport in ergodic magnetic fields and, therefore, heat deposition onto divertor targets.

There are several lines of research that can be followed with the imposed pedestal build-up at fixed pedestal width established in this thesis. Some have already been started through various collaborations: the application of resonant magnetic perturbations (RMPs) to investigate ELM mitigation, free-boundary ELM cycles simulations, pellet-ELM pacing, and shaping effects onto the resistive PB modes in the QCE regime. Others, such as naturally ELM-free regimes (QH-mode or EDA H-mode, for instance), and the influence of pedestal position/collisionality, or of neutral particles onto the ELM dynamics, could be investigated with the respective adaptations in the simulation set-up. The influence of neutral particles can be studied with JOREK by using an existing fluid neutrals model. Note, however, that the imposed pedestal build-up with fixed pedestal width constitutes an incomplete model as it does not consider several dynamical effects that exist during (and influence) the pedestal build-up (neutrals penetration, stabilisation and/or destabilisation of various turbulent micro-instabilities, neoclassical physics, radiation losses, plasma-wall interactions, *etc.*). The pedestal width in experiments varies between two type-I ELM crashes, but the physical mechanisms that determine the widening are not completely understood. Including all the physical effects that influence the pedestal build-up would require resolving extremely small spatial scales and fast time scales. Unfortunately, there is no code available that can realistically account for all such effects. Therefore, developing a (reduced) model to characterise the inter-ELM particle and heat transport driven by micro-turbulence and neoclassical physics and coupling it to JOREK is a necessary step towards

more realistic simulations of type-I ELM cycles.

The current density and its gradient govern the destabilisation of edge localised external kink (peeling) modes, and they have a stabilising effect onto high-n ballooning modes. During the inter-ELM phase, the current density grows in the edge due to the neoclassical bootstrap current which forms as the density and temperature profiles steepen. The MHD model does not encompass the formation of the bootstrap current density. However, in its present version, JOREK considers an analytical expression that ties the density, temperature, and pressure profiles to the bootstrap current density. In such a way, the increase of the edge current density was considered in the simulations presented in this thesis. Said analytical expressions are not accurate throughout different collisionality regimes and can be improved with dedicated developments. This is foreseen as an important improvement that should be resolved before validation efforts can be conducted. This is true both for type-I ELM simulations and for resistive PB modes that underlie the QCE regime.

Code validation is perhaps the most critical step towards predictive simulations. In order to achieve this, simulation and experiments have to be closely intertwined in order to compare results from each of them. A systematic validation of the type-I ELM cycles simulations should be carried out in order to understand to what extent the results agree with experimental measurements. Similarly, the resistive PB modes have to be validated with medium-sized tokamaks where the QCE regime is accessible (AUG and/or TCV). Ultimately, after simulations and experiments in larger machines like JET and/or JT-60SA, the applicability of the QCE regime in ITER can be assessed through predictive simulations.



# Bibliography

- [1] Arthur S Eddington. The internal constitution of the stars, 1920.
- [2] C.M. Braams and P.E. Stott. *Nuclear Fusion - Half a century of magnetic confinement fusion research*,. Institute of Physics Publishing, Bristol, 2002. URL [https://library.psfc.mit.edu/catalog/online\\_pubs/conference%20proceedings/fusion%20energy%20conferences/Nuclear%20Fusion%20\(IOP\)%20half%20a%20century.pdf](https://library.psfc.mit.edu/catalog/online_pubs/conference%20proceedings/fusion%20energy%20conferences/Nuclear%20Fusion%20(IOP)%20half%20a%20century.pdf).
- [3] J Ongena, R Koch, R Wolf, and H Zohm. Magnetic-confinement fusion. *Nature Physics*, 12(5):398–410, 2016. doi:[10.1038/nphys3745](https://doi.org/10.1038/nphys3745).
- [4] What is ITER? <https://www.iter.org/proj/inafewlines>, Accessed: 2021-03-08.
- [5] Small but fierce: SPARC. Expert Insight with Hartmut Zohm. <https://www.euro-fusion.org/news/2020/november/small-but-fierce-sparc>, Accessed: 2021-03-08.
- [6] P Helander, C D Beidler, T M Bird, M Drevlak, Y Feng, R Hatzky, F Jenko, R Kleiber, J H E Proll, Yu Turkin, and P Xanthopoulos. Stellarator and tokamak plasmas: a comparison. *Plasma Physics and Controlled Fusion*, 54(12):124009, nov 2012. doi:[10.1088/0741-3335/54/12/124009](https://doi.org/10.1088/0741-3335/54/12/124009). URL <https://doi.org/10.1088/0741-3335/54/12/124009>.
- [7] Jeffrey P Freidberg. *Plasma physics and fusion energy*. Cambridge university press, 2008.
- [8] A. Bock, E. Fable, R. Fischer, M. Reich, D. Rittich, J. Stober, M. Bernert, A. Burckhart, H. Doerk, M. Dunne, B. Geiger, L. Giannone, V. Igochine, A. Kappatou, R. McDermott, A. Mlynek, T. Odstrčil, G. Tardini, and H. Zohm and. Non-inductive improved H-mode operation at ASDEX upgrade. *Nuclear Fusion*, 57(12):126041, oct 2017. doi:[10.1088/1741-4326/aa8967](https://doi.org/10.1088/1741-4326/aa8967).
- [9] Martin Greenwald. Density limits in toroidal plasmas. *Plasma Physics and Controlled Fusion*, 44(8):R27–R53, jul 2002. doi:[10.1088/0741-3335/44/8/201](https://doi.org/10.1088/0741-3335/44/8/201). URL <https://doi.org/10.1088/0741-3335/44/8/201>.
- [10] P C Stangeby. Basic physical processes and reduced models for plasma detachment. *Plasma Physics and Controlled Fusion*, 60(4):044022, mar 2018. doi:[10.1088/1361-6587/aaacf6](https://doi.org/10.1088/1361-6587/aaacf6). URL <https://doi.org/10.1088/1361-6587/aaacf6>.

## Bibliography

---

- [11] John Wesson. *Tokamaks; 4th ed.* International series of monographs on physics. Oxford Univ. Press, Oxford, 2011. URL <http://cds.cern.ch/record/1427009>.
- [12] Eurofusion: From doughnuts to bananas. [https://www.euro-fusion.org/news/detail/?tx\\_news\\_pi1%5Bnews%5D=569&cHash=958a68913c5551bca8d093559bb2c811](https://www.euro-fusion.org/news/detail/?tx_news_pi1%5Bnews%5D=569&cHash=958a68913c5551bca8d093559bb2c811), Accessed: 2021-03-09.
- [13] F. L. Hinton and R. D. Hazeltine. Theory of plasma transport in toroidal confinement systems. *Rev. Mod. Phys.*, 48:239–308, Apr 1976. doi:[10.1103/RevModPhys.48.239](https://doi.org/10.1103/RevModPhys.48.239). URL <https://link.aps.org/doi/10.1103/RevModPhys.48.239>.
- [14] Kenro Miyamoto. *Confinement of Plasma (Ideal Cases)*, pages 85–96. Springer Berlin Heidelberg, Berlin, Heidelberg, 2016. ISBN 978-3-662-49781-4. doi:[10.1007/978-3-662-49781-4\\_5](https://doi.org/10.1007/978-3-662-49781-4_5). URL [https://doi.org/10.1007/978-3-662-49781-4\\_5](https://doi.org/10.1007/978-3-662-49781-4_5).
- [15] Hartmut Zohm. *Magnetohydrodynamic Stability of Tokamaks*. Wiley, 2014. ISBN 9783527412327. doi:[10.1002/9783527677375](https://doi.org/10.1002/9783527677375).
- [16] F. Wagner. The history of research into improved confinement regimes. *The European Physical Journal H*, 43(4-5):523–549, 2018. doi:[10.1140/epjh/e2016-70064-9](https://doi.org/10.1140/epjh/e2016-70064-9).
- [17] F. Wagner, G. Becker, K. Behringer, D. Campbell, A. Eberhagen, W. Engelhardt, G. Fussmann, O. Gehre, J. Gernhardt, G. v. Gierke, G. Haas, M. Huang, F. Karger, M. Keilhacker, O. Klüber, M. Kornherr, K. Lackner, G. Lisitano, G. G. Lister, H. M. Mayer, D. Meisel, E. R. Müller, H. Murnmann, H. Niedermeyer, W. Poschenrieder, H. Rapp, H. Röhr, F. Schneider, G. Siller, E. Speth, A. Stäbler, K. H. Steuer, G. Venus, O. Vollmer, and Z. Yü. Regime of improved confinement and high beta in neutral-beam-heated divertor discharges of the ASDEX tokamak. *Phys. Rev. Lett.*, 49:1408–1412, 1982. doi:[10.1103/PhysRevLett.49.1408](https://doi.org/10.1103/PhysRevLett.49.1408).
- [18] S. Sengoku, A. Funahashi, M. Hasegawa, K. Hoshino, S. Kasai, T. Kawakami, H. Kawashima, T. Matoba, T. Matsuda, H. Matsumoto, Y. Miura, M. Mori, H. Ogawa, T. Ogawa, H. Ohtsuka, T. Shoji, N. Suzuki, H. Tamai, Y. Uesugi, T. Yamamoto, and T. Yamauchi. Regime of improved confinement in neutral-beam–heated limiter discharges of a tokamak. *Phys. Rev. Lett.*, 59:450–453, Jul 1987. doi:[10.1103/PhysRevLett.59.450](https://doi.org/10.1103/PhysRevLett.59.450). URL <https://link.aps.org/doi/10.1103/PhysRevLett.59.450>.
- [19] S. Sengoku, A. Funahashi, M. Hasegawa, K. Hoshino, S. Kasai, T. Kawakami, H. Kawashima, T. Matoba, T. Matsuda, H. Matsumoto, Y. Miura, M. Mori, H. Ogawa, T. Ogawa, H. Ohtsuka, T. Shoji, N. Suzuki, H. Tamai, Y. Uesugi,

- T. Yamamoto, and T. Yamauchi. Regime of improved confinement in neutral-beam-heated limiter discharges of a tokamak. *Phys. Rev. Lett.*, 59:1492–1492, Sep 1987. doi:[10.1103/PhysRevLett.59.1492.3](https://doi.org/10.1103/PhysRevLett.59.1492.3). URL <https://link.aps.org/doi/10.1103/PhysRevLett.59.1492.3>.
- [20] K H Burrell, S L Allen, G Bramson, N H Brooks, R W Callis, T N Carlstrom, M S Chu, A P Colleraine, D Content, J C DeBoo, R R Dominguez, J R Ferron, R L Freeman, P Gohil, C M Greenfield, R J Groebner, G Haas, W W Heidbrink, D N Hill, F L Hinton, R M Hong, W Howl, C L Hsieh, G L Jackson, G L Jahns, R A James, A G Kellman, J Kim, L L Lao, E A Lazarus, T Lehecka, J Lister, J Lohr, T C Luce, J L Luxon, M A Mahdavi, H Matsumoto, M Mayberry, C P Moeller, Y Neyatani, T Ohkawa, N Ohyabu, T Okazaki, T H Osborne, D O Overskei, T Ozeki, A Peebles, S Perkins, M Perry, P I Petersen, T W Petrie, R Philipona, J C Phillips, R Pinsker, P A Politzer, G D Porter, R Prater, M E Rensink, M J Schaffer, D P Schissel, J T Scoville, R P Seraydarian, M Shimada, T C Simonen, R T Snider, G M Staebler, B W Stallard, R D Stambaugh, R D Stav, H St John, R E Stockdale, E J Strait, Taylor P L, T S Taylor, P K Trost, U Stroth, R E Waltz, S M Wolfe, R D Wood, and D Wroblewski. Confinement physics of H-mode discharges in DIII-D. *Plasma Physics and Controlled Fusion*, 31(10):1649–1664, aug 1989. doi:[10.1088/0741-3335/31/10/012](https://doi.org/10.1088/0741-3335/31/10/012).
- [21] T.H. Osborne, N.H. Brooks, K.H. Burrell, T.N. Carlstrom, R.J. Groebner, W. Howl, A.G. Kellman, L.L. Lao, T.S. Taylor, D.N. Hill, N. Ohyabu, and M.E. Perry. Observation of the h-mode in ohmically heated divertor discharges on DIII-d. *Nuclear Fusion*, 30(10):2023–2028, oct 1990. doi:[10.1088/0029-5515/30/10/004](https://doi.org/10.1088/0029-5515/30/10/004). URL <https://doi.org/10.1088/0029-5515/30/10/004>.
- [22] F Laggner. *Inter-ELM pedestal structure development in ASDEX Upgrade*. PhD thesis, Technische Universität Wien Wien, 2017. URL <https://repository.tuwien.at/handle/20.500.12708/5101>.
- [23] X Garbet, P Mantica, F Ryter, G Cordey, F Imbeaux, C Sozzi, A Manini, E Asp, V Parail, R Wolf, and the JET EFDA Contributors. Profile stiffness and global confinement. *Plasma Physics and Controlled Fusion*, 46(9):1351–1373, jul 2004. doi:[10.1088/0741-3335/46/9/002](https://doi.org/10.1088/0741-3335/46/9/002). URL <https://doi.org/10.1088/0741-3335/46/9/002>.
- [24] J. W. Connor, R. J. Hastie, H. R. Wilson, and R. L. Miller. Magnetohydrodynamic stability of tokamak edge plasmas. *Physics of Plasmas*, 5(7):2687–2700, 1998. doi:[10.1063/1.872956](https://doi.org/10.1063/1.872956).
- [25] H. R. Wilson, J. W. Connor, A. R. Field, S. J. Fielding, R. L. Miller, L. L. Lao, J. R. Ferron, and A. D. Turnbull. Ideal magnetohydrodynamic stability

- of the tokamak high-confinement-mode edge region. *Physics of Plasmas*, 6(5):1925–1934, 1999. doi:[10.1063/1.873492](https://doi.org/10.1063/1.873492).
- [26] M Keilhacker, G Becker, K Bernhardi, A Eberhagen, M ElShaer, G FuBmann, O Gehre, J Gernhardt, G v Gierke, E Glock, G Haas, F Karger, S Kissel, O Kluber, K Kornherr, K Lackner, G Lisitano, G G Lister, J Massig, H M Mayer, K McCormick, D Meisel, E Meservey, E R Muller, H Murmann, H Niedermeyer, W Poschenrieder, H Rapp, B Richter, H Rohr, F Ryter, F Schneider, S Siller, P Smeulders, F Soldner, E Speth, A Stabler, K Steinmetz, K-H Steuer, Z Szymanski, G Venus, O Vollmer, and F Wagner. Confinement studies in L and H-type ASDEX discharges. *Plasma Physics and Controlled Fusion*, 26(1A):49–63, jan 1984. doi:[10.1088/0741-3335/26/1a/305](https://doi.org/10.1088/0741-3335/26/1a/305). URL <https://doi.org/10.1088/0741-3335/26/1a/305>.
- [27] E. J. Doyle, R. J. Groebner, K. H. Burrell, P. Gohil, T. Lehecka, N. C. Luhmann Jr., H. Matsumoto, T. H. Osborne, W. A. Peebles, and R. Philipona. Modifications in turbulence and edge electric fields at the L–H transition in the DIII-D tokamak. *Physics of Fluids B: Plasma Physics*, 3(8):2300–2307, 1991. doi:[10.1063/1.859597](https://doi.org/10.1063/1.859597).
- [28] H Zohm. Edge localized modes (ELMs). *Plasma Physics and Controlled Fusion*, 38(2):105, 1996. URL <http://stacks.iop.org/0741-3335/38/i=2/a=001>.
- [29] M Bécoulet, G Huysmans, Y Sarazin, X Garbet, Ph Ghendrih, F Rimini, E Joffrin, X Litaudon, P Monier-Garbet, J-M Ané, P Thomas, A Grosman, V Parail, H Wilson, P Lomas, P deVries, K-D Zastrow, G F Matthews, J Lonnroth, S Gerasimov, S Sharapov, M Gryaznevich, G Counsell, A Kirk, M Valovic, R Buttery, A Loarte, G Saibene, R Sartori, A Leonard, P Snyder, L L Lao, P Gohil, T E Evans, R A Moyer, Y Kamada, A Chankin, N Oyama, T Hatae, N Asakura, O Tudisco, E Giovannozzi, F Crisanti, C P Perez, H R Koslowski, T Eich, A Sips, L Horton, A Hermann, P Lang, J Stober, W Suttrop, P Beyer, S Saarelma, and Contributors to JET-EFDA Workprogramme. Edge localized mode physics and operational aspects in tokamaks. *Plasma Physics and Controlled Fusion*, 45(12A):A93–A113, nov 2003. doi:[10.1088/0741-3335/45/12a/007](https://doi.org/10.1088/0741-3335/45/12a/007). URL <https://doi.org/10.1088/0741-3335/45/12a/007>.
- [30] G T A Huysmans. ELMs: MHD instabilities at the transport barrier. *Plasma Physics and Controlled Fusion*, 47(12B):B165–B178, 2005. doi:[10.1088/0741-3335/47/12b/s13](https://doi.org/10.1088/0741-3335/47/12b/s13).
- [31] J. W. Connor, A. Kirk, and H. R. Wilson. Edge localised modes (ELMs): Experiments and theory. *AIP Conference Proceedings*, 1013(1):174–190, 2008. doi:[10.1063/1.2939030](https://doi.org/10.1063/1.2939030).

- [32] A. W. Leonard. Edge-localized-modes in tokamaks. *Physics of Plasmas*, 21(9):090501, 2014. doi:[10.1063/1.4894742](https://doi.org/10.1063/1.4894742).
- [33] A. Kirk, D. Dunai, M. Dunne, G. Huijsmans, S. Pamela, M. Becoulet, J.R. Harrison, J. Hillesheim, C. Roach, and S. Saarelma. Recent progress in understanding the processes underlying the triggering of and energy loss associated with type I ELMs. *Nuclear Fusion*, 54(11):114012, nov 2014. doi:[10.1088/0029-5515/54/11/114012](https://doi.org/10.1088/0029-5515/54/11/114012). URL <https://doi.org/10.1088/0029-5515/54/11/114012>.
- [34] T. Eich, R.J. Goldston, A. Kallenbach, B. Sieglin, H.J. Sun, and and. Correlation of the tokamak H-mode density limit with ballooning stability at the separatrix. *Nuclear Fusion*, 58(3):034001, 2018. doi:[10.1088/1741-4326/aaa340](https://doi.org/10.1088/1741-4326/aaa340).
- [35] J.P. Gunn, S. Carpentier-Chouchana, F. Escourbiac, T. Hirai, S. Panayotis, R.A. Pitts, Y. Corre, R. Dejarnac, M. Firdaouss, M. Kočan, M. Komm, A. Kukushkin, P. Languille, M. Missirlian, W. Zhao, and G. Zhong. Surface heat loads on the ITER divertor vertical targets. *Nuclear Fusion*, 57(4):046025, mar 2017. doi:[10.1088/1741-4326/aa5e2a](https://doi.org/10.1088/1741-4326/aa5e2a). URL <https://doi.org/10.1088/1741-4326/aa5e2a>.
- [36] G. T. A. Huijsmans, C. S. Chang, N. Ferraro, L. Sugiyama, F. Waelbroeck, X. Q. Xu, A. Loarte, and S. Futatani. Modelling of edge localised modes and edge localised mode control. *Physics of Plasmas*, 22(2):021805, 2015. doi:[10.1063/1.4905231](https://doi.org/10.1063/1.4905231).
- [37] A. Cathey, M. Hoelzl, K. Lackner, G.T.A. Huijsmans, M.G. Dunne, E. Wolfrum, S.J.P. Pamela, F. Orain, and S. Günter. Non-linear extended MHD simulations of type-I edge localised mode cycles in ASDEX Upgrade and their underlying triggering mechanism. *Nuclear Fusion*, 60(12):124007, nov 2020. doi:[10.1088/1741-4326/abbc87](https://doi.org/10.1088/1741-4326/abbc87).
- [38] E. Viezzer. Access and sustainment of naturally ELM-free and small-ELM regimes. *Nuclear Fusion*, 58(11):115002, sep 2018. doi:[10.1088/1741-4326/aac222](https://doi.org/10.1088/1741-4326/aac222). URL <https://doi.org/10.1088/1741-4326/aac222>.
- [39] P.T. Lang, A. Loarte, G. Saibene, L.R. Baylor, M. Becoulet, M. Cavinato, S. Clement-Lorenzo, E. Daly, T.E. Evans, M.E. Fenstermacher, Y. Gribov, L.D. Horton, C. Lowry, Y. Martin, O. Neubauer, N. Oyama, M.J. Schaffer, D. Stork, W. Suttrop, P. Thomas, M. Tran, H.R. Wilson, A. Kavin, and O. Schmitz. ELM control strategies and tools: status and potential for ITER. *Nuclear Fusion*, 53(4):043004, mar 2013. doi:[10.1088/0029-5515/53/4/043004](https://doi.org/10.1088/0029-5515/53/4/043004). URL <https://doi.org/10.1088/0029-5515/53/4/043004>.
- [40] Georg Harrer. *On the origin and transport of small ELMs*. PhD thesis, Technische Universität Wien Wien, 2020.

## Bibliography

---

- [41] B. Labit, T. Eich, G.F. Harrer, E. Wolfrum, M. Bernert, M.G. Dunne, L. Frassinetti, P. Hennequin, R. Maurizio, A. Merle, et al. Dependence on plasma shape and plasma fueling for small edge-localized mode regimes in TCV and ASDEX upgrade. *Nuclear Fusion*, 59(8):086020, jun 2019. doi:[10.1088/1741-4326/ab2211](https://doi.org/10.1088/1741-4326/ab2211). URL <https://doi.org/10.1088/1741-4326/ab2211>.
- [42] G.F. Harrer, E. Wolfrum, M.G. Dunne, P. Manz, M. Cavedon, P.T. Lang, B. Kurzan, T. Eich, B. Labit, J. Stober, H. Meyer, M. Bernert, F.M. Laggner, F. Aumayr, and and. Parameter dependences of small edge localized modes (ELMs). *Nuclear Fusion*, 58(11):112001, sep 2018. doi:[10.1088/1741-4326/aad757](https://doi.org/10.1088/1741-4326/aad757). URL <https://doi.org/10.1088/1741-4326/aad757>.
- [43] P.T. Lang, D. Frigione, A. Géraud, T. Alarcon, P. Bennett, G. Cseh, D. Garnier, L. Garzotti, F. Köchl, G. Kocsis, M. Lennholm, R. Neu, R. Mooney, S. Saarelma, and B. Sieglin and. ELM pacing and trigger investigations at JET with the new ITER-like wall. *Nuclear Fusion*, 53(7):073010, may 2013. doi:[10.1088/0029-5515/53/7/073010](https://doi.org/10.1088/0029-5515/53/7/073010). URL <https://doi.org/10.1088/0029-5515/53/7/073010>.
- [44] P.T. Lang, A. Burckhart, M. Bernert, L. Casali, R. Fischer, O. Kardaun, G. Kocsis, M. Maraschek, A. Mlynek, B. Plöckl, M. Reich, F. Ryter, J. Schweinzer, B. Sieglin, W. Suttrop, T. Szepesi, G. Tardini, E. Wolfrum, D. Zasche, and H. Zohm and. ELM pacing and high-density operation using pellet injection in the ASDEX Upgrade all-metal-wall tokamak. *Nuclear Fusion*, 54(8):083009, jun 2014. doi:[10.1088/0029-5515/54/8/083009](https://doi.org/10.1088/0029-5515/54/8/083009). URL <https://doi.org/10.1088/0029-5515/54/8/083009>.
- [45] S. Futatani, A. Cathey, M. Hoelzl, P.T. Lang, G.T.A. Huijsmans, M. Dunne, the JOREK Team, the ASDEX Upgrade Team, and the EUROfusion MST1 Team. Transition from no-ELM response to pellet ELM triggering during pedestal build-up—insights from extended MHD simulations. *Nuclear Fusion*, 61(4):046043, mar 2021. doi:[10.1088/1741-4326/abdfb4](https://doi.org/10.1088/1741-4326/abdfb4).
- [46] A. Cathey, M. Hoelzl, S. Futatani, P. T. Lang, K. Lackner, G. T. A. Huijsmans, S. J. P. Pamela, S. Günter, the JOREK team, the ASDEX Upgrade Team, and the EUROfusion MST1 Team. Comparing spontaneous and pellet-triggered ELMs via non-linear extended MHD simulations. *Plasma Physics and Controlled Fusion*, 2021. doi:<https://doi.org/10.1088/1361-6587/abf80b>.
- [47] G T A Huysmans. External kink (peeling) modes in X-point geometry. *Plasma Physics and Controlled Fusion*, 47(12):2107–2121, 2005. doi:[10.1088/0741-3335/47/12/003](https://doi.org/10.1088/0741-3335/47/12/003).

- [48] G.T.A. Huijsmans and O. Czarny. MHD stability in X-point geometry: simulation of ELMs. *Nuclear Fusion*, 47(7):659, 2007. doi:[10.1088/0029-5515/47/7/016](https://doi.org/10.1088/0029-5515/47/7/016).
- [49] Olivier Czarny and Guido Huijsmans. Bezier surfaces and finite elements for MHD simulations. *Journal of Computational Physics*, 227(16):7423 – 7445, 2008. ISSN 0021-9991. doi:[10.1016/j.jcp.2008.04.001](https://doi.org/10.1016/j.jcp.2008.04.001).
- [50] M Hoelzl, GTA Huijsmans, SJP Pamela, M Becoulet, E Nardon, FJ Artola, B Nkonga, CV Atanasiu, V Bandaru, A Bhole, D Bonfiglio, A Cathey, O Czarny, A Dvornova, T Feher, A Fil, E Franck, S Futatani, M Gruca, H Guillard, JW Haverkort, I Holod, D Hu, SK Kim, SQ Korving, L Kos, I Krebs, L Kripner, G Latu, F Liu, P Merkel, D Meshcheriakov, V Mitterauer, S Mochalskyy, JA Morales, R Nies, N Nikulsin, F Orain, D Penko, J Pratt, R Ramasamy, P Ramet, C Reux, N Schwarz, P Singh Verma, SF Smith, C Sommariva, E Strumberger, DC vanVugt, M Verbeek, E Westerhof, F Wieschollek, and J Zielinski. The JOREK non-linear extended MHD code and applications to large-scale instabilities and their control in magnetically confined fusion plasmas. *Nuclear Fusion*, 2021. doi:<https://doi.org/10.1088/1741-4326/abf99f>. URL <http://iopscience.iop.org/article/10.1088/1741-4326/abf99f>. preprint at <https://arxiv.org/abs/2011.09120>.
- [51] Richard Fitzpatrick. *Plasma physics: an introduction*. Crc Press, 2014. URL <http://farside.ph.utexas.edu/teaching/plasma/Plasma/index.html>.
- [52] E Franck, M Hoelzl, A Lessig, and E Sonnendrücker. Energy conservation and numerical stability for the reduced MHD models of the non-linear JOREK code. *ESAIM: M2AN*, 49(5):1331–1365, 2015. doi:[10.1051/m2an/2015014](https://doi.org/10.1051/m2an/2015014). preprint at <https://arxiv.org/abs/1408.2099>.
- [53] Hervé Guillard. The mathematical theory of reduced MHD models for fusion plasmas. Research Report RR-8715, INRIA, April 2015. URL <https://hal.inria.fr/hal-01145009>.
- [54] Dalton D. Schnack. *Lectures in Magnetohydrodynamics*. Springer, 2009. ISBN 978-3-642-00688-3. doi:[10.1007/978-3-642-00688-3](https://doi.org/10.1007/978-3-642-00688-3).
- [55] Jeffrey P. Freidberg. *Ideal MHD*. Cambridge University Press, 2014. doi:[10.1017/CBO9780511795046](https://doi.org/10.1017/CBO9780511795046).
- [56] S. J. P. Pamela, A. Bhole, G. T. A. Huijsmans, B. Nkonga, M. Hoelzl, I. Krebs, and E. Strumberger. Extended full-MHD simulation of non-linear instabilities in tokamak plasmas. *Physics of Plasmas*, 27(10):102510, 2020. doi:[10.1063/5.0018208](https://doi.org/10.1063/5.0018208). URL <https://doi.org/10.1063/5.0018208>.

- [57] A H Glasser, C R Sovinec, R A Nebel, T A Gianakon, S J Plimpton, M S Chu, D D Schnack, and the NIMROD Team. The NIMROD code: a new approach to numerical plasma physics. *Plasma Physics and Controlled Fusion*, 41(3A): A747–A755, jan 1999. doi:[10.1088/0741-3335/41/3a/067](https://doi.org/10.1088/0741-3335/41/3a/067).
- [58] Y. Todo and T. Sato. Linear and nonlinear particle-magnetohydrodynamic simulations of the toroidal Alfvén eigenmode. *Physics of Plasmas*, 5(5):1321–1327, 1998. doi:[10.1063/1.872791](https://doi.org/10.1063/1.872791).
- [59] Harold Grad and Hanan Rubin. Hydromagnetic equilibria and force-free fields. *Journal of Nuclear Energy (1954)*, 7(3-4):284–285, 1958. URL <https://www.math.nyu.edu/mfdd/files/HaroldGradPapers/Grad.Rubin%20-%20Hydromagnetic%20equilibria%20and%20force%20free%20fields.pdf>.
- [60] VD Shafranov. Plasma equilibrium in a magnetic field. *Reviews of plasma physics*, 2:103, 1966.
- [61] H.R. Strauss. Finite-aspect-ratio MHD equations for tokamaks. *Nuclear Fusion*, 23(5):649–655, may 1983. doi:[10.1088/0029-5515/23/5/006](https://doi.org/10.1088/0029-5515/23/5/006).
- [62] H. R. Strauss. Reduced MHD in nearly potential magnetic fields. *Journal of Plasma Physics*, 57(1):83–87, 1997. doi:[10.1017/S0022377896005296](https://doi.org/10.1017/S0022377896005296).
- [63] J P Graves, D Zullino, D Brunetti, S Lanthaler, and C Wahlberg. Reduced models for parallel magnetic field fluctuations and their impact on pressure gradient driven MHD instabilities in axisymmetric toroidal plasmas. *Plasma Physics and Controlled Fusion*, 61(10):104003, aug 2019. doi:[10.1088/1361-6587/ab368b](https://doi.org/10.1088/1361-6587/ab368b).
- [64] Eleonora Viezzer. *Radial electric field studies in the plasma edge of ASDEX Upgrade*. PhD thesis, Ludwig-Maximilians-Universität München, February 2013. URL <http://nbn-resolving.de/urn:nbn:de:bvb:19-161574>.
- [65] F. Orain, M. Bécoulet, G. T. A. Huijsmans, G. Dif-Pradalier, M. Hoelzl, J. Morales, X. Garbet, E. Nardon, S. Pamela, C. Passeron, G. Latu, A. Fil, and P. Cahyna. Resistive reduced MHD modeling of multi-edge-localized-mode cycles in tokamak X-point plasmas. *Phys. Rev. Lett.*, 114:035001, Jan 2015. doi:[10.1103/PhysRevLett.114.035001](https://doi.org/10.1103/PhysRevLett.114.035001).
- [66] O. Sauter, C. Angioni, and Y. R. Lin-Liu. Neoclassical conductivity and bootstrap current formulas for general axisymmetric equilibria and arbitrary collisionality regime. *Physics of Plasmas*, 6(7):2834–2839, 1999. doi:[10.1063/1.873240](https://doi.org/10.1063/1.873240).
- [67] O. Sauter, C. Angioni, and Y. R. Lin-Liu. Erratum: “neoclassical conductivity and bootstrap current formulas for general axisymmetric equilibria and

- arbitrary collisionality regime” [phys. plasmas 6, 2834 (1999)]. *Physics of Plasmas*, 9(12):5140–5140, 2002. doi:[10.1063/1.1517052](https://doi.org/10.1063/1.1517052).
- [68] Matthias Hölzl. *Diffusive Heat Transport across Magnetic Islands and Stochastic Layers in Tokamaks*. Dissertation, Technische Universität München, 2010. URL <https://mediatum.ub.tum.de/820982>.
- [69] N Aiba. Impact of ion diamagnetic drift on ideal ballooning mode stability in rotating tokamak plasmas. *Plasma Physics and Controlled Fusion*, 58(4):045020, feb 2016. doi:[10.1088/0741-3335/58/4/045020](https://doi.org/10.1088/0741-3335/58/4/045020). URL <https://doi.org/10.1088/0741-3335/58/4/045020>.
- [70] E. Viezzer, T. Puetterich, C. Angioni, A. Bergmann, R. Dux, E. Fable, R.M. McDermott, U. Stroth, E. Wolfrum, and the ASDEX Upgrade Team. Evidence for the neoclassical nature of the radial electric field in the edge transport barrier of ASDEX Upgrade. *Nuclear Fusion*, 54(1):012003, 2014. URL <http://stacks.iop.org/0029-5515/54/i=1/a=012003>.
- [71] B. N. Rogers and J. F. Drake. Diamagnetic stabilization of ideal ballooning modes in the edge pedestal. *Physics of Plasmas*, 6(7):2797–2801, 1999. doi:[10.1063/1.873237](https://doi.org/10.1063/1.873237).
- [72] G. T. A. Huysmans, S. E. Sharapov, A. B. Mikhailovskii, and W. Kerner. Modeling of diamagnetic stabilization of ideal magnetohydrodynamic instabilities associated with the transport barrier. *Physics of Plasmas*, 8(10):4292–4305, 2001. doi:[10.1063/1.1398573](https://doi.org/10.1063/1.1398573).
- [73] R. J. Hastie, Peter J. Catto, and J. J. Ramos. Effect of strong radial variation of the ion diamagnetic frequency on internal ballooning modes. *Physics of Plasmas*, 7(11):4561–4566, 2000. doi:[10.1063/1.1310201](https://doi.org/10.1063/1.1310201).
- [74] E. Nardon, M. Bécoulet, G. Huysmans, and O. Czarny. Magnetohydrodynamics modelling of H-mode plasma response to external resonant magnetic perturbations. *Physics of Plasmas*, 14(9):092501, 2007. doi:[10.1063/1.2759889](https://doi.org/10.1063/1.2759889).
- [75] G T A Huysmans, S Pamela, E van der Plas, and P Ramet. Non-linear MHD simulations of edge localized modes (ELMs). *Plasma Physics and Controlled Fusion*, 51(12):124012, 2009. URL <http://stacks.iop.org/0741-3335/51/i=12/a=124012>.
- [76] S. Futatani, G. Huijsmans, A. Loarte, L.R. Baylor, N. Commaux, T.C. Jernigan, M.E. Fenstermacher, C. Lasnier, T.H. Osborne, and B. Pegourié. Non-linear MHD modelling of ELM triggering by pellet injection in DIII-D and implications for ITER. *Nuclear Fusion*, 54(7):073008, 2014. URL <http://stacks.iop.org/0029-5515/54/i=7/a=073008>.

## Bibliography

---

- [77] F.J. Artola, G.T.A. Huijsmans, M. Hoelzl, P. Beyer, A. Loarte, and Y. Grivov. Non-linear magnetohydrodynamic simulations of edge localised mode triggering via vertical position oscillations in ITER. *Nuclear Fusion*, 58(9):096018, jul 2018. doi:[10.1088/1741-4326/aace0e](https://doi.org/10.1088/1741-4326/aace0e).
- [78] E Nardon, A Fil, M Hoelzl, G Huijsmans, and JET contributors. Progress in understanding disruptions triggered by massive gas injection via 3D non-linear MHD modelling with JOREK. *Plasma Physics and Controlled Fusion*, 59(1):014006, 2017. URL <http://stacks.iop.org/0741-3335/59/i=1/a=014006>.
- [79] D. Hu, E. Nardon, G.T.A. Huijsmans, and M. Lehnen. Investigation of MHD activity caused by shattered pellet injection via JOREK 3D non-linear MHD simulation. In *44th European Physical Society Conference on Plasma Physics (EPS), Belfast, Northern Ireland*, page P2.142, 2017. URL <http://ocs.ciemat.es/EPS2017PAP/pdf/P2.142.pdf>.
- [80] Fabian Wieschollek. Non-linear MHD simulation of mode locking and disruption onset. Master's thesis, Technische Universität München, 5 2019.
- [81] G.T.A. Huysmans and O. Czarny. Implementation of cubic Bezier elements in the non-linear MHD code JOREK (technical report, project ASTER). Technical report, ANR, 2006. URL [http://aster.gforge.inria.fr/reports/huysmans\\_report\\_aster\\_001.pdf](http://aster.gforge.inria.fr/reports/huysmans_report_aster_001.pdf).
- [82] S J P Pamela, G T A Huijsmans, A Kirk, I T Chapman, J R Harrison, R Scannell, A J Thornton, M Becoulet, and F Orain and. Resistive MHD simulation of edge-localized-modes for double-null discharges in the MAST device. *Plasma Physics and Controlled Fusion*, 55(9):095001, jul 2013. doi:[10.1088/0741-3335/55/9/095001](https://doi.org/10.1088/0741-3335/55/9/095001).
- [83] Lyman Spitzer and Richard Härm. Transport phenomena in a completely ionized gas. *Phys. Rev.*, 89:977–981, Mar 1953. doi:[10.1103/PhysRev.89.977](https://doi.org/10.1103/PhysRev.89.977).
- [84] M. Hoelzl, D. Hu, E. Nardon, and G. T. A. Huijsmans. First predictive simulations for deuterium shattered pellet injection in ASDEX Upgrade. *Physics of Plasmas*, 27(2):022510, 2020. doi:[10.1063/1.5133099](https://doi.org/10.1063/1.5133099).
- [85] Peter C Stangeby et al. *The plasma boundary of magnetic fusion devices*, volume 224. Institute of Physics Pub. Philadelphia, Pennsylvania, 2000. doi:[10.1201/9780367801489](https://doi.org/10.1201/9780367801489).
- [86] Y R Martin, T Takizuka, and the ITPA CDBM H-mode Threshold Data Group. Power requirement for accessing the h-mode in ITER. *Journal of Physics: Conference Series*, 123:012033, jul 2008. doi:[10.1088/1742-6596/123/1/012033](https://doi.org/10.1088/1742-6596/123/1/012033).

- [87] H. Biglari, P. H. Diamond, and P. W. Terry. Influence of sheared poloidal rotation on edge turbulence. *Physics of Fluids B: Plasma Physics*, 2(1):1–4, 1990. doi:[10.1063/1.859529](https://doi.org/10.1063/1.859529).
- [88] R. J. Groebner, K. H. Burrell, and R. P. Seraydarian. Role of edge electric field and poloidal rotation in the L-H transition. *Physical Review Letters*, 64(25):3015–3018, Jun 1990. doi:[10.1103/PhysRevLett.64.3015](https://doi.org/10.1103/PhysRevLett.64.3015).
- [89] J W Connor and H R Wilson. A review of theories of the l-h transition. *Plasma Physics and Controlled Fusion*, 42(1):R1–R74, dec 1999. doi:[10.1088/0741-3335/42/1/201](https://doi.org/10.1088/0741-3335/42/1/201).
- [90] T. Eich, B. Sieglin, A.J. Thornton, M. Faitsch, A. Kirk, A. Herrmann, and W. Suttrop. ELM divertor peak energy fluence scaling to iter with data from jet, mast and ASDEX Upgrade. *Nuclear Materials and Energy*, 12:84, 2017. ISSN 2352-1791. doi:[10.1016/j.nme.2017.04.014](https://doi.org/10.1016/j.nme.2017.04.014).
- [91] P. B. Snyder, H. R. Wilson, J. R. Ferron, L. L. Lao, A. W. Leonard, T. H. Osborne, A. D. Turnbull, D. Mossessian, M. Murakami, and X. Q. Xu. Edge localized modes and the pedestal: A model based on coupled peeling–ballooning modes. *Physics of Plasmas*, 9(5):2037–2043, 2002. doi:[10.1063/1.1449463](https://doi.org/10.1063/1.1449463).
- [92] Y Kamada, T Oikawa, L Lao, T Takizuka, T Hatae, A Isayama, J Manickam, M Okabayashi, T Fukuda, and K Tsuchiya. Disappearance of giant ELMs and appearance of minute grassy ELMs in JT-60u high-triangularity discharges. *Plasma Physics and Controlled Fusion*, 42(5A):A247–A253, may 2000. doi:[10.1088/0741-3335/42/5a/329](https://doi.org/10.1088/0741-3335/42/5a/329). URL <https://doi.org/10.1088/0741-3335/42/5a/329>.
- [93] G Saibene, P.J Lomas, R Sartori, A Loarte, J Stober, Y Andrew, S.A Arshad, G.D Conway, E. de la Luna, K Günther, L.C Ingesson, M.A.H Kempenaars, A Korotkov, H.R Koslowski, J.S Lönnroth, D.C McDonald, A Meigs, P Monier-Garbet, V Parail, C.P Perez, F.G Rimini, S Sharapov, and P.R Thomas. Characterization of small ELM experiments in highly shaped single null and quasi-double-null plasmas in JET. *Nuclear Fusion*, 45(5):297–317, apr 2005. doi:[10.1088/0029-5515/45/5/001](https://doi.org/10.1088/0029-5515/45/5/001). URL <https://doi.org/10.1088/0029-5515/45/5/001>.
- [94] N Oyama, P Gohil, L D Horton, A E Hubbard, J W Hughes, Y Kamada, K Kamiya, A W Leonard, A Loarte, R Maingi, G Saibene, R Sartori, J K Stober, W Suttrop, H Urano, W P West, and the ITPA Pedestal Topical Group. Pedestal conditions for small ELM regimes in tokamaks. *Plasma Physics and Controlled Fusion*, 48(5A):A171–A181, apr 2006. doi:[10.1088/0741-3335/48/5a/s16](https://doi.org/10.1088/0741-3335/48/5a/s16). URL <https://doi.org/10.1088/0741-3335/48/5a/s16>.
- [95] J Stober, M Maraschek, G.D Conway, O Gruber, A Herrmann, A.C.C Sips, W Treutterer, H Zohm, and ASDEX Upgrade Team. Type II ELMy h modes

## Bibliography

---

- on ASDEX upgrade with good confinement at high density. *Nuclear Fusion*, 41(9):1123–1134, sep 2001. doi:[10.1088/0029-5515/41/9/301](https://doi.org/10.1088/0029-5515/41/9/301). URL <https://doi.org/10.1088/0029-5515/41/9/301>.
- [96] Elisabeth Wolfrum, M Bernert, JE Boom, A Burckhart, IGJ Classen, GD Conway, T Eich, R Fischer, A Gude, A Herrmann, et al. Characterization of edge profiles and fluctuations in discharges with type-ii and nitrogen-mitigated edge localized modes in asdex upgrade. *Plasma Physics and Controlled Fusion*, 53(8):085026, 2011. doi:[10.1088/0741-3335/53/8/085026](https://doi.org/10.1088/0741-3335/53/8/085026).
- [97] R Sartori, G Saibene, L D Horton, M Becoulet, R Budny, D Borba, A Chankin, G D Conway, G Cordey, D McDonald, K Guenther, M G von Hellermann, Yu Igithkanov, A Loarte, P J Lomas, O Pogutse, and J Rapp. Study of type III ELMs in JET. *Plasma Physics and Controlled Fusion*, 46 (5):723–750, mar 2004. doi:[10.1088/0741-3335/46/5/002](https://doi.org/10.1088/0741-3335/46/5/002).
- [98] A Loarte, G Saibene, R Sartori, D Campbell, M Becoulet, L Horton, T Eich, A Herrmann, G Matthews, N Asakura, A Chankin, A Leonard, G Porter, G Federici, G Janeschitz, M Shimada, and M Sugihara. Characteristics of type I ELM energy and particle losses in existing devices and their extrapolation to iter. *Plasma Physics and Controlled Fusion*, 45(9):1549, 2003. URL <http://stacks.iop.org/0741-3335/45/i=9/a=302>.
- [99] A. E. Hubbard, R. L. Boivin, R. S. Granetz, M. Greenwald, J. W. Hughes, I. H. Hutchinson, J. Irby, B. LaBombard, Y. Lin, E. S. Marmar, A. Mazurenko, D. Mossessian, E. Nelson-Melby, M. Porkolab, J. A. Snipes, J. Terry, S. Wolfe, S. Wukitch, B. A. Carreras, V. Klein, and T. Sunn Pedersen. Pedestal profiles and fluctuations in c-mod enhanced d-alpha h-modes. *Physics of Plasmas*, 8(5):2033–2040, 2001. doi:[10.1063/1.1348329](https://doi.org/10.1063/1.1348329).
- [100] L. Gil, C. Silva, T. Happel, G. Birkenmeier, G.D. Conway, L. Guimarais, A. Kallenbach, T. Pütterich, J. Santos, P.A. Schneider, M. Schubert, E. Selinin, A. Silva, J. Stober, U. Stroth, E. Trier, E. Wolfrum, and and. Stationary ELM-free h-mode in ASDEX upgrade. *Nuclear Fusion*, 60(5):054003, apr 2020. doi:[10.1088/1741-4326/ab7d1b](https://doi.org/10.1088/1741-4326/ab7d1b). URL <https://doi.org/10.1088/1741-4326/ab7d1b>.
- [101] A. Loarte, G. Huijsmans, S. Futatani, L.R. Baylor, T.E. Evans, D. M. Orlov, O. Schmitz, M. Becoulet, P. Cahyna, Y. Gribov, A. Kavin, A. Sashala Naik, D.J. Campbell, T. Casper, E. Daly, H. Frerichs, A. Kischnner, R. Laengner, S. Lisgo, R.A. Pitts, G. Saibene, and A. Wingen. Progress on the application of ELM control schemes to ITER scenarios from the non-active phase to DT operation. *Nuclear Fusion*, 54(3):033007, feb 2014. doi:[10.1088/0029-5515/54/3/033007](https://doi.org/10.1088/0029-5515/54/3/033007). URL <https://doi.org/10.1088/0029-5515/54/3/033007>.

- [102] R P Wenninger, T H Eich, G T A Huysmans, P T Lang, S Devaux, S Jachmich, F Köchl, and JET EFDA Contributors. Scrape-off layer heat transport and divertor power deposition of pellet-induced edge localized modes. *Plasma Physics and Controlled Fusion*, 53(10):105002, aug 2011. doi:[10.1088/0741-3335/53/10/105002](https://doi.org/10.1088/0741-3335/53/10/105002).
- [103] Shimpei Futatani, Andres Cathey, Matthias Hoelzl, Peter Lang, Guido Huijsmans, and Mike G Dunne. Transition from no-elm response to pellet elm triggering during pedestal build-up – insights from extended mhd simulations. *Nuclear Fusion*, 2021. URL <http://iopscience.iop.org/article/10.1088/1741-4326/abdfb4>.
- [104] C.F. Maggi, S. Saarelma, F.J. Casson, C. Challis, E. de la Luna, L. Frassinetti, C. Giroud, E. Joffrin, J. Simpson, M. Beurskens, I. Chapman, J. Hoibirk, M. Leyland, P. Lomas, C. Lowry, I. Nunes, F. Rimini, A.C.C. Sips, and H. Urano. Pedestal confinement and stability in JET-ILW ELMMy h-modes. *Nuclear Fusion*, 55(11):113031, sep 2015. doi:[10.1088/0029-5515/55/11/113031](https://doi.org/10.1088/0029-5515/55/11/113031). URL <https://doi.org/10.1088/0029-5515/55/11/113031>.
- [105] A. Burckhart, M. Dunne, E. Wolfrum, R. Fischer, R. McDermott, E. Viezzer, and M. Willensdorfer and. ELM behaviour and linear MHD stability of edge ECRH heated ASDEX upgrade plasmas. *Nuclear Fusion*, 56(5):056011, apr 2016. doi:[10.1088/0029-5515/56/5/056011](https://doi.org/10.1088/0029-5515/56/5/056011). URL <https://doi.org/10.1088/0029-5515/56/5/056011>.
- [106] ITER Physics Expert Group on Disrup MHD and ITER Physics Basis Editors. Chapter 3: MHD stability, operational limits and disruptions. *Nuclear Fusion*, 39(12):2251–2389, dec 1999. doi:[10.1088/0029-5515/39/12/303](https://doi.org/10.1088/0029-5515/39/12/303). URL <https://doi.org/10.1088/0029-5515/39/12/303>.
- [107] P A Schneider, E Wolfrum, M G. Dunne, R Dux, A Gude, B Kurzan, T Pütterich, S K. Rathgeber, J Vicente, A Weller, R Wenninger, and the ASDEX Upgrade Team. Observation of different phases during an ELM crash with the help of nitrogen seeding. *Plasma Physics and Controlled Fusion*, 56(2):025011, 2014. URL <http://stacks.iop.org/0741-3335/56/i=2/a=025011>.
- [108] L. Frassinetti, M.G. Dunne, M. Beurskens, E. Wolfrum, A. Bogomolov, D. Carralero, M. Cavedon, R. Fischer, F.M. Laggner, R.M. McDermott, H. Meyer, G. Tardini, E. Viezzer, and and. ELM behavior in ASDEX upgrade with and without nitrogen seeding. *Nuclear Fusion*, 57(2):022004, sep 2016. doi:[10.1088/0029-5515/57/2/022004](https://doi.org/10.1088/0029-5515/57/2/022004). URL <https://doi.org/10.1088/0029-5515/57/2/022004>.
- [109] F.Mink, M.Hoelzl, E.Wolfrum, F.Orain, M.Dunne, A.Lessig, S.Pamela, P.Manz, M.Maraschek, G.T.A.Huijsmans, M.Becoulet, F.M.Laggner,

## Bibliography

---

- M.Cavedon, K.Lackner, S.Guenter, U.Stroth, and the ASDEX Upgrade Team. Nonlinear coupling induced toroidal structure of edge localized modes. *Nuclear Fusion*, 58:026011, 2018. doi:[10.1088/1741-4326/aa98f7](https://doi.org/10.1088/1741-4326/aa98f7).
- [110] M Cavedon, T Pütterich, E Viezzer, F M Laggner, A Burckhart, M Dunne, R Fischer, A Lebschy, F Mink, U Stroth, M Willensdorfer, and E Wolfrum and. Pedestal and profile evolution during an edge localized mode cycle at ASDEX upgrade. *Plasma Physics and Controlled Fusion*, 59(10):105007, aug 2017. doi:[10.1088/1361-6587/aa7ad0](https://doi.org/10.1088/1361-6587/aa7ad0). URL <https://doi.org/10.1088/1361-6587/aa7ad0>.
- [111] R.J. Groebner, T.H. Osborne, A.W. Leonard, and M.E. Fenstermacher. Temporal evolution of h-mode pedestal in DIII-d. *Nuclear Fusion*, 49(4):045013, mar 2009. doi:[10.1088/0029-5515/49/4/045013](https://doi.org/10.1088/0029-5515/49/4/045013). URL <https://doi.org/10.1088/0029-5515/49/4/045013>.
- [112] A Burckhart, E Wolfrum, R Fischer, K Lackner, H Zohm, and the ASDEX Upgrade Team. Inter-ELM behaviour of the electron density and temperature pedestal in ASDEX Upgrade. *Plasma Physics and Controlled Fusion*, 52 (10):105010, 2010. URL <http://stacks.iop.org/0741-3335/52/i=10/a=105010>.
- [113] F M Laggner, E Wolfrum, M Cavedon, F Mink, E Viezzer, M G Dunne, P Manz, H Doerk, G Birkenmeier, R Fischer, S Fietz, M Maraschek, M Willensdorfer, F Aumayr, the EUROfusion MST1 Team, and the ASDEX Upgrade Team. High frequency magnetic fluctuations correlated with the inter-ELM pedestal evolution in ASDEX Upgrade. *Plasma Physics and Controlled Fusion*, 58(6):065005, 2016. URL <http://stacks.iop.org/0741-3335/58/i=6/a=065005>.
- [114] C.F. Maggi, L. Frassinetti, L. Horvath, A. Lunniss, S. Saarelma, H. Wilson, J. Flanagan, M. Leyland, I. Lupelli, S. Pamela, H. Urano, L. Garzotti, E. Lerche, I. Nunes, and F. Rimini and. Studies of the pedestal structure and inter-ELM pedestal evolution in JET with the ITER-like wall. *Nuclear Fusion*, 57(11):116012, aug 2017. doi:[10.1088/1741-4326/aa7e8e](https://doi.org/10.1088/1741-4326/aa7e8e). URL <https://doi.org/10.1088/1741-4326/aa7e8e>.
- [115] C.P. Perez, H.R. Koslowski, G.T.A. Huysmans, T.C. Hender, P. Smeulders, B. Alper, E. de la Luna, R.J. Hastie, L. Meneses, M.F.F. Nave, V. Parail, M. Zerbini, and JET-EFDA Contributors. Type-i ELM precursor modes in jet. *Nuclear Fusion*, 44(5):609, 2004. URL <http://stacks.iop.org/0029-5515/44/i=5/a=005>.
- [116] A. Diallo, J. W. Hughes, M. Greenwald, B. LaBombard, E. Davis, S-G. Baek, C. Theiler, P. Snyder, J. Canik, J. Walk, T. Golfinopoulos, J. Terry, M. Churchill, A. Hubbard, M. Porkolab, L. Delgado-Aparicio, M. L. Reinke,

- A. White, and Alcator C-Mod team. Observation of edge instability limiting the pedestal growth in tokamak plasmas. *Phys. Rev. Lett.*, 112:115001, Mar 2014. doi:[10.1103/PhysRevLett.112.115001](https://doi.org/10.1103/PhysRevLett.112.115001).
- [117] J.E. Lee, G.S. Yun, M. Kim, J. Lee, W. Lee, H.K. Park, C.W. Domier, N.C. Luhmann, and W.H. Ko and. Toroidal mode number transition of the edge localized modes in the KSTAR plasmas. *Nuclear Fusion*, 55(11):113035, sep 2015. doi:[10.1088/0029-5515/55/11/113035](https://doi.org/10.1088/0029-5515/55/11/113035). URL <https://doi.org/10.1088/0029-5515/55/11/113035>.
- [118] A. Diallo, J. Dominski, K. Barada, M. Knolker, G. J. Kramer, and G. Mc-Kee. Direct observation of nonlinear coupling between pedestal modes leading to the onset of edge localized modes. *Phys. Rev. Lett.*, 121:235001, Dec 2018. doi:[10.1103/PhysRevLett.121.235001](https://doi.org/10.1103/PhysRevLett.121.235001). URL <https://link.aps.org/doi/10.1103/PhysRevLett.121.235001>.
- [119] B. Vanovac, E. Wolfrum, M. Hoelzl, M. Willensdorfer, M. Cavedon, G.F. Harrer, F. Mink, S.S. Denk, S. Freethy, M. Dunne, P. Manz, and N.C. Luhmann and. Characterization of low-frequency inter-ELM modes of h-mode discharges at ASDEX upgrade. *Nuclear Fusion*, 58(11):112011, oct 2018. doi:[10.1088/1741-4326/aada20](https://doi.org/10.1088/1741-4326/aada20).
- [120] A L Colton, R J Buttery, S J Fielding, D A Gates, T C Hender, J Hugill, A W Morris, M Valovic, the COMPASS-D, and ECRH teams. ELM studies on the COMPASS-d tokamak. *Plasma Physics and Controlled Fusion*, 38(8):1359–1365, aug 1996. doi:[10.1088/0741-3335/38/8/037](https://doi.org/10.1088/0741-3335/38/8/037). URL <https://doi.org/10.1088/0741-3335/38/8/037>.
- [121] W Suttrop, K Büchl, H J de Blank, J Schweinzer, H Zohm, ASDEX Upgrade team, NBI group, and ICRH group. Characteristics of edge localized modes in ASDEX upgrade. *Plasma Physics and Controlled Fusion*, 38(8):1407–1410, aug 1996. doi:[10.1088/0741-3335/38/8/045](https://doi.org/10.1088/0741-3335/38/8/045). URL <https://doi.org/10.1088/0741-3335/38/8/045>.
- [122] M Manso, F Serra, B Kurzan, I Nunes, J Santos, A Silva, W Suttrop, P Varela, and S Vergamota. H-mode studies with microwave reflectometry on ASDEX upgrade. *Plasma Physics and Controlled Fusion*, 40(5):747–752, may 1998. doi:[10.1088/0741-3335/40/5/036](https://doi.org/10.1088/0741-3335/40/5/036). URL <https://doi.org/10.1088/0741-3335/40/5/036>.
- [123] T Kass, S Günter, M Maraschek, W Suttrop, H Zohm, and ASDEX Upgrade Team. Characteristics of type i and type III ELM precursors in ASDEX upgrade. *Nuclear Fusion*, 38(1):111–116, jan 1998. doi:[10.1088/0029-5515/38/1/310](https://doi.org/10.1088/0029-5515/38/1/310). URL <https://doi.org/10.1088/0029-5515/38/1/310>.
- [124] T Bolzonella, H Zohm, M Maraschek, E Martines, S Saarelma, S Günter, and ASDEX Upgrade Team. High frequency MHD activity related to type i

## Bibliography

---

- ELMs in ASDEX upgrade. *Plasma Physics and Controlled Fusion*, 46(5A): A143–A149, apr 2004. doi:[10.1088/0741-3335/46/5a/015](https://doi.org/10.1088/0741-3335/46/5a/015). URL <https://doi.org/10.1088/0741-3335/46/5a/015>.
- [125] N Oyama, K Shinohara, Y Kamada, Y Miura, T Oikawa, and S Takeji. Collapse of density pedestal by giant ELM on JT-60u. *Plasma Physics and Controlled Fusion*, 43(5):717–726, apr 2001. doi:[10.1088/0741-3335/43/5/306](https://doi.org/10.1088/0741-3335/43/5/306). URL <https://doi.org/10.1088/0741-3335/43/5/306>.
- [126] G.T.A Huysmans, T.C Hender, and B Alper. Identification of external kink modes in JET. *Nuclear Fusion*, 38(2):179–187, feb 1998. doi:[10.1088/0029-5515/38/2/303](https://doi.org/10.1088/0029-5515/38/2/303). URL <https://doi.org/10.1088/0029-5515/38/2/303>.
- [127] C. Perez von Thun, L. Frassinetti, L. Horvath, S. Saarelma, L. Meneses, E. de la Luna, M. Beurskens, J. Boom, J. Flanagan, J.C. Hillesheim, C.F. Maggi, S.J.P. Pamela, and E.R. Solano and. Long-lived coupled peeling ballooning modes preceding ELMs on JET. *Nuclear Fusion*, 59(5):056004, mar 2019. doi:[10.1088/1741-4326/ab0031](https://doi.org/10.1088/1741-4326/ab0031). URL <https://doi.org/10.1088/1741-4326/ab0031>.
- [128] M. A. Mahdavi, R. Maingi, R. J. Groebner, A. W. Leonard, T. H. Osborne, and G. Porter. Physics of pedestal density profile formation and its impact on h-mode density limit in burning plasmas. *Physics of Plasmas*, 10(10): 3984–3991, 2003. doi:[10.1063/1.1605101](https://doi.org/10.1063/1.1605101).
- [129] M.E Fenstermacher, T.H Osborne, A.W Leonard, P.B Snyder, D.M Thomas, J.A Boedo, T.A Casper, R.J Groebner, M Groth, M.A.H Kempenaars, A Loarte, G.R McKee, W.M Meyer, G Saibene, M.A VanZeeland, X.Q Xu, L Zeng, and the DIII-D Team. Structure, stability and ELM dynamics of the h-mode pedestal in DIII-d. *Nuclear Fusion*, 45(12):1493–1502, nov 2005. doi:[10.1088/0029-5515/45/12/004](https://doi.org/10.1088/0029-5515/45/12/004). URL <https://doi.org/10.1088/0029-5515/45/12/004>.
- [130] M. N. A. Beurskens, T. H. Osborne, P. A. Schneider, E. Wolfrum, L. Frassinetti, R. Groebner, P. Lomas, I. Nunes, S. Saarelma, R. Scannell, P. B. Snyder, D. Zarzoso, I. Balboa, B. Bray, M. Brix, J. Flanagan, C. Giroud, E. Giovannozzi, M. Kempenaars, A. Loarte, E. de la Luna, G. Maddison, C. F. Maggi, D. McDonald, R. Pasqualotto, G. Saibene, R. Sartori, Emilia R. Solano, M. Walsh, and L. Zabeo. H-mode pedestal scaling in diii-d, asdex upgrade, and jet. *Physics of Plasmas*, 18(5):056120, 2011. doi:[10.1063/1.3593008](https://doi.org/10.1063/1.3593008).
- [131] T H Osborne, R J Groebner, L L Lao, A W Leonard, R Maingi, R L Miller, G D Porter, D M Thomas, and R E Waltz. H-mode pedestal characteristics, ELMs, and energy confinement in ITER shape discharges on DIII-d. *Plasma Physics and Controlled Fusion*, 40(5):845–850, may 1998. doi:[10.1088/0741-3335/40/5/054](https://doi.org/10.1088/0741-3335/40/5/054). URL <https://doi.org/10.1088/0741-3335/40/5/054>.

- [132] R.J Groebner, D.R Baker, K.H Burrell, T.N Carlstrom, J.R Ferron, P Gohil, L.L Lao, T.H Osborne, D.M Thomas, W.P West, J.A Boedo, R.A Moyer, G.R McKee, R.D Deranian, E.J Doyle, C.L Rettig, T.L Rhodes, and J.C Rost. Progress in quantifying the edge physics of the h mode regime in DIII-d. *Nuclear Fusion*, 41(12):1789–1802, dec 2001. doi:[10.1088/0029-5515/41/12/306](https://doi.org/10.1088/0029-5515/41/12/306). URL <https://doi.org/10.1088/0029-5515/41/12/306>.
- [133] H. Urano, T. Takizuka, Y. Kamada, N. Oyama, and H. Takenaga and. Dimensionless parameter dependence of h-mode pedestal width using hydrogen and deuterium plasmas in JT-60u. *Nuclear Fusion*, 48(4):045008, mar 2008. doi:[10.1088/0029-5515/48/4/045008](https://doi.org/10.1088/0029-5515/48/4/045008). URL <https://doi.org/10.1088/0029-5515/48/4/045008>.
- [134] P A Schneider, E Wolfrum, R J Groebner, T H Osborne, M N A Beurskens, M G Dunne, J R Ferron, S Günter, B Kurzan, K Lackner, P B Snyder, H Zohm, , and and. Differences in the h-mode pedestal width of temperature and density. *Plasma Physics and Controlled Fusion*, 54(10):105009, aug 2012. doi:[10.1088/0741-3335/54/10/105009](https://doi.org/10.1088/0741-3335/54/10/105009). URL <https://doi.org/10.1088/0741-3335/54/10/105009>.
- [135] P. B. Snyder, R. J. Groebner, A. W. Leonard, T. H. Osborne, and H. R. Wilson. Development and validation of a predictive model for the pedestal height. *Physics of Plasmas*, 16(5):056118, 2009. doi:[10.1063/1.3122146](https://doi.org/10.1063/1.3122146).
- [136] L. Frassinetti, S. Saarelma, G. Verdoolaege, M. Groth, J.C. Hillesheim, P. Bilkova, P. Bohm, M. Dunne, R. Fridström, E. Giovannozzi, F. Imbeaux, B. Labit, E. de la Luna, C. Maggi, M. Owiak, and R. Scannell. Pedestal structure, stability and scalings in JET-ILW: the EUROfusion JET-ILW pedestal database. *Nuclear Fusion*, 61(1):016001, nov 2020. doi:[10.1088/1741-4326/abb79e](https://doi.org/10.1088/1741-4326/abb79e). URL <https://doi.org/10.1088/1741-4326/abb79e>.
- [137] James D Callen, Chris C Hegna, Bradley W Rice, Edward J Strait, and Alan D Turnbull. Growth of ideal magnetohydrodynamic modes driven slowly through their instability threshold: Application to disruption precursors. *Physics of Plasmas*, 6(8):2963–2967, 1999. doi:[10.1063/1.873583](https://doi.org/10.1063/1.873583).
- [138] A. Kirk, B. Koch, R. Scannell, H. R. Wilson, G. Counsell, J. Dowling, A. Herrmann, R. Martin, and M. Walsh. Evolution of filament structures during edge-localized modes in the mast tokamak. *Phys. Rev. Lett.*, 96:185001, May 2006. doi:[10.1103/PhysRevLett.96.185001](https://doi.org/10.1103/PhysRevLett.96.185001). URL <https://link.aps.org/doi/10.1103/PhysRevLett.96.185001>.
- [139] R.P. Wenninger, H. Reimerdes, O. Sauter, and H. Zohm. Non-linear magnetic perturbations during edge-localized modes in TCV dominated by low-n mode components. *Nuclear Fusion*, 53(11):113004, sep 2013. doi:[10.1088/0029-5515/53/11/113004](https://doi.org/10.1088/0029-5515/53/11/113004). URL <https://doi.org/10.1088/0029-5515/53/11/113004>.

- [140] A F Mink, E Wolfrum, M Dunne, M Hoelzl, M Maraschek, R Fischer, M Caven-  
don, G F Harrer, and U Stroth. Scaling of the toroidal structure and nonlinear  
dynamics of ELMs on ASDEX Upgrade. *Plasma Physics and Controlled Fu-  
sion*, 60(12):125011, nov 2018. doi:[10.1088/1361-6587/aae33a](https://doi.org/10.1088/1361-6587/aae33a).
- [141] Christopher Ham, Andrew Kirk, Stanislas Pamela, and Howard Wilson. Fil-  
amentary plasma eruptions and their control on the route to fusion energy.  
*Nature Reviews Physics*, 2(3):159–167, 2020. doi:[10.1038/s42254-019-0144-1](https://doi.org/10.1038/s42254-019-0144-1).
- [142] G.T.A. Huijsmans and A. Loarte. Non-linear MHD simulation of ELM en-  
ergy deposition. *Nuclear Fusion*, 53(12):123023, nov 2013. doi:[10.1088/0029-5515/53/12/123023](https://doi.org/10.1088/0029-5515/53/12/123023).
- [143] A. W. Leonard, T. H. Osborne, M. E. Fenstermacher, R. J. Groebner,  
M. Groth, C. J. Lasnier, M. A. Mahdavi, T. W. Petrie, P. B. Snyder, J. G.  
Watkins, and L. Zeng. Transport of edge localized modes energy and parti-  
cles into the scrape off layer and divertor of dIII-D. *Physics of Plasmas*, 10(5):  
1765–1772, 2003. doi:[10.1063/1.1567723](https://doi.org/10.1063/1.1567723).
- [144] J. Linke, T. Loewenhoff, V. Massaut, G. Pintsuk, G. Ritz, M. Rödig,  
A. Schmidt, C. Thomser, I. Uytdenhouwen, V. Vasechko, and M. Wirtz. Per-  
formance of different tungsten grades under transient thermal loads. *Nuclear  
Fusion*, 51(7):073017, jun 2011. doi:[10.1088/0029-5515/51/7/073017](https://doi.org/10.1088/0029-5515/51/7/073017). URL  
<https://doi.org/10.1088/0029-5515/51/7/073017>.
- [145] R.A. Pitts, S. Carpentier, F. Escourbiac, T. Hirai, V. Komarov,  
A.S. Kukushkin, S. Lisgo, A. Loarte, M. Merola, R. Mitteau, A.R.  
Raffray, M. Shimada, and P.C. Stangeby. Physics basis and de-  
sign of the ITER plasma-facing components. *Journal of Nuclear  
Materials*, 415(1, Supplement):S957–S964, 2011. ISSN 0022-3115.  
doi:<https://doi.org/10.1016/j.jnucmat.2011.01.114>. URL  
<https://www.sciencedirect.com/science/article/pii/S0022311511001620>. Proceed-  
ings of the 19th International Conference on Plasma-Surface Interactions in  
Controlled Fusion.
- [146] A Loarte, B Lipschultz, A.S Kukushkin, G.F Matthews, P.C Stangeby,  
N Asakura, G.F Counsell, G Federici, A Kallenbach, K Krieger, A Mah-  
davi, V Philipps, D Reiter, J Roth, J Strachan, D Whyte, R Doerner,  
T Eich, W Fundamenski, A Herrmann, M Fenstermacher, P Ghendrih,  
M Groth, A Kirschner, S Konoshima, B LaBombard, P Lang, A.W Leonard,  
P Monier-Garbet, R Neu, H Pacher, B Pegourie, R.A Pitts, S Takamura,  
J Terry, E Tsitrone, the ITPA Scrape-off Layer, and Diver Group. Chap-  
ter 4: Power and particle control. *Nuclear Fusion*, 47(6):S203–S263, jun  
2007. doi:[10.1088/0029-5515/47/6/s04](https://doi.org/10.1088/0029-5515/47/6/s04). URL  
<https://doi.org/10.1088/0029-5515/47/6/s04>.

- [147] F. Wagner, R. Bartiromo, G. Becker, H.S. Bosch, A. Eberhagen, G. Fussmann, O. Gehre, J. Gernhardt, G.V. Gierke, E. Clock, O. Gruber, G. Haas, G. Janeschitz, F. Karger, M. Keilhacker, A. Kislyakov, O. Klüber, M. Kornherr, P.B. Kotzé, K. Lackner, M. Lenoci, G. Lisitano, A. Mahdavi, H.-M. Mayer, K. McCormick, D. Meisel, V. Mertens, E.R. Müller, H. Murmann, H. Niedermeyer, W. Poschenrieder, H. Rapp, F. Ryter, J. Roth, F. Schneider, G. Siller, P. Smeulders, F. Söldner, E. Speth, K. Steinmetz, K.-H. Steuer, and O. Vollmer. Experimental evidence for neoclassical ion transport effects in the h-transition of ASDEX. *Nuclear Fusion*, 25(10):1490–1495, oct 1985. doi:[10.1088/0029-5515/25/10/013](https://doi.org/10.1088/0029-5515/25/10/013). URL <https://doi.org/10.1088/0029-5515/25/10/013>.
- [148] T. Eich, A. Kallenbach, R.A. Pitts, S. Jachmich, J.C. Fuchs, A. Herrmann, and J. Neuhauser. Divertor power deposition and target current asymmetries during type-i elms in asdex upgrade and jet. *Journal of Nuclear Materials*, 363-365:989–993, 2007. ISSN 0022-3115. doi:<https://doi.org/10.1016/j.jnucmat.2007.01.240>. URL <https://www.sciencedirect.com/science/article/pii/S0022311507002036>. Plasma-Surface Interactions-17.
- [149] T. Eich, A. Kallenbach, W. Fundamenski, A. Herrmann, and V. Naulin. On the asymmetries of ELM divertor power deposition in jet and ASDEX Upgrade. *Journal of Nuclear Materials*, 390(Supplement C):760 – 763, 2009. ISSN 0022-3115. doi:[10.1016/j.jnucmat.2009.01.202](https://doi.org/10.1016/j.jnucmat.2009.01.202). Proceedings of the 18th International Conference on Plasma-Surface Interactions in Controlled Fusion Device.
- [150] P. B. Snyder, H. R. Wilson, and X. Q. Xu. Progress in the peeling-balloonning model of edge localized modes: Numerical studies of nonlinear dynamics. *Physics of Plasmas*, 12(5):056115, 2005. doi:[10.1063/1.1873792](https://doi.org/10.1063/1.1873792).
- [151] X.Q. Xu, B.D. Dudson, P.B. Snyder, M.V. Umansky, H.R. Wilson, and T. Casper. Nonlinear ELM simulations based on a nonideal peeling-balloonning model using the BOUT++ code. *Nuclear Fusion*, 51(10):103040, sep 2011. doi:[10.1088/0029-5515/51/10/103040](https://doi.org/10.1088/0029-5515/51/10/103040). URL <https://doi.org/10.1088/0029-5515/51/10/103040>.
- [152] Alexander Kendl, Bruce D. Scott, and Tiago T. Ribeiro. Nonlinear gyrofluid computation of edge localized ideal ballooning modes. *Physics of Plasmas*, 17(7):072302, 2010. doi:[10.1063/1.3449807](https://doi.org/10.1063/1.3449807).
- [153] S.J.P. Pamela, G.T.A. Huijsmans, T. Eich, S. Saarelma, I. Lupelli, C.F. Maggi, C. Giroud, I.T. Chapman, S.F. Smith, L. Frassinetti, M. Becoulet, M. Hoelzl, F. Orain, S. Futatani, and JET Contributors. Recent progress in the quantitative validation of JOREK simulations of ELMs in JET. *Nuclear*

## Bibliography

---

- Fusion*, 57(7):076006, 2017. URL <http://stacks.iop.org/0029-5515/57/i=7/a=076006>.
- [154] L. E. Sugiyama and H. R. Strauss. Magnetic x-points, edge localized modes, and stochasticity. *Physics of Plasmas*, 17(6):062505, 2010. doi:[10.1063/1.3449301](https://doi.org/10.1063/1.3449301).
  - [155] A Y Pankin, G Bateman, D P Brennan, A H Kritz, S Kruger, P B Snyder, C Sovinec, and the NIMROD team. Modelling of ELM dynamics for DIII-d and ITER. *Plasma Physics and Controlled Fusion*, 49(7):S63–S75, jun 2007. doi:[10.1088/0741-3335/49/7/s04](https://doi.org/10.1088/0741-3335/49/7/s04). URL <https://doi.org/10.1088/0741-3335/49/7/s04>.
  - [156] Anthony J. Webster. Magnetohydrodynamic tokamak plasma edge stability. *Nuclear Fusion*, 52(11):114023, oct 2012. doi:[10.1088/0029-5515/52/11/114023](https://doi.org/10.1088/0029-5515/52/11/114023). URL <https://doi.org/10.1088/0029-5515/52/11/114023>.
  - [157] François Orain, M Bécoulet, J Morales, G T A Huijsmans, G Dif-Pradalier, M Hoelzl, X Garbet, S Pamela, E Nardon, C Passeron, G Latu, A Fil, and P Cahyna. Non-linear MHD modeling of edge localized mode cycles and mitigation by resonant magnetic perturbations. *Plasma Physics and Controlled Fusion*, 57(1):014020, nov 2014. doi:[10.1088/0741-3335/57/1/014020](https://doi.org/10.1088/0741-3335/57/1/014020). URL <https://doi.org/10.1088/0741-3335/57/1/014020>.
  - [158] X. Q. Xu, T. Y. Xia, N. Yan, Z. X. Liu, D. F. Kong, A. Diallo, R. J. Groebner, A. E. Hubbard, and J. W. Hughes. Toward integrated multi-scale pedestal simulations including edge-localized-mode dynamics, evolution of edge-localized-mode cycles, and continuous fluctuations. *Physics of Plasmas*, 23(5):055901, 2016. doi:[10.1063/1.4948283](https://doi.org/10.1063/1.4948283).
  - [159] Y B Wu, T Y Xia, F C Zhong, Z Zheng, and J B Liu and. Simulations of particle and heat fluxes in an ELM<sub>h</sub>-mode discharge on EAST using BOUT++ code. *Plasma Physics and Controlled Fusion*, 60(5):055007, mar 2018. doi:[10.1088/1361-6587/aab52c](https://doi.org/10.1088/1361-6587/aab52c). URL <https://doi.org/10.1088/1361-6587/aab52c>.
  - [160] F. Ebrahimi. Nonlinear reconnecting edge localized modes in current-carrying plasmas. *Physics of Plasmas*, 24(5):056119, 2017. doi:[10.1063/1.4983631](https://doi.org/10.1063/1.4983631).
  - [161] M. Bécoulet, M. Kim, G. Yun, S. Pamela, J. Morales, X. Garbet, G.T.A. Huijsmans, C. Passeron, O. Fevrier, M. Hoelzl, A. Lessig, and F. Orain. Non-linear MHD modelling of edge localized modes dynamics in kstar. *Nuclear Fusion*, 57(11):116059, 2017. URL <http://stacks.iop.org/0029-5515/57/i=11/a=116059>.

- [162] M Hoelzl, G T A Huijsmans, F Orain, F J Artola, S Pamela, M Becoulet, D van Vugt, F Liu, S Futatani, A Lessig, E Wolfrum, F Mink, E Trier, M Dunne, E Viezzzer, T Eich, B Vanovac, L Frassinetti, S Guenter, K Lackner, I Krebs, ASDEX Upgrade Team, and EUROfusion MST1 Team. Insights into type-I ELMs and ELM control methods from JOREK MHD simulations. *Contributions to Plasma Physics*, 58:518, 2018. doi:[10.1002/ctpp.201700142](https://doi.org/10.1002/ctpp.201700142).
- [163] D. C. van Vugt, G. T. A. Huijsmans, M. Hoelzl, and A. Loarte. Kinetic modeling of ELM-induced tungsten transport in a tokamak plasma. *Physics of Plasmas*, 26(4):042508, 2019. doi:[10.1063/1.5092319](https://doi.org/10.1063/1.5092319).
- [164] S.F. Smith, S.J.P. Pamela, A. Fil, M. Hödl, G.T.A. Huijsmans, A. Kirk, D. Moulton, O. Myatra, A.J. Thornton, and H.R. Wilson. Simulations of edge localised mode instabilities in MAST-U Super-X tokamak plasmas. *Nuclear Fusion*, 60(6):066021, 2020. doi:[10.1088/1741-4326/ab826a](https://doi.org/10.1088/1741-4326/ab826a).
- [165] G.T.A. Huijsmans, D.C. van Vugt, S. Franssen, S.Q. Korving, and M. Becoulet. Non-linear MHD simulations of ELMs in a high recycling deuterium-tritium deuterator. In *46th European Physical Society Conference on Plasma Physics (EPS), Milan, Italy*, page P2.1059, 2019. URL <http://ocs.ciemat.es/EPS2019PAP/pdf/P1.1059.pdf>.
- [166] F. Orain, M. Hoelzl, F. Mink, M. Willensdorfer, M. Bécoulet, M. Dunne, S. Günter, G. Huijsmans, K. Lackner, S. Pamela, W. Suttrop, and E. Viezzzer. Non-linear modeling of the threshold between ELM mitigation and ELM suppression by resonant magnetic perturbations in ASDEX Upgrade. *Physics of Plasmas*, 26(4):042503, 2019. doi:[10.1063/1.5091843](https://doi.org/10.1063/1.5091843).
- [167] S.K. Kim, S. Pamela, O. Kwon, M. Becoulet, G.T.A. Huijsmans, Y. In, M. Hoelzl, J.H. Lee, M. Kim, G.Y. Park, H. S. Kim, Y.H. Lee, G.J. Choi, C.Y. Lee, A. Kirk, A. Thornton, and Y.-S. Na and. Nonlinear modeling of the effect of  $n = 2$  resonant magnetic field perturbation on peeling-balloonning modes in KSTAR. *Nuclear Fusion*, 60(2):026009, jan 2020. doi:[10.1088/1741-4326/ab5cf0](https://doi.org/10.1088/1741-4326/ab5cf0).
- [168] M Becoulet, G T A Huijsmans, et al. Understanding of physics of Edge Localized Modes suppression by Resonant Magnetic Perturbations based on non-linear MHD modelling. In *17th H-mode Workshop*, Shanghai, China, 2019.
- [169] M Becoulet, G T A Huijsmans, D M Orlov, R A Moyer, T E Evans, and S Futatani. Non-linear MHD modelling of 3-D plasma edge with Resonant Magnetic Perturbations in DIII-D and ITER. In *46th conference on plasma physics*, Milan, Italy, July 2019. URL <https://hal.archives-ouvertes.fr/hal-02796565>.

## Bibliography

---

- [170] R.S. Wilcox, A. Wingen, M.R. Cianciosa, N.M. Ferraro, S.P. Hirshman, C. Paz-Soldan, S. K. Seal, M.W. Shafer, and E.A. Unterberg. Modeling of 3d magnetic equilibrium effects on edge turbulence stability during RMP ELM suppression in tokamaks. *Nuclear Fusion*, 57(11):116003, jul 2017. doi:[10.1088/1741-4326/aa7bad](https://doi.org/10.1088/1741-4326/aa7bad).
- [171] R. A. Moyer, C. Paz-Soldan, R. Nazikian, D. M. Orlov, N. M. Ferraro, B. A. Grierson, M. Knölker, B. C. Lyons, G. R. McKee, T. H. Osborne, T. L. Rhodes, O. Meneghini, S. Smith, T. E. Evans, M. E. Fenstermacher, R. J. Groebner, J. M. Hanson, R. J. La Haye, T. C. Luce, S. Mordijk, W. M. Solomon, F. Turco, Z. Yan, and L. Zeng. Validation of the model for elm suppression with 3d magnetic fields using low torque iter baseline scenario discharges in dIII-d. *Physics of Plasmas*, 24(10):102501, 2017. doi:[10.1063/1.5000276](https://doi.org/10.1063/1.5000276).
- [172] Q.M. Hu, R. Nazikian, B.A. Grierson, N.C. Logan, C. Paz-Soldan, and Q. Yu. The role of edge resonant magnetic perturbations in edge-localized-mode suppression and density pump-out in low-collisionality DIII-d plasmas. *Nuclear Fusion*, 60(7):076001, may 2020. doi:[10.1088/1741-4326/ab8545](https://doi.org/10.1088/1741-4326/ab8545). URL <https://doi.org/10.1088/1741-4326/ab8545>.
- [173] Q. M. Hu, R. Nazikian, B. A. Grierson, N. C. Logan, D. M. Orlov, C. Paz-Soldan, and Q. Yu. Wide operational windows of edge-localized mode suppression by resonant magnetic perturbations in the dIII-d tokamak. *Phys. Rev. Lett.*, 125:045001, Jul 2020. doi:[10.1103/PhysRevLett.125.045001](https://doi.org/10.1103/PhysRevLett.125.045001). URL <https://link.aps.org/doi/10.1103/PhysRevLett.125.045001>.
- [174] Mao Li, Jizhong Sun, Yumin Wang, and Tianyang Xia. Nonlinear simulation of edge localized mode with pressure profile modified by pellet injection through a bout++ three-field mhd model. *Nuclear Materials and Energy*, 26:100888, 2021. ISSN 2352-1791. doi:<https://doi.org/10.1016/j.nme.2020.100888>. URL <https://www.sciencedirect.com/science/article/pii/S2352179120301514>.
- [175] Stephanie Diem, Larry Baylor, Nathaniel M. Ferraro, Brendan Lyons, Daisuke Shiraki, and Robert Wilcox. Utilizing m3d-c1 to understand triggering of elms in dIII-d pellet pacing experiments. In *46th European Physical Society Conference on Plasma Physics (EPS), Milan, Italy*, page P1.1055, 2019. URL <http://ocs.ciemat.es/EPS2019PAP/pdf/P1.1055.pdf>.
- [176] Andreas Wingen, Robert Wilcox, Brendan Lyons, Larry Baylor, Steffie Diem, Morgan Shafer, and Daisuke Shiraki. M3d-c1 modeling of pellet elm triggering in low-collisionality discharges. In *62nd Annual Meeting of the APS Division of Plasma Physics*, page TP15.00019, 2020. URL [http://absimage.aps.org/image/DPP20/MWS\\_DPP20-2020-000052.pdf](http://absimage.aps.org/image/DPP20/MWS_DPP20-2020-000052.pdf).

- [177] A. Wingen, R.S. Wilcox, B.C. Lyons, L.R. Baylor, M.W. Shafer, and D. Shiraki. M3d-c1 modeling of pellet ELM triggering in low-collisionality discharges. In *37th ITPA meeting of the Pedestal and Edge Physics Group*, 2020.
- [178] S. Futatani, S. Pamela, L. Garzotti, G.T.A. Huijsmans, M. Hoelzl, D. Frijione, M. Lennholm, and and. Non-linear magnetohydrodynamic simulations of pellet triggered edge-localized modes in JET. *Nuclear Fusion*, 60(2):026003, dec 2019. doi:[10.1088/1741-4326/ab56c7](https://doi.org/10.1088/1741-4326/ab56c7).
- [179] M Hoelzl, P Merkel, G T A Huysmans, E Nardon, E Strumberger, R McAdams, I Chapman, S Günter, and K Lackner. Coupling JOREK and STARWALL codes for non-linear resistive-wall simulations. *Journal of Physics: Conference Series*, 401:012010, dec 2012. doi:[10.1088/1742-6596/401/1/012010](https://doi.org/10.1088/1742-6596/401/1/012010).
- [180] G. S. Xu, Q. Q. Yang, N. Yan, Y. F. Wang, X. Q. Xu, H. Y. Guo, R. Maingi, L. Wang, J. P. Qian, X. Z. Gong, V. S. Chan, T. Zhang, Q. Zang, Y. Y. Li, L. Zhang, G. H. Hu, and B. N. Wan. Promising high-confinement regime for steady-state fusion. *Phys. Rev. Lett.*, 122:255001, Jun 2019. doi:[10.1103/PhysRevLett.122.255001](https://doi.org/10.1103/PhysRevLett.122.255001). URL <https://link.aps.org/doi/10.1103/PhysRevLett.122.255001>.
- [181] F Liu, G T A Huijsmans, A Loarte, A M Garofalo, W M Solomon, M Hoelzl, B Nkonga, S Pamela, M Becoulet, F Orain, and D Van Vugt. Nonlinear MHD simulations of QH-mode DIII-D plasmas and implications for ITER high Q scenarios. *Plasma Physics and Controlled Fusion*, 60(1):014039, nov 2017. doi:[10.1088/1361-6587/aa934f](https://doi.org/10.1088/1361-6587/aa934f).
- [182] J. R. King, S. E. Kruger, K. H. Burrell, X. Chen, A. M. Garofalo, R. J. Groebner, K. E. J. Olofsson, A. Y. Pankin, and P. B. Snyder. Mhd modeling of a diii-d low-torque qh-mode discharge and comparison to observations. *Physics of Plasmas*, 24(5):055902, 2017. doi:[10.1063/1.4977467](https://doi.org/10.1063/1.4977467).
- [183] A.Y. Pankin, J.R. King, S.E. Kruger, Xi Chen, K.H. Burrell, A.M. Garofalo, R. J. Groebner, G.R. McKee, and Z. Yan. Towards validated MHD modeling of edge harmonic oscillation in DIII-d QH-mode discharges. *Nuclear Fusion*, 60(9):092004, jul 2020. doi:[10.1088/1741-4326/ab9afe](https://doi.org/10.1088/1741-4326/ab9afe). URL <https://doi.org/10.1088/1741-4326/ab9afe>.
- [184] J. G. Chen, X. Q. Xu, C. H. Ma, P. W. Xi, D. F. Kong, and Y. A. Lei. Impact of ExB shear flow on low-n MHD instabilities. *Physics of Plasmas*, 24(5):050704, 2017. doi:[10.1063/1.4984257](https://doi.org/10.1063/1.4984257).
- [185] M. Faitsch, T. Eich, G.F. Harrer, E. Wolfrum, D. Brida, P. David, M. Griener, and U. Stroth. Broadening of the power fall-off length

## Bibliography

---

- in a high density, high confinement h-mode regime in asdex upgrade. *Nuclear Materials and Energy*, 26:100890, 2021. ISSN 2352-1791. doi:<https://doi.org/10.1016/j.nme.2020.100890>. URL <https://www.sciencedirect.com/science/article/pii/S2352179120301526>.
- [186] J Neuhauser, D Coster, H U Fahrbach, J C Fuchs, G Haas, A Herrmann, L Horton, M Jakobi, A Kallenbach, M Laux, J W Kim, B Kurzan, H W Müller, H Murmann, R Neu, V Rohde, W Sandmann, W Suttrop, E Wolfrum, and the ASDEX Upgrade Team. Transport into and across the scrape-off layer in the ASDEX upgrade divertor tokamak. *Plasma Physics and Controlled Fusion*, 44(6):855–869, may 2002. doi:[10.1088/0741-3335/44/6/316](https://doi.org/10.1088/0741-3335/44/6/316). URL <https://doi.org/10.1088/0741-3335/44/6/316>.
- [187] M Bernert, T Eich, A Kallenbach, D Carralero, A Huber, P T Lang, S Potzel, F Reimold, J Schweinzer, E Viezzner, and H Zohm. The h-mode density limit in the full tungsten ASDEX upgrade tokamak. *Plasma Physics and Controlled Fusion*, 57(1):014038, nov 2014. doi:[10.1088/0741-3335/57/1/014038](https://doi.org/10.1088/0741-3335/57/1/014038). URL <https://doi.org/10.1088/0741-3335/57/1/014038>.
- [188] M. Griener, E. Wolfrum, G. Birkenmeier, M. Faitsch, R. Fischer, G. Fuchert, L. Gil, G.F. Harrer, P. Manz, D. Wendler, and U. Stroth. Continuous observation of filaments from the confined region to the far scrape-off layer. *Nuclear Materials and Energy*, 25:100854, 2020. ISSN 2352-1791. doi:<https://doi.org/10.1016/j.nme.2020.100854>. URL <https://www.sciencedirect.com/science/article/pii/S2352179120301204>.
- [189] Hongjuan Sun, Robert James Goldston, Alexander Huber, Xueqiao Xu, Joanne Flanagan, Darren Charles McDonald, Elena de la Luna, Mikhail Maslov, James R Harrison, Fulvio Militello, John Fessey, and Simon Cramp. The role of edge plasma parameters in h-mode density limit on the jet-ilw. *Nuclear Fusion*, 2021. URL <http://iopscience.iop.org/article/10.1088/1741-4326/abf056>.
- [190] A Cathey, M Hoelzl, E Wolfrum, M Dunne, SJP Pamela, F Orain, AF Mink, GTA Huijsmans, S Guenter, EUROfusion MST1 Team, et al. Non-linear simulations of elms and edge localised instabilities during the inter-elm pedestal recovery at asdex-upgrade. In *17th International Workshop on H-mode Physics and Transport Barriers (HMWS 2019)*, 2019.
- [191] A Cathey, M Hoelzl, K Lackner, GTA Huijsmans, MG Dunne, E Wolfrum, SJP Pamela, F Orain, S Günter, ASDEX Upgrade Team, et al. Jorek simulations of multiple type-i elms and small elms in asdex upgrade. In *4th Asia Pacific Conference on Plasma Physics (AAPPS-DPP 2020)(Virtual)*, 2020.
- [192] Patrick J McCarthy, Peter Martin, and Wolfgang Schneider. The CLISTE interpretive equilibrium code. Technical report, Max-Planck-Institut für

- Plasmaphysik, 1999. URL [http://pubman.mpdl.mpg.de/pubman/item/escidoc:2130737/component/escidoc:2130736/IPP\\_5\\_85.pdf](http://pubman.mpdl.mpg.de/pubman/item/escidoc:2130737/component/escidoc:2130736/IPP_5_85.pdf). IPP Report 5/85.
- [193] Matthias Hölzl. *Diffusive heat transport across magnetic islands and stochastic layers in tokamaks*. PhD thesis, Technische Universität München, 2010. URL <https://mediatum.ub.tum.de/doc/820982/file.pdf>.
- [194] M.G. Dunne, P.J. McCarthy, E. Wolfrum, R. Fischer, L. Giannone, and A. Burckhart and. Measurement of neoclassically predicted edge current density at ASDEX upgrade. *Nuclear Fusion*, 52(12):123014, nov 2012. doi:[10.1088/0029-5515/52/12/123014](https://doi.org/10.1088/0029-5515/52/12/123014). URL <https://doi.org/10.1088/0029-5515/52/12/123014>.
- [195] Gregorij V Pereverzev and PN Yushmanov. Astra. automated system for transport analysis in a tokamak. Technical report, Max-Planck-Institut für Plasmaphysik, 2002. URL [https://pure.mpg.de/rest/items/item\\_2138238/component/file\\_2138237/content](https://pure.mpg.de/rest/items/item_2138238/component/file_2138237/content).
- [196] I. Krebs, M. Hoelzl, K. Lackner, and S. Guenter. Nonlinear excitation of low-n harmonics in reduced magnetohydrodynamic simulations of edge-localized modes. *Physics of Plasmas*, 20(8):082506, 2013. doi:[10.1063/1.4817953](https://doi.org/10.1063/1.4817953).
- [197] J. A. Morales, M. Bécoulet, X. Garbet, F. Orain, G. Dif-Pradalier, M. Hoelzl, S. Pamela, G. T. A. Huijsmans, P. Cahyna, A. Fil, E. Nardon, C. Passeron, and G. Latu. Edge localized mode rotation and the nonlinear dynamics of filaments. *Physics of Plasmas*, 23(4):042513, 2016. doi:[10.1063/1.4947201](https://doi.org/10.1063/1.4947201).
- [198] P. Sauter, T. Pütterich, F. Ryter, E. Viezzer, E. Wolfrum, G.D. Conway, R. Fischer, B. Kurzan, R.M. McDermott, and S.K. Rathgeber and. L- to h-mode transitions at low density in ASDEX upgrade. *Nuclear Fusion*, 52(1):012001, dec 2011. doi:[10.1088/0029-5515/52/1/012001](https://doi.org/10.1088/0029-5515/52/1/012001). URL <https://doi.org/10.1088/0029-5515/52/1/012001>.
- [199] M. Cavedon, G. Birkenmeier, T. Pütterich, F. Ryter, E. Viezzer, E. Wolfrum, R. Dux, T. Happel, P. Hennequin, U. Plank, U. Stroth, and M. Willensdorfer and. Connecting the global h-mode power threshold to the local radial electric field at ASDEX upgrade. *Nuclear Fusion*, 60(6):066026, may 2020. doi:[10.1088/1741-4326/ab8777](https://doi.org/10.1088/1741-4326/ab8777). URL <https://doi.org/10.1088/1741-4326/ab8777>.
- [200] M G Dunne, S Potzel, F Reimold, M Wischmeier, E Wolfrum, L Frassinetti, M Beurskens, P Bilkova, M Cavedon, R Fischer, B Kurzan, F M Laggner, R M McDermott, G Tardini, E Trier, E Viezzer, M Willensdorfer, and and. The role of the density profile in the ASDEX-upgrade pedestal structure. *Plasma Physics and Controlled Fusion*, 59(1):014017,

- oct 2016. doi:[10.1088/0741-3335/59/1/014017](https://doi.org/10.1088/0741-3335/59/1/014017). URL <https://doi.org/10.1088/0741-3335/59/1/014017>.
- [201] L. Frassinetti, M.G. Dunne, U. Sheikh, S. Saarelma, C.M. Roach, E. Stefanikova, C. Maggi, L. Horvath, S. Pamela, E. de la Luna, E. Wolfrum, M. Bernert, P. Blanchard, B. Labit, A. Merle, L. Guimarais, S. Coda, H. Meyer, J.C. Hillesheim, , , and and. Role of the pedestal position on the pedestal performance in AUG, JET-ILW and TCV and implications for ITER. *Nuclear Fusion*, 59(7):076038, jun 2019. doi:[10.1088/1741-4326/ab1eb9](https://doi.org/10.1088/1741-4326/ab1eb9). URL <https://doi.org/10.1088/1741-4326/ab1eb9>.
- [202] E A Belli, J Candy, O Meneghini, and T H Osborne. Limitations of bootstrap current models. *Plasma Physics and Controlled Fusion*, 56(4):045006, mar 2014. doi:[10.1088/0741-3335/56/4/045006](https://doi.org/10.1088/0741-3335/56/4/045006). URL <https://doi.org/10.1088/0741-3335/56/4/045006>.
- [203] Daniël Cornelis van Vugt. *Nonlinear coupled MHD-kinetic particle simulations of heavy impurities in tokamak plasmas*. PhD thesis, Technische Universiteit Eindhoven, Department of Applied Physics, 7 2019. URL <https://research.tue.nl/en/publications/nonlinear-coupled-mhd-kinetic-particle-simulations-of-heavy-impur>. Proefschrift.
- [204] A Diallo and F M Laggner. Review: Turbulence dynamics during the pedestal evolution between edge localized modes in magnetic fusion devices. *Plasma Physics and Controlled Fusion*, 63(1):013001, nov 2020. doi:[10.1088/1361-6587/abbf85](https://doi.org/10.1088/1361-6587/abbf85). URL <https://doi.org/10.1088/1361-6587/abbf85>.
- [205] D.R. Hatch, D. Told, F. Jenko, H. Doerk, M.G. Dunne, E. Wolfrum, E. Viezzer, and M.J. Pueschel and. Gyrokinetic study of ASDEX upgrade inter-ELM pedestal profile evolution. *Nuclear Fusion*, 55(6):063028, may 2015. doi:[10.1088/0029-5515/55/6/063028](https://doi.org/10.1088/0029-5515/55/6/063028). URL <https://doi.org/10.1088/0029-5515/55/6/063028>.
- [206] D.R. Hatch, M. Kotschenreuther, S. Mahajan, P. Valanju, F. Jenko, D. Told, T. Görler, and S. Saarelma. Microtearing turbulence limiting the JET-ILW pedestal. *Nuclear Fusion*, 56(10):104003, aug 2016. doi:[10.1088/0029-5515/56/10/104003](https://doi.org/10.1088/0029-5515/56/10/104003). URL <https://doi.org/10.1088/0029-5515/56/10/104003>.
- [207] K. Stimmel, A. Bañón Navarro, T. Happel, D. Told, T. Görler, E. Wolfrum, J. P. Martin Collar, R. Fischer, P. A. Schneider, and F. Jenko. Gyrokinetic investigation of the asdex upgrade i-mode pedestal. *Physics of Plasmas*, 26(12):122504, 2019. doi:[10.1063/1.5124986](https://doi.org/10.1063/1.5124986).
- [208] D R Hatch, R D Hazeltine, M K Kotschenreuther, and S M Mahajan. Flow shear suppression of pedestal ion temperature gradient turbulence-a

- first principles theoretical framework. *Plasma Physics and Controlled Fusion*, 60(8):084003, jun 2018. doi:[10.1088/1361-6587/aac7a7](https://doi.org/10.1088/1361-6587/aac7a7). URL <https://doi.org/10.1088/1361-6587/aac7a7>.
- [209] K. L. van de Plassche, J. Citrin, C. Bourdelle, Y. Camenen, F. J. Casson, V. I. Dagnelie, F. Felici, A. Ho, and S. Van Mulders. Fast modeling of turbulent transport in fusion plasmas using neural networks. *Physics of Plasmas*, 27(2):022310, 2020. doi:[10.1063/1.5134126](https://doi.org/10.1063/1.5134126).
  - [210] T Kass, S Günter, M Maraschek, W Suttrop, H Zohm, and ASDEX Upgrade Team. Characteristics of type i and type iii elm precursors in asdex upgrade. *Nuclear fusion*, 38(1):111, 1998. doi:[10.1088/0029-5515/38/1/310](https://doi.org/10.1088/0029-5515/38/1/310).
  - [211] Felician Mink, Elisabeth Wolfrum, Marc Maraschek, Hartmut Zohm, Laszki Horvath, Florian M Laggner, Peter Manz, Eleonora Viezzler, Ulrich Stroth, and the ASDEX Upgrade Team. Toroidal mode number determination of ELM associated phenomena on ASDEX Upgrade. *Plasma Physics and Controlled Fusion*, 58(12):125013, 2016. URL <http://stacks.iop.org/0741-3335/58/i=12/a=125013>.
  - [212] N Oyama, K Shinozaki, Y Kamada, Y Miura, T Oikawa, and S Takeji. Collapse of density pedestal by giant elm on jt-60u. *Plasma physics and controlled fusion*, 43(5):717, 2001. doi:[10.1088/0741-3335/43/5/306](https://doi.org/10.1088/0741-3335/43/5/306).
  - [213] CP Perez, HR Koslowski, GTA Huysmans, TC Hender, P Smeulders, B Alper, E De La Luna, RJ Hastie, L Meneses, MFF Nave, et al. Type-i elm precursor modes in jet. *Nuclear fusion*, 44(5):609, 2004. doi:[10.1088/0029-5515/44/5/005](https://doi.org/10.1088/0029-5515/44/5/005).
  - [214] R Maingi, CE Bush, ED Fredrickson, DA Gates, SM Kaye, BP LeBlanc, JE Menard, H Meyer, D Mueller, N Nishino, et al. H-mode pedestal, elm and power threshold studies in nstx. *Nuclear Fusion*, 45(9):1066, 2005. doi:[10.1088/0029-5515/45/9/006](https://doi.org/10.1088/0029-5515/45/9/006).
  - [215] A Kirk, D Dunai, M Dunne, G Huijsmans, S Pamela, M Becoulet, JR Harrison, J Hillesheim, C Roach, and S Saarelma. Recent progress in understanding the processes underlying the triggering of and energy loss associated with type i elms. *Nuclear Fusion*, 54(11):114012, 2014. doi:[10.1088/0029-5515/54/11/114012](https://doi.org/10.1088/0029-5515/54/11/114012).
  - [216] P Manz, J E Boom, E Wolfrum, G Birkenmeier, I G J Classen, N C Luhmann, and U Stroth and. Velocimetry analysis of type-i edge localized mode precursors in ASDEX upgrade. *Plasma Physics and Controlled Fusion*, 56(3):035010, feb 2014. doi:[10.1088/0741-3335/56/3/035010](https://doi.org/10.1088/0741-3335/56/3/035010). URL <https://doi.org/10.1088/0741-3335/56/3/035010>.

## Bibliography

---

- [217] James D Callen, Chris C Hegna, Bradley W Rice, Edward J Strait, and Alan D Turnbull. Growth of ideal magnetohydrodynamic modes driven slowly through their instability threshold: Application to disruption precursors. *Physics of Plasmas*, 6(8):2963–2967, 1999. doi:[10.1063/1.873583](https://doi.org/10.1063/1.873583).
- [218] Th Eich, A Herrmann, P Andrew, A Loarte, et al. Power deposition measurements in deuterium and helium discharges in jet mkiigb divertor by ir-thermography. *Journal of nuclear materials*, 313:919–924, 2003. doi:[10.1016/S0022-3115\(02\)01477-0](https://doi.org/10.1016/S0022-3115(02)01477-0).
- [219] GL Jackson, J Winter, TS Taylor, KH Burrell, JC DeBoo, CM Greenfield, RJ Groebner, T Hodapp, K Holtrop, EA Lazarus, et al. Regime of very high confinement in the boronized diii-d tokamak. *Physical review letters*, 67(22):3098, 1991. doi:[10.1103/PhysRevLett.67.3098](https://doi.org/10.1103/PhysRevLett.67.3098).
- [220] MFF Nave, P Smeulders, TC Hender, PJ Lomas, B Alper, P Bak, B Balet, JP Christiansen, S Clement, HPL De Esch, et al. An overview of mhd activity at the termination of jet hot ion h modes. *Nuclear fusion*, 37(6):809, 1997. doi:[10.1088/0029-5515/37/6/I08](https://doi.org/10.1088/0029-5515/37/6/I08).
- [221] AV Chankin, N Asakura, T Fukuda, A Isayama, K Itami, Y Kamada, H Kubo, Y Miura, T Nakano, N Oyama, et al. Influence of plasma–wall interactions on the behaviour of elms in jt-60u. *Journal of nuclear materials*, 313:828–833, 2003. doi:[10.1016/S0022-3115\(02\)01458-7](https://doi.org/10.1016/S0022-3115(02)01458-7).
- [222] GTA Huysmans, TC Hender, and B Alper. Identification of external kink modes in jet. *Nuclear fusion*, 38(2):179, 1998. doi:[10.1088/0029-5515/38/2/303](https://doi.org/10.1088/0029-5515/38/2/303).
- [223] A Loarte, M Becoulet, G Saibene, R Sartori, D J Campbell, T Eich, A Herrmann, M Laux, W Suttrop, B Alper, P J Lomas, G Matthews, S Jachmich, J Ongena, P Innocente, and EFDA-JET Workprogramme Collaborators. Characteristics and scaling of energy and particle losses during type i ELMs in JET h-modes. *Plasma Physics and Controlled Fusion*, 44(9):1815–1844, aug 2002. doi:[10.1088/0741-3335/44/9/303](https://doi.org/10.1088/0741-3335/44/9/303). URL <https://doi.org/10.1088/0741-3335/44/9/303>.
- [224] H. R. Wilson and S. C. Cowley. Theory for explosive ideal magnetohydrodynamic instabilities in plasmas. *Phys. Rev. Lett.*, 92:175006, Apr 2004. doi:[10.1103/PhysRevLett.92.175006](https://doi.org/10.1103/PhysRevLett.92.175006). URL <https://link.aps.org/doi/10.1103/PhysRevLett.92.175006>.
- [225] J Dominski and A Diallo. Identification of a network of nonlinear interactions as a mechanism triggering the onset of edge localized modes. *Plasma Physics and Controlled Fusion*, 62(9):095011, jul 2020. doi:[10.1088/1361-6587/ab9c48](https://doi.org/10.1088/1361-6587/ab9c48). URL <https://doi.org/10.1088/1361-6587/ab9c48>.

- [226] EDA ITER et al. Mhd stability, operational limits and disruptions. *Nuclear Fusion*, 39(12 ITER physics basis):2251–2389, 1999. doi:[10.1088/0029-5515/39/12/303](https://doi.org/10.1088/0029-5515/39/12/303).
- [227] T.E. Evans, M.E. Fenstermacher, R.A. Moyer, T.H. Osborne, J.G. Watkins, P. Gohil, I. Joseph, M.J. Schaffer, L.R. Baylor, M. Bécoulet, J.A. Boedo, K.H. Burrell, J.S. deGrassie, K.H. Finken, T. Jernigan, M.W. Jakubowski, C.J. Lasnier, M. Lehnert, A.W. Leonard, J. Lonnroth, E. Nardon, V. Parail, O. Schmitz, B. Unterberg, and W.P. West. Rmp ELM suppression in diii-d plasmas with iter similar shapes and collisionalities. *Nuclear Fusion*, 48(2):024002, 2008. URL <http://stacks.iop.org/0029-5515/48/i=2/a=024002>.
- [228] P.T. Lang, G.D. Conway, T. Eich, L. Fattorini, O. Gruber, S. Günter, L.D. Horton, S. Kalvin, A. Kallenbach, M. Kaufmann, G. Kocsis, A. Lorenz, M.E. Manso, M. Maraschek, V. Mertens, J. Neuhauser, I. Nunes, W. Schneider, W. Suttrop, H. Urano, and the ASDEX Upgrade Team. ELM pace making and mitigation by pellet injection in ASDEX Upgrade. *Nuclear Fusion*, 44(5):685, 2004. URL <https://iopscience.iop.org/article/10.1088/0029-5515/44/5/010/meta>.
- [229] L. R. Baylor, N. Commaux, T. C. Jernigan, N. H. Brooks, S. K. Combs, T. E. Evans, M. E. Fenstermacher, R. C. Isler, C. J. Lasnier, S. J. Meitner, R. A. Moyer, T. H. Osborne, P. B. Parks, P. B. Snyder, E. J. Strait, E. A. Unterberg, , and A. Loarte. Reduction of edge-localized mode intensity using high-repetition-rate pellet injection in tokamak H-Mode plasmas. *Physical Review Letters*, 110:245001, 2013. URL <https://doi.org/10.1103/PhysRevLett.110.245001>.
- [230] A Herrmann. Overview on stationary and transient divertor heat loads. *Plasma Physics and Controlled Fusion*, 44(6):883–903, may 2002. doi:[10.1088/0741-3335/44/6/318](https://doi.org/10.1088/0741-3335/44/6/318). URL <https://doi.org/10.1088/0741-3335/44/6/318>.
- [231] G. Kocsis, S. Kálvin, P.T. Lang, M. Maraschek, J. Neuhauser, W. Schneider, and T. Szepesi. Spatio-temporal investigations on the triggering of pellet induced ELMs. *Nuclear Fusion*, 47(9):1166–1175, aug 2007. doi:[10.1088/0029-5515/47/9/013](https://doi.org/10.1088/0029-5515/47/9/013). URL <https://doi.org/10.1088/0029-5515/47/9/013>.
- [232] F. Romanelli, R. Kamendje, and on behalf of JET-EFDA Contributors. Overview of JET results. *Nuclear Fusion*, 49(10):104006, 2009. URL <https://iopscience.iop.org/article/10.1088/0029-5515/49/10/104006/meta>.
- [233] P T Lang, H Meyer, G Birkenmeier, A Burckhart, I S Carvalho, E Delabie, L Frassinetti, G Huijsmans, A Loarte G Kocsi and, C F Maggi, M Maraschek,

- B Ploeckl, F Rimini, F Ryter, S Saarelma, T Szepesi, E Wolfrum, ASDEX Upgrade Team, and JET Contributors. ELM control at the L-H transition by means of pellet pacing in the asdex upgrade and JET all-metal-wall tokamaks. *Plasma Physics and Controlled Fusion*, 57(4):045011, 2015. URL <https://iopscience.iop.org/article/10.1088/0741-3335/57/4/045011/meta>.
- [234] P A Schneider, L Barrera Orte, A Burckhart, M G Dunne, C Fuchs, A Gude, B Kurzan, W Suttrop, E Wolfrum, and the ASDEX Upgrade Team. Pedestal and edge localized mode characteristics with different first wall materials and nitrogen seeding in ASDEX Upgrade. *Plasma Physics and Controlled Fusion*, 57(1):014029, 2015. URL <http://stacks.iop.org/0741-3335/57/i=1/a=014029>.
- [235] P. T. Lang, P. Cierpka, O. Gehre, M. Reich, C. Wittmann, A. Lorenz, D. Frigione, S. Kalvin, G. Kocsis, and S. Maruyama. A system for cryogenic hydrogen pellet high speed inboard launch into a fusion device via guiding tube transfer. *Review of Scientific Instruments*, 74(9):3974–3983, 2003. doi:[10.1063/1.1602940](https://doi.org/10.1063/1.1602940). URL <https://doi.org/10.1063/1.1602940>.
- [236] T Eich, A Herrmann, J Neuhauser, R Dux, J C Fuchs, S Günter, L D Horton, A Kallenbach, P T Lang, C F Maggi, M Maraschek, V Rohde, W Schneider, and the ASDEX Upgrade Team. Type-i ELM substructure on the divertor target plates in ASDEX Upgrade. *Plasma Physics and Controlled Fusion*, 47 (6):815, 2005. URL <http://stacks.iop.org/0741-3335/47/i=6/a=007>.
- [237] M.W. Jakubowski, T.E. Evans, M.E. Fenstermacher, M. Groth, C.J. Lasnier, A.W. Leonard, O. Schmitz, J.G. Watkins, T. Eich, W. Fundamenski, R.A. Moyer, R.C. Wolf, L.B. Baylor, J.A. Boedo, K.H. Burrell, H. Frerichs, J.S. de-Grassie, P. Gohil, I. Joseph, S. Mordijk, M. Lehnert, C.C. Petty, R.I. Pinsker, D. Reiter, T.L. Rhodes, U. Samm, M.J. Schaffer, P.B. Snyder, H. Stoschus, T. Osborne, B. Unterberg, E. Unterberg, and W.P. West. Overview of the results on divertor heat loads in RMP controlled h-mode plasmas on DIII-d. *Nuclear Fusion*, 49(9):095013, aug 2009. doi:[10.1088/0029-5515/49/9/095013](https://doi.org/10.1088/0029-5515/49/9/095013). URL <https://doi.org/10.1088%2F0029-5515%2F49%2F9%2F095013>.
- [238] F.M. Poli, P.T. Lang, S.E. Sharapov, B. Alper, and H.R. Koslowski and. Spectra of magnetic perturbations triggered by pellets in JET plasmas. *Nuclear Fusion*, 50(2):025004, jan 2010. doi:[10.1088/0029-5515/50/2/025004](https://doi.org/10.1088/0029-5515/50/2/025004). URL <https://doi.org/10.1088%2F0029-5515%2F50%2F2%2F025004>.

# Acknowledgements

Let's switch to first person. I end this thesis by saying that it was made possible with the support of several people throughout the past 3.5 years. First of all, I want to thank Sibylle Günter and Matthias Hoelzl for their remarkable supervision and guidance. Thank you for introducing me to fusion plasma physics with such an interesting research topic. My most sincere admiration to Sibylle who always found time to share her knowledge with me. I am immensely grateful with Matthias for his patience and support. Matthias spared no time in clarifying doubts about physics/computing/JOREK/etc. I feel fortunate for having been under their supervision, and I am eager to continue working together. Before moving forward, I want to stress how important they have been in keeping me motivated and inspired.

I would also like to thank Karl Lackner for the motivating discussions which helped deepen my understanding of physical processes in confined plasmas. Thank you to Elisabeth Wolfrum who gave me great support and sat down with me to clarify several doubts. Thanks to Mike Dunne for dedicating time to help me when I felt all my simulations were nonsense. I am specially grateful to Guido Huijsmans for always being kind with me and helping me when needed, and also for agreeing to act as external referee for the thesis.

Big thanks to everyone in the JOREK team for creating such a friendly environment. I would like to thank Stanislas Pamela, Javier Artola, and Francois Orain for their support at various stages during my PhD years. I want to specifically thank Shimpei Futatani for all the work we produced together. For help with proof-reading different chapters of the thesis, thank you Vinodh Bandaru, Michael Bergmann, Georg Harrer, and Rohan Ramasamy.

I would like to thank many people at IPP who have made me feel welcome. Thank you to Hartmut Zohm for showing interest in my work and for discussing with me even on his bike. I am grateful to Peter Lang, who helped me understand many things regarding the triggering of ELMs through pellet injection, to Thomas Eich, for his optimism and for sharing some of his great knowledge on ELMs with me. Thank you to Clemente Angioni who sat down with me to clarify doubts on several occasions and helped me understand more about neoclassical physics. My

## Bibliography

---

gratitude to Eleonora Viezzer, who was often willing to discuss with me about ELMs and the edge radial electric field, and to Marco Cavedon, who sat down with me several times to answer questions regarding plasma physics and climbing. A special thanks goes to Georg Harrer for helping me expand my knowledge on small ELMs from the experimental point of view. Thank you to Wei Zhang and Anton Jansen van Vuuren for showing interest in my results and for the collaborations that were forged. Thanks to the EUROfusion MST1 team and, in particular, to Hendrik Mayer and Benoit Labit for insightful comments on the various documents that passed through the pinboard.

I also want to express my gratitude to the friends that I have found at IPP. To the Office 300+Nathan group: Victor Artigues, Michael Bergmann, Alessandro di Siena, Robin Greif, Daniel Groselj, Francisco Matos and, the honorary member, Felipe Nathan. To the *gringos*: Robert Brzozowski, Paul Crandall, Cole Stephens, and Karl Stimmel. To my climbing buddies: Tom Body, Teo Luda, and Adam Pataki. Thanks also to Nicola Bonanomi, Pierre David, Monika Kolleva, Dmytro Meshcheriakov, Pedro Molina, Davide Silvagni, Fabian Wieschollek, Vladimir Zholobenko. Michael Bergmann and the people that lived in the IPP guest house, Diego Calderon, Mauricio Cuevas, Saso Drenik, Felipe Nathan, Manca Novinek, and Adam Pataki, have made me feel particularly welcome in Germany, and I am very grateful for them.

También quiero agradecerles a mis amigos más viejos: Georgios Billis, Ramiro Cadena, Harold Cardona, David Hervas, George Holder, Santiago Paredes, Jordan Pierce y Alessandro Veltri por apoyarme aún cuando la distancia lo dificultaba. Con énfasis particular quiero agradecer a mis padres, Alan y Mónica, y a mi hermano, Alejandro, por tenerme paciencia y por ayudarme a despertar y mantener mi curiosidad. Finalmente, mil gracias a las dos personas más importantes de mi vida, mi esposa Paula y mi hija Luna. La Paula me ha enseñado como ser mejor en todos los pasos de este viaje. Al mismo tiempo, me ha hecho reír a caracajadas y me ha mantenido motivado. No tengo palabras para expresar la gratitud que siento por ella y por el apoyo que me ha dado mientras escribía esta tesis. La Luna ha sido mi fuente inagotable de inspiración y de energía. De cierta forma, ella es mi *reactor de fusión nuclear*. Como diría René: “*Todo lo que hago lo hago por ti; es que tú me sacas lo mejor de mí. Soy todo lo que soy, porque tú eres todo lo que quiero.*”

“*Bueno y de ahí a la selva, a la playa, a las montañas y al bosque.*”